

AD-784 594

INVESTIGATION OF THE EFFECTS OF BLADE
STRUCTURAL DESIGN PARAMETERS ON HELI-
COPTER STALL BOUNDARIES

R. H. Blackwell, et al

United Aircraft Corporation

Prepared for:

Army Air Mobility Research and
Development Laboratory

May 1974

DISTRIBUTED BY:

NTIS

National Technical Information Service
U. S. DEPARTMENT OF COMMERCE
5285 Port Royal Road, Springfield Va. 22151

**Best
Available
Copy**

Unclassified

SECURITY CLASSIFICATION OF THIS PAGE (When Data Entered)

REPORT DOCUMENTATION PAGE		READ INSTRUCTIONS BEFORE COMPLETING FORM	
1. REPORT NUMBER USAAMPDL-TR-74-25	2. GOVT ACCESSION NO.	3. RECIPIENT'S CATALOG NUMBER AD 784 594	
4. TITLE (and Subtitle) INVESTIGATION OF THE EFFECTS OF BLADE STRUCTURAL DESIGN PARAMETERS ON HELICOPTER STALL BOUNDARIES		5. TYPE OF REPORT & PERIOD COVERED Final Report	
		6. PERFORMING ORG. REPORT NUMBER	
7. AUTHOR(s) R. H. Blackwell G. L. Commerford		8. CONTRACT OR GRANT NUMBER(s) Contract DAAJ02-72-C-0105	
9. PERFORMING ORGANIZATION NAME AND ADDRESS Sikorsky Aircraft Division of United Aircraft Corporation Stratford, Connecticut 06602		10. PROGRAM ELEMENT, PROJECT, TASK AREA & WORK UNIT NUMBERS Project 1F162208AA82	
11. CONTROLLING OFFICE NAME AND ADDRESS Eustis Directorate U. S. Army Air Mobility R&D Laboratory Fort Eustis, Virginia 23604		12. REPORT DATE May 1974	
		13. NUMBER OF PAGES 157	
14. MONITORING AGENCY NAME & ADDRESS (if different from Controlling Office)		15. SECURITY CLASS. (of this report) Unclassified	
		15a. DECLASSIFICATION/DOWNGRADING SCHEDULE	
16. DISTRIBUTION STATEMENT (of this Report) Approved for public release; distribution unlimited.			
17. DISTRIBUTION STATEMENT (of the abstract entered in Block 20, if different from Report)			
18. SUPPLEMENTARY NOTES			
19. KEY WORDS (Continue on reverse side if necessary and identify by block number) Helicopters Stalling Flutter Rotor blades Reproduced by NATIONAL TECHNICAL INFORMATION SERVICE U. S. Department of Commerce Springfield, VA 22151			
20. ABSTRACT (Continue on reverse side if necessary and identify by block number) An experimental and analytical study was conducted to determine the effects of blade structural design parameters on the stall-related operating boundaries of helicopter main rotors. Emphasis was placed on the effects of blade torsional properties on the buildup of vibratory control loads in stall. The analytical methods used in the study were evaluated through correlation with data for two full-scale rotors and data obtained (under			

DDC
RECEIVED
SEP 10 1974
REGISTRY
D

DD FORM 1473 1 JAN 73

EDITION OF 1 NOV 65 IS OBSOLETE

Unclassified

SECURITY CLASSIFICATION OF THIS PAGE (When Data Entered)

Unclassified

SECURITY CLASSIFICATION OF THIS PAGE(When Data Entered)

20. Continued.

this contract) on a two-dimensional airfoil system whose torsional dynamics simulated those of a rotor blade. Results of the correlation led to the selection of an unsteady aerodynamic model (α , A, B model) and confirmed the general accuracy of the rotor aeroelastic analysis. Application of the analysis to study the effect of blade structural design parameters indicated beneficial effects of (1) increased airfoil stall angle, (2) reduced blade torsional stiffness, (3) reduced blade torsional inertia, (4) forward placement of the combined elastic, feathering and center of gravity axis relative to the aerodynamic center axis, and (5) increased blade twist. These analytic trends were in general agreement with the data from the two-dimensional tests.

Unclassified

1a
SECURITY CLASSIFICATION OF THIS PAGE(When Data Entered)

EUSTIS DIRECTORATE POSITION STATEMENT

This report has been reviewed by the Eustis Directorate, U. S. Army Air Mobility Research and Development Laboratory and is considered to be technically sound.

The technical monitor for this contract was Paul H. Mirick, Aeromechanics, Technology Applications Division.

ACCESSION for	
NTIS	White Section <input checked="" type="checkbox"/>
DOC	Buff Section <input type="checkbox"/>
UNANNOUNCED	<input type="checkbox"/>
JUSTIFICATION.....	
BY.....	
DISTRIBUTION/AVAILABILITY CODES	
Dist.	AVAIL. and/or SPECIAL
A	

DISCLAIMERS

The findings in this report are not to be construed as an official Department of the Army position unless so designated by other authorized documents.

When Government drawings, specifications, or other data are used for any purpose other than in connection with a definitely related Government procurement operation, the United States Government thereby incurs no responsibility nor any obligation whatsoever; and the fact that the Government may have formulated, furnished, or in any way supplied the said drawings, specifications, or other data is not to be regarded by implication or otherwise as in any manner licensing the holder or any other person or corporation, or conveying any rights or permission, to manufacture, use, or sell any patented invention that may in any way be related thereto.

Trade names cited in this report do not constitute an official endorsement or approval of the use of such commercial hardware or software.

DISPOSITION INSTRUCTIONS

Destroy this report when no longer needed. Do not return it to the originator.

PREFACE

This work was performed for the Eustis Directorate, U. S. Army Air Mobility Research and Development Laboratory, Fort Eustis, Virginia, under Contract DAAJ02-72-C-0105, Project 1F162208AA82. Technical monitor for the contract was Mr. Paul Mirick. The testing of the flexured airfoil model and reduction of the experimental data were performed at the United Aircraft Research Laboratories, East Hartford, Connecticut. The airfoil models and experimental hardware were designed and constructed by Mr. W. Hayden. The testing was conducted by Mr. P. G. Vogt. Processing of the stall flutter data and correlation with the UARL unsteady aerodynamic analysis were performed by Mr. G. L. Commerford. The investigation of the effects of blade parameters on helicopter stall boundaries was conducted at the Sikorsky Aircraft Division of United Aircraft Corporation, Stratford, Connecticut, by Mr. R. H. Blackwell.

TABLE OF CONTENTS

	<u>Page</u>
PREFACE	iii
LIST OF ILLUSTRATIONS.	vii
LIST OF TABLES	xiii
INTRODUCTION	1
TWO-DIMENSIONAL DYNAMIC STALL EXPERIMENTS.	2
Test Facility and Models.	2
Steady-State Tests.	3
Dynamic Tests	4
CORRELATION STUDY OF TWO-DIMENSIONAL RESULTS	7
Description of the Unsteady Models.	7
α , A, B Model	7
Time Delay Model.	9
Comparison of Measured and Predicted Two-Dimensional Airfoil Response	11
SURVEY OF EXISTING STALL BOUNDARY PREDICTION TECHNIQUES.	14
FULL-SCALE CORRELATION STUDY	17
Analytic Methods	17
CH-53A Flight Test Correlation Study	18
CH-54B Flight Test Correlation Study.	21
General Discussion of Correlation	21
GENERATION OF STALL BOUNDARIES FOR THE CH-53A HELICOPTER	23
PARAMETRIC DESIGN STUDY	26
Airfoil Properties	27
Torsional Mode Shape	28
Bending Stiffness.	29
Elastic, Center-of-Gravity and Aerodynamic Center Axes.	29
Blade Twist	31
Torsional Frequency	32
Torsional Inertia	35
REEVALUATION OF PRELIMINARY STALL BOUNDARY PREDICTION METHODS.	37

	<u>Page</u>
CONCLUSIONS.	39
RECOMMENDATIONS.	40
REFERENCES	41
LIST OF SYMBOLS	140

LIST OF ILLUSTRATIONS

<u>Figure</u>		<u>Page</u>
1	Acoustics Research Wind Tunnel Test Section	52
2	Two-Dimensional Model Airfoil	53
3	Capacitive Angular Transducer	54
4	Model Airfoil Drive System	55
5	Flexible Connector Detail	56
6	Measured Steady-State Lift Characteristics of the NACA 0012 and SC 1095 Airfoil Models.	57
7	Measured Steady-State Pitching Moment Characteristics of the NACA 0012 and SC 1095 Airfoil Models.	58
8	Measured Steady-State Drag Characteristics of the NACA 0012 and SC 1095 Airfoil Models	59
9	Airfoil Steady-State Lift Characteristics Corrected for Open Jet Tunnel Effects	60
10	Airfoil Steady-State Pitching Moment Characteristics Corrected for Open Jet Tunnel Effects	61
11	Airfoil Steady-State Drag Characteristics Corrected for Open Jet Tunnel Effects	62
12	NACA 0012 Model Airfoil Drag Polar.	63
13	NACA 0012 Model Airfoil Angle of Attack Time Histories. . .	64
14	NACA 0012 Model Airfoil Elastic Response Time Histories . .	65
15	Comparison of Measured and Time Averaged Elastic Response Time Histories for Two Test Points	66
16	Elastic Deflection Amplitudes for the NACA 0012 Airfoil . .	67
17	Elastic Deflection Amplitudes for the SC 1095 Airfoil. . .	68
18	Time Delay Unsteady Aerodynamic Model	69
19	Correlation of Measured and Calculated Lift Hysteresis Loops	70
20	Correlation of Measured and Calculated Pitching Moment Hysteresis Loops	71

<u>Figure</u>		<u>Page</u>
21	Correlation of Two-Dimensional Aerodynamic Damping Obtained With Time Delay Unsteady Aerodynamic Model for $\bar{\alpha} = 6^\circ$	72
22	Correlation of Two-Dimensional Damping Variation With Mean Incidence Angle	73
23	Comparison of Measured and Calculated Two-Dimensional Damping for $\bar{\alpha} = 8^\circ$	74
24	Effect of Mean Incidence Angle on Model Airfoil Torsional Response.	75
25	Effect of Torsional Natural Frequency on Model Airfoil Torsional Response.	76
26	Effect of Pitch Axis on Model Airfoil Torsional Response	77
27	Effect of Airfoil Contour on Model Airfoil Torsional Response	78
28	Correlation of NACA 0012 Airfoil Response Amplitude Obtained With Two Unsteady Aerodynamic Methods.	79
29	Correlation of SC 1095 Airfoil Response Amplitude Obtained With Two Unsteady Aerodynamic Methods.	80
30	Effect of Torsional Natural Frequency on Vibratory Torsional Moment	81
31	Effect of Pitch Axis Location on Vibratory Torsional Moment	82
32	Effect of Airfoil Torsional Inertia on Vibratory Torsional Moment	83
33	Effect of Mean Incidence Angle on Vibratory Torsional Moment	84
34	Selected Stall Boundary Prediction Techniques.	85
35	Selected Measured Stall Boundaries	86
36	CH-53A Helicopter	87
37	CH-54B Helicopter	88
38	The Buildup of CH-53A Pushrod Loads With Airspeed	89

<u>Figure</u>		<u>Page</u>
39	Effect of Nonuniform Inflow on the Correlation of CH-53A Blade Stress at 137 Kn and 42,000 Lb Gross Weight .	90
40	Effect of Nonuniform Inflow on Correlation of the Radial Distribution of CH-53A Blade Stress at 137 Kn and 42,000 Lb Gross Weight	91
41	Correlation of CH-53A Pushrod Load Time Histories at 137 Kn and 42,000 Lb Gross Weight.	92
42	CH-53A Blade Stress Calculated With and Without Unsteady Aerodynamics at 137 Kn and 42,000 Lb Gross Weight	93
43	Effect of Unsteady Aerodynamics on Calculated CH-53A Pushrod Loads at 137 Kn and 42,000 Lb Gross Weight	94
44	Correlation of CH-53A Blade Stress With α , A, B and Time Delay Unsteady Aerodynamics at 137 Kn and 42,000 Lb Gross Weight	95
45	Correlation of CH-53A Pushrod Load Obtained With α , A, B and Time Delay Unsteady Aerodynamics at 137 Kn and 42,000 Lb Gross Weight	96
46	Correlation of CH-53A Pushrod Load Obtained With α , A, B and Time Delay Unsteady Aerodynamics at 155 Kn and 42,000 Lb Gross Weight	97
47	Correlation of CH-53A Vibratory Pushrod Loads at 42,000 Lb Gross Weight	98
48	Correlation of CH-53A Vibratory Blade Stress at 42,000 Lb Gross Weight.	99
49	Correlation of CH-53A Required Power at 42,000 Lb Gross Weight	100
50	The Buildup of CH-54B Pushrod Loads With Airspeed.	101
51	Correlation of CH-54B Pushrod Load Time Histories at 115 Kn and 47,000 Lb Gross Weight	102
52	Correlation of Measured and Calculated CH-54B Pushrod Load Amplitudes at 47,000 Lb Gross Weight.	103
53	Correlation of CH-54B Maximum Blade Stress at 47,000 Lb Gross Weight	104
54	Flight Conditions Used To Generate CH-53A Stall Boundaries.	105

<u>Figure</u>		<u>Page</u>
55	The Buildup of Calculated Pushrod Loads With Airspeed for the CH-53A at $C_T/\sigma = 0.083$	106
56	The Buildup of Calculated Pushrod Loads With Thrust Coefficient at $\mu = 0.33$	107
57	Agreement Between Test and Analytical Pushrod Load Amplitudes and Stall Boundaries for the CH-53A	108
58	Calculation of CH-53A Fixed System Control Load Amplitudes	109
59	Calculated Buildup of CH-53A Vibratory Blade Stresses. . . .	110
60	Variation of CH-53A Available Control Moment and Required Power With Airspeed and Thrust Coefficient	111
61	Calculated Stall Boundaries for the CH-53A Rotor	112
62	Calculated CH-53A Blade Torsional Moments at 140 Kn and 49,000 Lb Gross Weight	113
63	Effect of Increased Airfoil Stall Angle on CH-53A Pushrod Load Time History at 140 Kn and 49,000 Lb Gross Weight	114
64	Effect of Airfoil Stall Characteristics on CH-53A Pushrod Load Time History at 140 Kn and 49,000 Lb Gross Weight . . .	115
65	Effect of Blade C.G. Location on CH-53A Pushrod Load Time History at 140 Kn and 49,000 Lb Gross Weight	116
66	Effect of Displacing Blade Elastic and Center-of-Gravity Axes From the Aerodynamic Center on the CH-53A Pushrod Load Time History at 140 Kn and 49,000 Lb Gross Weight . . .	117
67	Effect of Forward Movement of Elastic and Center-of- Gravity Axes on CH-53A Vibratory Pushrod Loads and Required Power	118
68	Effect of Forward Movement of Elastic and Center-of- Gravity Axes on CH-53A Vibratory Blade Stresses.	119
69	Effect of Forward Movement of Elastic and Center-of- Gravity Axes on CH-53A Stall Boundaries	120
70	Effect of Increased Blade Twist on CH-53A Pushrod Load Time Histories	121
71	Effect of Increased Blade Twist on CH-53A Vibratory Pushrod Load and Required Power	122

<u>Figure</u>		<u>Page</u>
72	Effect of Increased Blade Twist on CH-53A Blade Stresses and Available Control Moment	123
73	Effect of Increased Blade Twist on CH-53A Stall Boundaries	124
74	Effect of Torsional Frequency on Calculated CH-53A Pushrod Load Time Histories at 140 Kn and 49,000 Lb Gross Weight	125
75	Variation of Stall Flutter Pushrod Load and Elastic Tip Deflection Amplitudes for the CH-53A at 140 Kn and 49,000 Lb Gross Weight	126
76	Variation of Torsional Response Frequency With Natural Frequency	127
77	Effect of Decreasing Torsional Natural Frequency on Calculated CH-53A Torsional Moments at 140 Kn and 49,000 Lb Gross Weight.	128
78	Effect of Reducing Torsional Natural Frequency on CH-53A Vibratory Pushrod Load and Required Power.	129
79	Effect of Reducing Torsional Natural Frequency on CH-53A Blade Stresses and Available Control Moment.	130
80	Effect of Reducing Torsional Natural Frequency on CH-53A Stall Boundaries	131
81	Variation in CH-53A Pushrod Load Time History With Changes in Torsional Inertia and Stiffness at 140 Kn and 49,000 Lb Gross Weight.	132
82	Variation in CH-53A Pushrod Load Time History With Changes in Torsional Inertia at 140 Kn and 49,000 Lb Gross Weight..	133
83	Trends of Stall Flutter Spike Amplitude With Torsional Frequency and Stiffness Ratios	134
84	Effect of Decreased Torsional Inertia and Torsional Stiffness on CH-53A Vibratory Pushrod Load and Required Power	135
85	Effect of Decreased Torsional Inertia and Torsional Stiffness on CH-53A Blade Stress and Available Control Moment	136
86	Effect of Decreased Torsional Inertia and Torsional Stiffness on CH-53A Stall Boundaries	137

<u>Figure</u>		<u>Page</u>
87	Effect of Blade Design Changes on the CH-53A Control Load Boundary	138
88	Modifications to the Control Load Stall Boundary To Pe Used in Preliminary Design.. . . .	139

LIST OF TABLES

<u>Table</u>		<u>Page</u>
I	Two-Dimensional Airfoil Test Points	44
II	Model Airfoil Elastic Response Amplitudes	45
III	Model Airfoil Elastic Response Amplitudes Calculated Using α , A, B Unsteady Aerodynamics	47
IV	Model Airfoil Elastic Response Amplitudes Calculated Using Time Delay Unsteady Aerodynamics.	49
V	CH-53A and CH-54B Blade Natural Frequencies	51

INTRODUCTION

In the preliminary design of helicopter rotors, the rotor and blade properties are established by applying a set of design criteria. Important criteria that must be considered are those imposed by retreating blade stall in forward flight. The rotor's operating capability tends to be determined by the degree to which stall can be penetrated before any adverse effects become intolerable. As a result, the form which the stall-induced limitation assumes depends upon the specific rotor design. For example, one rotor may experience stall-induced drag rise or loss in lifting capability or control power. Another may be limited by a buildup in control loads due to stall flutter. Still others may experience flatwise or edgewise stress limits. Most experience in evolving preliminary design criteria accounting for retreating blade stall has been based on simple static aerodynamic criteria such as maximum angle of attack, profile drag divergence, etc. Based on correlation with their previous flight test experience, different organizations have relied on the correspondence of their primary stall limitation (excessive blade stress, sharp rise in control loads, loss of control power, etc.) with a particular value of the chosen static aerodynamic criterion. Clearly, the reliability of this type of prediction method decreases when new configurations and/or flight regimes are being considered. An ideal preliminary design method should predict the effects of all the governing design parameters on the various forms of stall limitation. Obviously, the fewer the generalized parameters involved, the simpler and more convenient would be the design criteria. Progress toward this goal has been hampered by a lack of understanding of the complex rotor aeroelastic response phenomena in stall. Only recently, with the incorporation of important unsteady aerodynamic effects, have blade response analyses become capable of modeling rotor aeroelastic response in stall (Reference 1).

In light of these recent advances, it was appropriate to conduct the work described below. The principal objectives of this effort were (1) to employ the latest available analytical techniques to define systematically retreating blade stall boundaries for a typical rotor, (2) to assess the impact of blade design parameters on these boundaries, and (3) where possible, to provide a set of more generalized stall boundaries useful for preliminary design purposes. A further objective of the work was to confirm the general accuracy of the analysis and point out any problem areas through correlation with flight test data for two helicopters and with stall flutter data obtained in a two-dimensional airfoil wind tunnel test. The correlation of two-dimensional airfoil stall flutter results provided a unique opportunity to evaluate different unsteady stall aerodynamic models and to gain insight into stall-induced torsional response phenomena without the complicating effects of nonuniform rotor inflow and blade flexibility.

TWO-DIMENSIONAL DYNAMIC STALL EXPERIMENTS

One of the primary objectives of this investigation was to provide data useful in evaluating the unsteady aerodynamic methods presently used in blade aeroelastic response analyses. Previous evaluations of unsteady aerodynamic stall models have centered on the correlation between measured and calculated lift and pitching moment hysteresis loops of rigid airfoils forced through sinusoidal angle of attack changes. The best measure of an aerodynamic method is its ability to predict the stall-induced torsional oscillations experienced on a full-scale helicopter in forward flight. However, the complexity of the rotor operating environment (blade bending and plunging motion, inflow fluctuation and three-dimensional effects) prevents fundamental study of stall flutter response phenomena on a full-scale rotor. As an intermediate approach, the test program described below was conducted. Blade torsional response to stall was tested with a flexured two-dimensional airfoil dynamically scaled to simulate the first torsional mode of a rotor blade. In this way the analytical capability for predicting stall flutter response could be examined without the uncertainties of rotor blade translational motion and inflow. Additionally, this type of test provided the opportunity for experimentally determining the effect of blade section design parameters on torsional response behavior.

TEST FACILITY AND MODELS

The facility chosen for the two-dimensional experiments was the UARL Acoustic Research Wind Tunnel. Although this facility was specifically designed for aerodynamic noise research, it has many features which also made it useful for this study. It is a low turbulence level, open circuit, open jet wind tunnel whose test section is surrounded by a large anechoic chamber. The test section of the tunnel is shown in Figure 1. Air is drawn from the atmosphere through a large bellmouth and then through the test section by a centrifugal fan at the exhaust end.

The facility permits the use of models of adequate size to obtain Reynolds number of order 10^6 . The size of the facility permitted airfoil effective aspect ratios of about 16 as compared to an aspect ratio of 9.5 in the tests of Reference 1.

The airfoil models were required to be as stiff as possible along their span in order to maintain the two-dimensionality of the test. A second requirement was that they be light weight so that they would be reasonably representative of scaled helicopter blade mass and inertia properties. To satisfy these requirements, models were constructed with fiberglass skins over a hollow steel spar with end ribs, and foam-type filler material. A schematic of the model construction is shown in Figure 2. Two different airfoil sections, one an NACA 0012 and one an SC 1095, were fabricated. In each case the airfoil chord was 0.5 ft and the span was 1.75 ft. Maximum deviation between designed and measured airfoil thickness was .005 c.

Each end of the airfoil had a drive shaft which could be moved to place the pitch axis at two chordwise locations (.22c and .25c). The airfoil was driven from one side of the wind tunnel by a variable length torque bar which served as the torsional spring used to set the blade pitch frequency. The opposite side of the airfoil had a larger shaft mounted in a pair of roller bearings in the tunnel side wall. It extended beyond the outer edge of the wind tunnel and had the rotor of a capacitive position measuring device affixed to its end. The capacitive angular transducer was described in detail in Reference 1. The transducer is a parallel plate capacitor of concentric cylindrical configuration whose output signal is proportional to the overlap area (Figure 3). The stator or fixed portion of this transducer was attached to the outside of the wind tunnel side wall. The free shaft end was threaded so that an inertial disk could be mounted on the shaft to increase airfoil torsional inertia by approximately 50%.

The oscillatory mechanism which was described in Reference 1 is shown schematically in Figure 4 along with the details of the transmission system. The spring connector between the airfoil and the transmission was modified for this program as shown in the cutaway drawing in Figure 5. The drive shaft from the transmission was a thick-walled hollow tube. A collet mechanism was mounted inside this tube in a keyway. The collet held the smaller diameter shaft (the torque bar) of the airfoil and could be moved axially to clamp this shaft. The far end of the hollow shaft was supported in a large bearing in the tunnel side wall.

The mean angle of attack of the airfoil was set by adjusting the relative positions of the solid and hollow portions of the drive shaft. This was accomplished by decoupling the airfoil from the transmission and setting both parts of the system at their maximum noseup positions (e.g., to set $\alpha_M = 14$ deg, the airfoil was placed at $\alpha_M + \bar{\alpha} = 14 + 8 = 22$ deg and the transmission cam was adjusted to its maximum positive displacement). The airfoil was then locked to the transmission by a clamp. During this procedure a second angular position transducer, mounted on the solid shaft, was used to measure the input angular time history.

STEADY-STATE TESTS

The steady-state normal force and moment were obtained for the two test airfoils in the Acoustics Research Tunnel. The tunnel speed was 275 fps corresponding to a Mach number of 0.25. These steady-state data were used to modify the tabulated unsteady data of Reference 1 to obtain the unsteady data for this study. Furthermore, the Time Delay method of analysis (described in a later section) uses empirically established variations of the steady data to model unsteady effects.

The unsteady normal force and moment data reported in Reference 1 were obtained in the UARL Low Speed Cascade Tunnel. The Reynolds number and Mach number of the current test program were approximately the same as those of the tests of Reference 1. However, the Acoustics Research Tunnel used for this study is an open-jet facility, and differences were expected in the steady and unsteady aerodynamic forces and moments.

The steady normal force, moment and drag were obtained using a three-component balance and standard force balance techniques typical of those discussed in Reference 2. Figures 6 through 8 show the uncorrected lift, drag and pitching moment versus angle of attack for both the NACA 0012 airfoil (top panels) and SC 1095 airfoil (bottom panels) as obtained in the open-jet wind tunnel.

In Reference 2 Pope discusses the effect of making these measurements in an open-jet (i.e., no floor or ceiling) wind tunnel and derives the following corrections whereby measurements made in an open-jet can be modified to be consistent with free air measurements:

$$\Delta\alpha \text{ (Rad.)} = -\left[\frac{1}{4}\left(\frac{c}{h}\right)c_1 + \frac{\pi}{24}\left(\frac{c}{h}\right)^2 c_1\right] \quad (1)$$

$$\Delta c_d = -\frac{1}{4}\left(\frac{c}{h}\right) c_1^2 \quad (2)$$

$$\Delta c_{m_c/4} = -\frac{\pi^2}{96}\left(\frac{c}{h}\right)^2 c_1 \quad (3)$$

where $\Delta\alpha$, Δc_d , and $\Delta c_{m_c/4}$ are the amounts by which the original measurements must be modified at equivalent values of c_1 , c is the airfoil chord, and h is the jet height. If these modifications are applied to the data of Figures 6 through 8 the corrected c_l , c_d and c_m versus angle of attack curves of Figures 9 through 11 are obtained. As a check on the accuracy of these results, Figure 12 shows the comparison of the corrected drag polar (i.e., c_l vs. c_d) data for the NACA 0012 airfoil to the results on page 94 of Reference 3. The agreement is considered to be good.

DYNAMIC TESTS

After the steady-state balance tests were completed, the balance was removed and the airfoil was attached to the oscillating mechanism previously described. The wind tunnel velocity was established from the pressure difference between the total pressure upstream of the inlet nozzle and the static pressure at the jet exit. The wind velocity for all tests was 275 ± 2 fps.

The time-varying input angular motion from the transmission and the output angular motion at the free end of the airfoil were obtained from the angular position transducers and were recorded on FM tape. The airfoil and drive mechanism were coupled as described earlier. The airfoil mean angle of attack was measured with a clinometer. Calibration records were taken on FM tape of the steady zero output (airfoil at α_M), the steady full-scale outputs (airfoil at $\alpha_M \pm 8$ deg) and the unsteady no flow time history at $\Omega = 8$ cps. The tunnel velocity was then set to 275 fps and unsteady time histories were recorded at nominal driving frequencies of 8.0, 10.0 and 12.5 cps. This gives three torsional natural frequency ratios (ω_0/Ω) for

the same torsional natural frequency. This test procedure was repeated at each angle of attack for all the various combinations of pitch axis, torsional inertia, torsional natural frequency and airfoil type. The total matrix of test conditions is shown in Table I.

The test program outlined above generated such a large volume of time-varying data that cycle-by-cycle inspection and data reduction were not practical. Accordingly, the data reduction was automated, with the bulk of the processing being done on the Univac 1108 digital computer. The FM tape was converted to a digital format using the UARL WISARD data system described in Reference 4 and procedures discussed in Reference 1. Data were recorded for sufficient lengths of time such that more than ten cycles of the LP driving motion were included at the lowest oscillatory frequency (8.0 cps). A typical set of time histories for the basic reference condition (NACA 0012 airfoil, 25 percent pivot axis, blade alone (reference) inertia, and 5P natural frequency ratio) is shown for the four mean angles of attack in Figure 13. These time histories were obtained directly from the computer by a 10-cycle signal averaging process. This procedure enhanced the repeatable elements of the time history while at the same time reducing the noise or random portion of the signal. The signal to noise ratio was improved by $\sqrt{10} = 3.16$ by this process (see pages 116-118 of Reference 5).

The elastic torsional deflection of the airfoil (the difference between the total angular motion and the input angular motion) was obtained for each test condition by subtracting the input angular position time history from the averaged airfoil angular position time history.

$$\theta(\tau) = \alpha(\tau) - [\alpha_M + \bar{a} \sin 2\pi\tau] \quad (4)$$

where $\theta(\tau)$ is the difference between the measured nondimensional angular time history response, $\alpha(\tau)$, and the input driving motion. The nondimensional time, τ , is given by t/P , where the period, P , was established from the ten-cycle time-averaging process for that run. Figure 14 shows the elastic deflection time histories corresponding to the angle of attack time histories of Figure 13.

Two measures of stall response are noted in Figure 14. The first parameter $\Delta\theta_1$ is half the amplitude of the first cycle of unsteady motion which corresponds to the initial stall. The second, $\theta_{p\text{pp}}$, is half the peak-to-peak or maximum deviation angle. These two parameters were extracted from each time history and are presented in Table II for the 10 cps driving frequency. Since stall flutter is not always present or clearly defined, these two parameters could not always be extracted and are not entered in the table for such cases.

Examination of the angle of attack time histories indicated that there were some statistical variations in measured response when stall flutter was present. It was recognized that the signal averaging process could result in significantly reduced unsteady amplitude if there was appreciable phase shift from cycle to cycle. Sample comparison of measured cycles of elastic deflection angle data and the corresponding time-averaged cycles are

shown in Figure 15. The top panel of Figure 15 which is typical of most of the data shows that little statistical variation exists and that the time-averaged cycle is representative of the individual cycles of motion. For an extreme stall flutter condition shown in the lower panel, the measured data shows a more transient characteristic, and unfortunately, time-averaging the data distorts the measured response during the period of maximum flutter. The general character of the response (i.e., frequency, time and amplitude of initial stall response) is retained, however. Because this phenomenon was not typical of most of the data and because no obvious way of choosing the average or nominal cycle of data for each of the nearly 200 conditions tested was evident, the time-averaged cycle of motion was used in the time history and amplitude correlation studies to follow.

There are many ways in which the data from Table II can be presented in graphic form. Figure 16 depicts the initial stall angular deviation $\Delta\theta_1$ versus mean angle of attack for the NACA 0012 airfoil. The side and top headings of the six inserts identify the particular insert as to pitch axis location x_{PA} and the nominal LP frequency Ω . In each small figure, there are four curves which are further identified to indicate the moment of inertia and the nominal airfoil natural frequency (these were intended to be 50 cps and 70 cps although one frequency was inadvertently set to 55 cps). Corresponding results for the SC 1095 airfoil are shown in Figure 17. Trends obtained in these tests will be discussed in a later section.

CORRELATION STUDY OF TWO-DIMENSIONAL RESULTS

A major goal of the two-dimensional flexured airfoil test program was to provide dynamic response data which could be compared with predictions based on various unsteady aerodynamic methods. The study of helicopter rotor stall flutter experienced in flight is complicated by uncertainties as to rotor inflow, spanwise flow, and blade bending and plunging motion. In the present tests these effects were eliminated and direct comparison of unsteady aerodynamic models was possible. Two analytical models were considered as discussed below.

The single torsional degree of freedom differential equation of motion for the flexibly mounted airfoil section oscillating in the wind tunnel test section is given by

$$I\ddot{\alpha} + C\dot{\alpha} + K(\alpha - \alpha_M) = M_a(t) + T_o \sin \Omega t \quad (5)$$

where I = airfoil torsional inertia per unit span,
(ft-lb-sec²/ft)

α = airfoil angle of attack, rad

C = equivalent mechanical damping per unit span,
(ft-lb-sec/rad)/ft

K = torsional spring constant, (ft-lb/rad)/ft

α_M = mean angle of the oscillation, rad

$M_a(t)$ = applied aerodynamic moment, ft-lb/ft

T_o = magnitude of the applied torque, ft-lb/ft

Ω = angular frequency of the applied torque, rad/sec

t = time, sec

The numerical techniques used to solve this equation are detailed in Appendix III of Reference 1.

DESCRIPTION OF THE UNSTEADY MODELS

α , A, B Model

In the present investigation two models of the unsteady applied moment, $M_a(t)$, were examined. In the α , A, B method described in Reference 1 unsteady aerodynamic moment is assumed to be a function of angle of attack and its first two time derivatives. Tabulations of aerodynamic coefficients as functions of α , $A = \frac{c\dot{\alpha}}{2U_o}$ and $B = \left(\frac{c}{2}\right)^2 \frac{\ddot{\alpha}}{U_o^2}$ (where c is the airfoil

chord and U_∞ is the free-stream velocity) were generated for an NACA 0012 airfoil. The airfoil was mounted in a wind tunnel and oscillated in pitch at combinations of mean incidence angle, amplitude of angular oscillation and reduced frequency. Instantaneous lift and pitching moment coefficients based on chordwise pressure distributions and instantaneous values of α , $\dot{\alpha}$ and $\ddot{\alpha}$ were determined during the oscillating airfoil tests. Curve fitting procedures were then used to determine tables of lift and pitching moment as functions of α , A , B . It was demonstrated in Reference 1 that unsteady normal force and moment data generated during the sinusoidal airfoil tests could be used to predict the aerodynamic response of an airfoil executing a nonsinusoidal motion. In a limited number of flexured airfoil tests described in Reference 1, good qualitative correlation of measured and predicted airfoil dynamic response was achieved. To model the present test conditions, two changes were made to the calculation procedure. First, since pitch axis was a variable in this study, provision was made to include pitching moment due to chordwise offset of the aerodynamic center from the pitch axis, i.e.,

$$c_{m_{\bar{x}_{PA}}}(\alpha, A, B) = c_{m_C}/4(\alpha, A, B) + (\bar{x}_{PA} - 0.25)c_l(\alpha, A, B) \quad (6)$$

The functional terms $c_{m_C}/4$ and c_l were obtained from interpolation of the unsteady data tabulations of Reference 1.

The second change involved variations of the steady-state lift and moment for the present test program from the corresponding steady data obtained in Reference 1. As mentioned earlier in this report, the actual steady force and moment were different even for the NACA 0012 airfoil because the tests were conducted in an open jet wind tunnel and because the airfoil effective aspect ratio was much higher. It was necessary to scale the data tabulations of Reference 1 to account for these effects. The method of scaling used for these analyses required a shift in the entire data tabulation by constant values of angle of attack, unsteady lift coefficient, and moment coefficient according to the following relations.

$$c_l(\alpha, A, B)_{\text{OPEN JET}} = c_l(\alpha + \delta\alpha_l, A, B)_{\text{TAB}} + \delta c_l \quad (7)$$

and

$$c_m(\alpha, A, B)_{\text{OPEN JET}} = c_m(\alpha + \delta\alpha_m, A, B)_{\text{TAB}} + \delta c_m \quad (8)$$

The constants $\delta\alpha_l$, $\delta\alpha_m$, δc_l and δc_m were established for each airfoil and were equal to the amount of shift necessary to make the open jet steady-state stall points (in both lift and moment) match the steady-state stall points of the airfoil of Reference 1.

Time Delay Model

Wind tunnel airfoil dynamic response was also calculated using the recently developed Sikorsky Time Delay unsteady aerodynamic method. This formulation has been developed empirically by generalizing the results of a set of oscillating airfoil test programs and is aimed at predicting the unsteady aerodynamic characteristics of arbitrary airfoils. Its goal is to provide the blade designer with unsteady lift and pitching moment characteristics of various airfoils while minimizing the need to conduct extensive oscillating airfoil test programs. This model is based on a hypothesis of physical separation process and differs from most other approaches in that it does not depend on an assumed harmonic variation of angle of attack. The basic assumption is that there exists a maximum quasi-static angle of attack at which the pressure distribution and the boundary layer are in equilibrium. During increases in angle of attack beyond this static stall angle, there are finite time delays before a redistribution of pressure causes first a moment break and then a lift divergence corresponding to flow separation. The relative phasing of the moment and lift breaks with angle of attack produces either positive or negative damping of the motion.

In order to test the Time Delay hypothesis, oscillating airfoil test data from Reference 6 were examined. It was noted that the occurrence of dynamic lift stall could not be correlated with maximum angle of attack or with the time derivative of angle of attack. The onset of stall was found to occur prior to, coincident with, or after the maximum amplitude of the angle of attack oscillation. Best correlation of the angle of attack for dynamic lift stall was achieved by evaluating the spread between the static moment stall angle and dynamic lift stall in terms of elapsed time non-dimensionalized by free-stream velocity and chord length, $\tau^* = \Delta t_{SEP}(U_o/c)$. It was found that dynamic lift stall generally occurred when an elapsed time parameter τ_2 (which starts counting when the static stall angle is reached) attains a τ^* value of about 6.

Dynamic pitching moment stall has been handled similarly. From inspection of the test data it was evident that, in general, an abrupt change in the dynamic moment occurred prior to the lift stall. This has been noted in Reference 7 and attributed to the shedding of a vortex at the airfoil leading edge at the beginning of the separation process. Rearward movement of the vortex over the surface of the airfoil tends to maintain lift but drastically alter the pitching moment. Examination of pitching moment hysteresis loops from Reference 6 showed that pitching moment stall generally occurred when the elapsed time parameter τ_2 reached a pitching moment stall time constant τ_s of about 2.

In order to apply the Time Delay model to a given airfoil, only static aerodynamic data are required. First, the airfoil static lift and pitching moment data are used to define the approximate variation in center of pressure between the static moment stall angle α_1 and an angle of attack α_2 above which the center of pressure is assumed fixed. Second, an approximation is made to the c_l versus α curve for fully separated flow. The sequence of events occurring during one stall-unstall cycle is detailed in Figure 18. Briefly stated, lift and pitching moment are determined from

potential flow theory until the nondimensional time τ_2 reaches τ_3 . At this point the pressure distribution begins to change, leading to a rearward movement of the center of pressure and a loss in potential flow pitching moment. At a later time when $\tau_2 = \tau^*$, the lift breaks from the static line and decreases gradually with time to the fully separated value, $c_{lSEP}(\alpha)$. For $\tau_2 > \tau^*$ the center of pressure coincides with C.P._{SEP}(α). At the point where $\dot{\alpha} = 0$ the rates at which c_l approaches $c_{lSEP}(\alpha)$ and C.P. approaches C.P._{SEP}(α) (if it does not already equal C.P._{SEP}(α)) are increased. When α falls back below the quasi-static stall angle, α_1 , the center of pressure returns to the quarter chord, potential flow pitching moment effects are reintroduced and a second time parameter τ_3 is recorded to govern the rate at which c_l returns to c_{lPOT} .

Although additional correlation studies must be made to identify the effects of airfoil type on the time delay constants and although a number of refinements to the present model may be implemented, this rather simple model gives a good representation of the essential features of the dynamic stall process. Correlation typical of that claimed for other empirical methods (References 9 and 10) has been found with data from References 1, 6, and 8. Only the α, A, B method has produced better correlation (Reference 1), but it suffers from the requirement for extensive testing and data processing. Figures 19 and 20 compare the NACA 0012 unsteady lift and pitching moment hysteresis loops measured in Reference 1 with Time Delay results. This correlation was achieved by setting the lift break time constant τ^* equal to 4.0 instead of 6.0. Apparently, three-dimensional effects encountered in this test reduced the time interval between static stall and dynamic lift stall. Also shown are the hysteresis loops predicted using the α, A, B method. The α, A, B method correlation is with the data from which the α, A, B coefficients were derived. In addition to predicting the exact form of lift and moment hysteresis loops, an unsteady model should faithfully represent aerodynamic pitch damping. Accordingly, the Time Delay model was used to calculate two-dimensional aerodynamic damping for the reduced frequency/mean angle of attack test points of Reference 11. The results plotted versus reduced frequency and mean incidence angle are shown in Figures 21 and 22. Included in Figure 21 is the variation in damping predicted using potential flow theory. Generally excellent correlation of measured and predicted damping is noted. In Figure 23, damping calculated with the Time Delay model and the α, A, B method using the data tabulations of the early unsteady tests (Reference 8) are compared. The accuracy of the two methods is similar when compared on this basis. However, as noted earlier and as shown in Figures 19 and 20 the α, A, B does more faithfully reproduce the original hysteresis loops.

The Time Delay model was applied to the calculation of wind tunnel airfoil dynamic response using the numerical procedures outlined for the α, A, B solution. The uncorrected steady-state lift and pitching moment data shown in Figures 6 through 8 served as inputs in the Time Delay calculations. Additionally the airfoil mean incidence angle used in the Time Delay solution was two degrees less than that set in the wind tunnel. The open jet flow deflection experienced at high unsteady lift coefficients was sufficient to decrease actual peak angles of attack to a value somewhat lower than the geometrically impressed pitch angle. The two degree correction to α_M gave consistently better correlation of the initial stall time.

COMPARISON OF MEASURED AND PREDICTED TWO-DIMENSIONAL AIRFOIL RESPONSE

Correlation between measured wind tunnel model response and response calculated with the unsteady models described above was examined for thirty-six test conditions. The set of cases studied, denoted in Table II, was sufficient to evaluate the independent effects on airfoil response to stall of mean incidence angle, torsional natural frequency, chordwise pitch axis, torsional inertia, and airfoil type. Relative to a baseline case taken to be the NACA 0012 airfoil at $\alpha_M = 14^\circ$, $\omega_0/\Omega = 5$, $\bar{x}_{PA} = 0.25$, and $I = I_{REF}$, Figures 24 through 27 show measured and predicted effects of mean angle, torsional natural frequency, pitch axis and airfoil type on time histories of elastic deflection. In Figure 24 the measured and predicted effects of airfoil mean angle of attack are shown for the NACA 0012 airfoil. Comparison of the two test results indicates that deeper penetration into stall results in sharper initial stall deflection and larger residual stall flutter response. Each unsteady model overpredicts the amplitude of response. As shown in Figure 25 the main effects of an increase in torsional natural frequency are a shift in response frequency and a decrease in the amplitude of elastic deflection. The lower panel of Figure 25 shows fair correlation of response amplitude, although both analyses predict an initial stall response earlier than that measured. The effects of moving the airfoil pitch axis forward are shown in Figure 26. A delay in the initial stall time and a reduction in the amplitude of response are indicated by the test data. The analytical results do predict the reduction in response amplitude, but the Time Delay model still results in overpredicted response. Finally, Figure 27 compares the NACA 0012 and the SC 1095 airfoils at the same mean angles of attack. A delay in the initial stall time is evident for the SC 1095 airfoil which had a static stall angle measured in this wind tunnel to be about three degrees higher than that of the NACA 0012. However, the SC 1095 stall flutter amplitude was comparable to that experienced by the NACA 0012 at this condition.

In general, the time history correlation was acceptable. The point and severity of initial response to stall and the response frequency were well modeled. The trends observed in test were matched by the analysis, although the Time Delay model generally overpredicted stall flutter response. The difficulties encountered in time-averaging the stall flutter response data may have contributed in some instances to this apparent overprediction of response. The basic effects of structural changes on blade response time histories were predicted by either analysis.

Wind tunnel and analytic results were also compared on the basis of initial stall response amplitude and overall peak-to-peak deflection. The time-averaged data were reduced and it was found that the initial stall response parameter $\Delta\theta_1$ gave the most consistent indication of susceptibility to stall flutter. The possible reduction in flutter amplitude introduced by the time-averaging procedure when there was cycle-to-cycle variation in phase made it somewhat difficult to assess the amplitude of flutter response. Fortunately, the initial stall deflection showed virtually no cycle-to-cycle variation. Tables III and IV show the response amplitudes calculated with the α , A, B and Time Delay models at $\Omega = 10$ cps. Figure 28 compares the measured NACA 0012 deflection angles from the $\Omega = 10$ cps plots

of Figure 16 with predicted values for all combinations of airfoil torsional natural frequency ratio, torsional inertia and pitch axis. The corresponding results for the SC 1095 airfoil are shown in Figure 29. Certain general trends of deflection angle can be identified in both the test and analytic results:

1. Elastic response increases with mean incidence angle.
2. For the same torsional inertia, the response is generally greater for the lower frequency airfoil section.
3. The amplitude of response is inversely related to torsional inertia.
4. Forward movement of the pitch axis leads to a decrease in response.
5. The SC 1095 airfoil dynamic stall response generally begins to build up at a higher mean incidence angle than the 0012, but the two airfoils have comparable responses once stall is penetrated.

Although the amplitude of elastic deflection is important in determining rotor stability and performance, the torsional moments resulting from stall flutter are the designer's primary concern. To gain a measure of the trends of torsional moment with parameter changes, the twisting moment experienced by the flexible connector in the model airfoil drive system was calculated for each test condition. The torsional moment, M_0 , was calculated using the equivalent spring stiffness of the connector.

$$M_0 = K_{eq}\theta = (I_0 \omega_0^2)\theta \quad (9)$$

where I_0 represents the airfoil torsional moment of inertia. The torsional moments corresponding to the ΔQ_1 values of Tables III and IV are used in Figures 30 through 33 to show the effects of blade parameters on structural moments. In Figure 30 it is clear that decreasing torsional natural frequency generally reduced stall flutter moments. Although the stiffer system experienced lower response amplitudes, the corresponding structural moments (proportional to the square of the natural frequency according to Equation (9)) were increased.

As seen in Figure 31 the effect of forward placement of the airfoil pitch axis was generally to decrease vibratory torsional moments. The two analyses predicted this trend with comparable accuracy. That forward movement of the airfoil pitch axis relative to the aerodynamic center reduces stall flutter moments can be understood by considering lift and pitching moment hysteresis loops. For an airfoil with pitch axis forward of the center of pressure, positive lift forces cause negative moments about the pitch axis. Usually for positive lift, the lift hysteresis loop is traversed in the clockwise direction, which results in a pitching moment loop (due to lift) which is traversed in the counterclockwise (stabilizing) direction. A decrease in test torsional moment amplitude with decreasing torsional

inertia is generally seen in Figure 32. The α , A, B program shows a somewhat less significant trend. Finally the two airfoils are compared in Figure 33. The trend that high stall flutter moments are delayed in mean angle with the SC 1095 airfoil is seen for two different combinations of inertia and pitch axis. The stalled blade loads for the two airfoils are comparable. Based on the model airfoil test results, the following guidelines for reducing section vibratory torsional moments can be established.

1. Reducing torsional frequency decreases vibratory moments although increasing the amplitude of torsional deflection.
2. Reducing airfoil section torsional inertia increases the elastic response amplitude but generally decreases stall flutter moments.
3. Movement of the airfoil pitch axis forward of the quarter chord reduces vibratory moments.
4. Use of the cambered airfoil delays the onset of stall flutter loads to higher angles of attack than measured with the NACA 0012. When stall is penetrated, however, no significant reduction in vibratory moments can be anticipated with the cambered airfoil.

These general trends will be investigated in the full-scale blade design study.

SURVEY OF EXISTING STALL BOUNDARY PREDICTION TECHNIQUES

As an introduction to the study of helicopter stall boundaries, a literature survey of available stall boundary prediction techniques has been conducted. The objective of this effort was to evaluate the state-of-the-art methodology used for rapid prediction of main rotor, stall-related, operating boundaries and to determine whether any of the procedures are sufficiently comprehensive to be of general usefulness in the preliminary design process. Although significant progress has been made in the prediction of rotor and control system loads using sophisticated aeroelastic analyses, a fairly reliable but less time-consuming approach would be quite valuable in preliminary stages of design. An objective of the present study was to determine whether the results of a systematically applied design study conducted with the latest aerodynamic and dynamic modeling techniques can be used to (1) refine the simple stall boundary prediction techniques or (2) offer insight into the importance of blade parameters not treated by current methods.

Historically, it appears that rotor solidity requirements have been determined from the maximum thrust coefficient-solidity ratios required in hover and forward flight. Forward flight has been the more difficult part of the problem to analyze because of the complexity of the operating environment and the multiplicity of ways in which stall effects can be manifested; e.g., buildup in power, stresses, gust sensitivity, vibration and control loads or loss in control power or lifting capability. To simplify the preliminary design process, some type of static aerodynamic stall criteria has generally been used. The aerodynamic parameters and their limiting values at the onset of stall have been chosen through extensive correlation with flight test data. Obviously, the reliability of this type of prediction technique decreases with the extent to which new rotor configurations, materials and/or flight regimes are being considered. This approach also hampers a detailed comparison of stall boundary prediction techniques found in the literature because individual companies have generally chosen stall criteria based only on their immediate experience. Detailed comparison of the various prediction techniques would require that they all be applied to a given set of rotors. This comparison would require more specific information about the manifestations of stall than is generally available in the literature.

The most commonly used form of stall boundary is a plot of maximum thrust coefficient-solidity ratio versus advance ratio. Figure 34 shows some sample stall boundary predictions expressed in this form for typical pure helicopter conditions. Curve 1 derives from the very earliest efforts to predict stall boundaries (Reference 12). In this method the rotor angle of attack at the tip of the blade at 270 deg azimuth is calculated using classical rotor theory for each of a series of advance ratios, thrust coefficients and parasite drag coefficients. Calculated tip angles of attack of 12 deg and 16 deg are taken as the incipient stall boundary and the practical operating boundary. Curve 1 taken from Reference 13 apparently represents the incipient stall boundary calculated in this manner for a Bell AH-1G. Curve 2 is a stall boundary calculated for a Kaman

UH-2C. The criterion that a local retreating blade angle of attack exceed 13.5 deg was stated in Reference 14 to agree well with Kaman experience. Blade angles of attack used to generate this curve were calculated using the NASA charts of Reference 15.

Use of the retreating blade angle of attack as the criterion for the rotor stall limit was replaced at Sikorsky by a method based on the correspondence of the knee of the control load curve with a limit value of the blade profile drag torque parameter $bC_{Q,D}/\sigma = 0.004$. Extensive examination of flight test data for different Sikorsky type rotors showed that $bC_{Q,D}/\sigma = 0.004$ indicated incipient stall and $bC_{Q,D}/\sigma = 0.008$ corresponded approximately to the practical limit of operation. Based on this criterion, stall boundaries are estimated from a rigid blade trim analysis which has shown good correlation between measured and predicted rotor performance. In this performance program the effects of aerodynamic design factors (e.g., number of blades, chord, airfoil and twist) on stall boundaries are modeled, but the effects of blade structural design properties are not included. Curve 3 shows the incipient stall boundary calculated for the CH-53A using the rotor torque criterion $bC_{Q,D}/\sigma = 0.004$.

Boeing-Vertol appears to use a very similar approach in predicting moment stall inception. Although the details of their estimation procedures are not available in the literature, Reference 16 indicates that flight test results have been generalized and a limiting value of a moment stall parameter $f(\rho, R, \mu, c, K, \omega_0, I_0)$ has been established as a function of calculated angle of attack at 270 deg azimuth. Based on this limit curve the stall boundaries for a proposed rotor design can be established by running a rigid blade trim analysis. The Boeing procedure appears to have gone further than the previous methods in that blade torsional frequency and inertia have been included as parameters.

A fourth curve included in Figure 34 is taken from the results of Reference 17. In this study an ideal rotor is postulated which has all blade sections operating at $c_{l_{MAX}}$ except for an advancing blade region for which c_l is reduced to maintain zero rolling moment. This calculation is based on an isolated rotor and uses steady-state airfoil data and uniform inflow.

The results shown above clearly indicate different boundaries for different types of rotor systems. A group of flight test boundaries shown in Figure 35 also points out the variety of stall boundaries presently encountered. Curve 1 from Reference 18 marks a stall boundary for a UH-1B rotor and is apparently determined from excessive blade torque requirements and oscillatory chordwise bending loads. Stall flutter is not a problem under these conditions. Reference 13 shows the overall stall boundary experienced by Bell helicopters which is characterized by rapidly rising power, blade loads and controllability problems. Reference 10 indicates that the CH-47C flight envelope is limited by stall flutter pitch-link loads. Curve 3 approximately locates this stall boundary. The stall operating limit measured for the Kaman 101 rotor is also shown; however, Reference 19 does not describe the form of stall effect encountered. Finally, curve 5 depicts the boundary corresponding to excessive CH-53A vibratory pushrod loads.

In summary, the results of the literature survey indicate a variety of stall boundaries and preliminary design procedures. None are documented in detail. However, it is clear that structural design factors as well as aerodynamic factors must be considered if generalized stall boundaries for rotors are to be determined. The remainder of this investigation is directed toward a systematic analytical study of the factors contributing to stall boundaries for an articulated rotor. This study is preceded by a correlation study to define the general accuracy of the aeroelastic analysis being employed.

FULL-SCALE CORRELATION STUDY

A full-scale helicopter correlation study was performed to evaluate the analytic capability for predicting the effects of stall on rotor characteristics of interest. The two unsteady aerodynamic models used in the correlation of two-dimensional stall flutter results were also compared based on full-scale correlation. It was essential that current aeroelastic and aerodynamic modeling techniques be evaluated systematically over a wide range of flight conditions so that confidence in the analysis could be gained before the parametric design study was performed. Additionally, the correlation study served to point out problem areas which require improvements to the current analytic methods.

Control loads, blade stresses and rotor performance were calculated for both stalled and unstalled flight conditions for the CH-53A and CH-54B aircraft. The CH-53A shown in Figure 36 is a high-speed assault transport helicopter. It has a rotor diameter of 72 feet, a chord of 2.167 feet and a solidity of 0.115. The nominal tip speed is 696 ft/sec and the -6 deg twist blades have a modified NACA 0011 airfoil section. Nominal aircraft gross weight is 34,000 lb. The CH-54B is shown in Figure 37. The CH-54B rotor is essentially the same as that of the CH-53A but with twist increased to -16 deg. Normal gross weight is 38,000 lb. Each rotor has 6 blades. Natural frequencies for the blades of the two aircraft are shown in Table V for the tip speeds used in correlation studies.

ANALYTIC METHODS

The Normal Modes Blade Aeroelastic Analysis was used to calculate the blade elastic response for each flight condition. In this analysis, which is described in Reference 20, the fully coupled blade equations of motion are solved by expanding them in terms of uncoupled flatwise, edgewise and torsional blade modes. The modal technique facilitates the numerical integration of the blade equations by minimizing dynamic coupling terms. Given a distribution of wake-induced velocities over the rotor disc and an aerodynamic model to represent section aerodynamic loads, blade elastic response, blade stresses and control loads are calculated for each flight condition.

Rotor inflow was calculated using the UAC Prescribed Wake Analysis as described in Reference 21. The function of this program is to compute a rotor circulation distribution that is compatible with a prescribed set of blade section operating conditions and a prescribed rotor wake geometry. In the present efforts a helical wake structure was assumed. Based on calculated circulation strengths, blade positions and wake geometry, this analysis applies the Biot-Savart Law to calculate induced velocity at each radial and azimuthal blade station. To avoid unrealistically high values of computed velocity when blades and trailing vortices pass close to one another, velocity inducing effects are eliminated for blade-vortex separation distances less than a specified vortex core radius. Because the blade response program employs a lifting line representation of blade aerodynamics, the large fluctuations in computed inflow velocities which result from

assuming too small a vortex core limit lead to greatly overpredicted fluctuations in lift coefficients and blade flatwise bending. In this study it was found that a vortex core radius of one-half the blade chord gave good agreement of predicted and measured flatwise blade stress.

An iteration procedure is used to couple the blade response and circulation programs, insuring compatibility of the induced velocities and the blade response. For a given flight condition the normal modes program is first run with uniform inflow and trimmed automatically to specified values of rotor lift and propulsive force. Tolerances of about $\pm 3\%$ on rotor lift and $\pm 8\%$ on propulsive force were used. One-per-rev rotor flapping was maintained at less than 2 - 3 degrees by adjusting cyclic pitch. Based on required control settings and resulting motion, rotor induced velocities are calculated. The induced velocity distribution is applied in the blade response calculations and the rotor is retrimmed by adjusting rotor collective pitch and shaft angle. The procedure is repeated until the blade motion resulting from the response calculations is consistent with that for which the induced velocities were calculated. Typically, two iterations are required to obtain reasonably converged results.

The two unsteady aerodynamic models described above, namely the α, A, B and the Time Delay model, were used to calculate blade unsteady lift and pitching moment coefficients. In the absence of unsteady drag data or proven unsteady drag modeling techniques, steady-state drag data were used throughout. A smoothed version of the α, A, B unsteady data tables of Reference 8 was used in the correlation study. Results of Reference 1 indicated that this set of unsteady data gave best full-scale correlation results. In the application of the α, A, B model the effects of blade unsteady motion on angle of attack for zero lift, lift curve slope and stall angle were applied in the circulation calculations.

CH-53A FLIGHT TEST CORRELATION STUDY

Extensive flight testing of the CH-53A aircraft has been performed. The primary source of flight test data chosen for the correlation study is the rotor loads program described in Reference 22. In this test program, detailed measurements of blade loads and responses were made and converted to time history form. Additional vibratory response data are available from the results of Reference 23. Based on the data of Reference 23, Figure 38 illustrates the buildup of vibratory CH-53A pushrod loads with airspeed. A rapid growth of oscillatory pushrod load is noted as stall is penetrated. In these results the Sikorsky ERITS (Equivalent Retreating Indicated Tip Speed) procedure has been used to correct measured airspeeds for small fluctuations in aircraft gross weight and load factor, tip speed and air density. ERITS is calculated according to the following relation:

$$\text{ERITS} = \left[\Omega R \sqrt{\rho/\rho_0} - v_c \right] \sqrt{\frac{W_0}{W} \frac{1}{\text{LF}}} \quad (10)$$

where ΩR = tip speed, kn
 V_C = calibrated airspeed, kn
 ρ = measured density of air, slugs/ft³
 ρ_0 = reference density, slugs/ft³
 W = measured gross weight, lb
 W_0 = reference gross weight, lb
 LF = load factor, nondimensional

According to this procedure, described in Reference 24, plotting vibratory control loads versus ERITS reduces the scatter in experimental data and facilitates comparisons of test and analytic results. When the mean ERITS curve has been compiled for a given aircraft, mean load versus airspeed curves can be generated for a nominal gross weight, tip speed and density altitude.

Correlation of control system loads, blade stresses and required power was studied at a nominal aircraft gross weight of 42,000 lb ($C_T/\sigma = 0.083$), a tip speed of 710 ft/sec and a 3000 ft density altitude for airspeeds ranging from 100 kn to 170 kn. The effects of nonuniform inflow on blade response were calculated at all flight conditions. Also, the results obtained with the two unsteady aerodynamic models were compared with predictions using steady aerodynamics.

The inclusion of variable inflow was found to be essential in calculating the proper levels of blade bending moments. Some improvement in the correlation of blade torsional moments was also found. Figure 39 shows the blade flatwise and edgewise stress correlation obtained with α, A, B unsteady aerodynamics at a typical stalled flight condition (137 kn/42,000 lb gross weight). Significant improvement in the correlation of blade stress results from the inclusion of variable inflow effects. The amplitude of the predicted edgewise stress is somewhat less than the measured value. It should be noted that the CH-53A blade has an edgewise natural frequency near 4P which undoubtedly causes computed stress to be sensitive to other-wise small errors in computed 4P loading. Figure 40 compares measured and predicted radial distributions of vibratory flatwise and edgewise stress for this flight condition. The improvement in stress correlation is directly traceable to increased third quadrant airloading which results from higher blade angles of attack calculated by the variable inflow program.

The effect of inflow on the correlation of pushrod loads is indicated in Figure 41. Although the nonuniform inflow results have a higher predicted stall flutter amplitude, the triggering of the oscillation near $\psi = 180$ deg is not predicted. Calculated two-dimensional angles of attack are generally below stall at this position. Possible reasons for the lack of agreement in the stall flutter initiation point are indicated in the following section.

Because it is fairly well established that accurate prediction of stalled blade loads requires the treatment of unsteady aerodynamic effects, only a few comparisons of steady and unsteady aerodynamics were made. Figures 42 and 43 compare computed blade stresses and pushrod loads. The increased edgewise stress calculated with steady aerodynamics apparently reflects the fact that without dynamic lift effects, higher blade angles of attack are required to generate a given rotor thrust resulting in higher calculated drag coefficients. As shown in Figure 43, although the initial calculated stall moments are similar, the buildup of torsional loads, characteristic of an undamped or negatively damped oscillation, is not modeled with steady pitching moment data.

The α, A, B and Time Delay unsteady aerodynamic models were compared at the 137 kn/42,000 lb flight condition. Although Figure 44 shows comparable computed blade stresses, the pushrod loads calculated with the Time Delay model are much less than the measured values (Figure 45). Figure 46 shows similar results at a more deeply stalled flight condition (155 kn/42,000 lb). Although the sharpness of the initial moment stall is comparable with the two unsteady methods, the Time Delay results do not indicate subsequent oscillations into and out of stall with pitching moments phased to promote the growth of torsional oscillations. It is not entirely clear why, relative to the α, A, B method, the Time Delay model underpredicts helicopter control loads while overpredicting the stall flutter oscillations of the two-dimensional wind tunnel model. Examination of several blade section pitching moment/angle of attack hysteresis loops indicates not so much that more negative pitch damping is present in the α, A, B results but that pitching moments along the blade are more in phase, leading to larger modal excitation. In the α, A, B formulation, pitching moment coefficients are tabulated as functions of $\alpha, \dot{\alpha}$ and $\ddot{\alpha}$. When a torsional response is present, blade elastic deflection contributes an oscillation to the $\alpha, \dot{\alpha}$ and $\ddot{\alpha}$ values all along the blade which leads to more similarly phased pitching moments along the span. In the Time Delay model described above, moments are calculated based only on the angles of attack exceeding the steady-state stall angle for a certain interval of time and are independent of the instantaneous angle of attack time histories. For small differences in calculated angles of attack, computed pitching moments for adjacent blade sections can be very different in phase. Because the wind tunnel airfoil was substantially two-dimensional in nature, the effects of simultaneous spanwise stalling were not a factor.

That better correlation of stall flutter moments was possible with the α, A, B method is evident in Figure 47, which shows the buildup of vibratory pushrod load amplitude with airspeed. The α, A, B model predicts a buildup rate almost identical to the mean of the test data. A discrepancy of no more than 10 knots in the so-called knee of the control load curve is evident. Corresponding results for flatwise and edgewise vibratory stress are shown in Figure 48. Maximum vibratory flatwise stress generally occurred at about the 0.8R radial station and maximum edgewise stress occurred at 0.5R. Unfortunately, blade bending stress data were not available at the highest airspeeds. Agreement between calculated and measured vibratory flatwise stress is equally good with the two models. At least until deep stall is reached, the analyses (especially the Time Delay

program) generally underpredict vibratory edgewise stress. Agreement of measured and calculated main rotor power required is shown in Figure 49.

CH-54B FLIGHT TEST CORRELATION STUDY

The stalled flight characteristics of the CH-54B rotor system were studied recently and reported in Reference 24. Control load data from the baseline flights of this test program serve as the basis for the pushrod load correlation study. Blade stress and required power data were taken from a general CH-54B flight test program described in Reference 25. The CH-54B flight envelope is limited by the buildup of vibratory control loads. Figure 50 illustrates the rapid buildup in half-peak-to-peak pushrod loads experienced at an aircraft gross weight of about 47,000 lb, and a reduced rotor speed (96% N_R), corresponding to a nominal thrust coefficient-solidity ratio C_T/σ of 0.10. Some uncertainty exists with regard to the zero azimuth reference point of these data. Based on other CH-54B pushrod load data, the zero azimuth position has been taken as the last nosedown peak in pushrod load before relief from stall causes noseup first quadrant deflection. Relative to the CH-53A data a decreased stall speed and a sharper buildup in vibratory load with airspeed are noted. Also, a larger one-per-rev component is evident in the azimuthal signature of the pushrod load resulting apparently from the high blade twist.

Calculated CH-54B control loads were generally less than measured values. Figure 51 compares pushrod load time histories at a flight condition of 115 kn, 47,000 lb gross weight and 96% normal rotor speed. Relative to comparable CH-53A results, the increase in LP blade pitching moment is predicted, but the amplitude of the stall flutter oscillation is underpredicted. In order to probe the stall boundary, a higher speed flight condition (130 kn/47,000 lb) was simulated analytically. The plot of vibratory pushrod load versus airspeed shown in the top panel of Figure 52 indicates that a definite stall boundary is predicted by the analysis. Relative to the CH-53A calculations, a decreased control load stall speed and an increased rate of buildup with airspeed are clearly predicted. Again, higher loads are computed based on the α, A, B model. The test results depicted in Figure 50 indicate that the rapid buildup of peak-to-peak loads with airspeed results from high frequency stall flutter oscillations. The comparison of measured and predicted stall flutter spike amplitudes shown in the lower plot of Figure 52 indicates that the α, A, B results reflect this buildup much more accurately than do the Time Delay calculations. A comparison of calculated vibratory stress with test data from Reference 25 is shown in Figure 54. Measured blade stresses are well below critical levels at the control load stall speed. Although flatwise stress is overpredicted, edgewise stress agreement is very good. Compared to results obtained for the CH-53A a greater increase in vibratory flatwise stress with increased twist is predicted than was measured.

GENERAL DISCUSSION OF CORRELATION

In general, the degree of correlation presented for the CH-53A and CH-54B was considered to be acceptable. The increases in blade stress, pushrod load and required power with severity of stall were well modeled. Best

results were obtained with the α , A, B unsteady aerodynamic model and non-uniform rotor inflow.

The azimuthal correlation of measured and computed blade flatwise and edge-wise stress was much better than that of the pushrod loads. Although approximately correct amplitudes of vibratory torsional moments were predicted, the analytic results do not generally predict torsional oscillations building up at $\psi = 180$ deg. Pushrod loads calculated for the CH-53A in Reference 1 indicated the potentially strong effect that blade-vortex interaction can have on the initiation of blade torsional oscillations. As indicated above, a large vortex core diameter was employed in the calculations of induced velocities to avoid the uncertain effects of blade-vortex proximity on calculated flatwise stress. It is possible that smoothing the rotor inflow in this way reduced torsional excitation. Problems of this type could be avoided by applying a lifting surface aerodynamic model. In fact, the results of Reference 26 indicate that for close blade-vortex passage, lifting line theory badly overpredicts instantaneous blade lift while underpredicting pitching moment. Another factor which could contribute to the discrepancy in the stall flutter initiation point is the uncertainty in the modeling of dynamic stall phenomena at moderate and high Mach numbers. The present unsteady models are based primarily on generalizing low Mach number dynamic stall behavior. Also, in view of the improvements in blade stress correlation resulting from the inclusion of variable inflow, a systematic study of the effects of wake distortion on blade stresses and torsional moments should be performed. The possibility that blade torsional oscillations are initiated on unstalled blades through motion of the control system should also be considered. Finally, three-dimensional flow effects and unsteady drag modeling may impact the initiation of blade torsional oscillations.

The failure of the Time Delay blade response program to predict full-scale blade torsional moments was disappointing. The correlation of hysteresis loops, two-dimensional aerodynamic damping and wind tunnel airfoil dynamic response indicated that the method is capable of predicting stall flutter response. When applied to the three-dimensional situation, blade response was underpredicted, apparently because simultaneous stalling of adjacent blade stations was not promoted. Work is presently under way to evaluate the possibility of including a spanwise stall propagation model in the representation of blade aerodynamics. Based on modeling of the flow separation process, the Time Delay method can easily be changed to speed up local separation due to stalling and separation of adjacent blade segments. Some evidence of this type of behavior can be found in blade pressure coefficients measured in flight, but quantitative modeling of stall propagation remains to be established. Because the need for a general unsteady model not dependent on extensive oscillating airfoil tests is obvious and because Time Delay computing times and storage requirements are much less than required by the α , A, B model, development of the Time Delay approach will continue. For the present investigation, however, better correlation was achieved using the α , A, B procedure; it was therefore chosen for use in the stall boundary generation and parametric design studies to follow. Because test data are available over a wider range of airspeeds and gross weights, the CH-53A aircraft was selected for use in the stall boundary investigation.

GENERATION OF STALL BOUNDARIES FOR THE CH-53A HELICOPTER

In order to define the limitations to helicopter flight envelope imposed by blade stall, the manifestations of stall were examined for a series of advance ratios and rotor thrust coefficients along the stall limit. To probe the stalled flight behavior of the CH-53A rotor, eight flight conditions were simulated using the Normal Modes Blade Aeroelastic Analysis in addition to the four conditions for which CH-53A correlation was studied. The α, A, B unsteady aerodynamic model and variable rotor inflow were used throughout. Relative to the CH-53A control load boundary from Figure 35, Figure 54 shows the flight conditions investigated. At each of three C_T/σ values a sufficient range of advance ratios was studied to show the effects of stall on rotor control loads, blade stresses, required power and aircraft controllability. Limiting values of each of these quantities were established and a limit speed based on each of the types of stall losses was determined for each C_T/σ . Consistent test data (i.e., same tip speed, fuselage center of gravity, ambient air density and temperature, etc.) were not available at each of the analytically simulated flight conditions. Agreement with available experimental data was examined where possible.

The nature of the analytic pushrod load buildup with advance ratio and blade loading is shown in Figures 55 and 56. Earlier initiation of stall response and larger vibratory loads are noted as airspeed or rotor thrust is increased. The top panel of Figure 57 shows the variation of half-peak-to-peak pushrod load with advance ratio for the three thrust coefficient-solidity ratios. The control load limit criterion was taken to be a vibratory pushrod load of ± 2200 lb which corresponds to the pushrod structural damage fatigue limit for the CH-53A. Measured and calculated limit speeds based on this criterion are compared in the lower portion of Figure 57. Actually, the control load boundary is characterized by high vibratory loads in all rotating and fixed control system hardware. For example, the loads experienced by the fixed system servomechanisms build up at a sharp rate. Servo loads were calculated in the normal modes program by transferring rotating system pushrod loads into the fixed system. Figure 58 compares measured and calculated vibratory loads on the fourth quadrant servomechanism which generally experiences the most severe load buildup. Calculated fixed system loads are sensitive to the degree of convergence of the rotating pushrod load waveform. A higher degree of scatter in the analytic fixed system loads is therefore present, and only an approximate faired curve is shown through the analytic data points. Good correlation of fixed system loads depends upon accurate prediction of not only the amplitude but also the harmonic content of the pushrod loads and is therefore more difficult to achieve. Some discrepancies are noted in the stall speed for the lower thrust coefficients, but the rate of servo load buildup is well modeled.

In order to determine the flight limits which result from excessive blade stress, flatwise and edgewise stresses were computed for each flight condition. Maximum vibratory edgewise stress was consistently found to occur at $0.5R$ and maximum flatwise stress at about $0.8R$. The calculated variation in maximum stress is shown in Figure 59. As discussed in the

correlation section, good agreement between measured and calculated blade stress has generally been found. A vibratory stress of ± 6000 psi has been used as the stress limit. Actually, allowable vibratory stress is dependent on local steady stress and therefore, varies along the blade. The ± 6000 psi value corresponds roughly to the infinite life limit for the aluminum spar under typical values of steady stress at 0.5R.

Two additional manifestations of stall are shown in Figure 60. The first is the loss in available control moment experienced in stall. In order to assure controllability and to maintain an adequate control margin for the execution of maneuvers, the pilot generally maintains the capability to apply a nosedown pitching moment with a longitudinal control input. In accordance with Military Specification MIL-H-8501A, an available control moment equal to ten percent of the control moment available in hover has been taken as the limit. For each of the computer cases described above (and shown in Figure 54), an additional case was run in which the longitudinal control input B_{1S} was changed from the trim value to the built-in limit of the aircraft. In each case the change in nosedown pitching moment was noted and compared with the calculated head moment available in hover. The top panel of Figure 60 shows the variation in available moment with airspeed for the three gross weights. These results correspond approximately to neutral center of gravity operation; although as noted, earlier head moments were not trimmed exactly to zero for each of the reference conditions. Examination of the results indicated that the control power derivative $\Delta PM / \Delta B_{1S}$ remained nearly constant even out to 200 knots. In other words, the control limitation is primarily imposed by the limit in stick travel or allowable cyclic pitch.

The last stall penalty, the buildup of required main rotor power, is also shown in Figure 60. Good correlation of measured and computed power required was shown for the intermediate gross weight in Figure 49. The indicated limit value of 6000 horsepower corresponds approximately to the normal rated main rotor power available from the CH-53A engines at the 3000-ft density altitude being used in the calculations.

The stall boundaries calculated above are collected in Figure 61 where maximum thrust coefficient-solidity ratios based on each of the stall losses are plotted versus advance ratio. The calculated boundaries actually fall very close to one another, being separated by no more than 30 knots. In general agreement with flight experience, blade stresses are first to reach critical values at lower C_T/σ while control loads tend to become more significant at gross weights and altitudes for which C_T/σ is high. The controllability boundary tends to be of least concern. Reference to Figure 57 indicates that the control load boundary experienced in flight occurs at lower airspeeds than have been calculated. Accordingly, extensive flight data detailing stress, power and controllability boundaries have not been available, especially at high C_T/σ . Nevertheless, the good prediction of blade response phenomena experienced as the rotor penetrates stall indicates that the stall mechanisms are being reasonably modeled and that predicted changes in the stall boundaries accompanying blade design changes can be used with confidence.

Of the boundaries considered, the control load limit imposes the most fundamental limitation on possible expansions to the flight envelope. Although Figure 59 indicates that blade stress, particularly edgewise stress, shows a significant buildup at the higher speeds, relatively simple design changes can be employed to alleviate stress for a given set of applied bending moments. For example, as noted earlier, the high levels of CH-53A edgewise stress result from the near resonant forcing of the first edgewise mode. Flight tests of modified CH-53 blade designs have shown that the edgewise stress problem was alleviated by detuning the edgewise mode from the 4P resonance. Also, since the control derivative $\Delta PM / \Delta B_{1S}$ does not show severe degradation with forward speed, additional control moment could apparently be obtained by increasing allowable cyclic pitch. Finally, although required power does build up rapidly with blade stall, an increase in installed power would permit increased forward speeds. The flight envelope determined by control loads is, however, more difficult to expand. Beyond the knee of the curve, control loads build up at such a rapid rate that strengthening of the control system to withstand higher loads would result in only small increases in maximum speed. Changing blade design to reduce the magnitude of the applied loading is one fundamental approach that can be followed in an attempt to reduce the control load buildup. The potential of this approach is examined in the parametric design study which follows.

PARAMETRIC DESIGN STUDY

The effects of blade structural design changes on the CH-53A calculated stall boundaries were examined. Results obtained in the correlation and boundary generation studies indicated that the mechanisms by which penetration into stall increased rotor loads were being well modeled by the analysis. It was appropriate, then, to investigate for a typical helicopter: (1) how the blade response mechanisms in stall are affected by changes in blade structural design parameters and (2) whether blade design changes can be made which delay the adverse effects of stall and permit expansion of helicopter flight envelopes. Particular emphasis was placed on the control load boundary which often presents an important limitation to possible expansion of helicopter operating envelopes. References 27 and 24 describe two specific efforts to reduce control loads by changes in blade and control system design. In the present work a more general study of the effects of blade parameters on stall boundaries was conducted. Examination of the torsional equation of motion which is solved in the Normal Modes Aeroelastic Blade Response Program indicates that a number of parameters can have fundamental effects on blade torsional response. Equation (89) of Reference 20, which describes the normal modes differential equations of motion, shows the sources of blade torsional excitation. It is possible to identify the blade torsional structural moment (which is directly related to the pushrod load) as being approximately equal to the sum of an applied aerodynamic moment, a torsional inertia moment, a moment due to the product of shear forces and blade bending deflections, and a moment due to the chordwise offset of the blade center of gravity from the elastic axis.

$$M_S = M_A + M_I + M_{SD} + M_{CG} \quad (11)$$

A group of blade parameters was chosen which altered each of these sources of torsional moment. Independent changes were made to each of the following eight parameters, and the effects of each of the terms on the mechanism of blade torsional response in stall were noted.

- (1) Airfoil
- (2) Torsional mode shape
- (3) Blade flatwise and edgewise stiffness
- (4) Chordwise center of gravity location
- (5) Chordwise elastic axis location
- (6) Blade twist
- (7) Torsional natural frequency
- (8) Torsional inertia

In order to concentrate efforts on the most important parameters, an exploratory study was first conducted at a previously studied flight condition which exhibited large amplitude retreating blade torsional oscillations. A 140 kn/49,000 lb gross weight flight condition, which is seen in Figures 57, 59 and 60 to be near the control load, blade stress and power boundaries, was chosen for this study. Figure 62 shows the total blade root structural moment for this flight condition and the component torsional moments contributing to the total. Moments are nondimensionalized according to the conventions of Reference 20. It is clear that blade torsional moment results largely from the combination of an aerodynamic pitching moment and the resulting torsional inertia moment. The inertia moment is almost directly out of phase with the aerodynamic moment and is of greater magnitude. The resulting structural moment is, therefore, in phase with the inertia moment. The so-called shear-deflection moments are small. The CH-53A blade, which has its elastic axis and center-of-gravity at approximately the quarter chord, does not experience moments around the elastic axis due to inertial forces acting at the center of gravity.

Independent changes were made to each of the eight blade parameters, the blade response calculations were repeated for this flight condition, and computed values of control loads, blade stress and power were compared with those calculated for the standard blade. In general, two parameter values were studied, one above and one below the corresponding CH-53A value. This procedure permitted the establishment of reliable trends. In each of the modified rotor configurations, the rotor inflow distribution was taken from the corresponding standard blade case and rotor lift and propulsive force were trimmed to required values by incrementing collective pitch angle and shaft angle. Based on the results of these preliminary calculations, the four parameter changes which had the most beneficial effect on control loads were chosen for further study. For these parameters, calculations were then made at a series of advance ratios and thrust coefficients to define modified stall operating limits.

AIRFOIL PROPERTIES

The first blade property to be studied was blade airfoil shape. It was found that increasing airfoil static stall angle had a clearly beneficial effect on vibratory control loads. Comparison of leading and trailing edge stall airfoils did not show a significant difference. Optimization of airfoil contour from the standpoint of dynamic stall behavior is a subject deserving a great deal of further research. Two-dimensional dynamic stall tests of the type described above and fundamental research into the effect of blade contour on the dynamic stall process such as described in Reference 28 must be done. Attempts to investigate fully the effects of airfoil shape on blade behavior in stall are limited by a lack of unsteady airfoil data or a proven method of modeling the unsteady characteristics of a given airfoil. In the present study the effects of two changes in airfoil characteristics on stall boundaries were investigated using the scaling techniques described in Reference 8.

First, a symmetric airfoil which, relative to the NACA 0012, had a 20 percent increase in static stall angle was used in the calculation of blade response at the 140 kn/49,000 lb flight condition. Unsteady lift and pitching moment data for this hypothetical airfoil were generated by scaling the α , A, B NACA 0012 data so that the static stall angle and c_{lMAX} were increased by 20 percent. Figure 63 compares the $c_m(\alpha, 0, 0)$ and $c_l(\alpha, 0, 0)$ values for the standard and scaled airfoil data. Standard steady-state drag data were used. The pushrod load time history shows that increasing the stall angle (as might be expected) gives a reduction in peak-to-peak load of more than 40 percent. Reference to Figure 57 indicates that if the slope of the pushrod load versus airspeed curve were not altered, an increased allowable airspeed of 30-40 knots would be realized with this airfoil. Improvements in lift-to-drag ratio and blade stresses were also predicted.

A second change to the unsteady aerodynamic data was made to approximate the pitching moment characteristics of a leading edge stall airfoil. To accomplish this goal, a correction function $\delta_m(\alpha)$ was added to the NACA 0012 data which increased the sharpness of the pitching moment stall. Corrections of the form shown in Figure 64 which increased positive pitching moment with angle of attack below the static stall angle were added to the NACA 0012 unsteady data.

$$c_{mLE}(\alpha, A, B) = c_{mNACA\ 0012}(\alpha, A, B) + \delta_m(\alpha) \quad (12)$$

Airfoil dynamic stall characteristics as reflected by the unsteady data tabulations were not changed but the sharpness of the static pitching moment break was increased as shown for a typical Mach number in Figure 64. Standard lift and drag data were used. Comparison of pushrod load time histories shows that the leading edge stall airfoil increases the overall amplitude of the pushrod load but does not have a strong effect on re-treating blade stall flutter moments. Changes in blade stresses and required power were not significant. Because unsteady airfoil data in the α , A, B form are only available for the NACA 0012 airfoil and because of the uncertainties involved in scaling the unsteady NACA 0012 data to represent airfoils with different stall characteristics, the effect of airfoil type on blade response was not studied at other flight conditions.

TORSIONAL MODE SHAPE

Independent changes to blade torsional mode shape which were also considered had only secondary effects on control loads at the flight condition studied. Changes in mode shape alter the radial variation of elastic twist angle and, therefore, change the angle of attack distribution and the resulting airloads and pitching moments. Because torsional natural frequency and torsional inertia were assumed to be fundamental parameters, independent changes to the torsional mode shape were made by varying blade and control system stiffness. For the standard torsional frequency ratio of 6.0P, the two limiting values of torsional mode shape (namely those corresponding to rigid blade/flexible control system and flexible blade/rigid control system configuration) were calculated using the natural frequency portion of the

normal modes program. Substitution of the two limiting mode shapes into the blade response calculations had little effect on blade torsional response. Examination of the two cases which were trimmed to the same rotor lift and propulsive force indicated that changing the radial distribution of elastic twist did not significantly affect blade angles of attack in the area of the three-quarter radius, where the largest pitching moment loading is experienced. Blade aerodynamic pitching moments and resulting torsional structural moments were, therefore, essentially unchanged. At least for deeply stalled flight conditions torsional mode shape does not have a significant effect on control loads.

BENDING STIFFNESS

The effects of blade flatwise and edgewise stiffness on control loads and blade stresses were examined. Changes to blade bending stiffness had virtually no effect on calculated pushrod loads. Blade bending stresses were, however, reduced in some cases. Blade bending response affects section angles of attack and therefore can alter blade airloads and pitching moments. Moreover, a torsional moment is produced by the blade flatwise and edgewise shear forces which act on the deflected blade. It is shown in Reference 20 that the importance of these shear-deflection effects is reduced as local blade flatwise and edgewise stiffnesses approach the matched condition. Three stiffness configurations were examined. In the first two cases, blade bending stiffnesses were changed by factors of 0.5 and 1.5. For the reduced stiffness blade the first flatwise frequency dropped from 2.72P to 2.64P and the first edgewise frequency dropped from 3.91P to 3.25P. At the 140 kn/49,000 lb flight condition the most significant effect on blade loads was a four to one reduction in the magnitude of the 4P edgewise bending moment at the critical radial station caused by the separation of the first edgewise frequency from the 4P aerodynamic loading. Overall edgewise bending moment was decreased only by about 20 percent because the 3P bending moments were increased. With the stiffer blade the first flatwise frequency changed from 2.72P to 2.79P and the edgewise frequency increased to 4.45P. In this case the 4P component of edgewise stress was reduced by 20 percent but the overall stress reduction was only about four percent. In neither case was there a significant effect on vibratory control loads. A third calculation was made in which blade flatwise and edgewise stiffnesses were matched so that shear-deflection moments were eliminated. This change had only a small effect on blade torsional response. This result was expected from the previous calculation of the sources of torsional moment for the standard blade where it was shown that the shear-deflection moments were quite small at this flight condition (Figure 62). It is clear that for this blade, torsional response is essentially uncoupled from flatwise and edgewise bending and that the primary source of torsional excitation is the aerodynamic pitching moment.

ELASTIC, CENTER-OF-GRAVITY AND AERODYNAMIC CENTER AXES

An area which was investigated in some detail was that of blade chordwise axis positioning. In the normal modes analysis the effects of displacing the chordwise center-of-gravity and aerodynamic center locations from the elastic axis are modeled. The elastic axis and pitch axis are assumed to

be coincident. Based on the reference blade which has all three axes at approximately the quarter chord, forward and aft movement of the center of gravity, aerodynamic center and elastic axis were considered independently. Of the cases considered, movement of the coincident elastic and center-of-gravity axes forward of the blade aerodynamic center had the most beneficial effect on vibratory control loads.

Figure 65 shows the effect on pushrod load of forward and aft placement of the center-of-gravity axis relative to the aerodynamic center and elastic axes. It is well known that chordwise offset of the blade center of gravity (c.g.) from the elastic axis can have a significant effect on blade torsional response. For example, classical flutter and static divergence phenomena depend upon the c.g. location. Coupling exists between the blade flatwise and torsional motions such that for a blade with its c.g. forward of the elastic axis, rotor centrifugal and inertial forces produce nosedown (stabilizing) moments when the blade moves upward. In the first analytic case, movement of the center of gravity aft of the elastic axis to $0.3c$ led to a subharmonic ($0.5P$) blade response involving coupled flatwise and torsional deflections. Rotor lift oscillated between 47,000 lb and 60,000 lb and there were substantial increases in vibratory head moments and control loads. On the other hand, well-behaved analytic responses were calculated for blades with $0.265c$ and $0.22c$ center-of-gravity locations. A gradual trend of decreasing vibratory pushrod load with forward movement of the c.g. from $0.25c$ to $0.22c$ is noted in Figure 65. The main effect of moving the center of gravity toward the leading edge is that the centrifugal forces introduce a steady nosedown moment. Neither center-of-gravity shift had a major effect on blade stresses although a required power reduction of about 10 percent was predicted for the forward c.g.

The second axis configuration studied involved a $\pm 0.05c$ shift of the elastic axis relative to the coincident aerodynamic center and the center of gravity. In each of these cases, the increment to the aerodynamic moment arising from the offset of the aerodynamic center and elastic axis was approximately balanced by a change in the inertial moment introduced by c.g. offset. As a result, the high frequency control loads were nearly unchanged.

Offset of the aerodynamic center from the coincident elastic axis and the c.g. was found to have the most beneficial effect on control loads at this flight condition. The two-dimensional airfoil results described earlier indicated that forward movement of the pitch axis (elastic axis for blade) relative to the aerodynamic center had the potential of decreasing stall flutter moments. Although the effect is not as strong for the rotor as it was with the model airfoil, Figure 66 does show a decrease in vibratory pushrod load of about 20 percent with movement of the elastic axis forward to the $0.22c$ position. An increase in steady nosedown moment and elastic deflection angle are predicted for this case.

Because there was a reduction in torsional moment predicted at this condition and measured on the wind tunnel airfoil for blades with pitch axis shifted forward to $0.22c$, similar calculations were performed throughout

the CH-53A flight envelope. Figures 67 and 68 summarize the potential effect of the forward pitch axis on rotor loads. Relative to the standard blade results, modest reductions in control loads and required power and slightly elevated levels of flatwise stress are evident. Limiting airspeeds based on control load, power and stress considerations were determined at each thrust coefficient, and the corresponding stall boundaries are shown in Figure 69. A 15-knot increase in the pushrod load limiting speed is predicted at the highest C_T/σ . However, the limiting speed determined by flatwise stress is reduced by about 15 knots at the highest C_T/σ .

BLADE TWIST

A similar investigation was performed to determine the effects of blade twist on stall boundaries. Linear twist angles of -12 deg and 0 deg were used at the reference flight condition. Small improvements in vibratory control loads and required power were calculated for the high twist blades. Because there was a calculated reduction in vibratory load and because there is current interest in high twist blades, seven flight conditions were simulated using the -12-deg twist blades. Typical time history comparisons are shown in Figure 70. At the 137 kn/42,000 lb gross weight flight condition shown in the top insert of Figure 70, the increased twist causes a nosedown moment at 140 deg azimuth. This nosedown moment is largely caused by shear-deflection effects. The increase in blade twist makes the advancing blade tip angle of attack more negative, which increases the tip down bending. Drag forces acting at the tip, therefore, produce a nosedown moment. Because the rotor is only lightly stalled this oscillation does not grow. In the fourth quadrant, the increase in built-in twist redistributes blade lift and decreases blade tip angles of attack so that applied aerodynamic moments and oscillatory response are reduced. At a higher speed flight condition (180 kn/35,000 lb), the second quadrant nosedown moment is larger and serves to initiate a stall flutter oscillation which grows in amplitude to such an extent that the potential unloading of the retreating blade tip is not effective in reducing vibratory pushrod load. Figure 71 illustrates the fact that high twist generally decreased the magnitude of the pushrod load. At the highest airspeeds, however, the effect of increased twist is detrimental. At all thrust coefficients the rate of control load buildup with airspeed is higher for the high twist blades. Corresponding results for power and blade stress are presented in Figures 71 and 72. Large increases in flatwise bending stress result from the negative tip loading of the advancing blade, and allowable airspeeds determined by flatwise stress are reduced at each C_T/σ . Six additional cases were analyzed to determine the effect of twist on available control moment. In each case the longitudinal cyclic pitch B_{1S} was set equal to the limiting value and the available nosedown pitching moment was noted. The results show that there is only a small change (Figure 72). The five stall boundaries are shown in Figure 73. Pushrod loads are alleviated up to an advance ratio of about 0.45. It is clear, however, that flatwise stress becomes the most important limitation.

TORSIONAL FREQUENCY

The model airfoil results described earlier showed that reducing torsional frequency decreased stall flutter moments. Additionally, experimental and analytic studies described in Reference 27 show the significant impact of torsional frequency on control loads. The results of Reference 27 showed that reducing torsional frequency either by reducing blade or control system stiffness or by increasing torsional inertia reduced stall flutter moments uniformly. It was verified in the torsional mode shape calculations above that for the same torsional frequency, the relative values of blade and control system stiffness did not have a strong effect on stall flutter response. For the present work, changes in torsional frequency were accomplished by varying blade and control system stiffness proportionately so that mode shape was not altered. Relative to the standard blade frequency of 6.0P, blade frequencies of 3.0, 4.0, 5.0, 8.0, 12.0 and ∞ times rotor frequency were analyzed at the 140 kn/49,000 lb flight condition. Figure 74 compares the pushrod load time histories calculated with four values of torsional frequency. Reducing frequency from the 6.0P value reduces vibratory pushrod load. The largest vibrating pushrod loads occurred for the 12P blades. However, the 12.0P results may be subject to some error because over a limited azimuth range the nondimensional $\dot{\alpha}$ and $\ddot{\alpha}$ values associated with the 12.0P response exceed the limits of the unsteady data tabulations. The stall flutter spike amplitude, shown in Figure 74, and the overall amplitude of pushrod load are plotted versus torsional frequency ratio in the top inserts of Figure 75. The elastic torsional tip deflections corresponding to the stall flutter spike and to the overall vibratory load are shown in the lower panels of Figure 75. It is interesting to note that at least in the frequency range from 3.0 to 6.0P the torsional deflection amplitude corresponding to the stall flutter spike remains relatively constant.

The stall flutter spiking frequency is compared with the torsional natural frequency in the top panel of Figure 76. The response frequency is in all cases greater than the natural frequency, and the spread between the two increases as natural frequency is reduced. The shift in frequency can be attributed to an aerodynamic stiffening caused by the generally negative slope of the pitching moment versus angle of attack curves. The aerodynamic pitching moment acts to apply a restoring moment in parallel with the structural restoring moment. (For negative slopes of the c_m versus α curves, as the blade undergoes noseup torsional deflection, angle of attack is increased and a nosedown pitching moment is experienced.) The lower panel of Figure 76 illustrates this effect schematically. The hysteresis loop determined by the generalized aerodynamic pitching moment and the first torsional mode response is shown over the range of blade azimuth corresponding to stall. As shown in the figure, the variation of generalized pitching moment M_{AG} with generalized torsional modal response θ_G can be linearly approximated in terms of constants c_1 and c_2 by

$$M_{AG} = c_1 + c_2 \theta_G \quad (13)$$

where the constant c_2 is negative. Based on this approximation a stall flutter spiking frequency can be calculated. For blades without c.g.

offset, the differential equation used to solve for the first torsional modal response can be approximated by

$$\overset{xx}{\theta}_G + \bar{\omega}_\theta^2 \theta_G = \frac{1}{I_G} M_{AG} \quad (14)$$

where $\overset{xx}{\theta}_G$ represents the second derivative of θ_G with respect to non-dimensional time Ωt and I_G denotes the generalized torsional blade inertia. If M_{AG} can be represented by Equation (13),

$$\overset{xx}{\theta}_G + \bar{\omega}_\theta^2 \theta_G = \frac{1}{I_G} [c_1 + c_2 \theta_G] \quad (15)$$

so that

$$\overset{xx}{\theta}_G + (\bar{\omega}_\theta^2 - c_2/I_G) \theta_G = \frac{c_1}{I_G} \quad (16)$$

and the torsional response frequency is given by

$$\bar{\omega}_{\text{response}} = \sqrt{\bar{\omega}_\theta^2 - c_2/I_G} \quad (17)$$

Examination of the calculated generalized moment/torsional response hysteresis loops shows that with the present airfoil data tabulations a value of $c_2/I_{\theta G}$ approximately equal to $-24/\text{rad}$ is found. This value in Equation (18) gives response frequency as a function of natural frequency, as shown in the top panel of Figure 76. This figure indicates that the trend exhibited by the normal modes cases is reasonably well represented by this simple model.

In order to understand the beneficial effect which reducing frequency has on vibratory control loads, the analytic solution to the torsional response equation was examined for the $\bar{\omega}_\theta = 4.0P$ blade. Figure 77 shows the torsional moments experienced by the soft blade and the standard 6.0P blade. The amplitudes of the aerodynamic pitching moments are approximately equal. It is clear that the reduction in structural moment results from a decrease in the inertial moment M_I . (For a second-order torsional system, having inertia I and responding harmonically at a frequency ω_θ , $M_I = I\omega_\theta^2 \theta$). The inertial moment is greater than and approximately out of phase with the aerodynamic moment, so that for a given amplitude of M_A , reducing M_I reduces the overall structural moment.

Explanation of the mechanism by which reducing frequency reduces structural moments requires understanding of the interaction between high frequency blade torsional motion and applied aerodynamic moments. The high frequency component of the unsteady aerodynamic moment depends on the amplitude and frequency of the blade elastic response. The elastic response depends in turn on the applied moment. In the present computation procedure, the pitching moment characteristics are extracted from the $c_m(\alpha, A, B)$ tables where the α , A and B values are strongly dependent on elastic response. The interpolated pitching moments are incorporated into the timewise integration of the blade equations of motion which proceeds until compatible blade

torsional response and applied aerodynamic moment time histories are established. Detailed analysis of blade response results is made difficult by the complex dependence of aerodynamic moments on unsteady motions and by the fact that the different blade designs iterate to different solutions involving different regions of the α , A, B tables. The results of the frequency study indicate that over the range of frequencies from 3.0P to 6.0P the shapes of the pitching moment coefficient/angle of attack hysteresis loops for outboard blade sections are very similar. In other words the amplitudes of the aerodynamic forcing functions extracted from the α , A, B tables are relatively insensitive to frequency over this range. Instead, the aerodynamic moments are amplitude dependent and a fixed amplitude limit cycle response is reached independent of frequency. For a given amplitude deflection, blade stiffness accounts for the difference in structural loads. The softer blade experiences a reduction in retreating blade vibratory load of about 50 percent at this flight condition. For frequencies above about 6.0P the form of the $c_m(\alpha, A, B)$ variation changes and different hysteretic behavior is evident. In this frequency range the dependence of the aerodynamic response on frequency is stronger and calculated moments are phased to reduce the amplitude of the torsional response. The vibratory pushrod load and elastic deflection results shown in Figure 75 show that relative to the standard blade, deflections for the 8.0 and 12.0P blades are decreased but increased stiffness causes comparable twisting moments.

The $\bar{\omega}_0 = 4.0P$ blade was selected for investigation throughout the flight envelope. For this blade the GJ and root spring values were 0.45 X the standard values. Figures 78 and 79 summarize the analytic results. Sizeable reductions in the overall vibratory pushrod load are shown in Figure 78. Reducing frequency has the most beneficial effects at high thrust coefficients. Results at the 160-kn, high C_T/σ flight condition may be subject to question because at this condition the retreating blade is so deeply stalled that angles of attack exceed the limits of the unsteady data tables. Allowable airspeed increases on the order of 15 knots are shown for the pushrod loads at the two highest C_T/σ values. The reduction shown in required power results from the fact that the increased compliance of the torsionally soft blades permits the blade to twist out of deep stall more readily and achieve a more optimum angle of attack distribution. Also, because the soft blades generally experienced a larger steady nosedown elastic twist angle for the same rotor lift, the center of lift was shifted inboard and tip angles of attack and drag forces were reduced. The stress results (Figure 79) indicate only a small impact of frequency. A limited number of calculations were made to determine the effects of torsional frequency on the available control moment boundary. A small decrease in control moment stall speed is shown in Figure 79. Some loss in pitching moment capability may result from inboard movement of the blade lift forces due to the change in angle of attack distribution. The changes in stall boundaries are presented in Figure 80. The pushrod load results show increases in allowable speed or allowable payload up to an advance ratio of about 0.47 with the $\bar{\omega}_0 = 4.0P$ blades.

TORSIONAL INERTIA

The final parameter to be investigated was blade torsional inertia. Because inertia changes independent of torsional frequency and mode shape were desired, blade inertia and blade stiffness and root stiffness were varied in proportion. Physically, this study would treat blades of the same material and section geometry but with differing cross section scale. Because torsional response phenomena were the primary concern, blade mass and flatwise and edgewise inertias were not changed. Three inertia values were used to calculate response at the 140 kn/49,000 lb flight condition. The resulting pushrod load time histories are shown in Figure 81. In a manner similar to that found for the low frequency blades, decreasing the inertia reduced the inertia moment without significantly affecting the aerodynamic moment. A limit cycle solution whose amplitude was relatively insensitive to inertia was calculated. The decrease in vibratory moment with decreasing inertia at the same frequency is not in agreement with the results of Reference 27 where it was stated that the controlling parameter was torsional frequency and that, for a given frequency, pitch-link loads were not dependent on the choice of stiffness and inertia values. To clarify this situation, cases were run in which frequency (and mode shape) were altered by changing inertia only. The results of these cases shown in Figure 82 imply that at this flight condition (140 kn/49,000 lb gross weight), decreasing frequency by increasing inertia is less beneficial than increasing frequency. As a summary, the amplitudes of the vibratory pushrod loads from all the frequency and inertia cases are plotted versus torsional natural frequency ratio in Figure 83. Distinct trends are obtained by changing GJ, GJ and inertia, and inertia only. The results are also plotted against the stiffness ratio (GJ/GJ_{STD}). It is clear that reducing stiffness below the standard CH-53A value reduces vibratory loads regardless of whether the frequency is reduced. It is also clear that the independent effect of reducing inertia is to decrease the amplitude of stall flutter spikes.

To determine the effect of inertia on control loads for the same torsional frequency, the behavior of blades having a 50-percent reduction in inertia and GJ was examined along the stall boundaries. The results are summarized in Figures 84 through 86. Decreases in peak-to-peak pushrod loads were predicted at all flight conditions. Relative to the 4.0P blade which also had $GJ = \frac{1}{2}GJ_{STD}$, the results of Figure 84 indicate that reducing inertia by 50% generally reduced loads even further. Pushrod load amplitude was reduced to such an extent that extrapolation of the results to the limiting load level was difficult without repeating calculations at airspeeds higher than previously studied. Because blade stress and power limits had already been reached, this was not done and the limiting airspeeds are determined only approximately. Reductions in required power comparable to those calculated with the $\bar{\omega}_0 = 4.0P$ blades were predicted. Small degradations in blade stress and available control moment are shown in Figure 85 for the low inertia blades. The stall boundaries based on each of the five performance indicators are shown in Figure 86.

The results of the analytic parameter variation study can be used to provide the following set of general design guidelines aimed at reducing high

frequency control loads. Findings 1-4 apply most directly to low twist blades with symmetrical airfoil sections and having little aerodynamic pitching moments resulting from adverse compressibility effects on the advancing blade.

1. Reducing torsional stiffness and/or torsional inertia decreases the amplitude of the vibratory torsional moments associated with retreating blade stall.
2. Moving the airfoil elastic and center-of-gravity axes forward of the aerodynamic center axis reduces the amplitude of the high frequency torsional moments.
3. Increasing blade twist generally delays the airspeed for control load buildup but increases the rate of control load buildup with airspeed.
4. Torsional mode shape and flatwise and edgewise stiffnesses do not strongly affect high frequency torsional moments.
5. An increase in airfoil static stall angle reduces vibratory pushrod load. Leading and trailing edge stall airfoils with the same stall angle result in approximately the same level of stall flutter response.

With regard to the position of the control load boundary, the results of the parametric study are presented graphically in Figure 87 where the various control load boundaries are compared and the increase in allowable advance ratio with each independent design change is extracted and plotted versus C_T/σ . The following general trends are evident:

1. Reducing torsional frequency to 4.0P by reducing blade stiffness has its most beneficial effects on the control load boundary at high C_T/σ .
2. Decreasing torsional inertia while maintaining the standard frequency has beneficial effects at all thrust coefficients. The maximum increase in allowable airspeed of 40 knots occurs at the intermediate thrust coefficient.
3. Forward movement of the blade elastic axis and increasing blade twist have smaller effects on the pushrod load boundary. High twist decreases the stall speed at low C_T/σ and high advance ratio.

REEVALUATION OF PRELIMINARY STALL BOUNDARY PREDICTION METHODS

In light of the results of the stall boundary generation and blade design studies, the preliminary stall boundary prediction techniques described earlier were reevaluated. The objectives were to determine (1) whether any of the simple methods can be expected to give accurate prediction of the stall boundaries of an arbitrary rotor design and (2) whether the results of the parametric design study can be used to extend simple design methods by including the effects of blade structural parameters on stall boundaries.

It is clear from the parametric design calculations that blade structural design changes can have potentially large effects on stall boundaries. Therefore, boundary prediction techniques which rely on the correspondence of stall-related flight limitation and a purely aerodynamic stall criterion should not necessarily be expected to predict accurately the difference in operating limits for two rotors with widely different structural design characteristics. The simple aerodynamic criteria are generally based on experience with a given type of rotor and become less valuable as departures from past rotor designs are considered. Also, the analytical results show that many types of stall boundaries exist (control loads, blade stress, power, etc.) and that design changes can have conflicting effects on different boundaries. Increased blade twist, for example, expanded the CH-53A control load boundary but reduced limiting speeds based on flatwise stress. Information such as this is not likely to be available from semiempirical design approaches which are generally based on experience with one type of stall boundary. It has also been noted that prediction of the effects of blade parameters on incipient stall boundaries may not be sufficient for design purposes. For example, increasing blade twist delayed the buildup of pushrod loads, but reduced the maximum allowable airspeed at low values of C_T/σ (Figure 71).

Because it is desirable to have rapid but accurate means of estimating stall boundaries in preliminary design trade-off studies, attempts must be made to integrate the results of the flexible blade analyses into preliminary design procedures. The effects of four blade parameters on the stall boundaries of a fairly typical low twist, symmetrical airfoil section rotor have been evaluated above. Hopefully, similar analyses can be performed which extend these results to include the effects of other parameters such as airfoil camber, tip geometry, and control system characteristics. If a catalogue of such results was available to the blade designer the effects of rotor structural design parameters on stall boundaries could be included in preliminary design calculations. One of the various aerodynamic stall criteria could be used to establish a baseline stall boundary, and then corrections to the boundary positions could be made for independent structural design changes. For example, $\Delta\mu$ versus C_T/σ relationships of the form shown in Figure 87 could be used to modify basic stall boundaries to account for independent blade property changes. As an illustration, Figure 88 shows the measured pushrod load limit and two simply calculated stall boundaries. The first curve is based on the rotor profile torque criterion $bC_{Q,D}/\sigma = 0.008$ and the second on $\alpha_{(1.0,270^\circ)} = 16$ deg. Both methods correspond to

an upper stall boundary and appear to give good agreement with the vibratory pushrod load structural limit. Also shown are the $\Delta\mu$ versus C_T/σ correction curves for four parameter changes. Use of the latest analytic methods to generate correction curves of this type will provide significantly increased capability for estimating stall boundaries by allowing the treatment of blade parameters not covered by rigid blade analyses. The complete aeroelastic analysis can then be used to verify results quantitatively and to investigate the effects of combining two or more design features.

CONCLUSIONS

1. Two-dimensional stall flutter tests indicate that reducing blade torsional stiffness, reducing blade torsional inertia and moving blade pitch axis forward decrease stall flutter induced moments. Inception of stall flutter was delayed with the SC 1095 airfoil relative to the NACA 0012 airfoil; however, once initiated, stall flutter loads for the two airfoils were generally comparable.
2. The trends shown by two-dimensional wind tunnel stall flutter tests can be predicted using two unsteady aerodynamic models. The Time Delay unsteady aerodynamic model gives a conservative prediction of response amplitude.
3. Acceptable correlation of CH-53A blade stresses, control loads and required power was obtained with a rotor aeroelastic analysis employing variable rotor inflow and unsteady aerodynamics. Best correlation was achieved using the α , A, B unsteady aerodynamic model of Reference 1 in which airfoil unsteady coefficients are expressed as functions of angle of attack and its first two time derivatives.
4. Analytical studies to determine the influence of design parameters on control loads generated by rotors having symmetrical airfoil sections generally substantiated two-dimensional airfoil test results. That is, reduced torsional blade stiffness, reduced torsional inertia, increased airfoil static stall angle and forward movement of the blade pitch axis all led to reduced dynamic control loads.
5. Increasing blade twist delayed the control load stall speed at high C_T/σ but increased the rate of control load buildup with airspeed. Increasing twist increased blade flatwise moments substantially.
6. Current techniques for predicting stall boundaries which are based on aerodynamic stall parameters alone are not equally applicable to blades having differing dynamic properties.

RECOMMENDATIONS

1. Further analytical studies should be conducted to examine the combined effects of the design parameters which have been found to be promising in this study. In addition, other design parameters not considered in this study, such as airfoil camber, blade tip sweep and number of blades, should be evaluated.
2. Model rotor tests should be conducted to substantiate the predicted beneficial effects of torsional stiffness, torsional inertia, twist and airfoil contour on stall boundaries.
3. Further work should be done to refine the Time Delay unsteady aerodynamic model or on similar techniques which do not require test data for the airfoil being modeled.
4. The sources of blade torsional moments experienced at $\Psi = 180$ deg should be studied. In this area, high Mach number unsteady airfoil pitching moment data should be obtained and improved procedures for predicting the lifts and moments associated with close blade-vortex passage should be developed. The influence of spanwise velocity components should also be assessed.
5. The present aeroelastic analysis should be extended to include the effects of fixed control system dynamics on blade response. Tests involving changes to fixed system design should be performed.

REFERENCES

1. Carta, F. O., Commerford, G. L., Carlson, R. G., and Blackwell, R. H., INVESTIGATION OF AIRFOIL DYNAMIC STALL AND ITS INFLUENCE ON HELICOPTER CONTROL LOADS, United Aircraft Research Laboratories; USAAMRDL TR 72-51, Eustis Directorate, U. S. Army Air Mobility Research and Development Laboratory, Fort Eustis, Virginia, September 1972, AD 752917.
2. Pope, A., and Harper, J. J., LOW-SPEED WIND TUNNEL TESTING, John Wiley & Sons, Inc., New York, 1966.
3. Young, R. A., HELICOPTER ENGINEERING, Ronald Press Company, New York, 1949.
4. Ward, D., and Cohen, W., WIDE BAND SYSTEM FOR ACQUIRING AND RECORDING DATA (WISARD), United Aircraft Research Laboratories Report H-076944-1, October 1969.
5. Oliver, B. M., and Cage, J. M., editors, ELECTRONIC MEASUREMENT AND INSTRUMENTATION, McGraw-Hill Book Company, Inc., New York, 1971.
6. Gray, L., and Liiva, J., WIND TUNNEL TESTS OF THIN AIRFOILS OSCILLATING NEAR STALL, The Boeing Company, Vertol Division; USAAVLABS TR 68-89A and 68-89B, U. S. Army Aviation Materiel Laboratories, Fort Eustis, Virginia, January 1969, AD 684323, AD 684324.
7. Ham, N. D., and Garelick, M. S., DYNAMIC STALL CONSIDERATIONS IN HELICOPTER ROTORS, Journal of the American Helicopter Society, Vol. 13, No. 2, April 1968.
8. Arcidiacono, P. J., Carta, F. O., Caselini, L. M., and Elman, H. L., INVESTIGATION OF HELICOPTER CONTROL LOADS INDUCED BY STALL FLUTTER, United Aircraft Corporation, Sikorsky Aircraft Division; USAAVLABS TR 70-2, U. S. Army Aviation Materiel Laboratories, Fort Eustis, Virginia, March 1970, AD 869823.
9. Ericsson, L. E., and Reding, J. P., UNSTEADY AIRFOIL STALL REVIEW AND EXTENSION, Journal of Aircraft, Vol. 8, No. 8, August 1971.
10. Tarzanin, F. J., PREDICTION OF CONTROL LOADS DUE TO BLADE STALL, American Helicopter Society, 27th Annual National Forum, May 1971.
11. Carta, F. O., and Niebanck, C. F., PREDICTION OF ROTOR INSTABILITY AT HIGH FORWARD SPEEDS, VOLUME III, STALL FLUTTER, United Aircraft Corporation, Sikorsky Aircraft Division; USAAVLABS TR 68-18C, U. S. Army Aviation Materiel Laboratories, Fort Eustis, Virginia, February 1969, AD 687322.

12. Gustafson, F. B., and Myers, Jr., G. C., STALLING OF HELICOPTER BLADES, NACA TN 1083, National Advisory Committee for Aeronautics, June 1946.
13. Wells, C. D., and Wood, T. L., MANEUVERABILITY - THEORY AND APPLICATION, Journal of the American Helicopter Society, Vol. 18, No. 1, January 1973.
14. Lemnios, A. Z., Smith, A. F., and Nettles, W. E., THE CONTROLLABLE TWIST ROTOR, PERFORMANCE AND BLADE DYNAMICS, American Helicopter Society, 28th Annual National Forum, May 1972.
15. Tanner, W. H., CHARTS FOR ESTIMATING ROTARY WING PERFORMANCE IN HOVER AND HIGH FORWARD SPEEDS, United Aircraft Corporation, Sikorsky Aircraft Division Report SER 50379, August 1964.
16. Hoffstedt, D. J., ADVANCED-GEOMETRY, GLASS-FIBER-REINFORCED PLASTIC ROTOR BLADE TEST PROGRAM, The Boeing Company, Vertol Division; USAAMRDL TR 71-42, Eustis Directorate, U. S. Army Air Mobility Research and Development Laboratory, Fort Eustis, Virginia, September 1971, AD 738203.
17. Arcidiacono, P. J., THEORETICAL PERFORMANCE OF HELICOPTERS HAVING SECOND AND HIGHER HARMONIC FEATHERING CONTROL, Journal of the American Helicopter Society, Vol. 6, No. 2, April 1961.
18. Cresap, W. L., et. al., THE 200+ KNOT FLIGHT RESEARCH HELICOPTER, American Helicopter Society, 21st Annual National Forum, May 1965.
19. Lemnios, A. J., ROTARY WING DESIGN METHODOLOGY, Advisory Group for Aerospace Research and Development, Specialists Meeting on Helicopter Rotor Loads Prediction Methods, March 1973.
20. Arcidiacono, P. J., PREDICTION OF ROTOR INSTABILITY AT HIGH FORWARD SPEEDS VOL. 1, STEADY FLIGHT DIFFERENTIAL EQUATIONS OF MOTION FOR A FLEXIBLE HELICOPTER BLADE WITH CHORDWISE MASS UNBALANCE, United Aircraft Corporation, Sikorsky Aircraft Division; USAAVLABS TR 68-18A, U. S. Army Aviation Materiel Laboratories, Fort Eustis, Virginia, February 1969, AD 685860.
21. Landgrebe, A. J., AN ANALYTICAL METHOD FOR PREDICTING ROTOR WAKE GEOMETRY, Journal of the American Helicopter Society, Vol. 14, No. 4, October 1969.
22. Beno, E., CH-53A MAIN ROTOR AND STABILIZER VIBRATORY AIRLOADS AND FORCES, United Aircraft Corporation, Sikorsky Aircraft Division Report SER 65593, NASC Report, Naval Air Systems Command, Washington, D. C., June 1970.
23. Gaieski, T. A., CH-53A HELICOPTER DEMONSTRATION DATA REPORT, United Aircraft Corporation, Sikorsky Aircraft Division Report SER 65254, December 1964.

24. Adams, D. O., EVALUATION OF A ROTATING CONTROL SYSTEM STALL-FLUTTER SPRING DAMPER ON A CH-54B HELICOPTER, United Aircraft Corporation, Sikorsky Aircraft Division; USAAMRDL TR 73-55, Eustis Directorate, U. S. Army Air Mobility Research and Development Laboratory, Fort Eustis, Virginia, August 1973.
25. Weckman, R. G., STRUCTURAL SUBSTANTIATION OF THE S-64F/CH-54B FOR FAA TYPE CERTIFICATION, United Aircraft Corporation, Sikorsky Aircraft Division Report SER 64500, April 1970.
26. Adamcyk, J., ANALYTIC INVESTIGATION OF COMPRESSIBILITY AND THREE-DIMENSIONALITY ON THE UNSTEADY BEHAVIOR OF AN AIRFOIL IN A FLUCTUATING FLOW FIELD, American Institute of Aeronautics, AIAA Paper No. 73-683, AIAA 6th Fluid and Plasma Dynamics Conference, July 1973.
27. Gabel, R., and Tarzanin, R. F., BLADE TORSIONAL TUNING TO MANAGE ROTOR STALL FLUTTER, AIAA Paper No. 72-958, American Institute of Aeronautics and Astronautics, September 1972.
28. Ham, N. D., SOME RECENT RESEARCH ON AIRFOIL DYNAMIC STALL WITH APPLICATION TO AIRFOIL DESIGN, MIT Aeroelastic and Structures Research Laboratory, September 1971.

TABLE I. TWO-DIMENSIONAL AIRFOIL TEST POINTS

$I_{REF} = 0.0005 \text{ slug ft}^2/\text{ft}, \bar{\alpha} = 8 \text{ deg}$								
Airfoil	Torsional Natural Frequency ω_n , cps	Oscillatory Frequency Ω , cps	Torsional Inertia Ratio	Pitch Axis Location \bar{x}_{PA}	Mean Incidence Angle α_m , deg			
NACA 0012 and SC 1095	50	8.0	I_R	0.25	7	11	14	18
	50	10.0	I_R	0.25	7*	11*	14*	18
	50	12.5	I_R	0.25	7	11	14	18
	70	8.0	I_R	0.25	7	11	14	18
	70	10.0	I_R	0.25	7*	11*	14*	18
	70	12.5	I_R	0.25	7	11	14	18
	50	8.0	$1.5 I_R$	0.25	7	11	14	18
	50	10.0	$1.5 I_R$	0.25	7*	11*	14*	18
	50	12.5	$1.5 I_R$	0.25	7	11	14	18
	70	8.0	$1.5 I_R$	0.25	7	11	14	18
	70	10.0	$1.5 I_R$	0.25	7*	11*	14*	18
	70	12.5	$1.5 I_R$	0.25	7	11	14	18
	50	8.0	I_R	0.22	7	11	14	18
	50	10.0	I_R	0.22	7*	11*	14*	18
	50	12.5	I_R	0.22	7	11	14	18
	70	8.0	I_R	0.22	7	11	14	18
	70	10.0	I_R	0.22	7*	11*	14*	18
	70	12.5	I_R	0.22	7	11	14	18
	50	8.0	$1.5 I_R$	0.22	7	11	14	18
	50	10.0	$1.5 I_R$	0.22	7*	11*	14*	18
	50	12.5	$1.5 I_R$	0.22	7	11	14	18
	70	8.0	$1.5 I_R$	0.22	7	11	14	18
	70	10.0	$1.5 I_R$	0.22	7*	11*	14*	18
	70	12.5	$1.5 I_R$	0.22	7	11	14	18

*Analytic Cases

TABLE II. MODEL AIRFOIL ELASTIC RESPONSE AMPLITUDES

NACA 0012 Airfoil $\Omega = 10$ cps, $\bar{x}_{PA} = 0.25$

Torsional Inertia Ratio I/I_{REF}	Torsional Natural Freq. ω_θ , cpm	Mean Incidence Angle α_M , deg	$\Delta\theta_1$ deg	$\theta_{\frac{1}{2}PTP}$ deg
1.0	50.7	7	*	0.75
1.0	50.7	11	1.20	1.20
1.0	50.7	14	1.95	2.01
1.0	50.7	18	1.95	2.43
1.0	70.0	7	*	0.40
1.0	70.0	11	0.95	1.33
1.0	70.0	14	1.00	1.73
1.0	70.0	18	1.25	1.65
1.5	54.8	7	*	0.62
1.5	54.8	11	0.64	1.06
1.5	54.8	14	1.47	1.65
1.5	54.8	18	1.24	2.30
1.5	69.0	7	*	0.61
1.5	69.0	11	0.69	1.04
1.5	69.0	14	1.20	1.44
1.5	69.0	18	1.07	1.52

NACA 0012 Airfoil $\Omega = 10$ cps, $\bar{x}_{PA} = 0.22$

1.0	49.5	7	*	0.82
1.0	49.5	11	0.61	0.80
1.0	49.5	14	1.47	1.90
1.0	49.5	18	1.70	2.00
1.0	69.5	7	*	0.45
1.0	69.5	11	*	0.43
1.0	69.5	14	1.07	1.15
1.0	69.5	18	1.13	1.35
1.5	50.0	7	*	0.50
1.5	50.0	11	0.90	0.99
1.5	50.0	14	1.56	1.59
1.5	50.0	18	1.79	1.85
1.5	69.0	7	*	0.45
1.5	69.0	11	*	0.49
1.5	69.0	14	0.65	1.20
1.5	69.0	18	1.79	1.85

* Stall Flutter not present

TABLE II - Concluded

SC 1095 Airfoil $\Omega = 10$ cps, $\bar{x}_{PA} = 0.25$

Torsional Inertia Ratio I/I_{REF}	Torsional Natural Freq. ω_θ , cpm	Mean Incidence Angle α_M , deg	$\Delta\theta_1$ deg	$\theta_{1/2PTP}$ deg
1.0	49.5	7	*	0.40
1.0	49.5	11	*	1.17
1.0	49.5	14	2.03	2.40
1.0	49.5	18	2.48	2.78
1.0	69.0	7	*	0.46
1.0	69.0	11	0.57	0.80
1.0	69.0	14	1.80	2.15
1.0	69.0	18	1.49	1.77
1.5	50.0	7	*	0.73
1.5	50.0	11	0.85	0.95
1.5	50.0	14	1.75	2.03
1.5	50.0	18	2.17	2.17
1.5	70.2	7	*	0.37
1.5	70.2	11	0.28	0.65
1.5	70.2	14	0.67	1.49
1.5	70.2	18	1.23	1.50

SC 1095 Airfoil $\Omega = 10$ cps, $\bar{x}_{PA} = 0.22$

1.0	50.0	7	*	0.15
1.0	50.0	11	*	0.33
1.0	50.0	14	1.65	1.80
1.0	50.0	18	2.25	2.40
1.0	69.0	7	*	0.95
1.0	69.0	11	*	0.38
1.0	69.0	14	1.08	1.33
1.0	69.0	18	1.55	1.55
1.5	50.0	7	*	0.26
1.5	50.0	11	0.25	0.67
1.5	50.0	14	1.35	2.70
1.5	50.0	18	3.60	4.63
1.5	70.0	7	*	0.33
1.5	70.0	11	0.39	0.68
1.5	70.0	14	1.07	1.15
1.5	70.0	18	1.43	2.59

* Stall Flutter not present

TABLE III. MODEL AIRFOIL ELASTIC RESPONSE AMPLITUDES
CALCULATED USING α, A, B UNSTEADY AERODYNAMICS

NACA 0012 Airfoil $\Omega = 10$ cps, $\bar{x}_{PA} = 0.25$

Torsional Inertia Ratio I/I_{REF}	Torsional Natural Freq. ω_θ , cpm	Mean Incidence Angle α_M , deg	$\Delta\theta_1$, deg	$\theta_{\frac{1}{2}PTP}$, deg
1.0	50.0	7	0.51	1.17
1.0	50.0	11	0.94	1.40
1.0	50.0	14	1.40	1.97
1.0	70.0	7	0.30	0.37
1.0	70.0	11	0.60	0.98
1.0	70.0	14	0.87	1.10
1.5	50.0	7	0.47	0.77
1.5	50.0	11	0.98	1.28
1.5	50.0	14	0.89	0.93
1.5	70.0	7	0.20	0.23
1.5	70.0	11	0.50	0.70
1.5	70.0	14	0.55	0.63

NACA 0012 Airfoil $\Omega = 10$ cps, $\bar{x}_{PA} = 0.22$

1.0	50.0	7	0.32	0.87
1.0	50.0	11	0.67	1.20
1.0	50.0	14	1.14	1.73
1.0	70.0	7	0.14	0.30
1.0	70.0	11	0.44	0.85
1.0	70.0	14	0.58	1.00
1.5	50.0	7	0.24	0.65
1.5	50.0	11	0.50	0.93
1.5	50.0	14	0.74	1.15
1.5	10.0	7	0.10	0.22
1.5	70.0	11	0.34	0.59
1.5	70.0	14	0.35	0.60

TABLE III - Concluded

SC 1095 Airfoil $\Omega = 10$ cps, $\bar{x}_{PA} = 0.25$

Torsional Inertia Ratio I/I_{REF}	Torsional Natural Freq. ω_θ , cpm	Mean Incidence Angle α_M , deg	ΔC_{L1} , deg	$\theta_{\frac{1}{2}PTP}$, deg
1.0	50.0	7	*	0.50
1.0	50.0	11	0.50	1.22
1.0	50.0	14	0.92	1.20
1.0	70.0	7	*	0.30
1.0	70.0	11	0.32	0.33
1.0	70.0	14	0.61	0.98
1.5	50.0	7	*	0.15
1.5	50.0	11	0.30	0.78
1.5	50.0	14	0.55	0.80
1.5	70.0	7	*	0.06
1.5	70.0	11	0.12	0.25
1.5	70.0	14	0.35	0.51

SC 1095 Airfoil $\Omega = 10$ cps, $\bar{x}_{PA} = 0.22$

1.0	50.0	7	*	0.45
1.0	50.0	11	0.32	0.80
1.0	50.0	14	0.64	0.78
1.0	70.0	7	*	0.20
1.0	70.0	11	0.18	0.25
1.0	70.0	14	0.47	0.60
1.5	50.0	7	*	0.30
1.5	50.0	11	0.20	0.66
1.5	50.0	14	0.59	0.98
1.5	70.0	7	*	0.11
1.5	70.0	11	0.20	0.39
1.5	70.0	14	0.45	0.85

* Stall Flutter not present

TABLE IV. MODEL AIRFOIL ELASTIC RESPONSE AMPLITUDES
CALCULATED USING TIME DELAY AERODYNAMICS

NACA 0012 Airfoil $\Omega = 10$ cps, $\bar{x}_{PA} = 0.25$				
Torsional Inertia Ratio I/I_{REF}	Torsional Natural Freq. ω_θ , cpm	Mean Incidence Angle α_M , deg	$\Delta\theta_1$, deg	$\theta_{1/2PTP}$, deg
1.0	50.0	7	0.44	0.82
1.0	50.0	11	1.28	2.31
1.0	50.0	14	2.05	3.04
1.0	70.0	7	0.22	0.42
1.0	70.0	11	0.86	1.40
1.0	70.0	14	1.02	1.33
1.5	50.0	7	0.39	0.77
1.5	50.0	11	1.0	1.36
1.5	50.0	14	1.68	1.40
1.5	70.0	7	0.18	0.36
1.5	70.0	11	0.65	0.80
1.5	70.0	14	0.70	0.92
NACA 0012 Airfoil, $\Omega = 10$ cps, $\bar{x}_{PA} = 0.22$				
1.0	50.0	7	0.32	0.57
1.0	50.0	11	0.85	1.57
1.0	50.0	14	1.66	2.58
1.0	70.0	7	0.15	0.15
1.0	70.0	11	0.72	1.21
1.0	70.0	14	0.95	1.23
1.5	50.0	7	0.28	0.59
1.5	50.0	11	1.14	1.20
1.5	50.0	14	1.60	2.13
1.5	70.0	7	0.15	0.15
1.5	70.0	11	0.57	0.74
1.5	70.0	14	0.65	0.87

TABLE IV - Concluded

SC 1095 Airfoil $\Omega = 10$ cps, $\bar{x}_{FA} = 0.25$

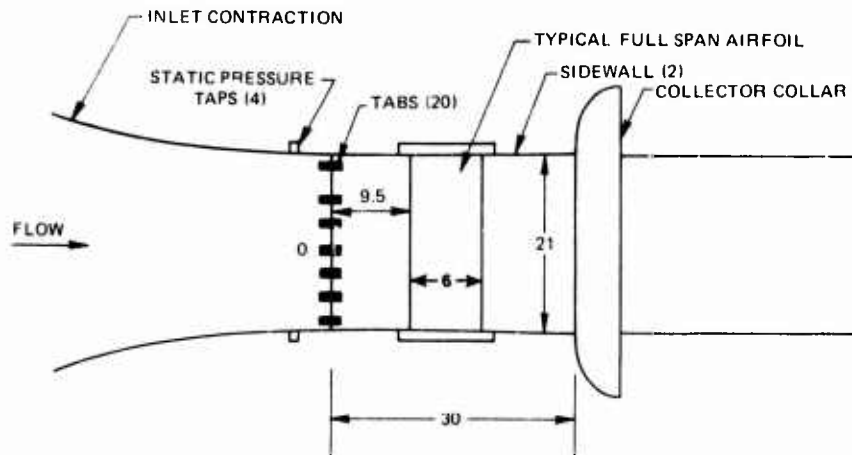
Torsional Inertia Ratio I/I_{REF}	Torsional Natural Freq. ω_θ , cpm	Mean Incidence Angle α_M , deg	$\Delta\theta_1$, deg	$\theta_{1/2PTP}$, deg
1.0	50.0	7	0.43	0.43
1.0	50.0	11	0.43	0.43
1.0	50.0	14	1.50	3.04
1.0	70.0	7	0.19	0.19
1.0	70.0	11	0.19	0.19
1.0	70.0	14	1.07	1.84
1.5	50.0	7	0.37	0.37
1.5	50.0	11	0.37	0.37
1.5	50.0	14	1.38	2.42
1.5	70.0	7	0.17	0.17
1.5	70.0	11	0.17	0.17
1.5	70.0	14	0.73	1.19

SC 1095 Airfoil $\Omega = 10$ cps, $\bar{x}_{FA} = 0.22$				
1.0	50.0	7	0.3	0.30
1.0	50.0	11	0.3	0.30
1.0	50.0	14	0.90	1.70
1.0	70.0	7	0.12	0.12
1.0	70.0	11	0.12	0.12
1.0	70.0	14	0.85	1.95
1.5	50.0	7	0.16	0.16
1.5	50.0	11	0.16	0.16
1.5	50.0	14	1.0	1.69
1.5	70.0	7	0.04	0.04
1.5	70.0	11	0.04	0.04
1.5	70.0	14	0.67	0.91

Table V. CH-53A and CH-54B Blade Natural Frequencies		
Mode	CH-53A $\Omega R = 710 \text{ ft/sec}$	CH-54B $\Omega R = 672 \text{ ft/sec}$
First Flatwise	2.72P	2.64P
Second Flatwise	4.92P	4.98P
Third Flatwise	8.00P	8.04P
First Edgewise	3.91P	3.93P
Second Edgewise	10.32P	10.89P
First Torsion	5.98P	6.48P

ALL DIMENSIONS IN INCHES

TOP VIEW WITH NACA 0012 FULL SPAN AIRFOIL INSTALLED



SIDE VIEW

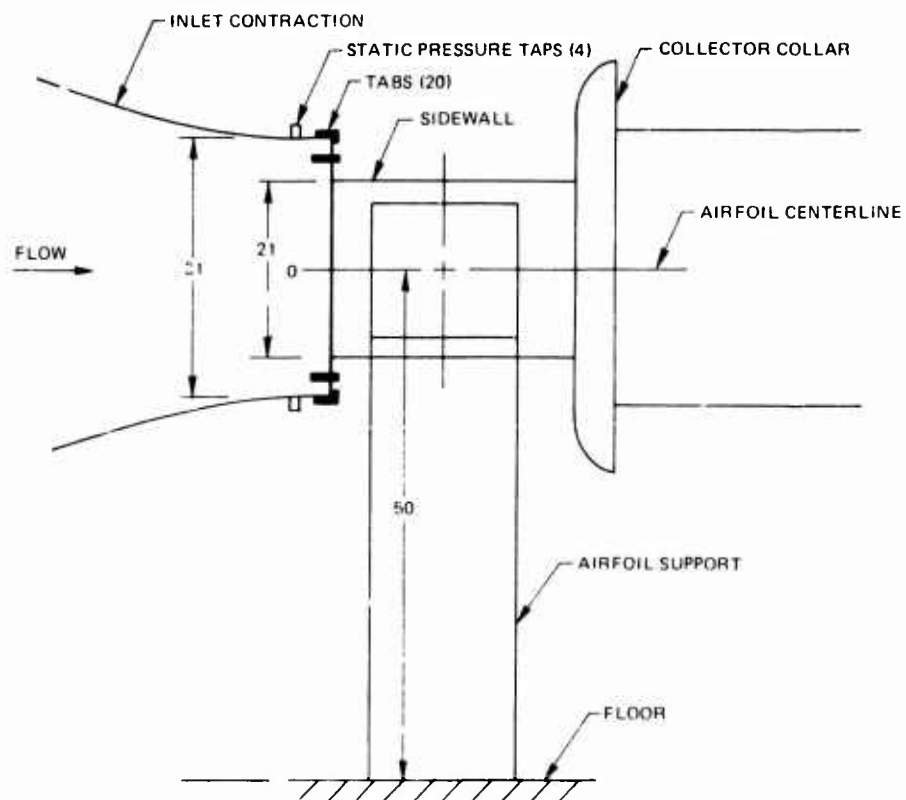


Figure 1. Acoustics Research Wind Tunnel Test Section.

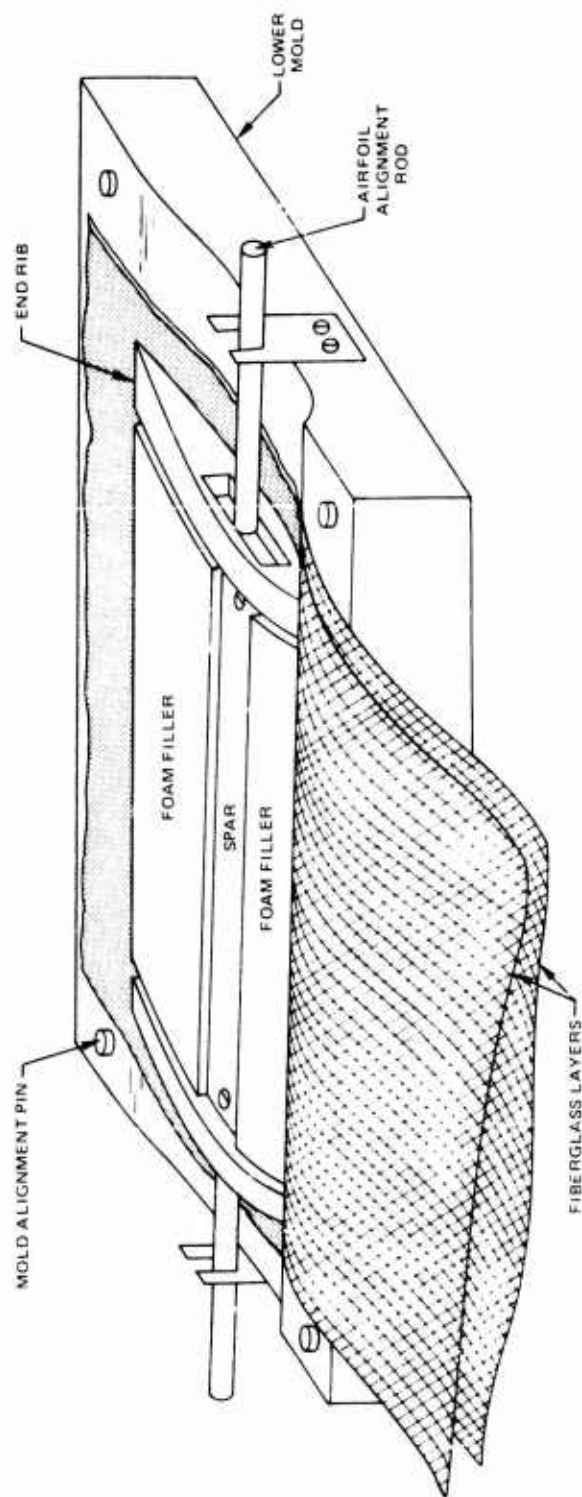


Figure 2. Two-Dimensional Model Airfoil.

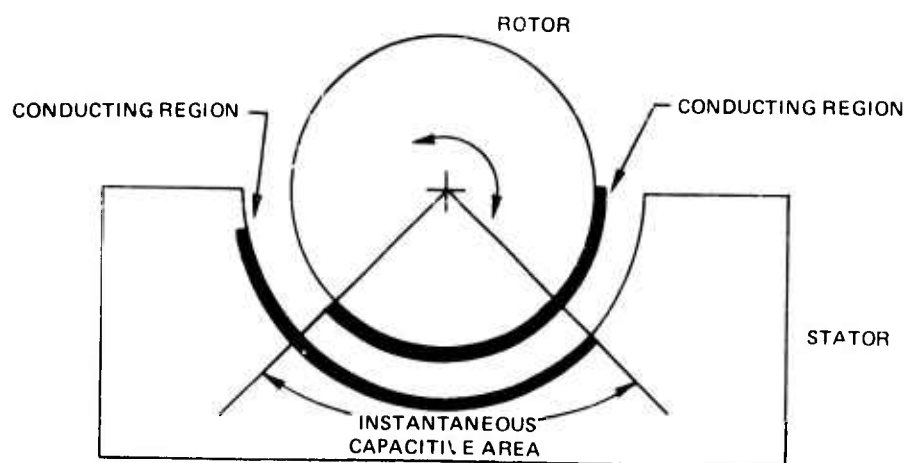
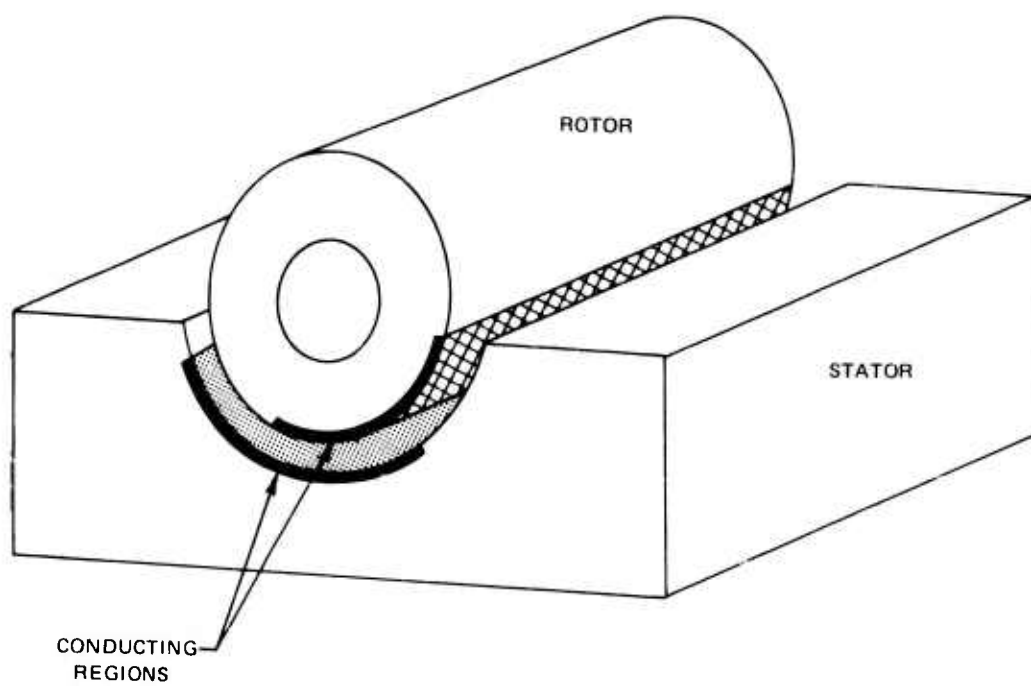
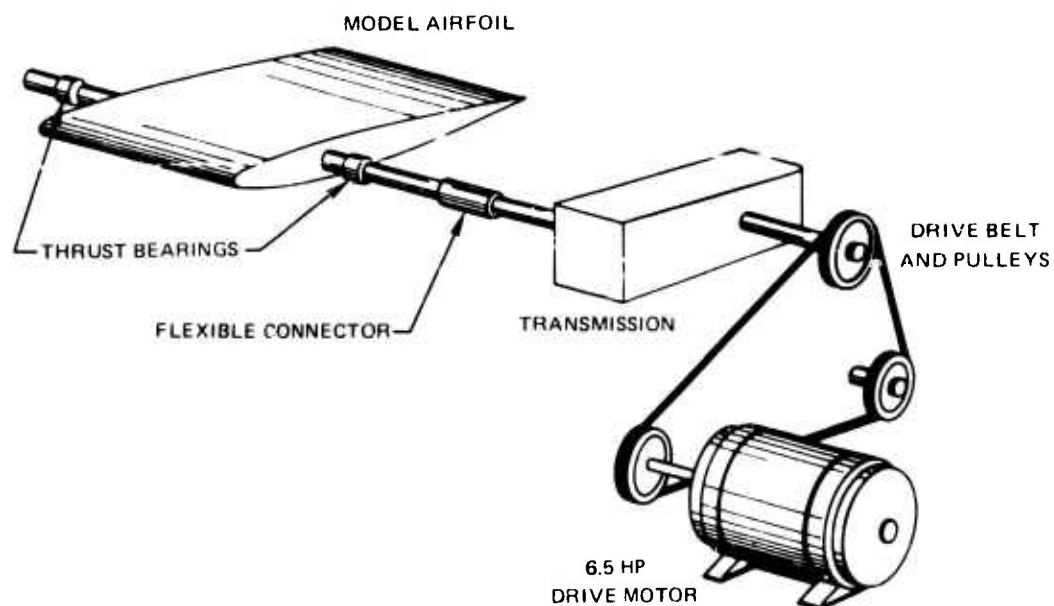


Figure 3. Capacitive Angular Transducer.



DETAIL OF INTERIOR OF TRANSMISSION

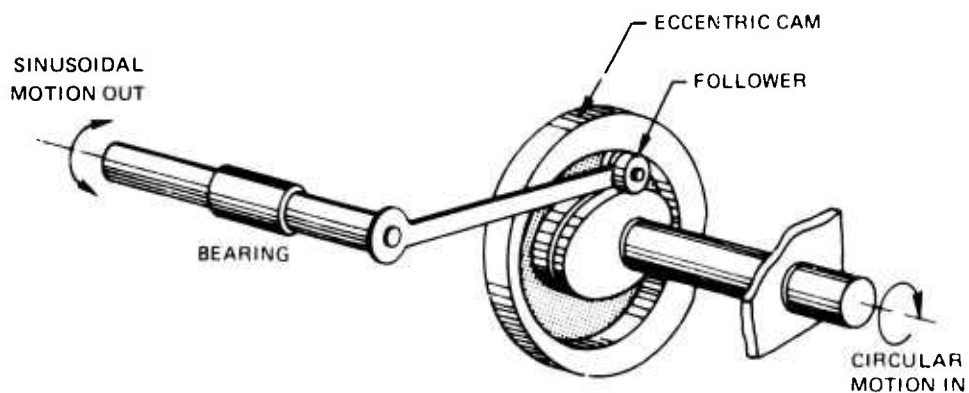


Figure 4. Model Airfoil Drive System

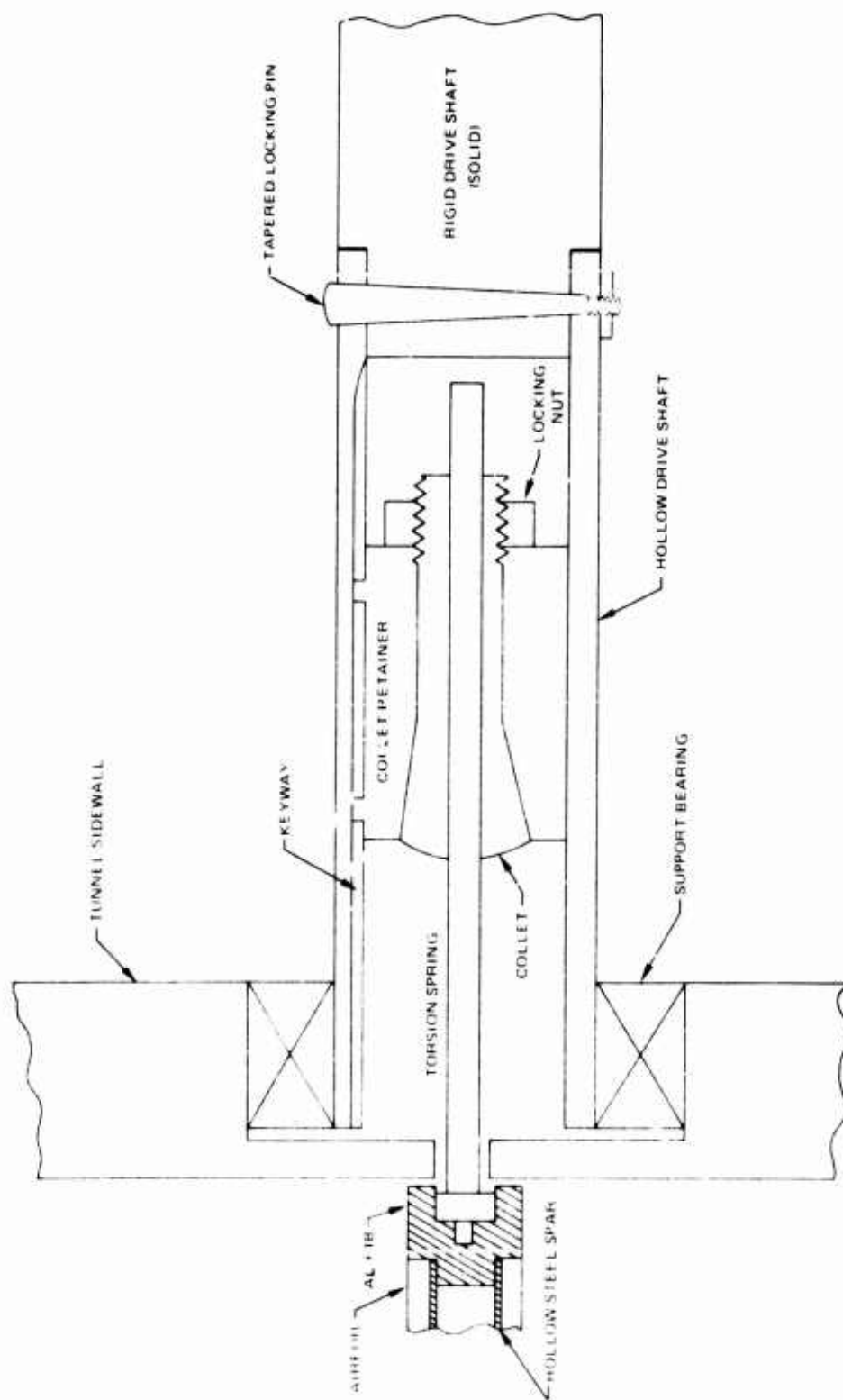


Figure 5. Flexible Connector Detail.

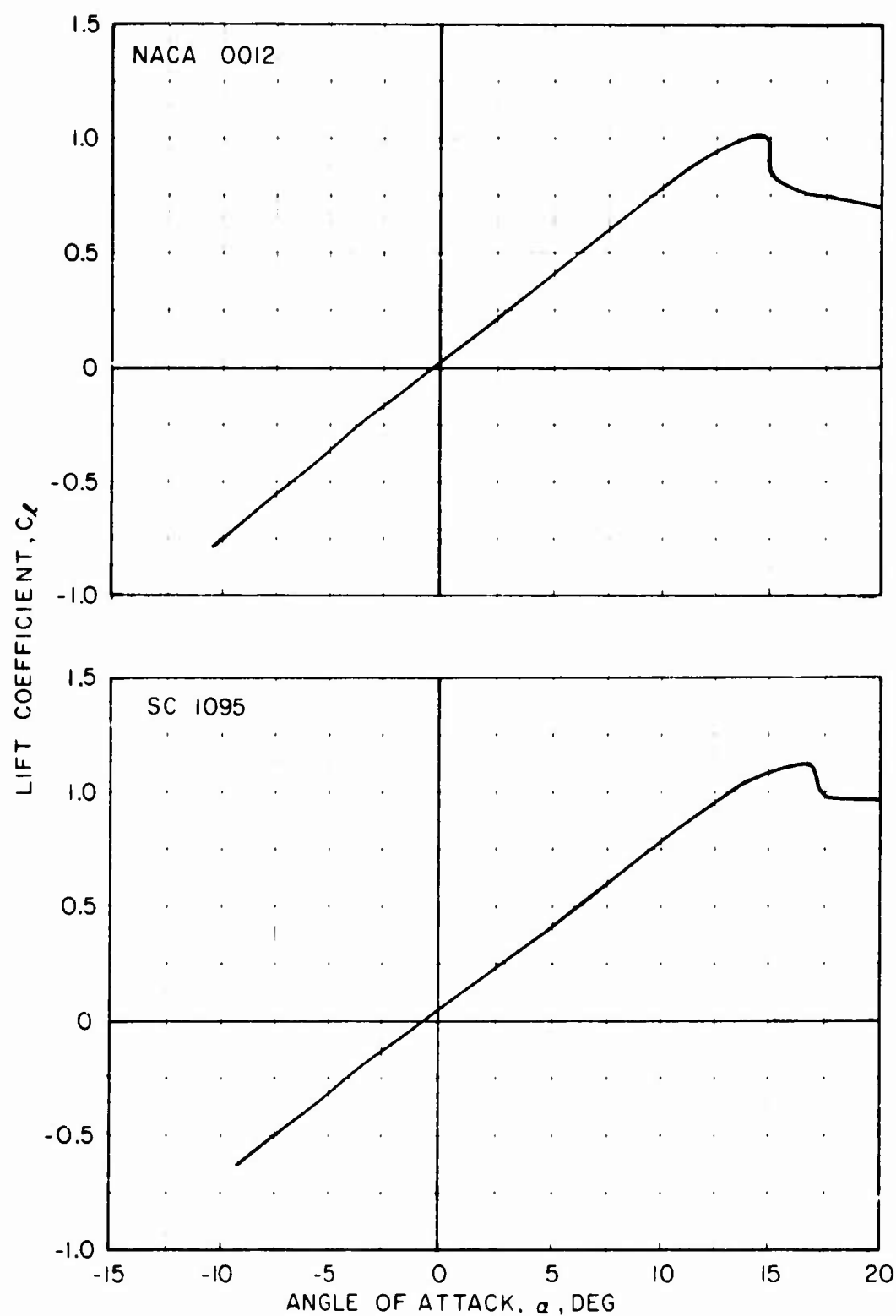


Figure 6. Measured Steady-State Lift Characteristics of the NACA 0012 and SC 1095 Airfoil Models.

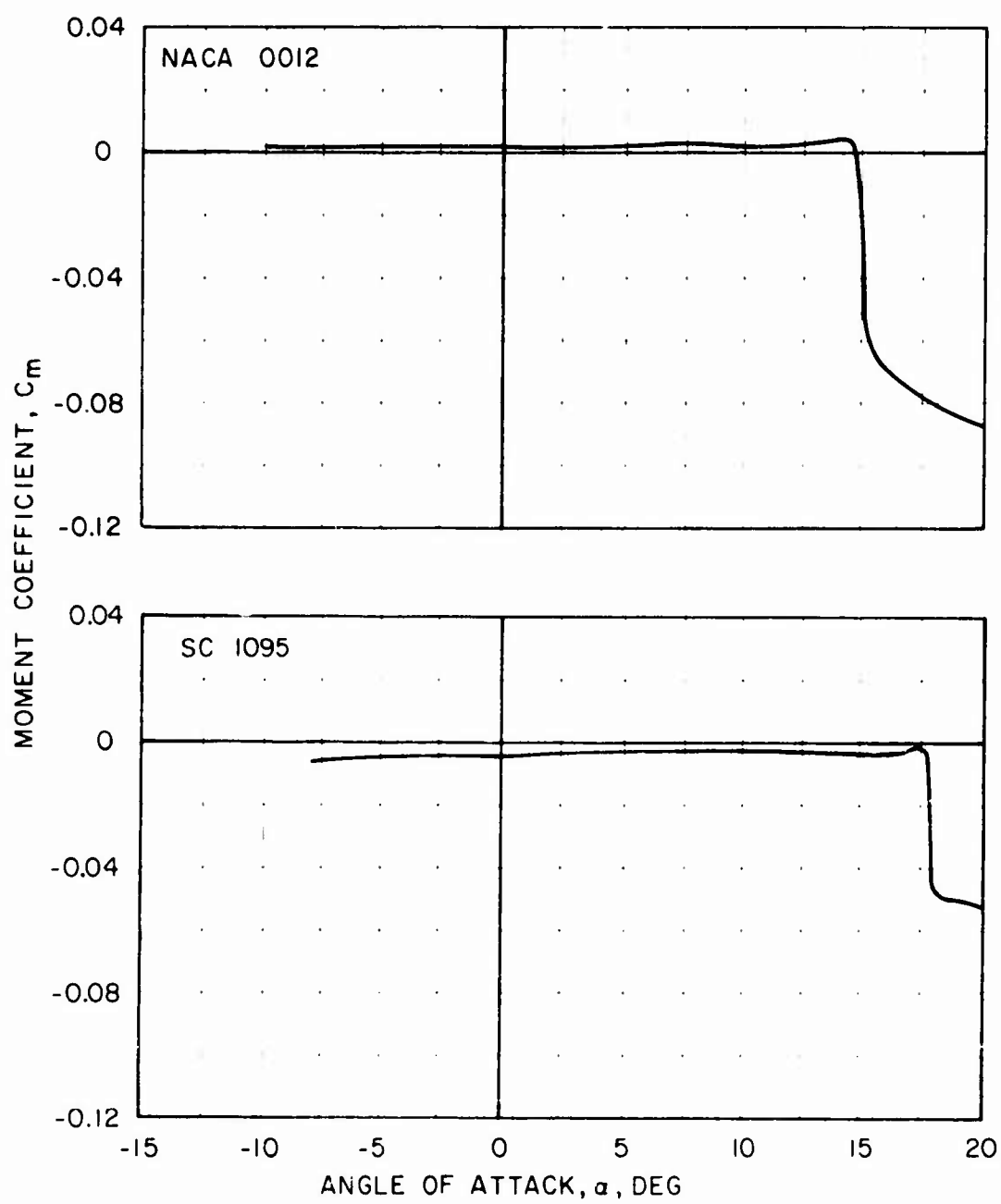


Figure 7. Measured Steady-State Pitching Moment Characteristics of the NACA 0012 and SC 1095 Airfoil Models.

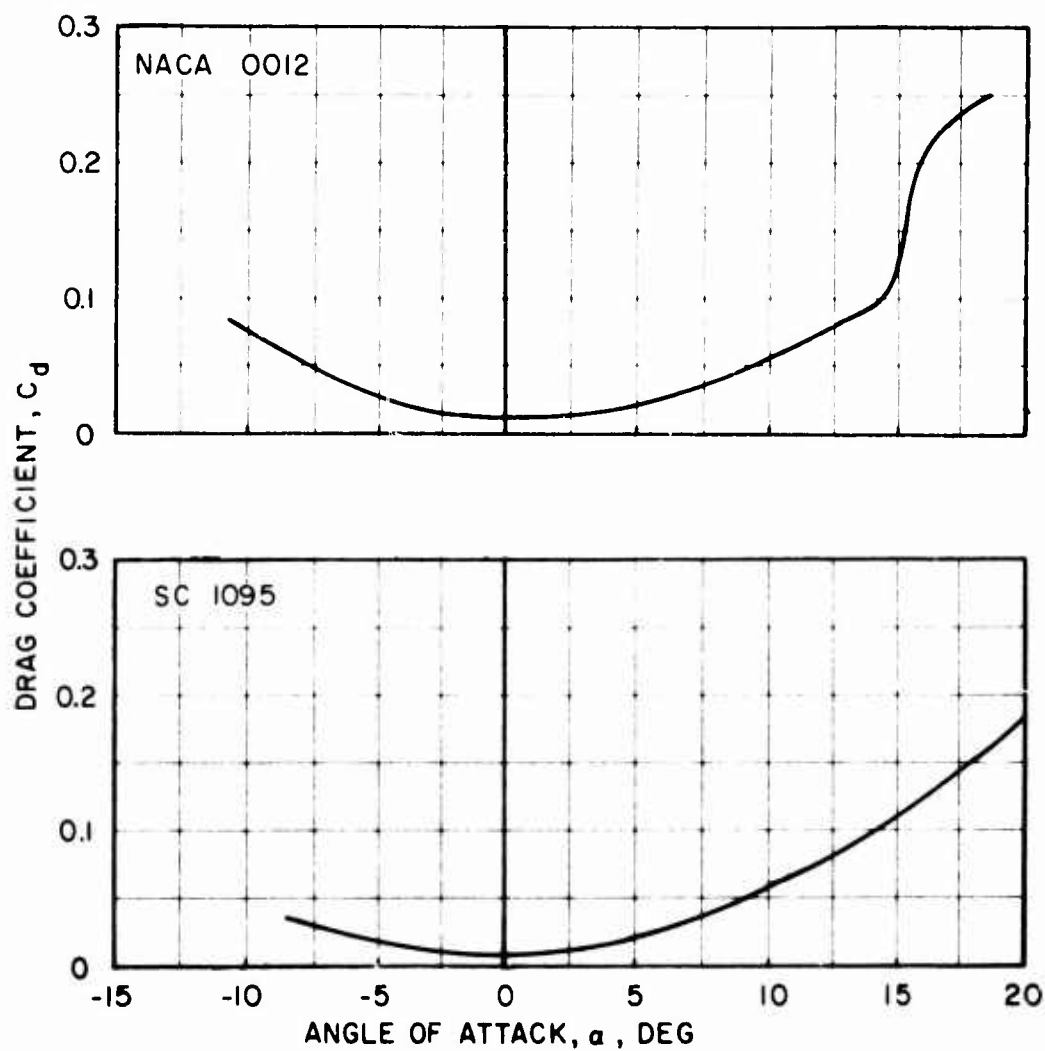


Figure 8. Measured Steady-State Drag Characteristics of the NACA 0012 and SC 1095 Airfoil Models.

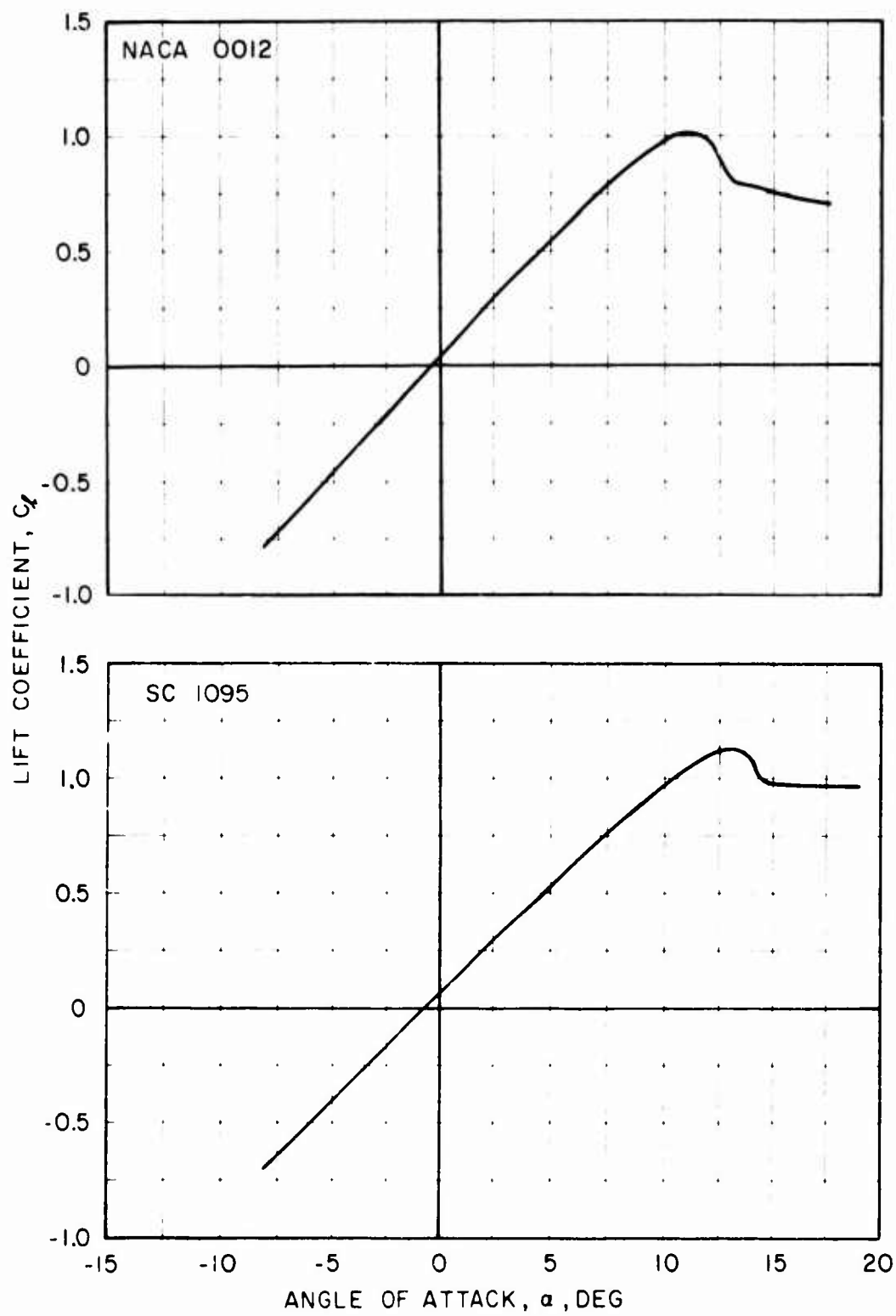


Figure 9. Airfoil Steady-State Lift Characteristics Corrected for Open Jet Tunnel Effects.

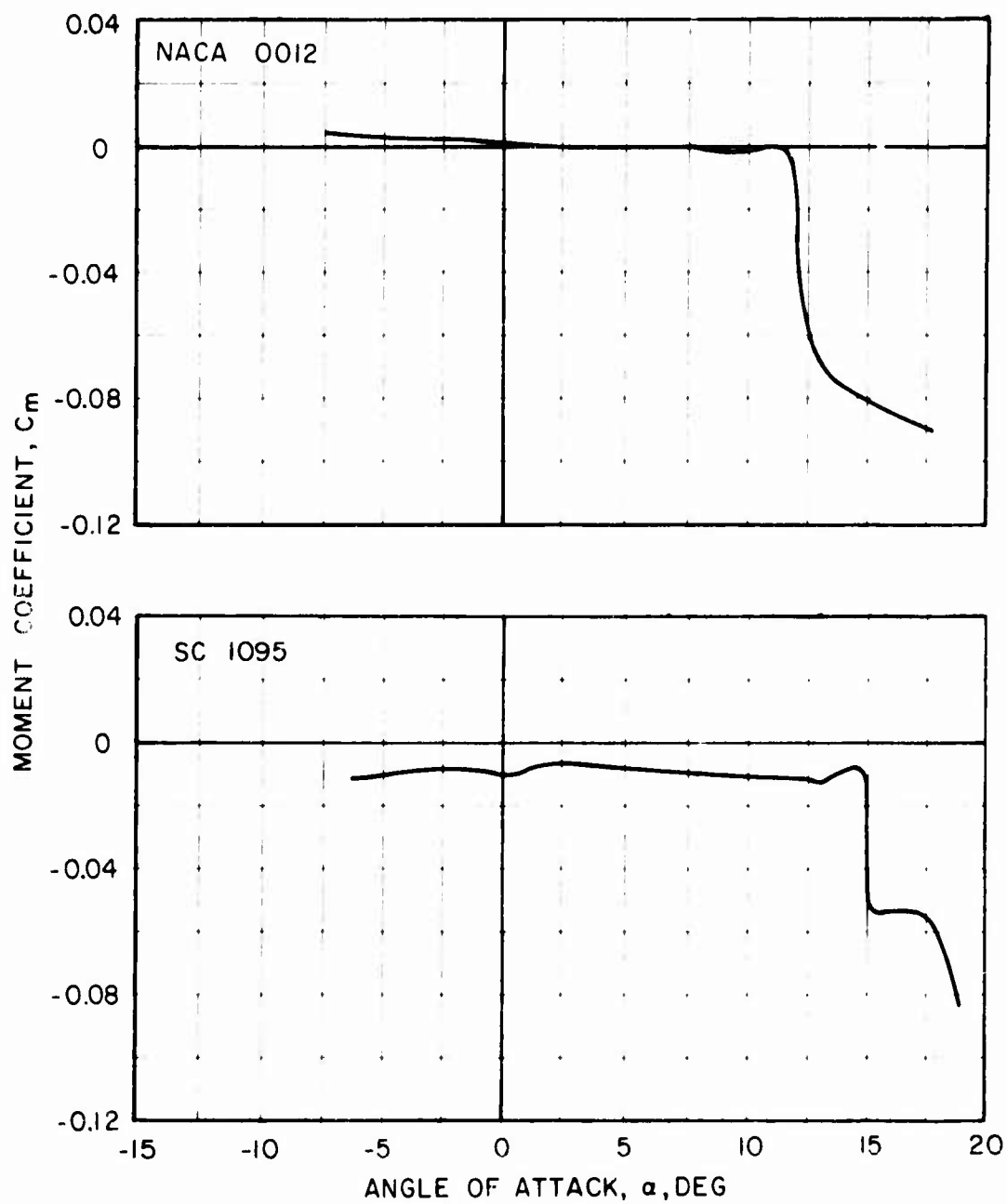


Figure 10. Airfoil Steady-State Pitching Moment Characteristics Corrected for Open Jet Tunnel Effects.

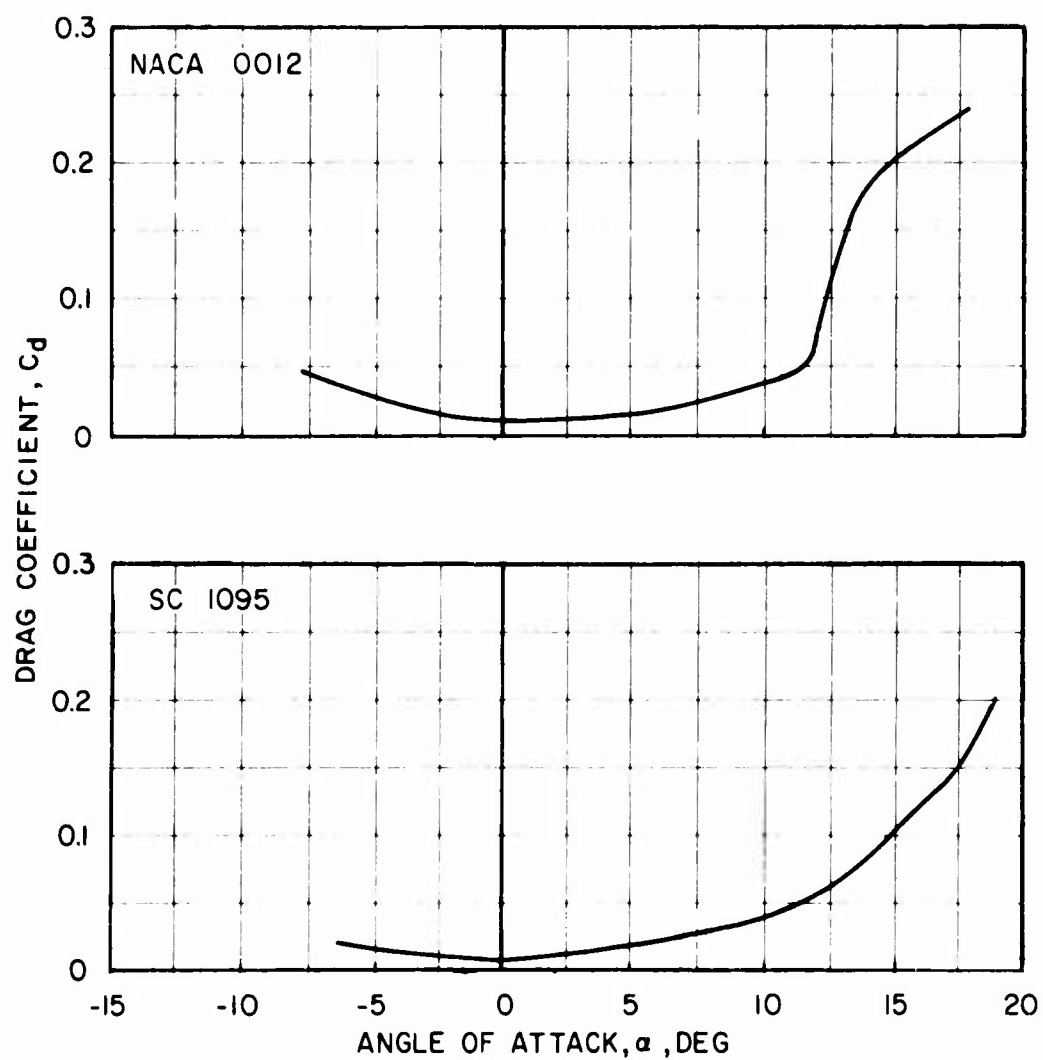


Figure 11. Airfoil Steady-State Drag Characteristics Corrected for Open Jet Tunnel Effects.

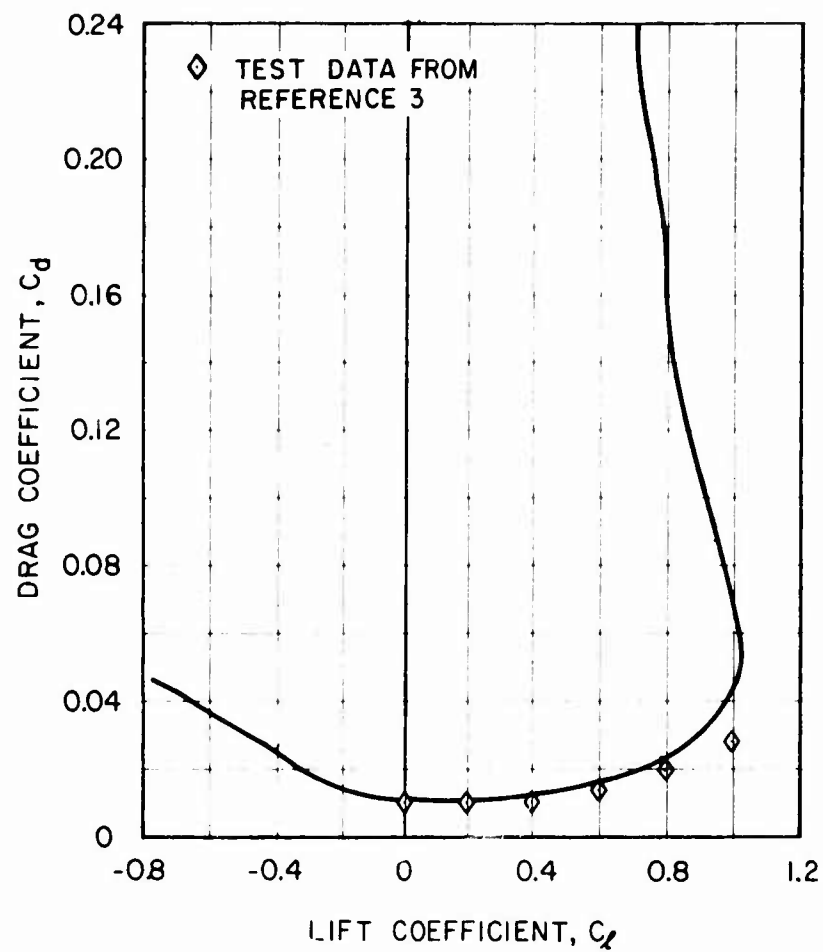


Figure 12. NACA 0012 Model Airfoil Drag Polar.

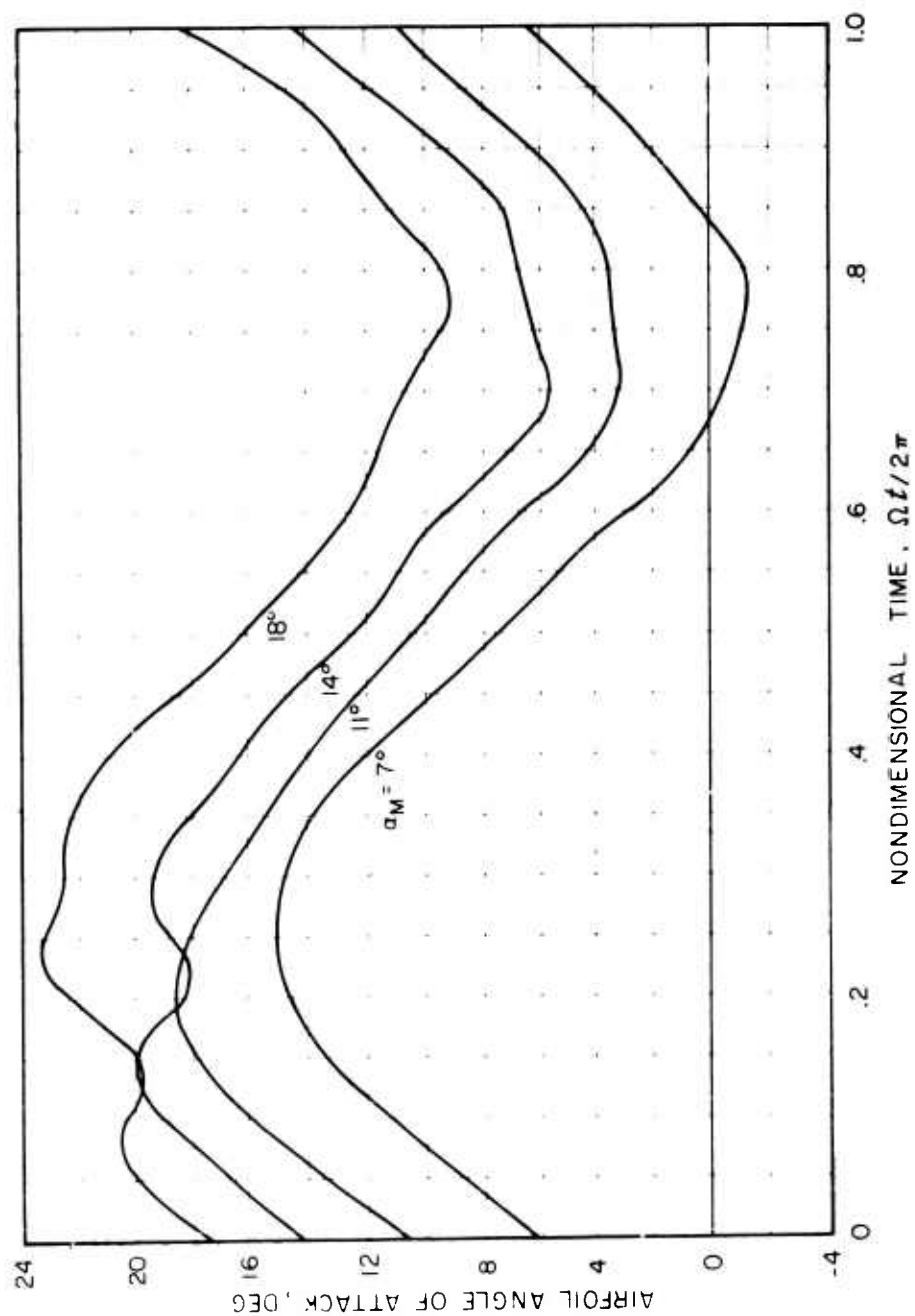


Figure 12. NACA 0012 Model Airfoil Angle of Attack Time Histories.

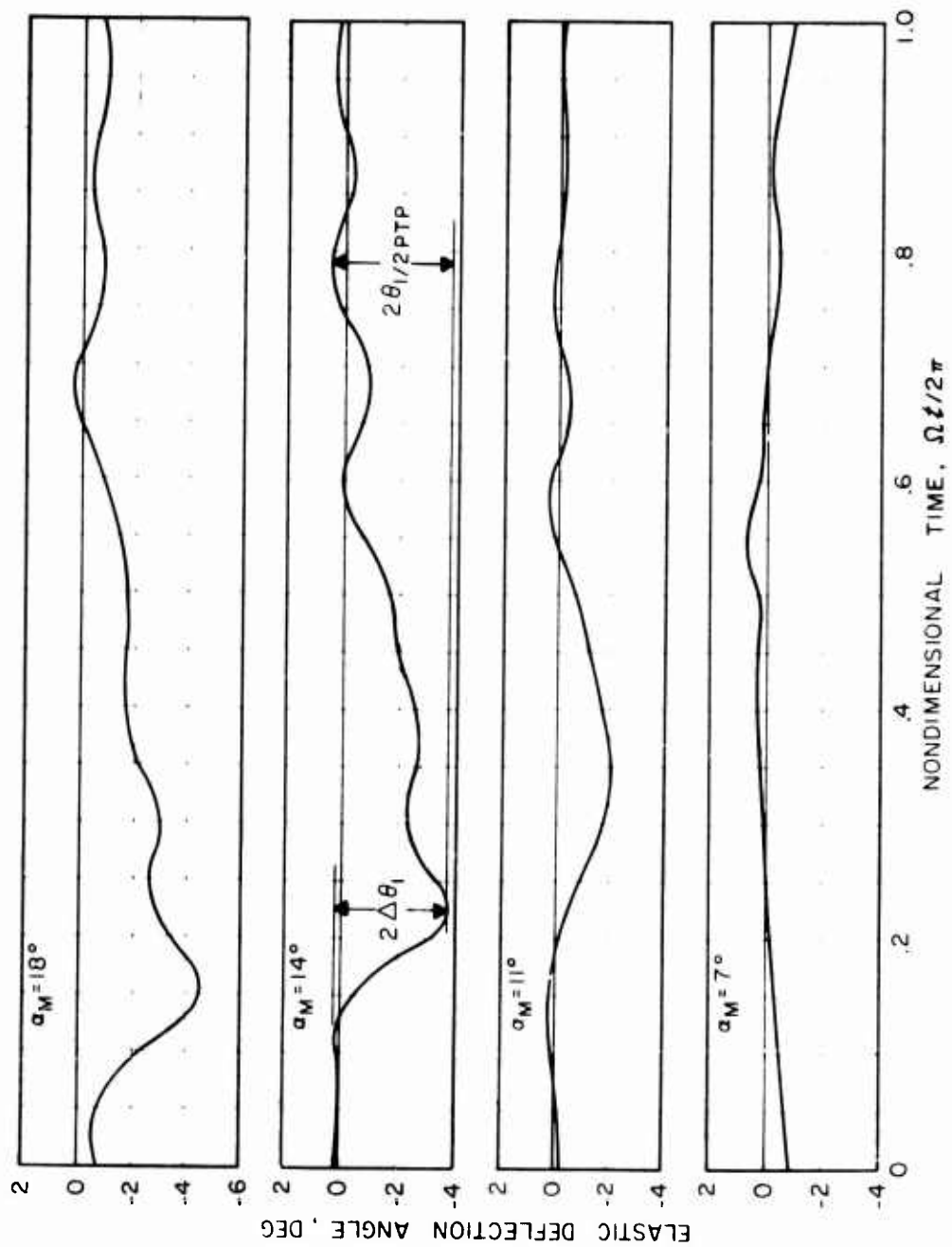


Figure 14. NACA 0012 Model Airfoil Elastic Response Time Histories.

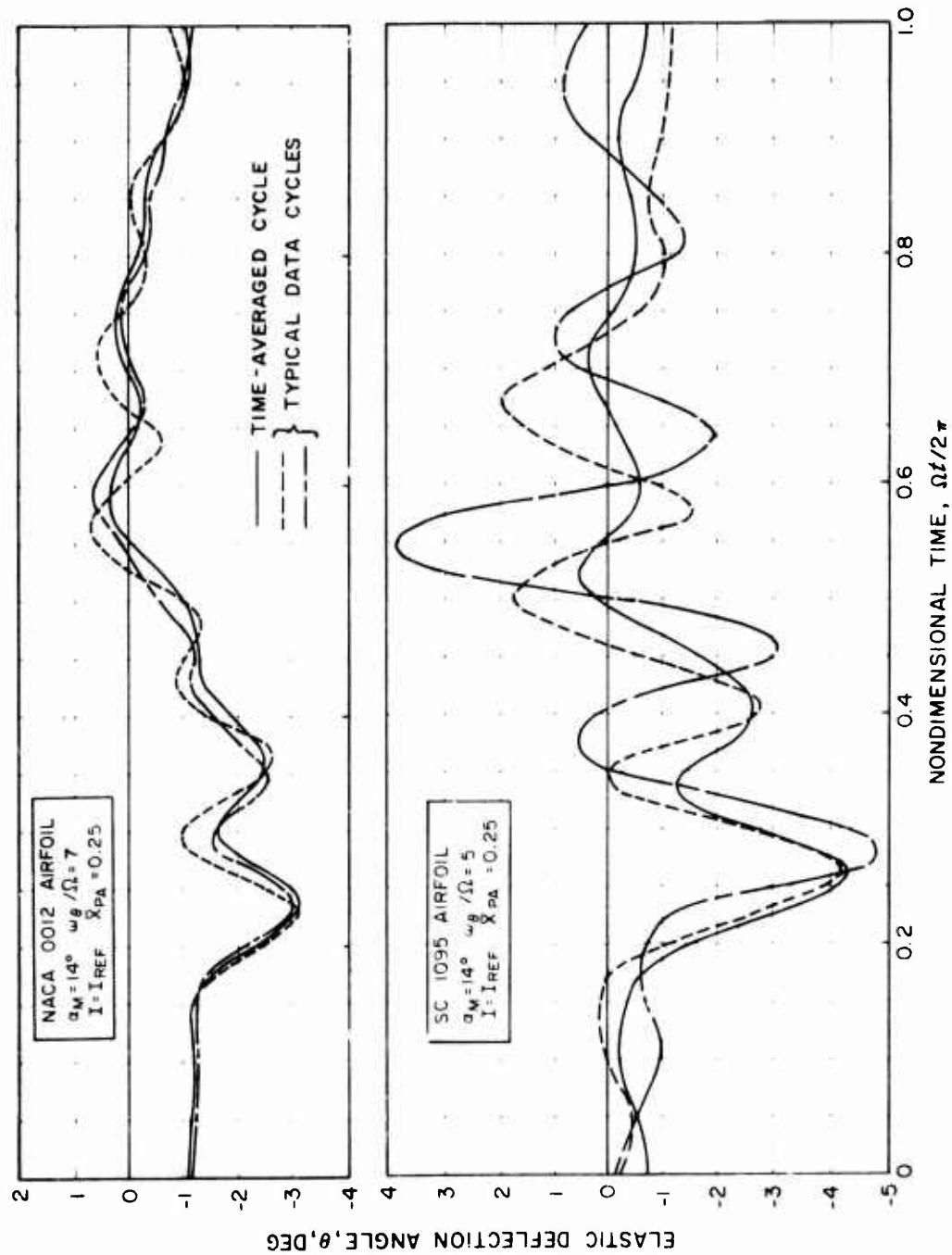


Figure 15. Comparison of Measured and Time Averaged Elastic Response Time Histories for Two Test Points.

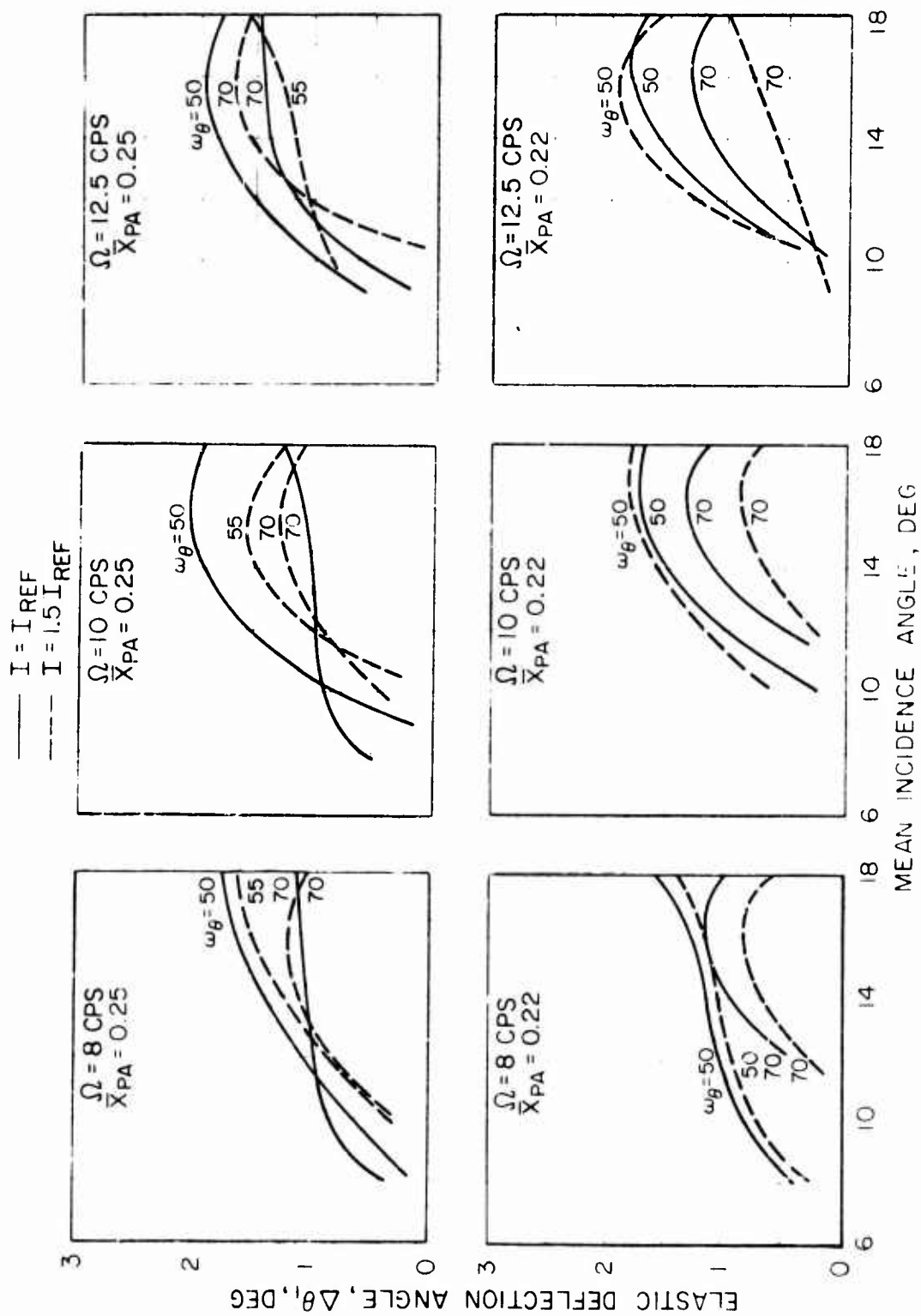


Figure 16. Elastic Deflection Amplitudes for the NACA 0012 Airfoil.

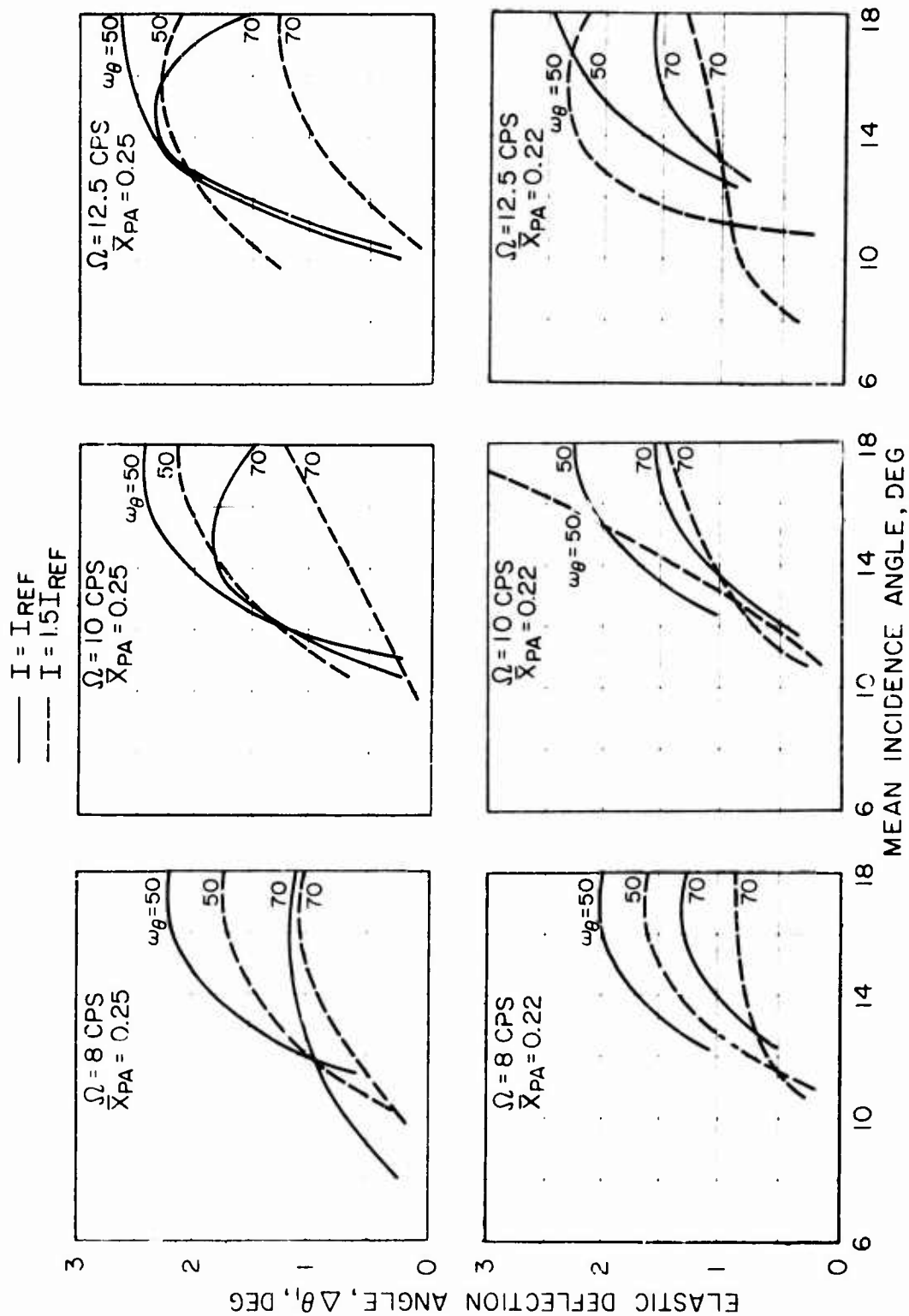


Figure 17. Elastic Deflection Amplitudes for the SC 1095 Airfoil.

- ① $\alpha < \alpha_1$
 - $c_1 = c_{1POT}$
 - C.P. = 0.25
 - $c_m = c_{mPOT} = -\frac{\pi}{4} \frac{d\theta}{dt}$
- ② $\alpha = \alpha_1$
 - τ_2 counting begins $\tau_2 = \sum_{n=0} \Delta t_n \frac{U_{on}}{c}$ at $\alpha = \alpha_1$
- ③ $\tau_2 =$ moment stall time constant $\tau_s = 2.0$
 - C.P. begins to move rearward with time toward C.P._{SEP}(α)
 - c_{mPOT} is eliminated
- ④ $\tau_s < \tau_2 < \tau^*$
 - c_1 remains equal to c_{1POT}
 - C.P. continues to shift aft with time, τ_2

$$C.P. = 0.25 + \frac{(\tau_2 - \tau_s)}{(\tau^* - \tau_s)} [C.P._{SEP}(\alpha) - 0.25]$$
 - $c_m = c_1(C.P. - 0.25)$
- ⑤ $\tau_2 =$ lift stall time constant $\tau^* = 6.0$
 - c_1 begins to decay toward $c_{1SEP}(\alpha)$

$$c_1 = c_{1POT} - [c_{1POT} - c_{1SEP}(\alpha)] [1 - e^{-(\tau_2 - \tau^*)/4}]$$
 - C.P. moves to C.P._{SEP}(α) independent of subsequent variation in α
- ⑥ $\dot{\alpha} = 0$
 - the exponential rate at which c_1 approaches $c_{1SEP}(\alpha)$ is increased by a factor of 3
 - if $\tau_s < \tau_2 < \tau^*$ the rate at which C.P. approaches C.P._{SEP}(α) is increased by doubling the time increment
$$\tau_{2n+1} = \tau_{2n} + 2\Delta t_n \left(\frac{U_{on}}{c} \right)$$
- ⑦ $\alpha < \alpha_1$
 - τ_3 counting begins $\tau_3 = \sum_{n=0} \Delta t_n \left(\frac{U_{oc}}{c} \right)$ at $\alpha = \alpha_1, \dot{\alpha} < 0$
 - c_1 moves back toward c_{1POT}
 - C.P. returns to 0.25
 - potential flow moment is reintroduced $c_m = c_{mPOT} e^{-\tau_3/4}$
- ⑧ $\dot{\alpha} = 0$
 - $\tau_2 = \tau_3 = 0$
 - $c_1 = c_{1POT}$
 - C.P. = 0.25
 - $c_m = c_{mPOT}$

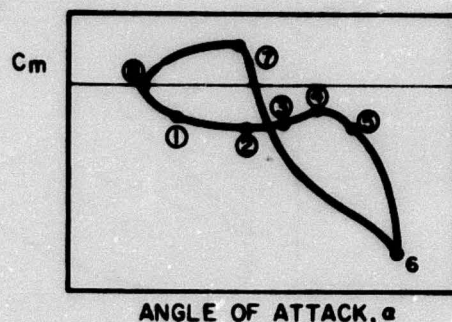
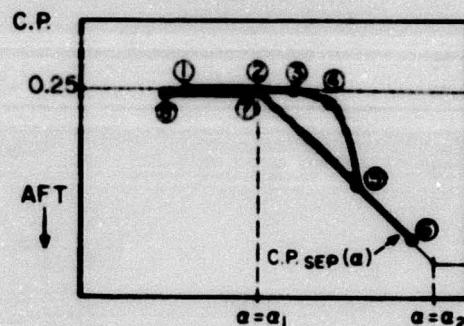
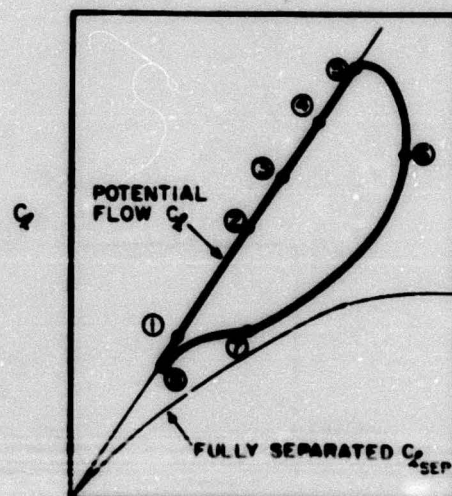


Figure 18. Time Delay Unsteady Aerodynamic Model.

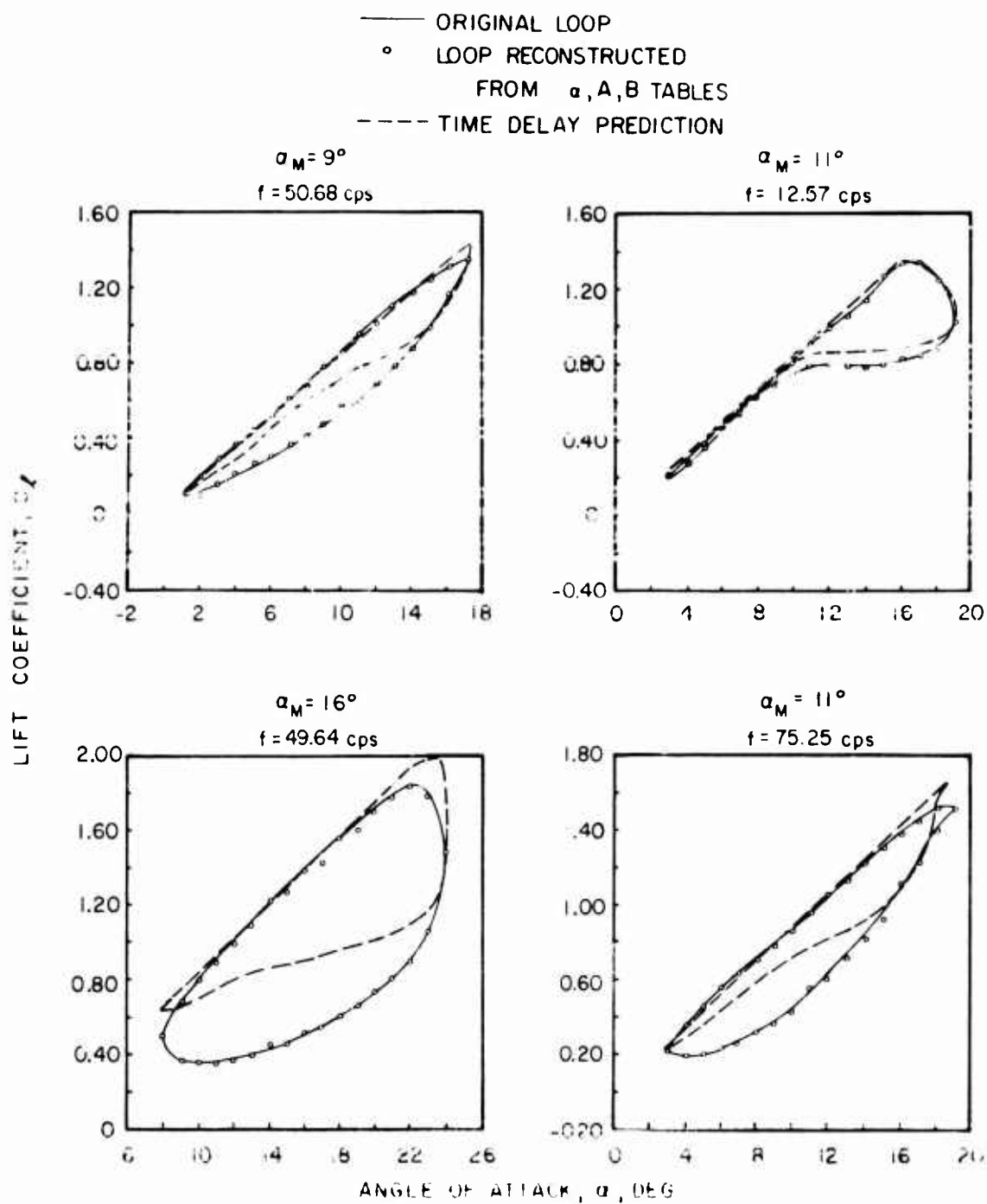
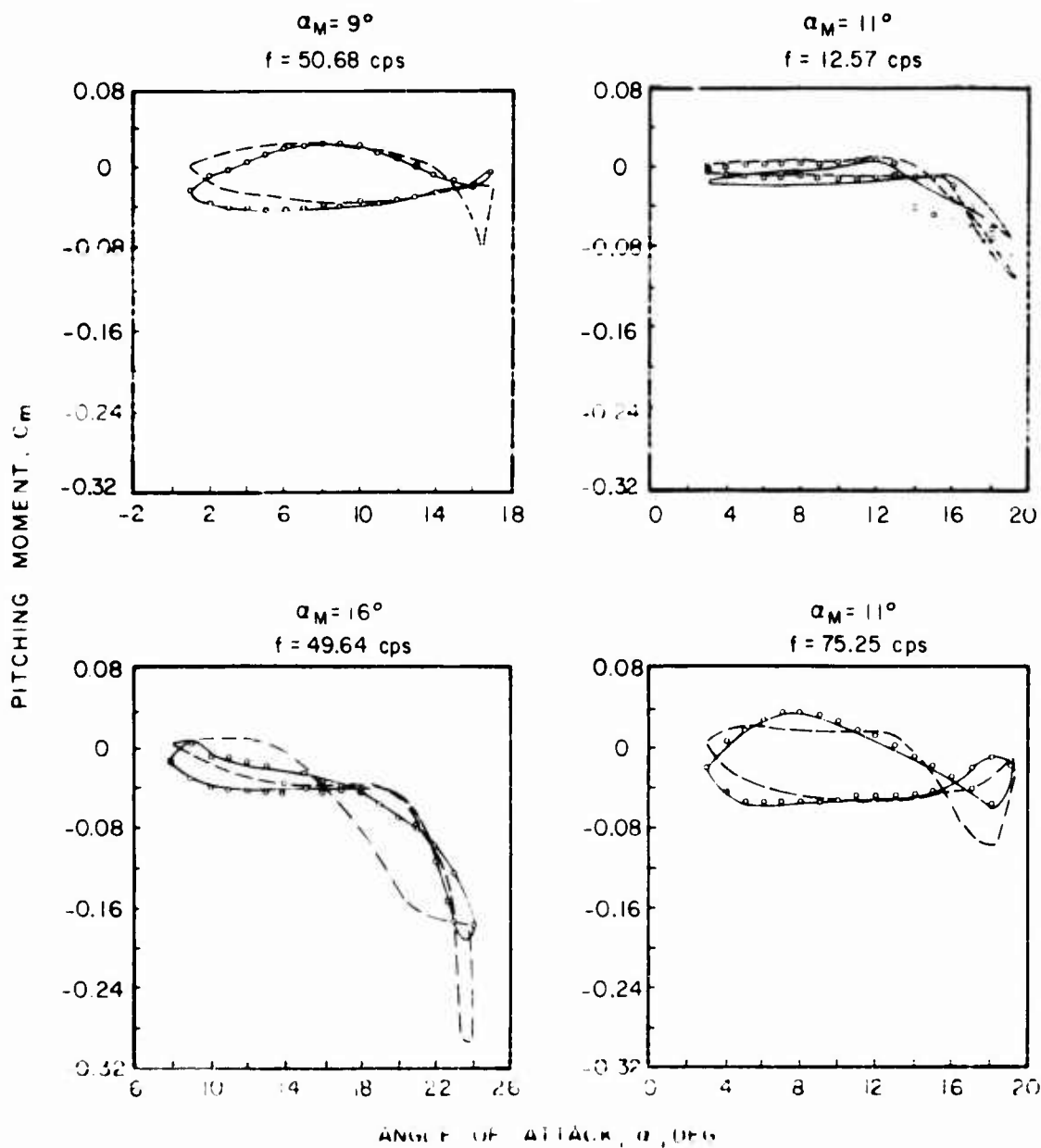
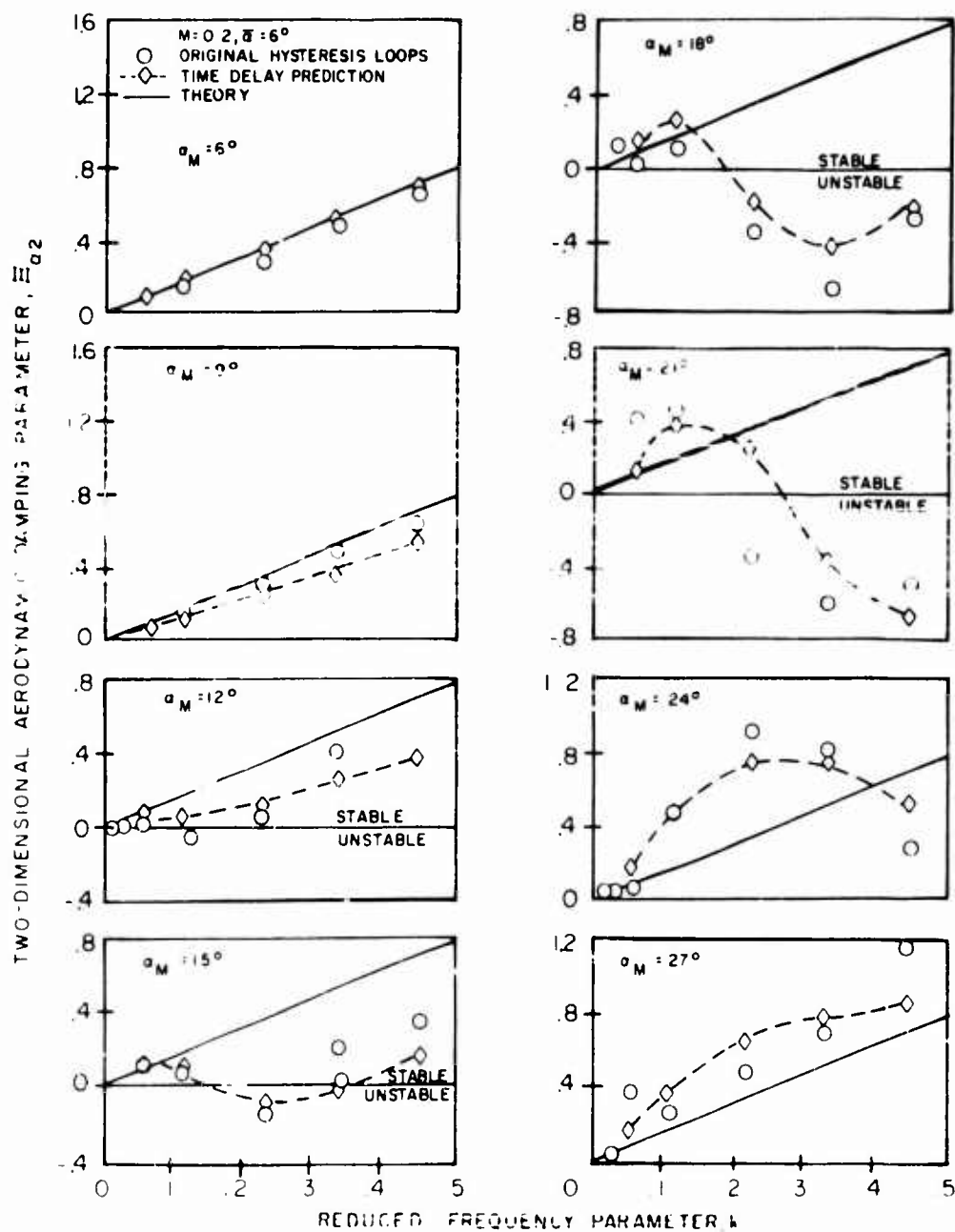
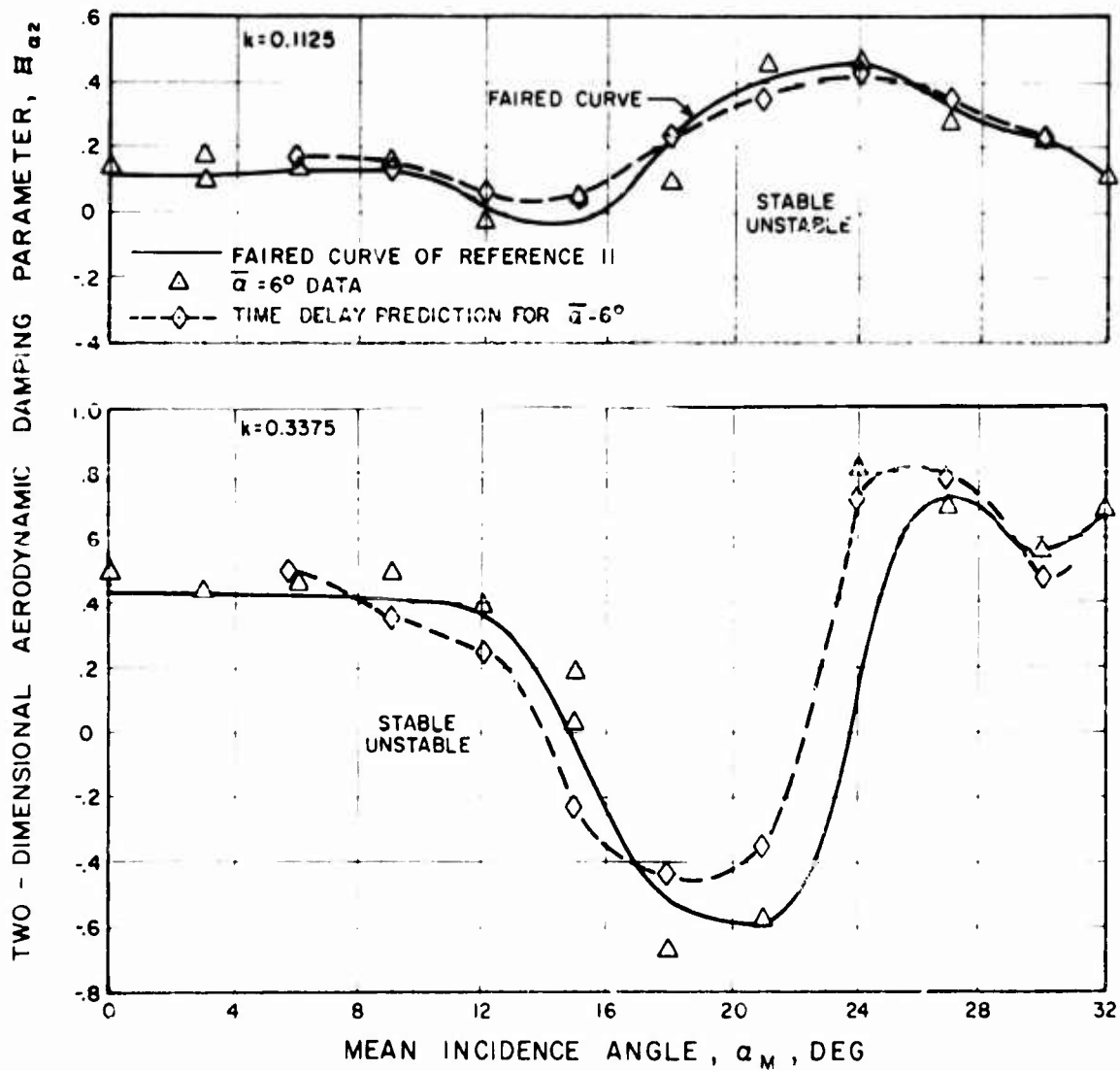


Figure 19. Correlation of flow visualization with measurements.

— ORIGINAL LOOP
 ° LOOP RECONSTRUCTED
 FROM α, A, B TABLES
 --- TIME DELAY PREDICTION







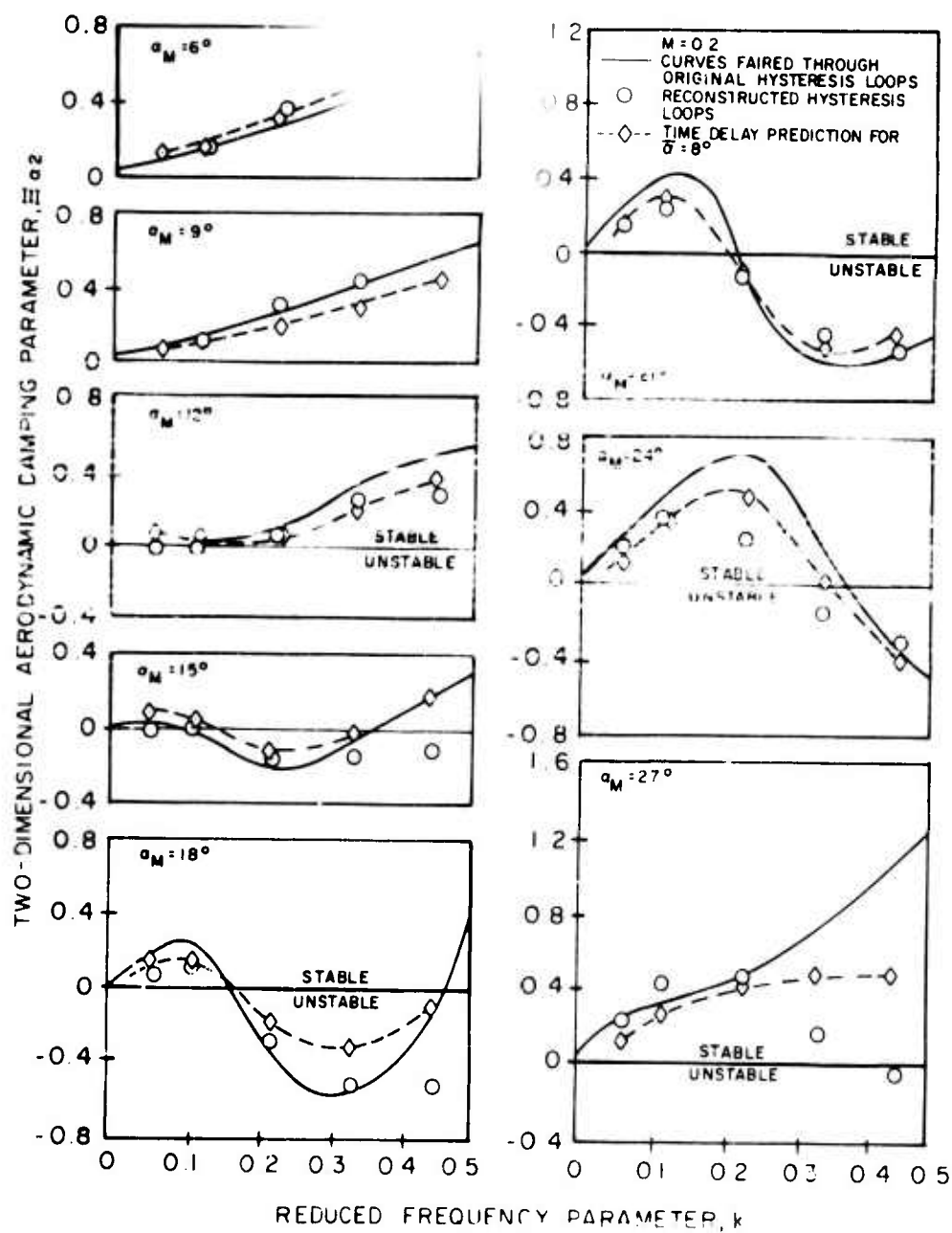


Figure 1. Variation of the two-dimensional aerodynamic damping parameter, Ξ_{a2} , with the reduced frequency parameter, k , for different angles of attack (α_M) and Mach numbers (M).

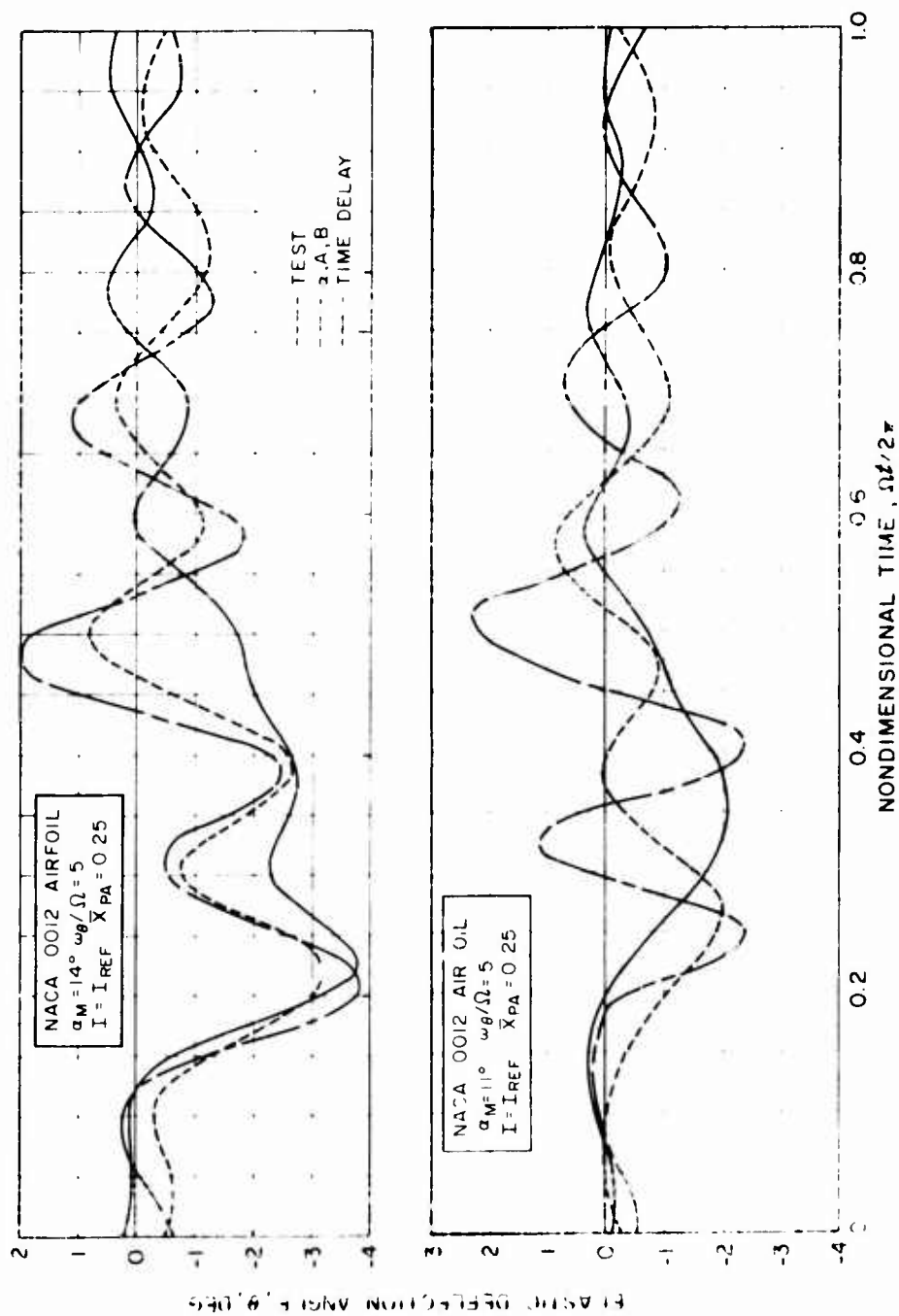


Figure 24. Effect of Mean Incidence Angle on Model Airfoil Torsional Response.

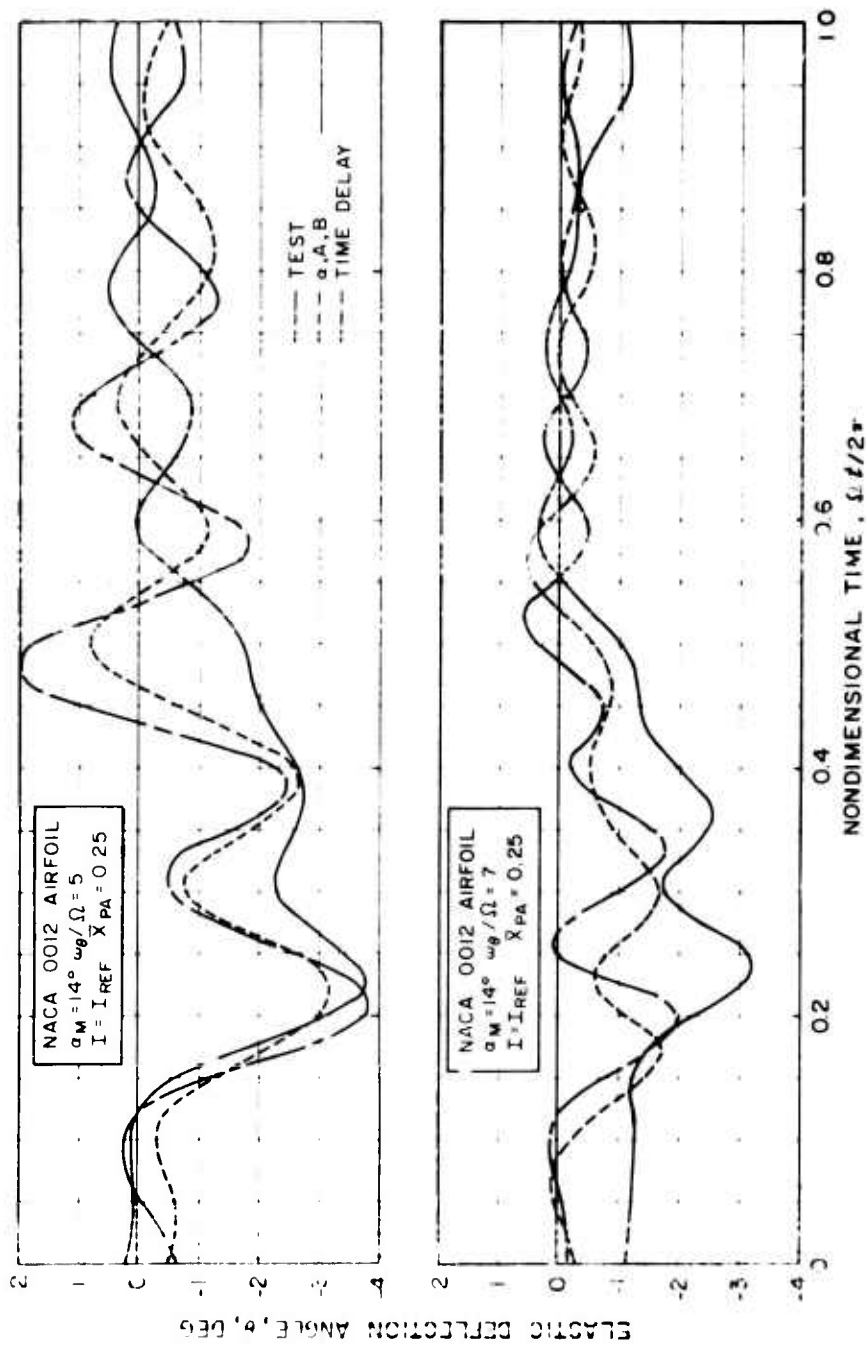


Figure 25. Effect of Torsional Natural Frequency on Model Airfoil Torsional Response.

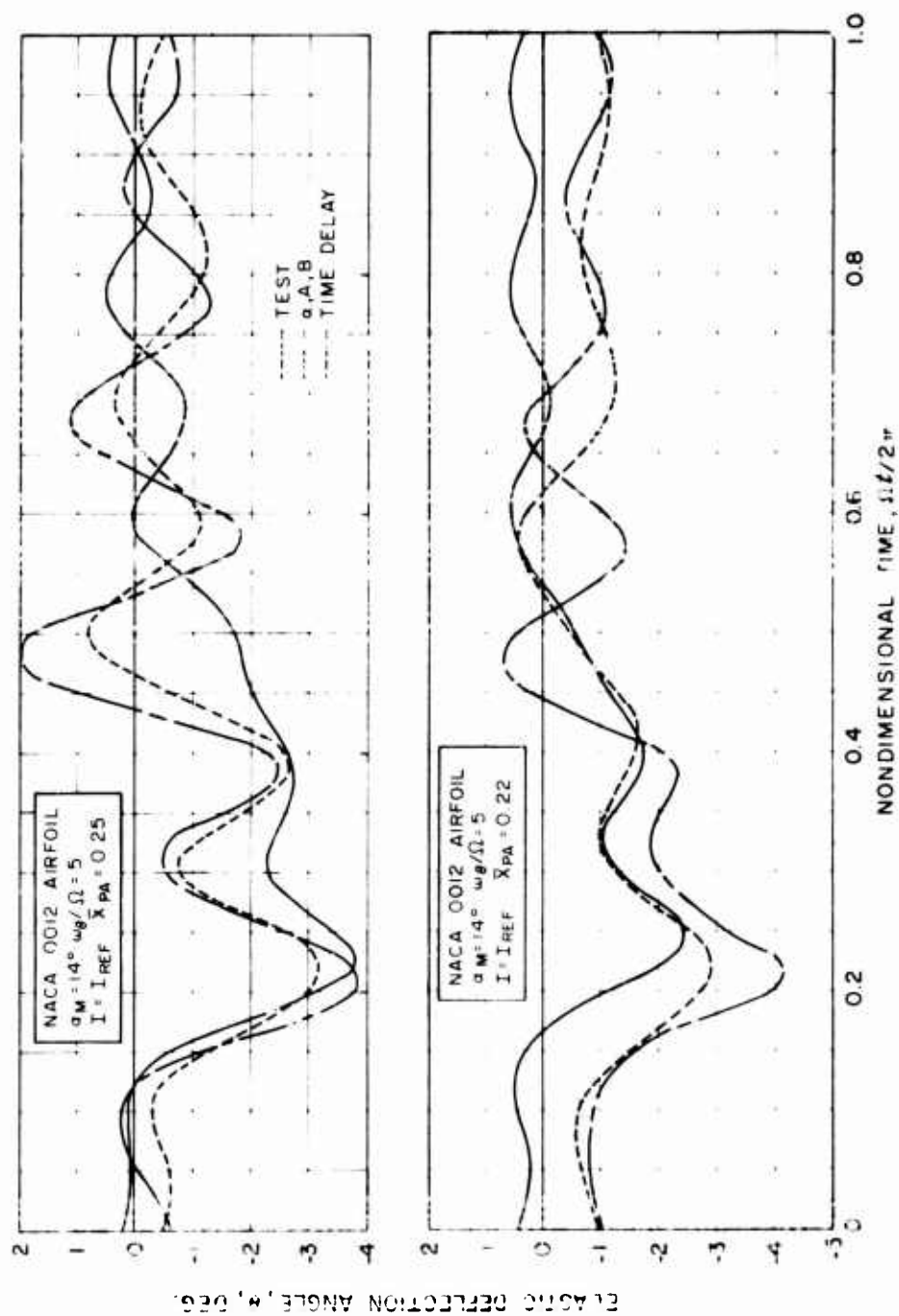


Figure 26. Effect of Pitch Axis on NACA 0012 Airfoil Torsional Response.

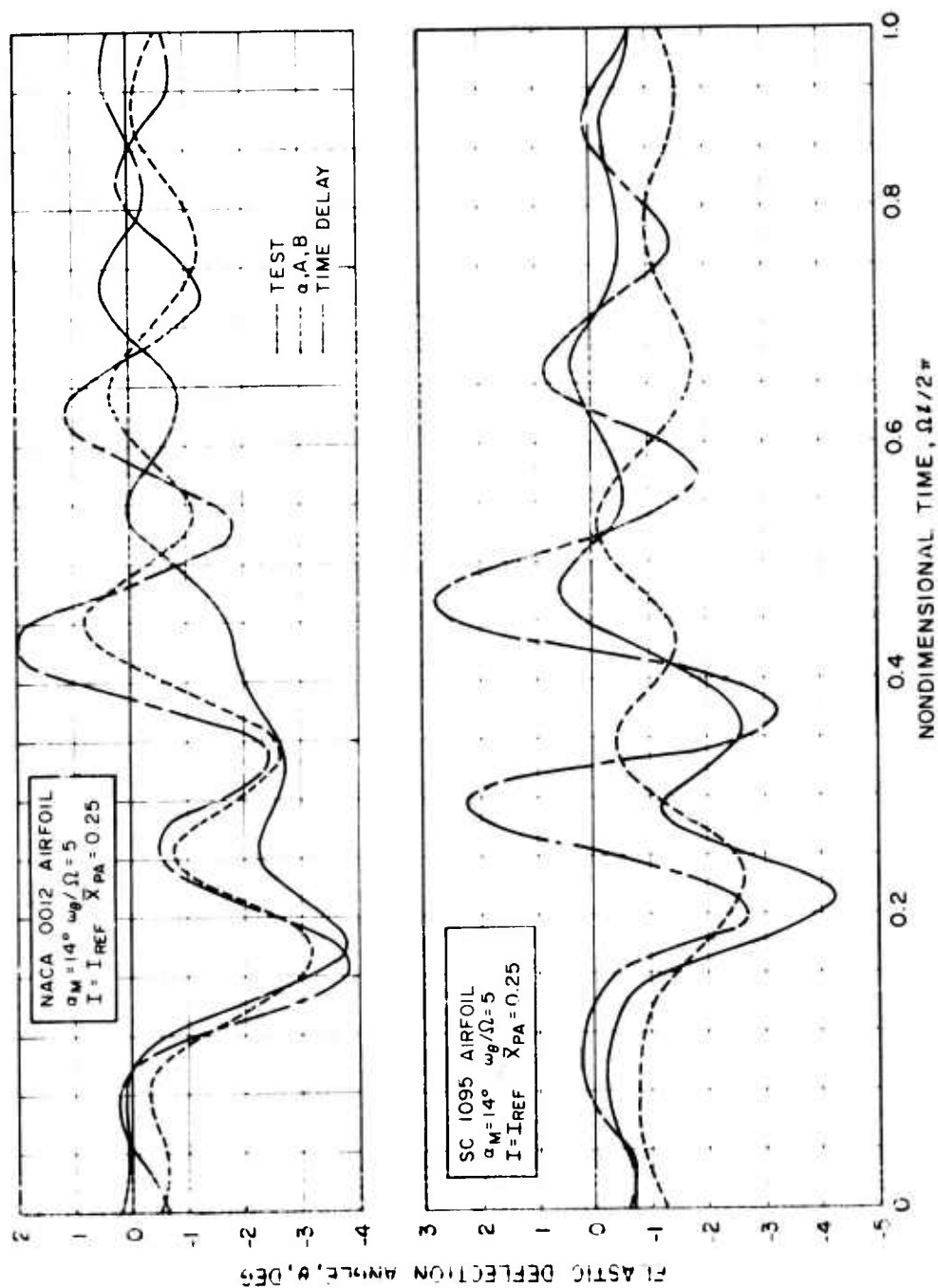


Figure 27. Effect of Airfoil Contour on Model Airfoil Torsional Response.

$I = I_{REF}$
 $I = 1.5 \times I_{REF}$

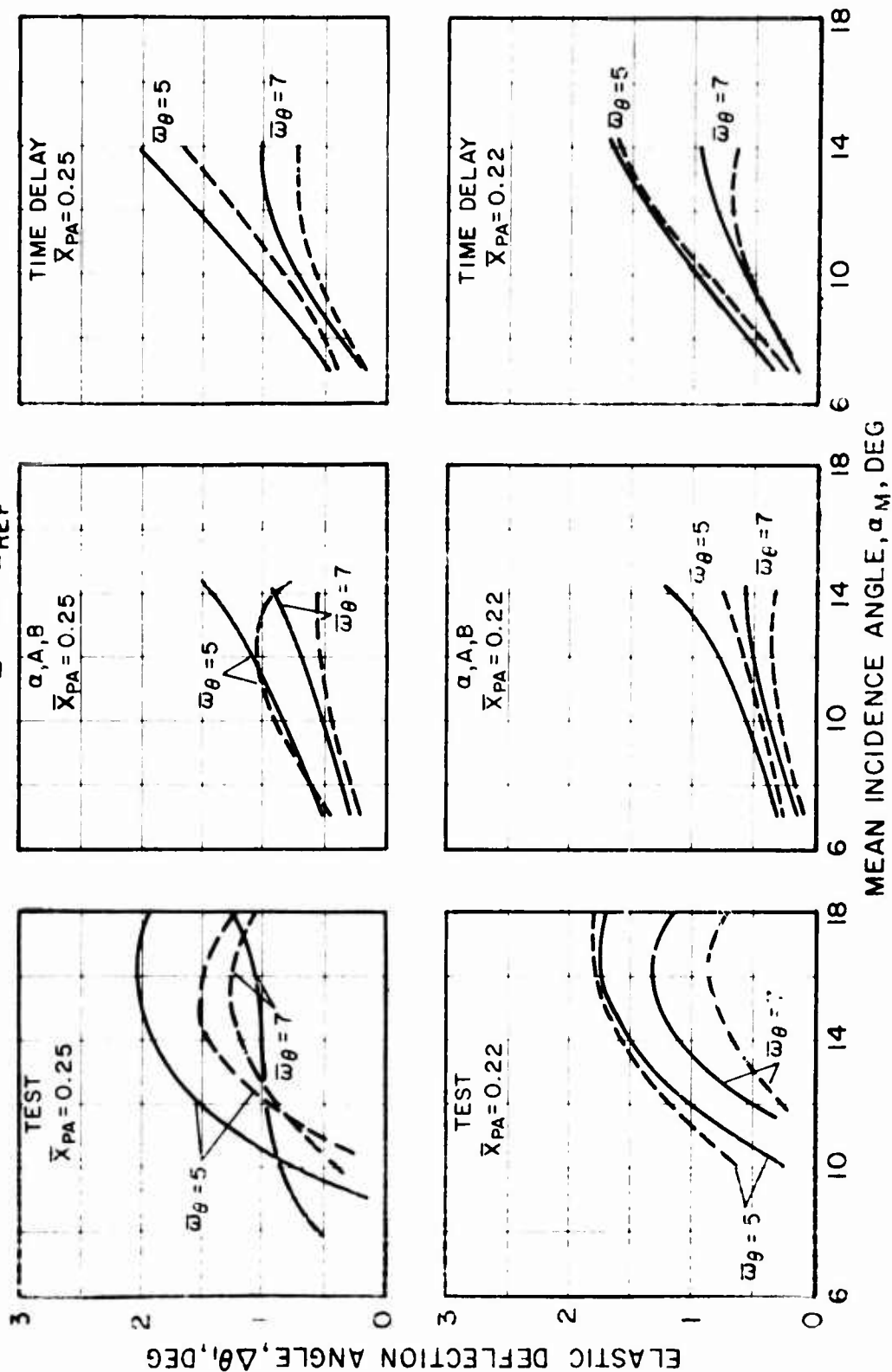


Figure 28. Correlation of NACA 0012 Airfoil Response Amplitude Obtained with Two Unsteady Aerodynamic Methods.

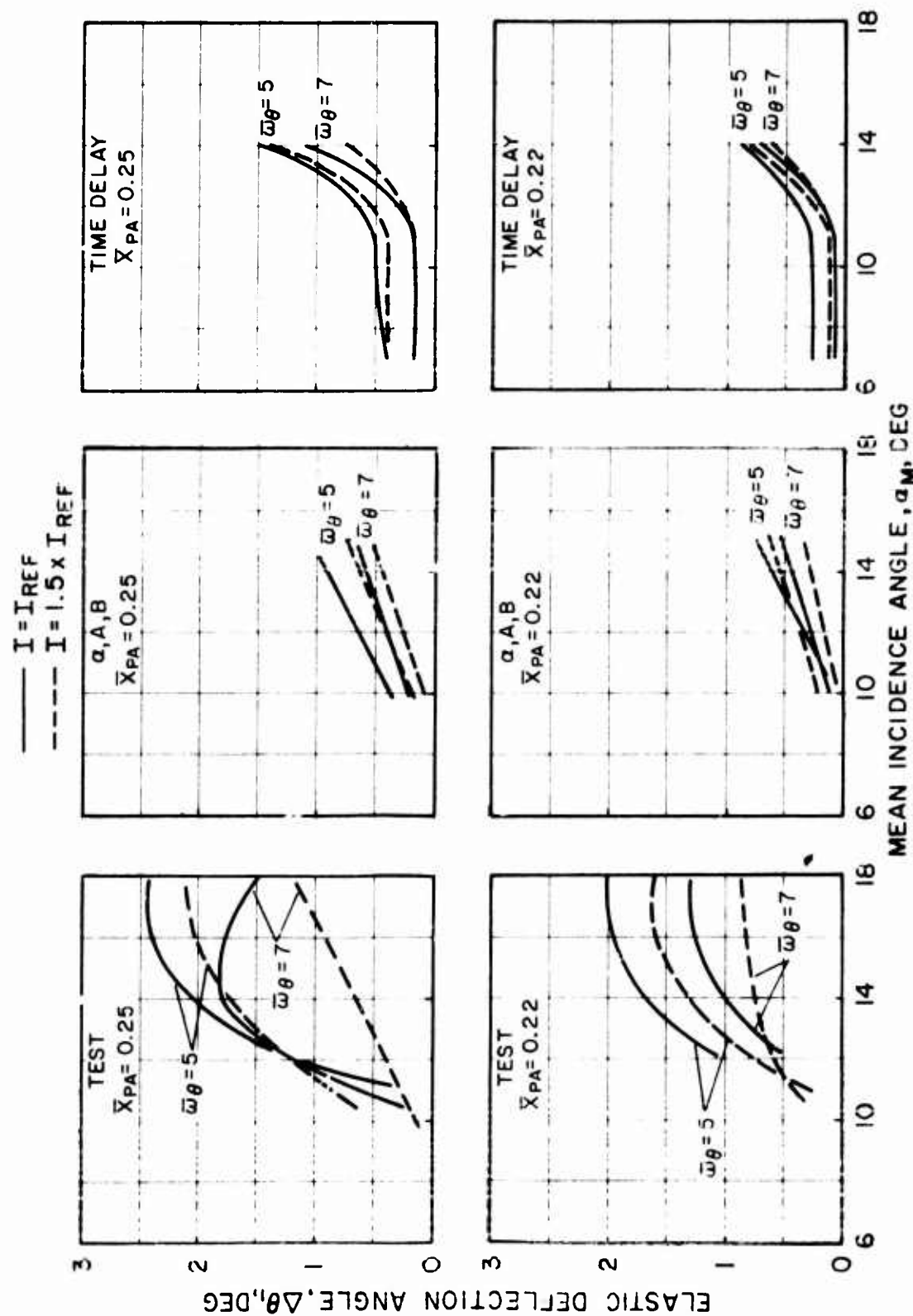


Figure 29. Correlation of SC 1095 Airfoil Response Amplitude Obtained With Two Unsteady Aerodynamic Methods.

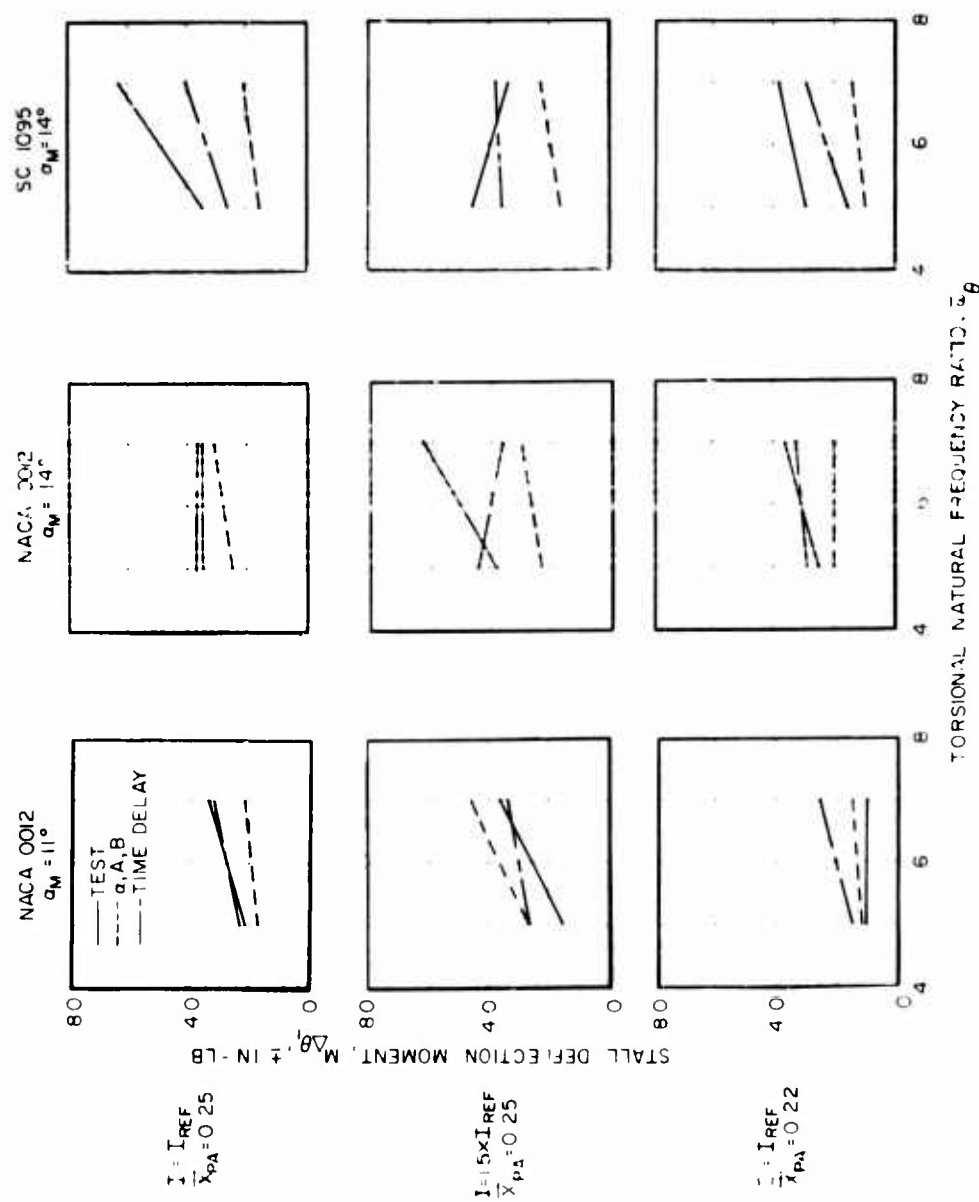


Figure 30. Effect of Torsional Natural Frequency on Vibratory Torsional Moment.

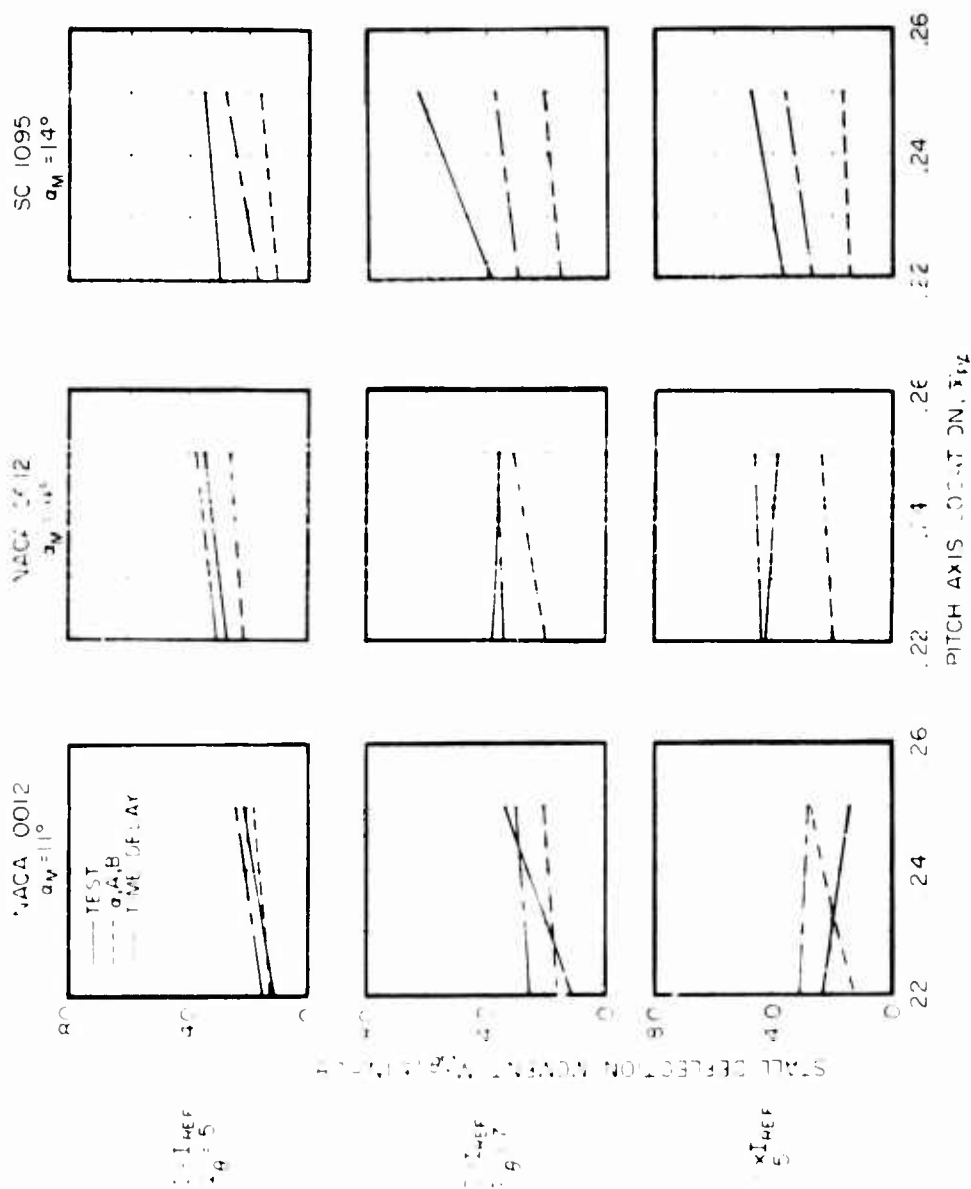


Figure 11. Effect of Pitch Axis Location on Vibratory Torsional Moment.

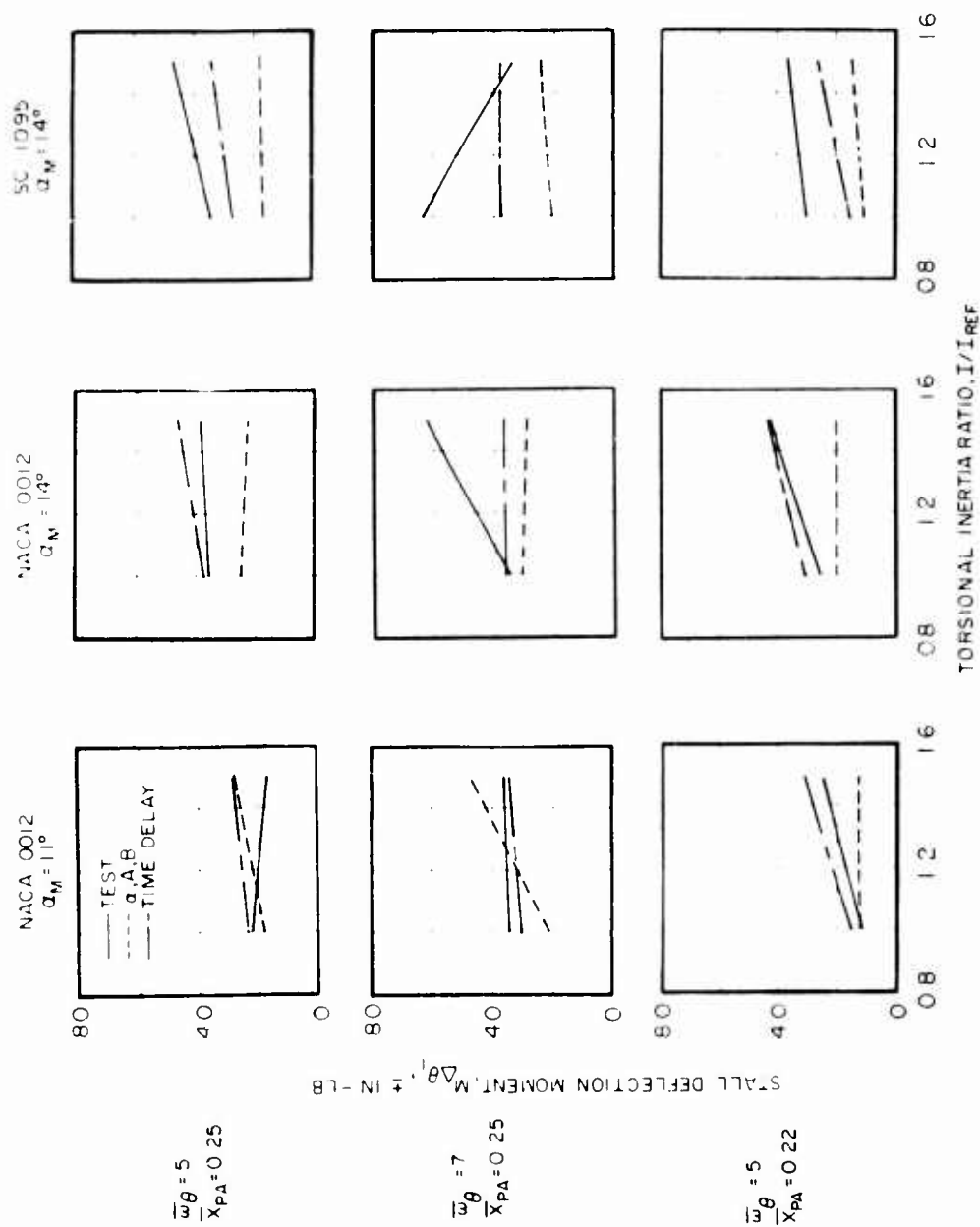


Figure 32. Effect of Airfoil Torsional Inertia on Vibratory Torsional Moment.

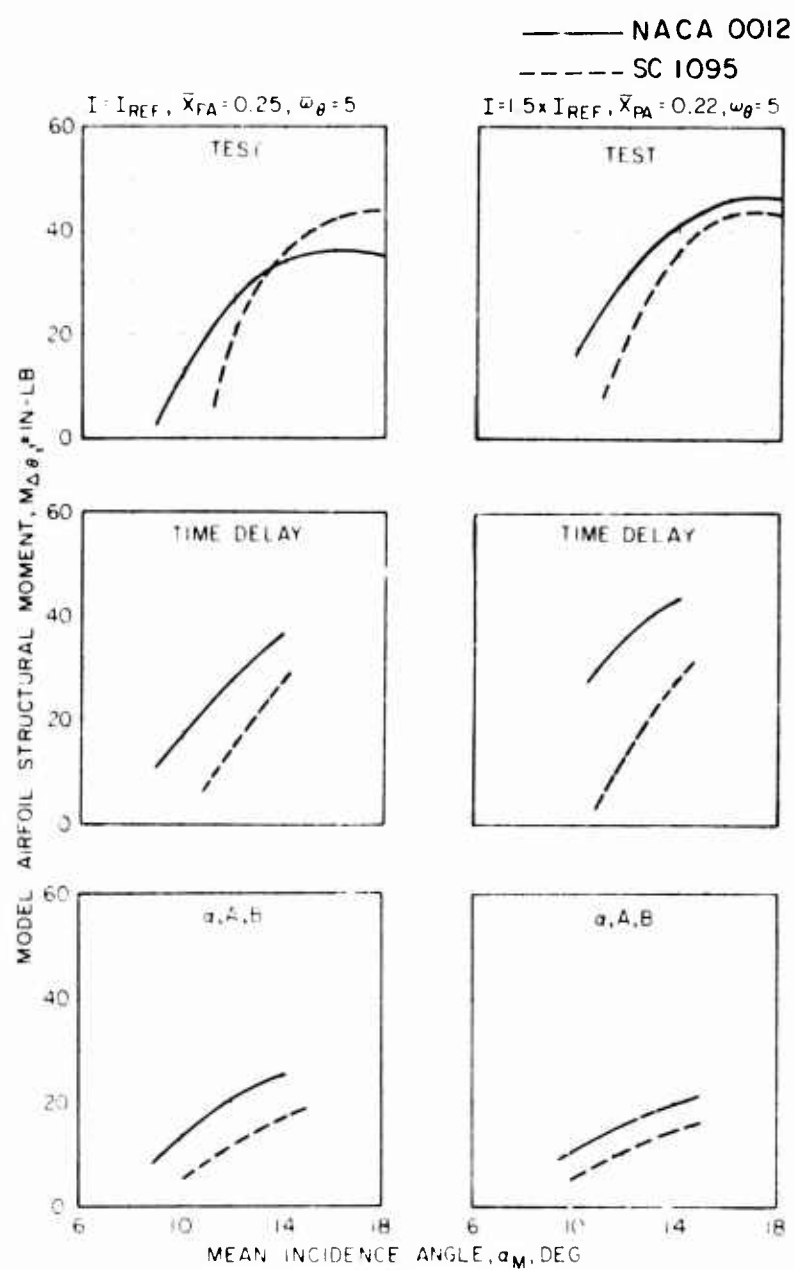


Figure 33. Effect of Mean Incidence Angle on Vibratory Torsional Moment.

- ① ——— $\alpha_{(1.0, 270^\circ)} = 12^\circ$ - BELL
- ② - - - - $\alpha > 13.5^\circ$ - KAMAN UH-2C
- ③ - - - - $bC_{Q,D}/\sigma = 0.004$ - SIKORSKY CH-53A
- ④ - - - - IDEAL ROTOR

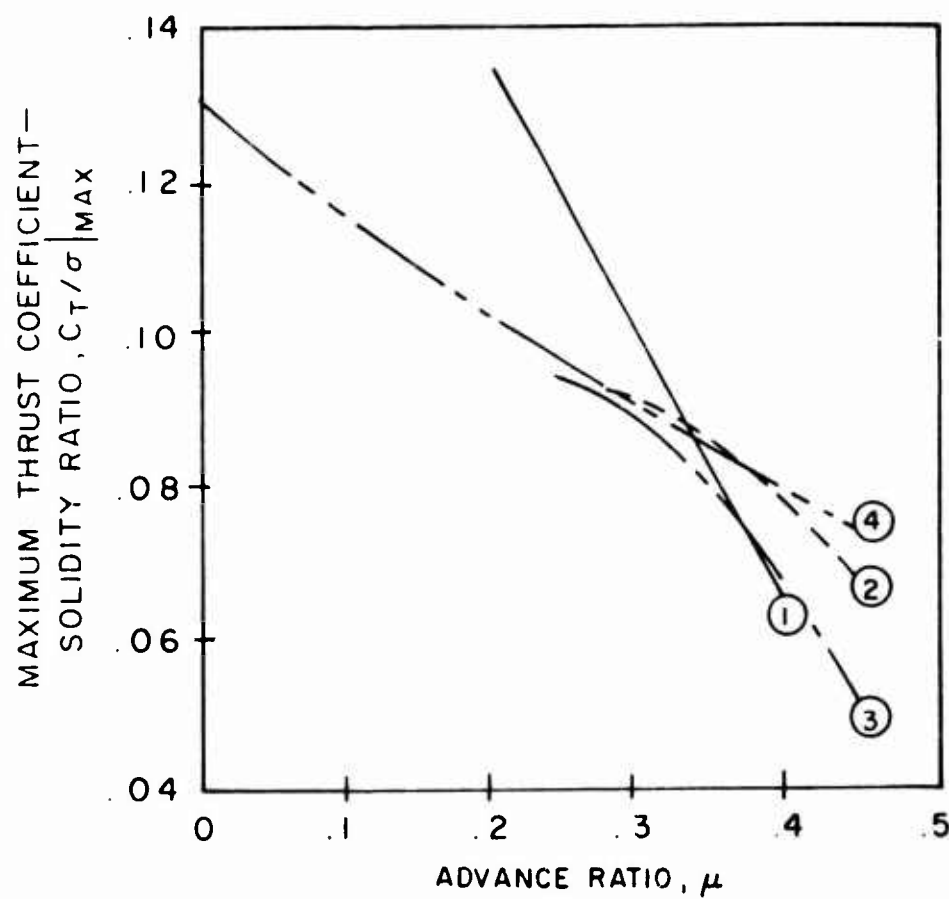


Figure 34. Selected Stall Boundary Prediction Techniques.

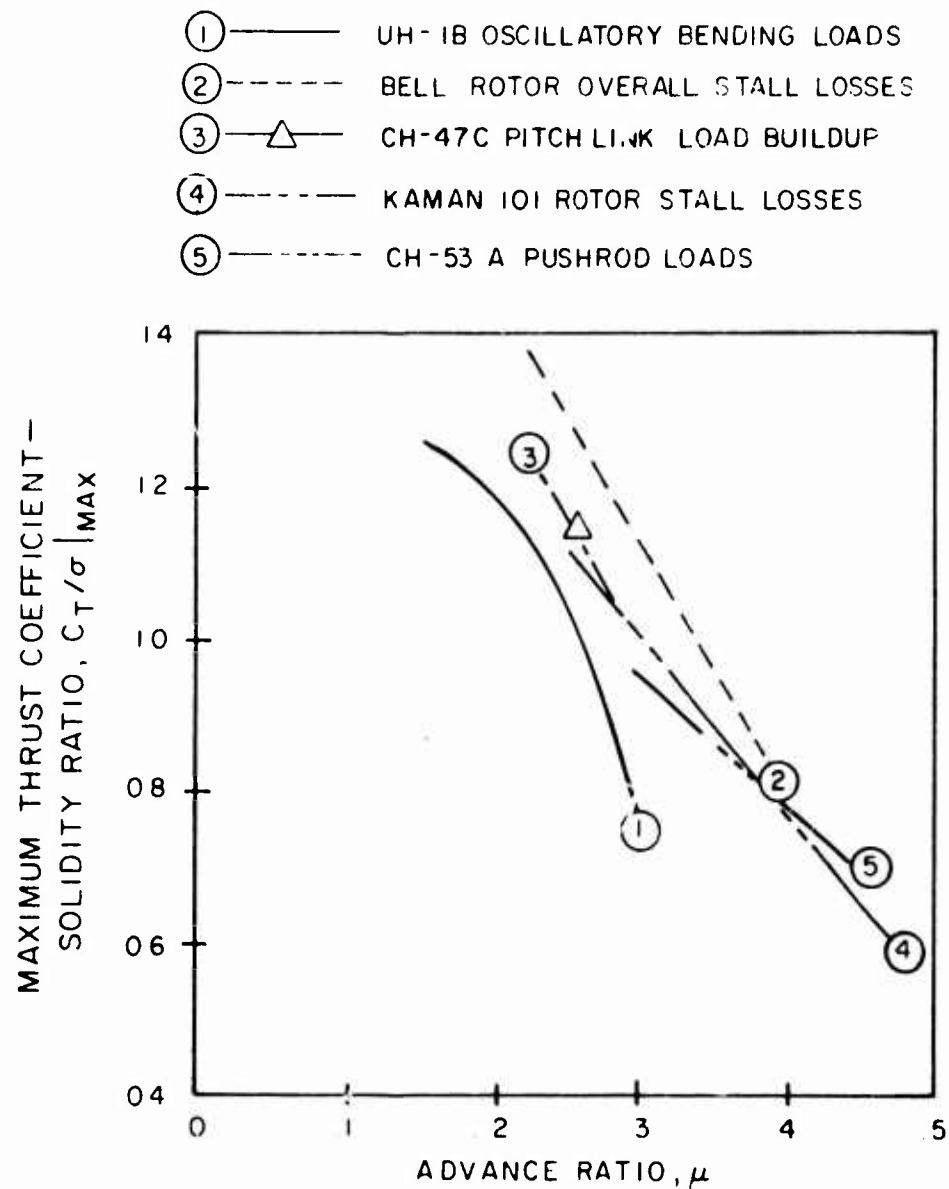


Figure 35. Selected Measured Stall Boundaries.



Figure 36. CH-53A Helicopter.



Figure 37. CH-54B Helicopter.

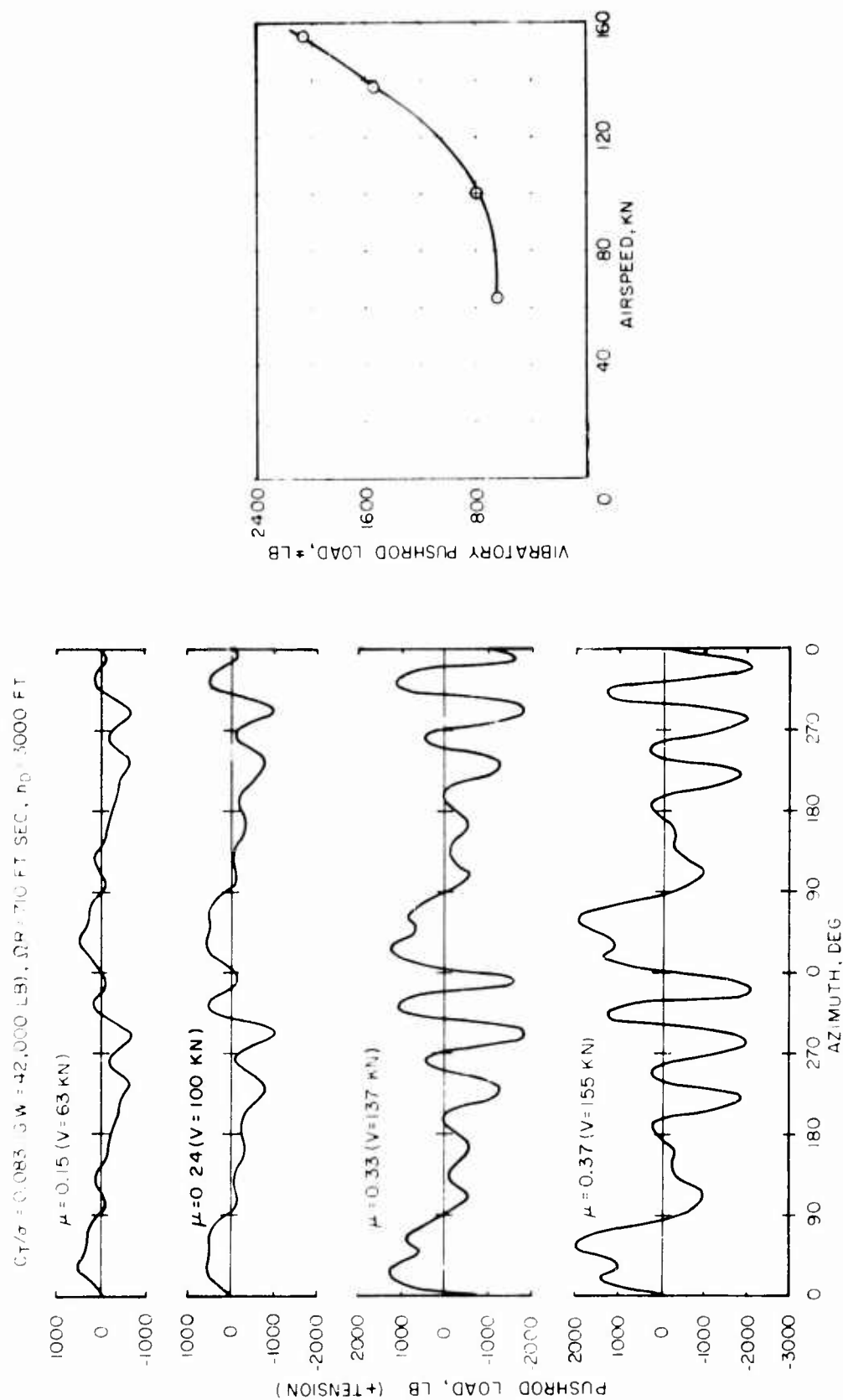


Figure 38. The Buildup of CH-53A Pushrod Loads With Airspeed.

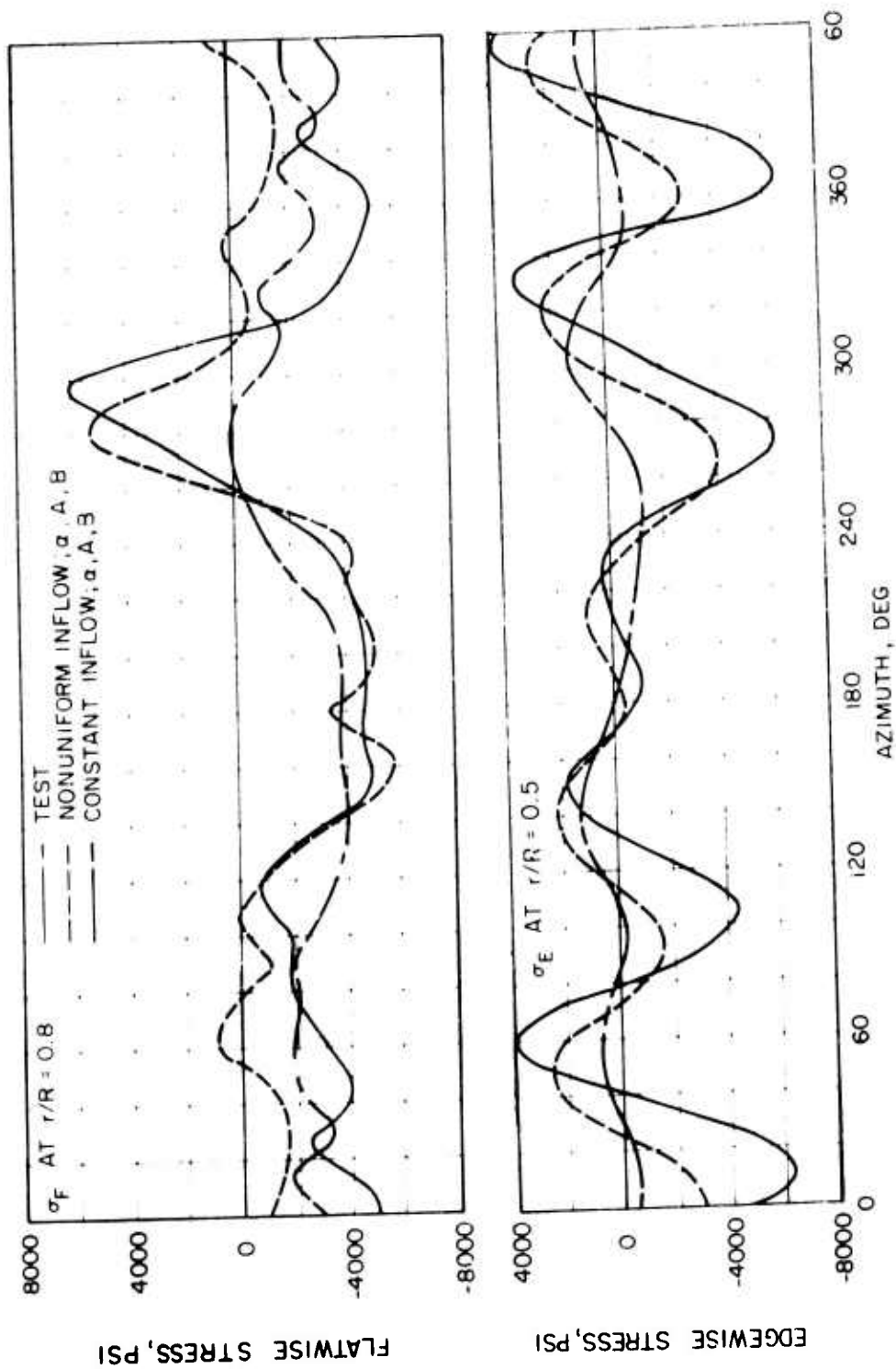


Figure 39. Effect of Nonuniform Inflow on the Correlation of CH-53A Blade Stress at 137 Kn and 42,000 Lb Gross Weight.

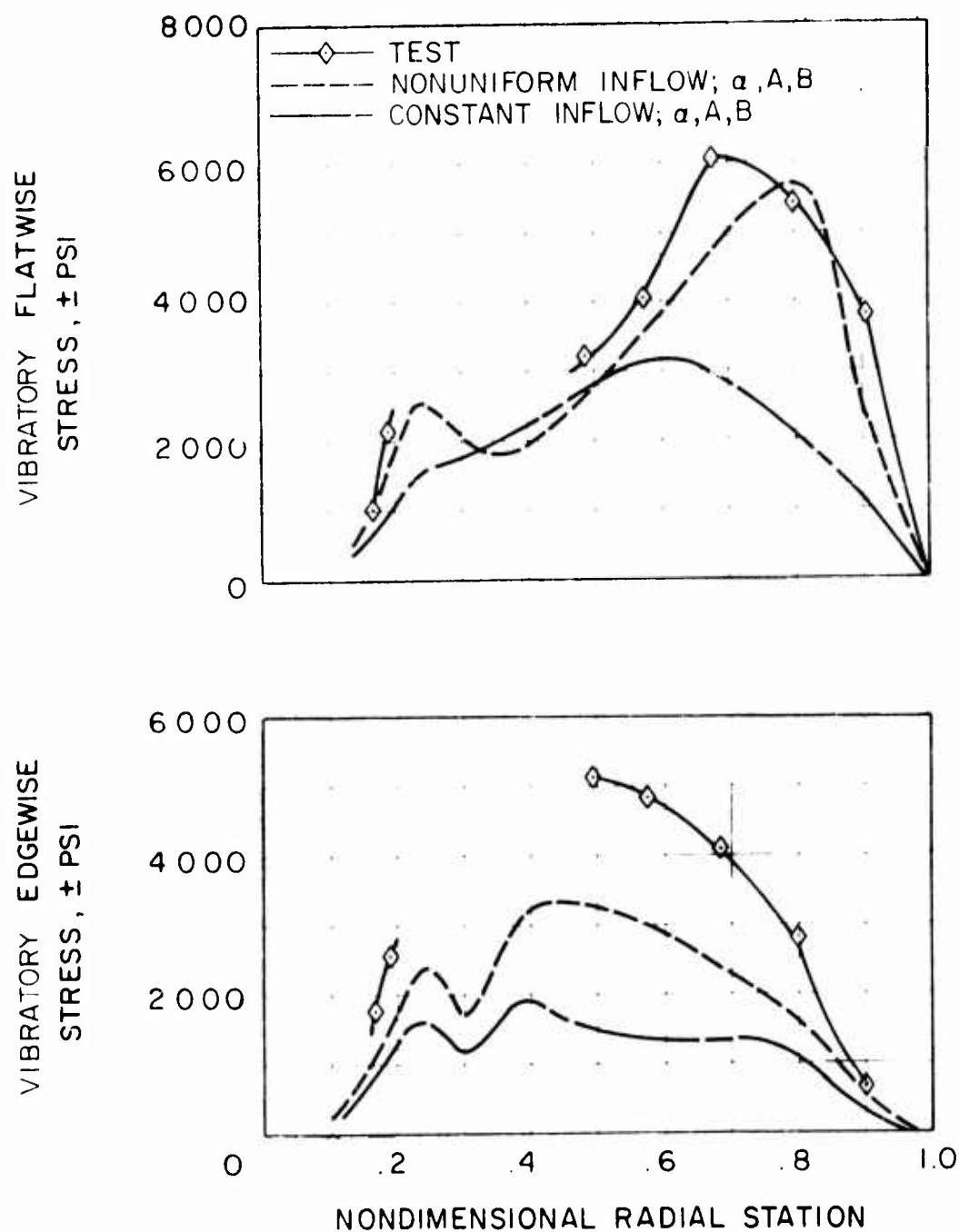


Figure 40. Effect of Nonuniform Inflow on Correlation of the Radial Distribution of CH-53A Blade Stress at 137 Kn and 42,000 Lb Gross Weight.

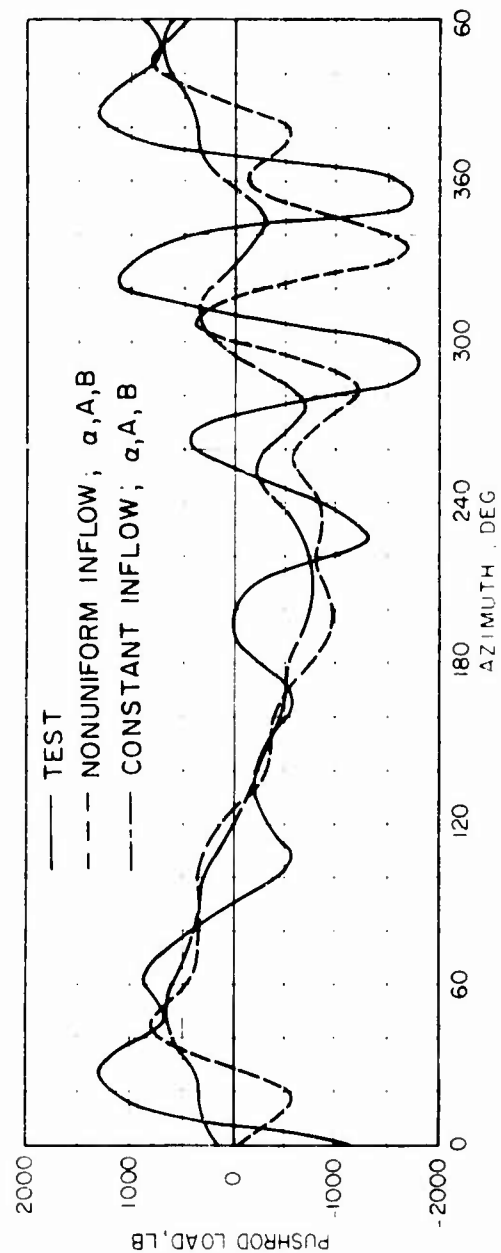


Figure 41. Correlation of CH-53A Pushrod Load Time Histories at 137 Kn and 42,000 Lb Gross Weight.

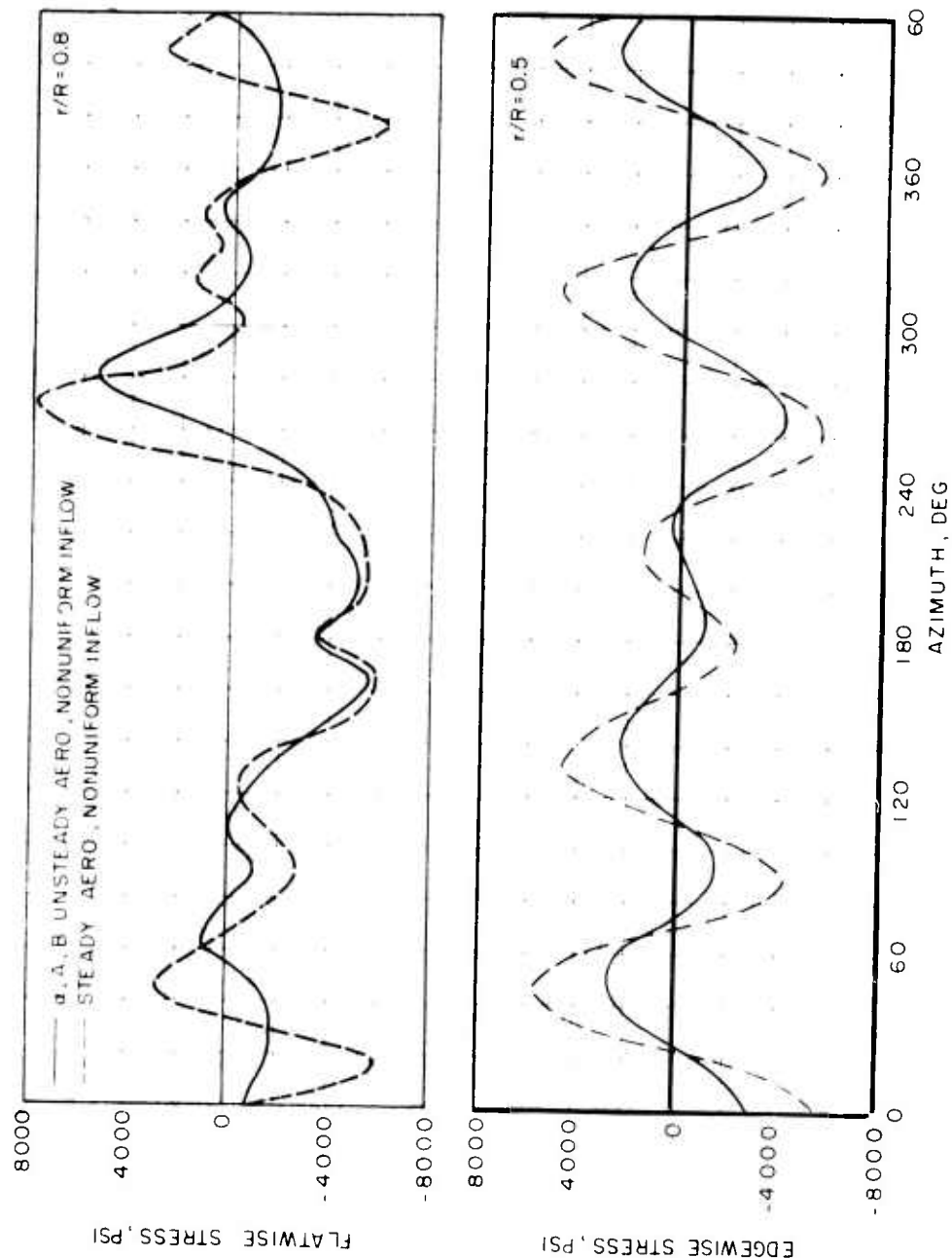


Figure 42. CH-53A Blade Stress Calculated With and Without Unsteady Aerodynamics at 137 Kn and 42,000 Lb Gross Weight.

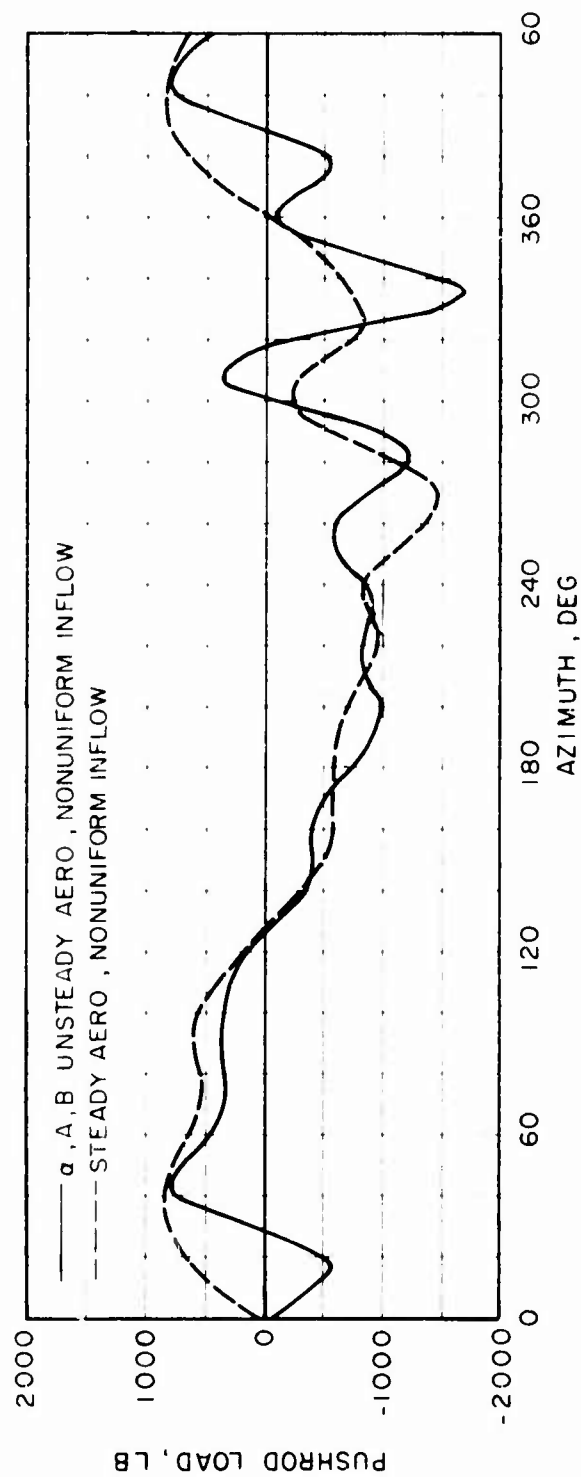


Figure 43. Effect of Unsteady Aerodynamics on Calculated CH-53A Pushrod Loads at 137 Kn and 42,000 Lb Gross Weight.

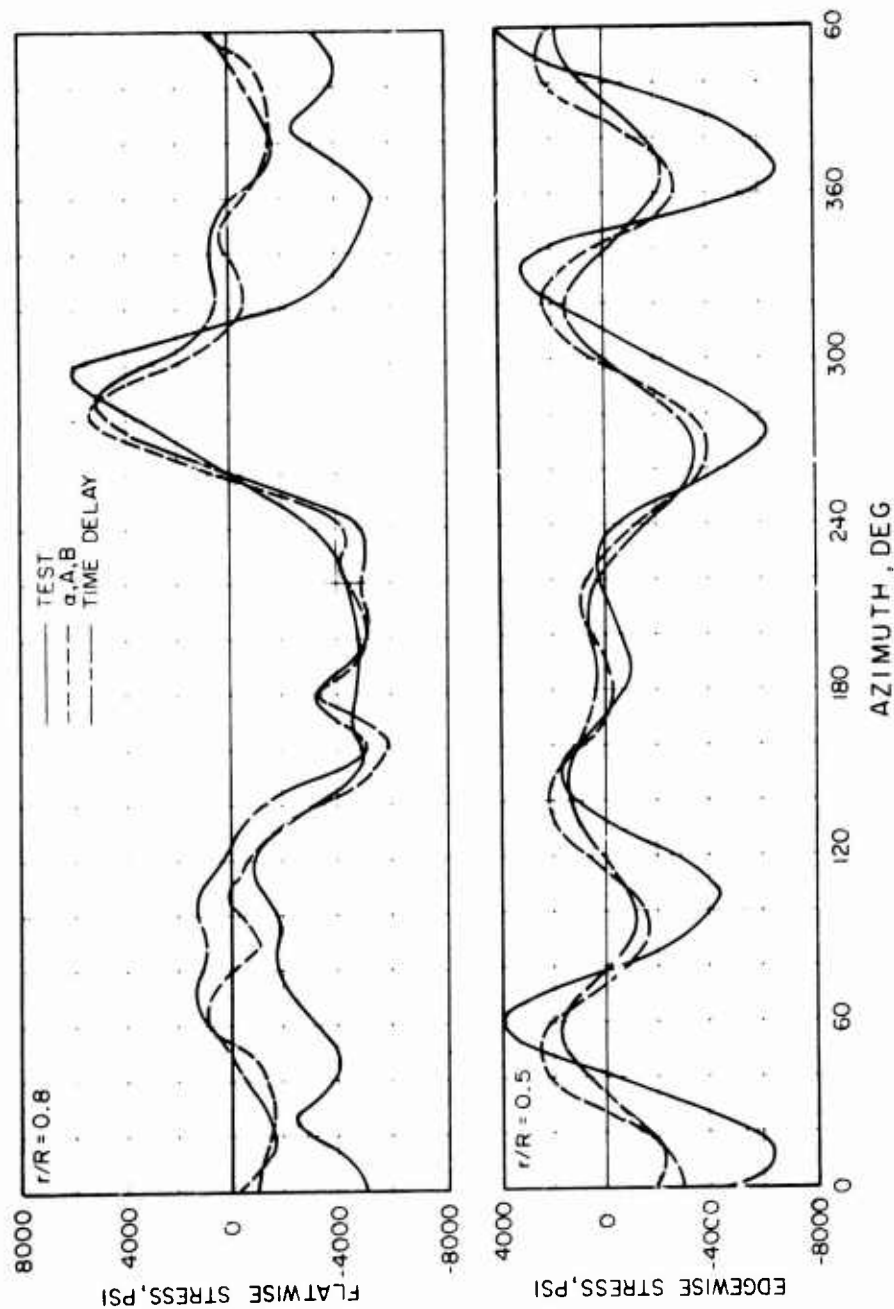


Figure 44. Correlation of CH-53A Blade Stress With α , A, B and Time Delay Unsteady Aerodynamics at 137 Kn and 42,000 Lb Gross Weight.

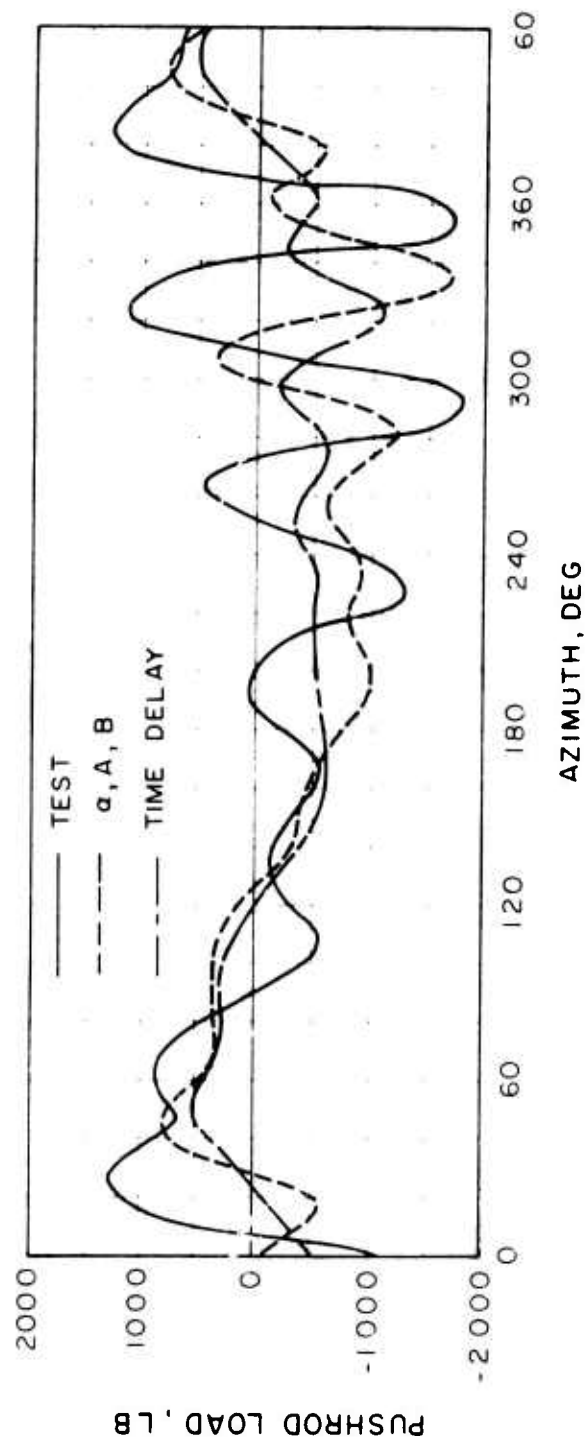


Figure 45. Correlation of CH-53A Pushrod Load Obtained With α, A, B and Time Delay Unsteady Aerodynamics at 137 Kn and 42,000 Lb Gross Weight.

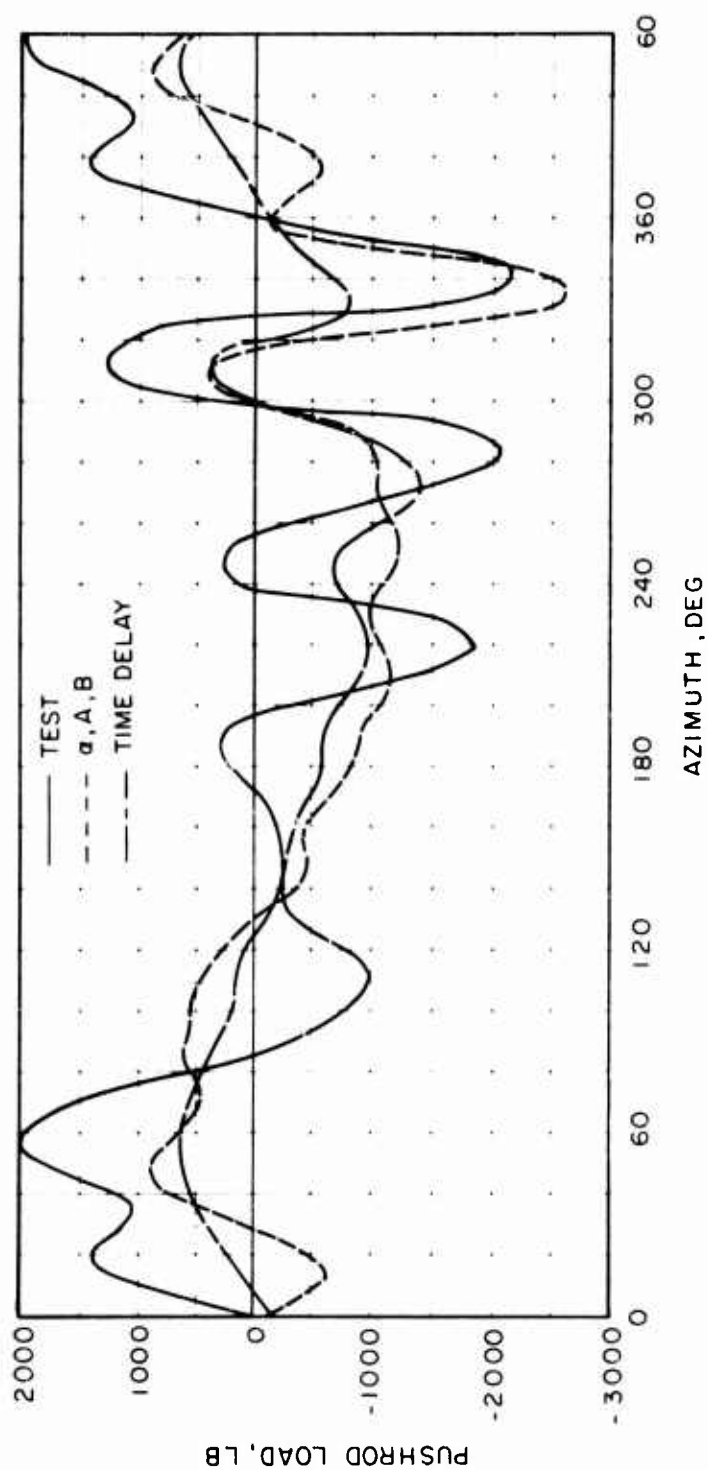


Figure 46. Correlation of CH-53A Pushrod Load Obtained With α, A, B and Time Delay Unsteady Aerodynamics at 155 Kn and 42,000 lb Gross Weight.

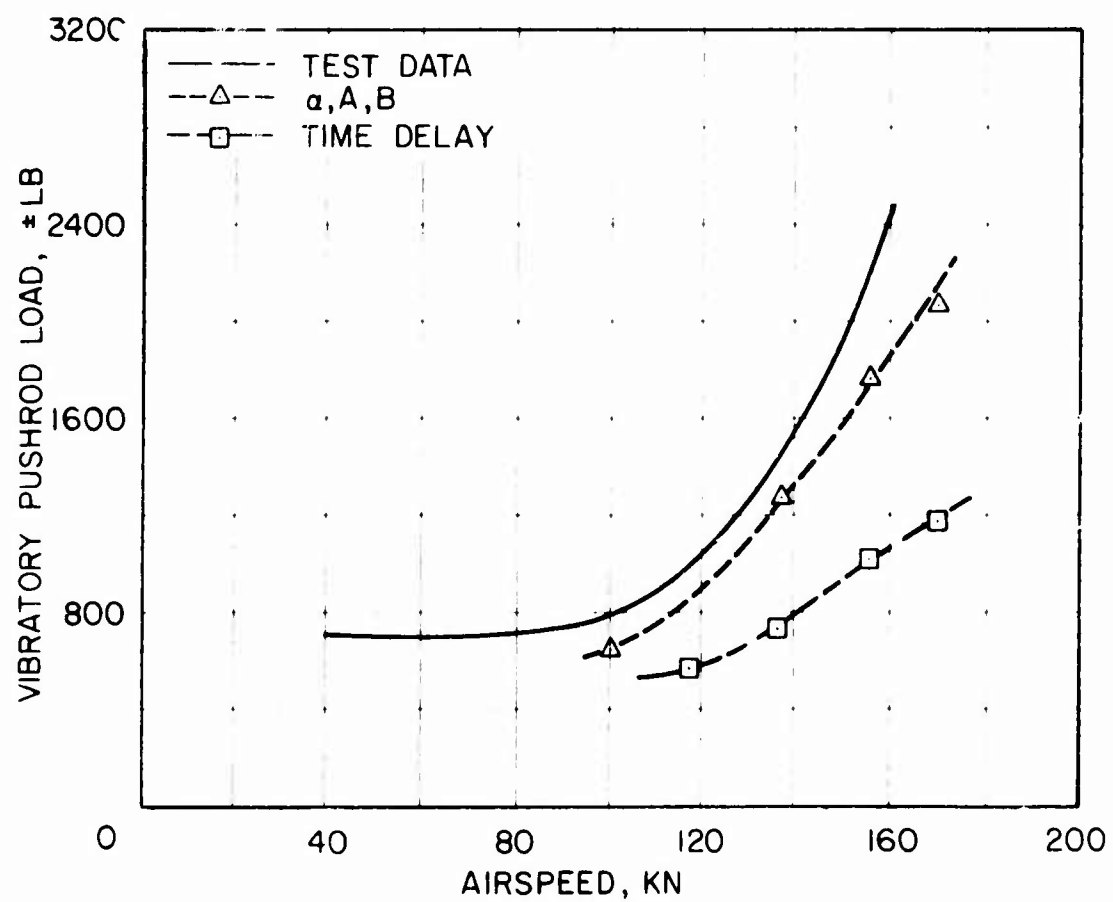


Figure 47. Correlation of CH-53A Vibratory Pushrod Loads at 42,000 Lb Gross Weight.

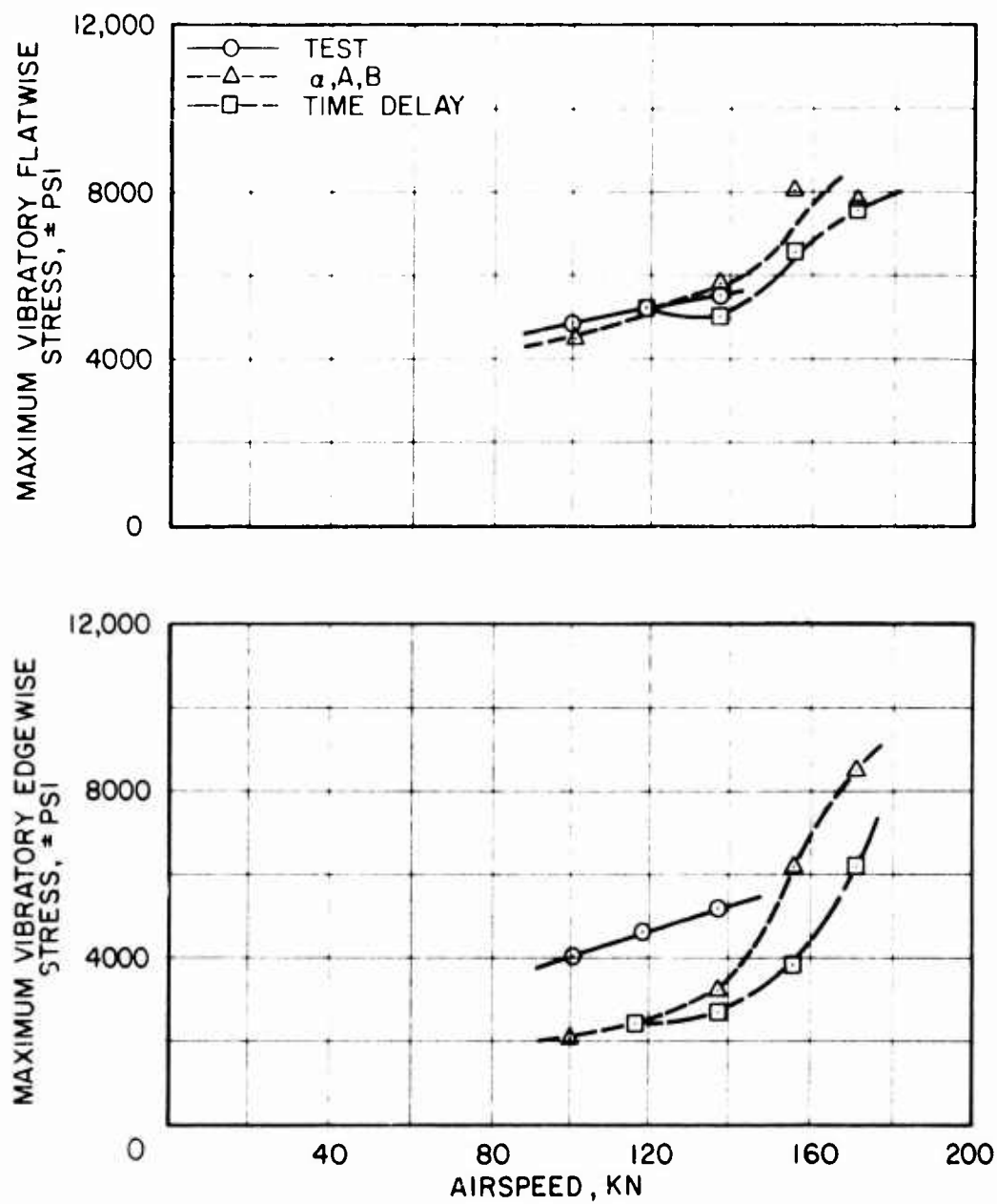


Figure 48. Correlation of CH-53A Vibratory Blade Stress at 42,000 Lb Gross Weight.

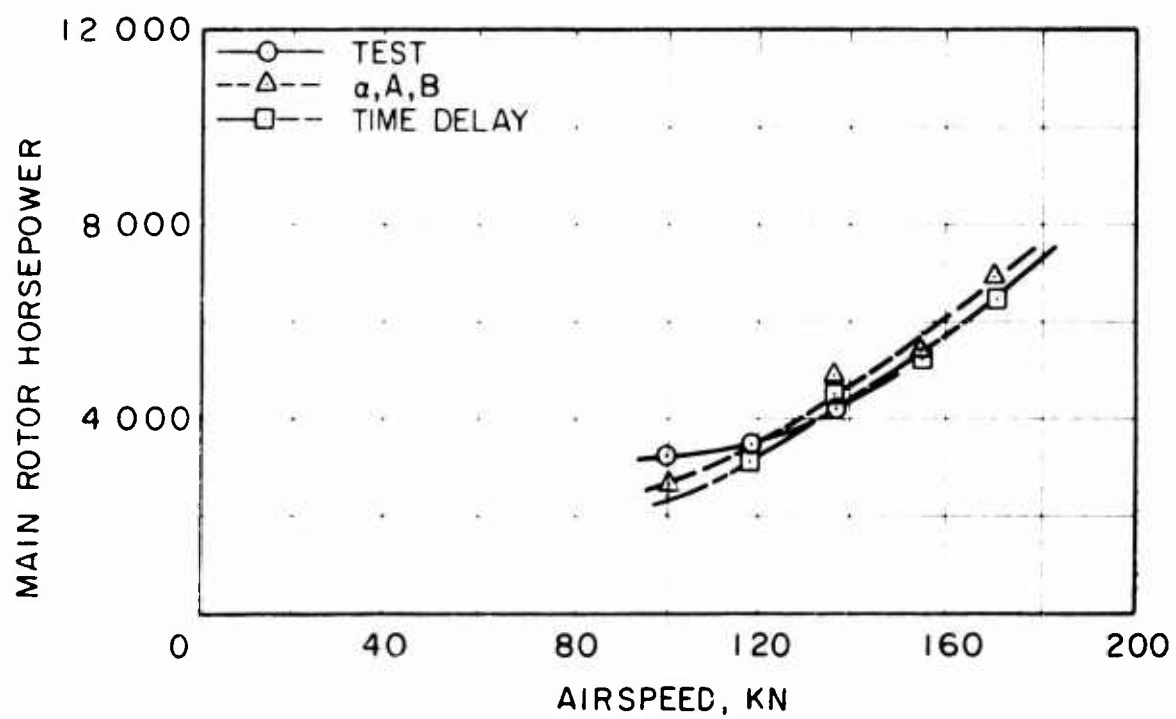


Figure 49. Correlation of CH-53A Required Power at 42,000 Lb Gross Weight.

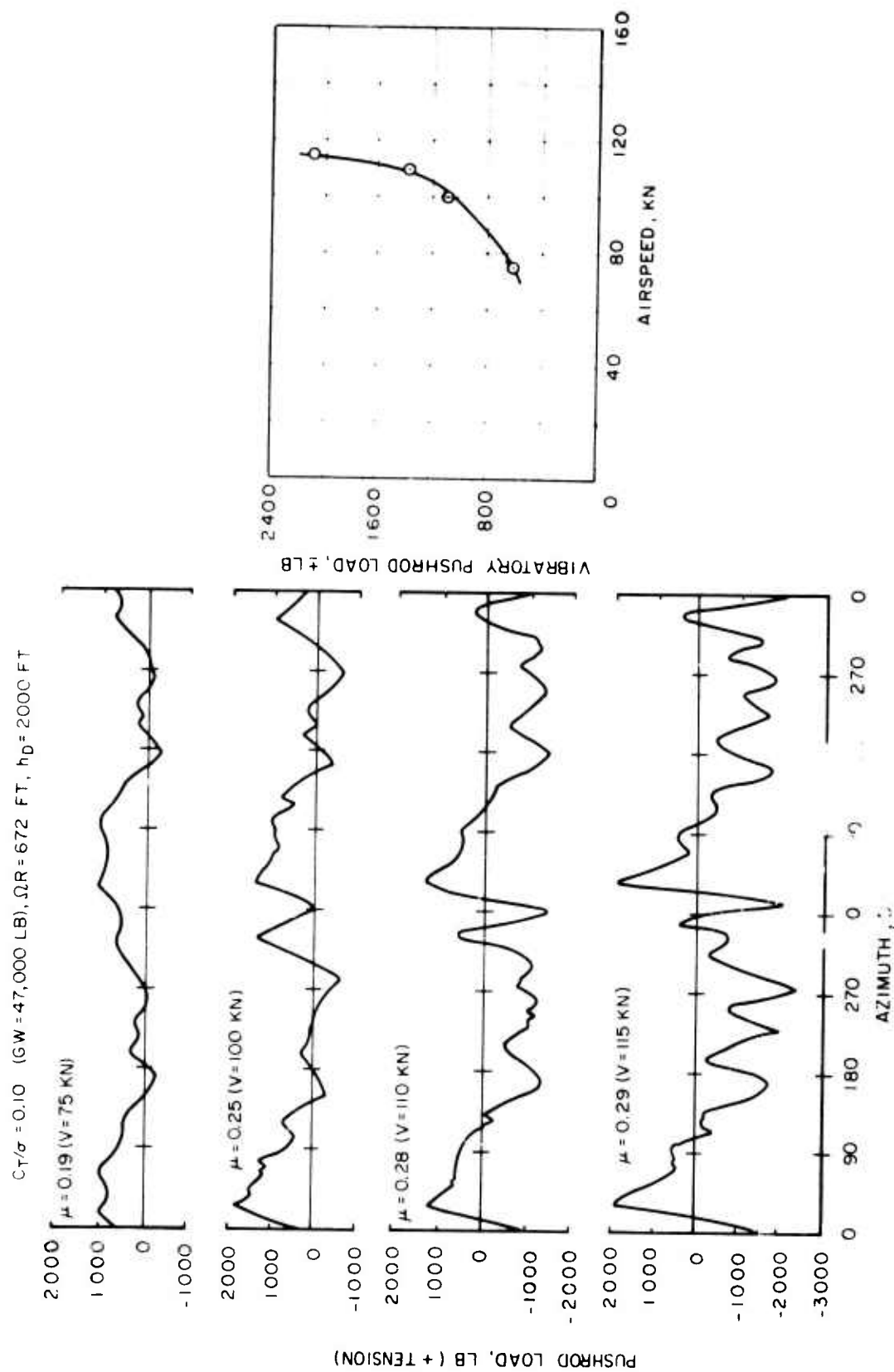


Figure 50. The Buildup of CH-54B Pushrod Loads With Airspeed.

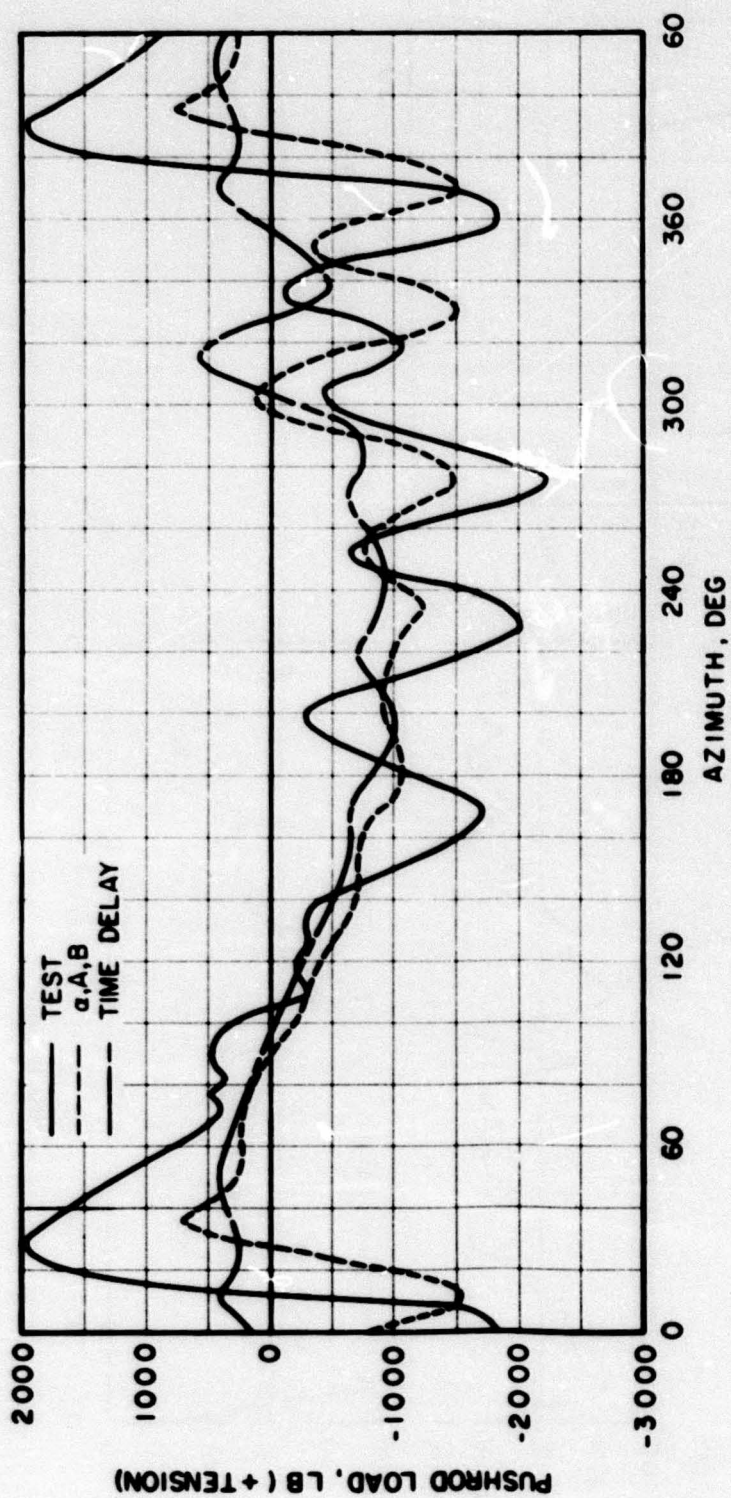


Figure 51. Correlation of CH-54B Pushrod Load Time Histories at 115 Kn and 47,000 Lb Gross Weight.

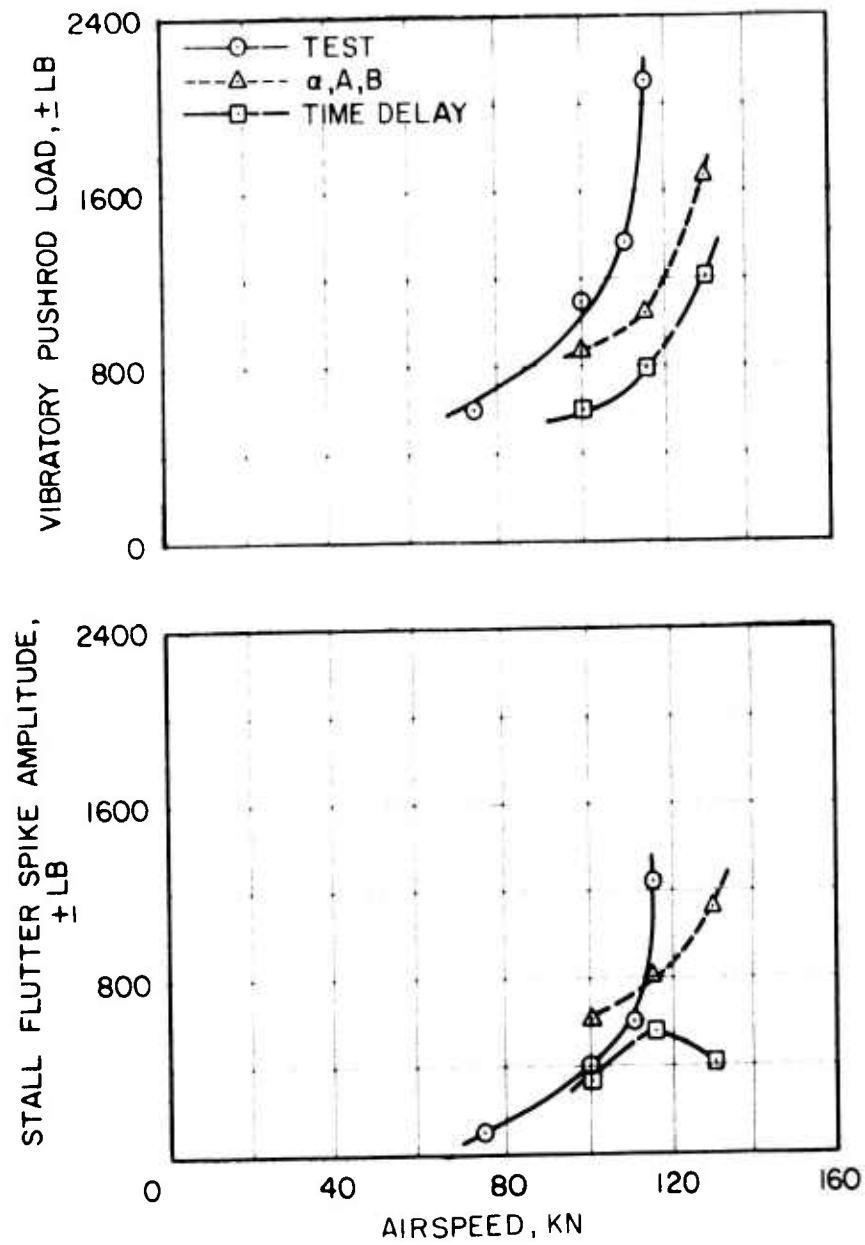


Figure 52. Correlation of Measured and Calculated CH-54B Pushrod Load Amplitudes at 47,000 Lb Gross Weight.

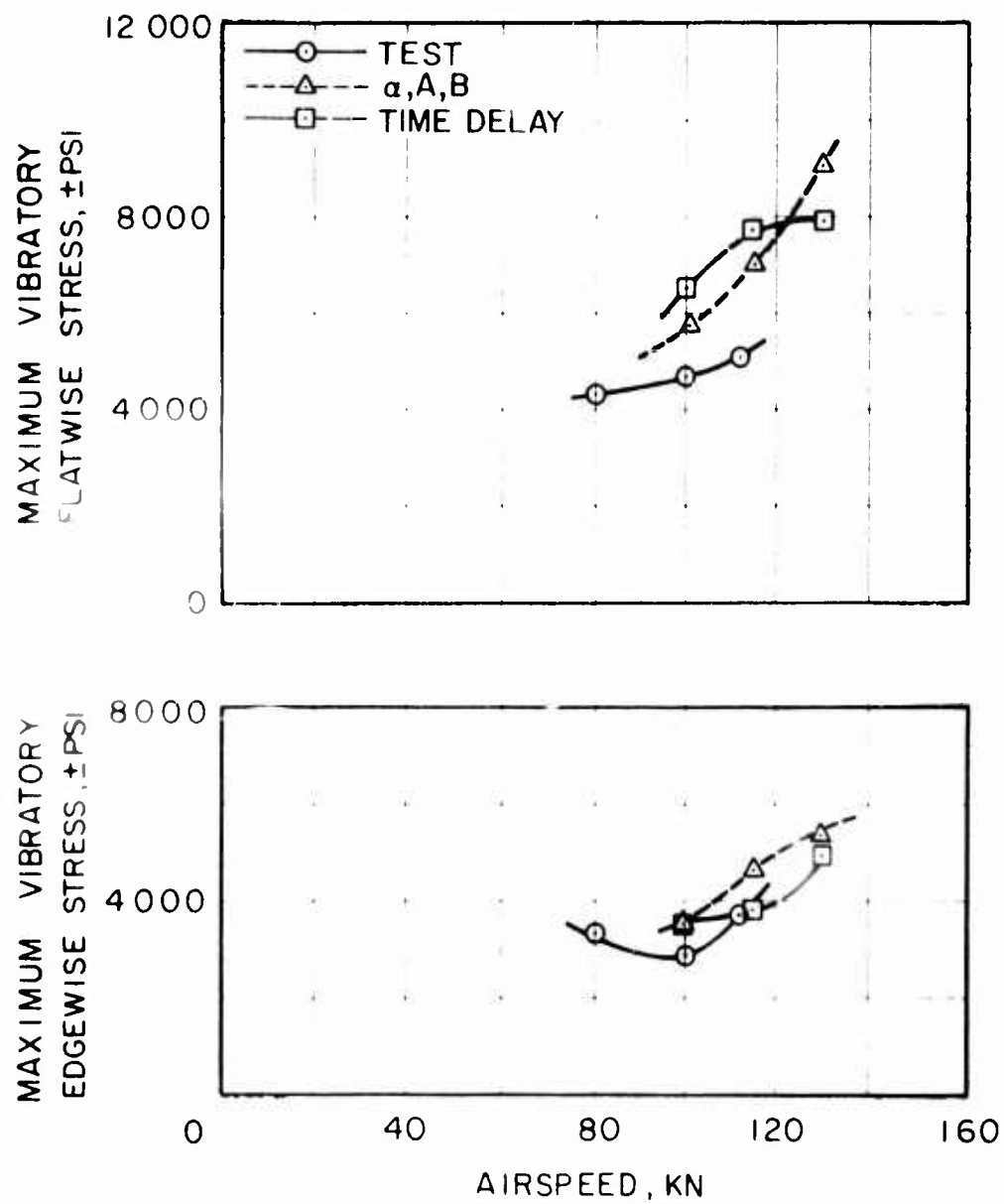


Figure 53. Correlation of CH-54B Maximum Blade Stress at 47,000 Lb Gross Weight.

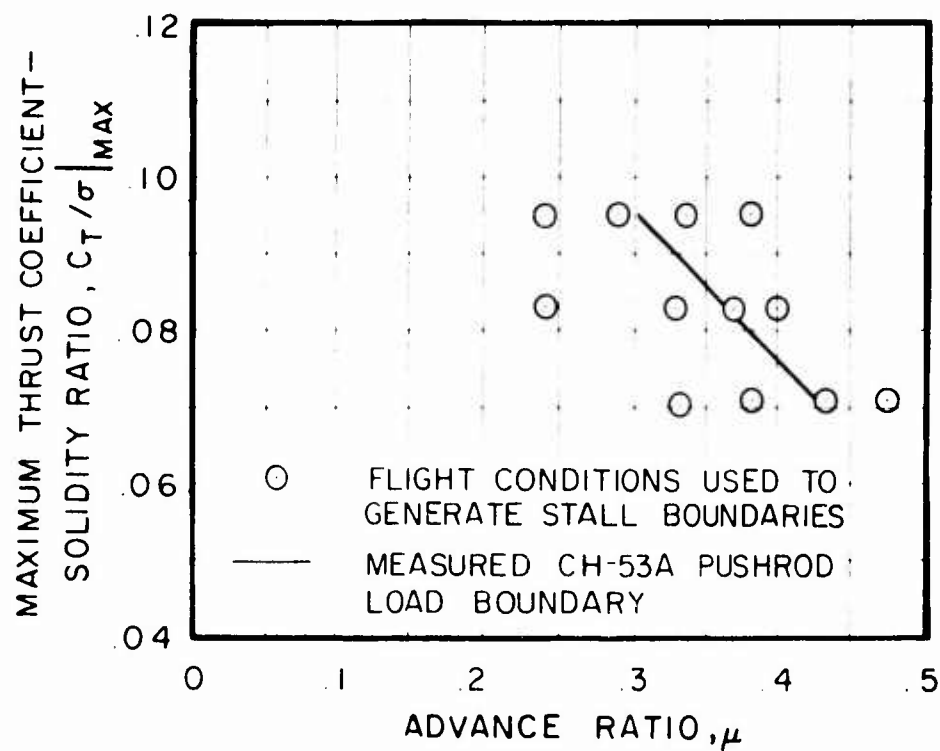


Figure 54. Flight Conditions Used To Generate CH-53A Stall Boundaries.

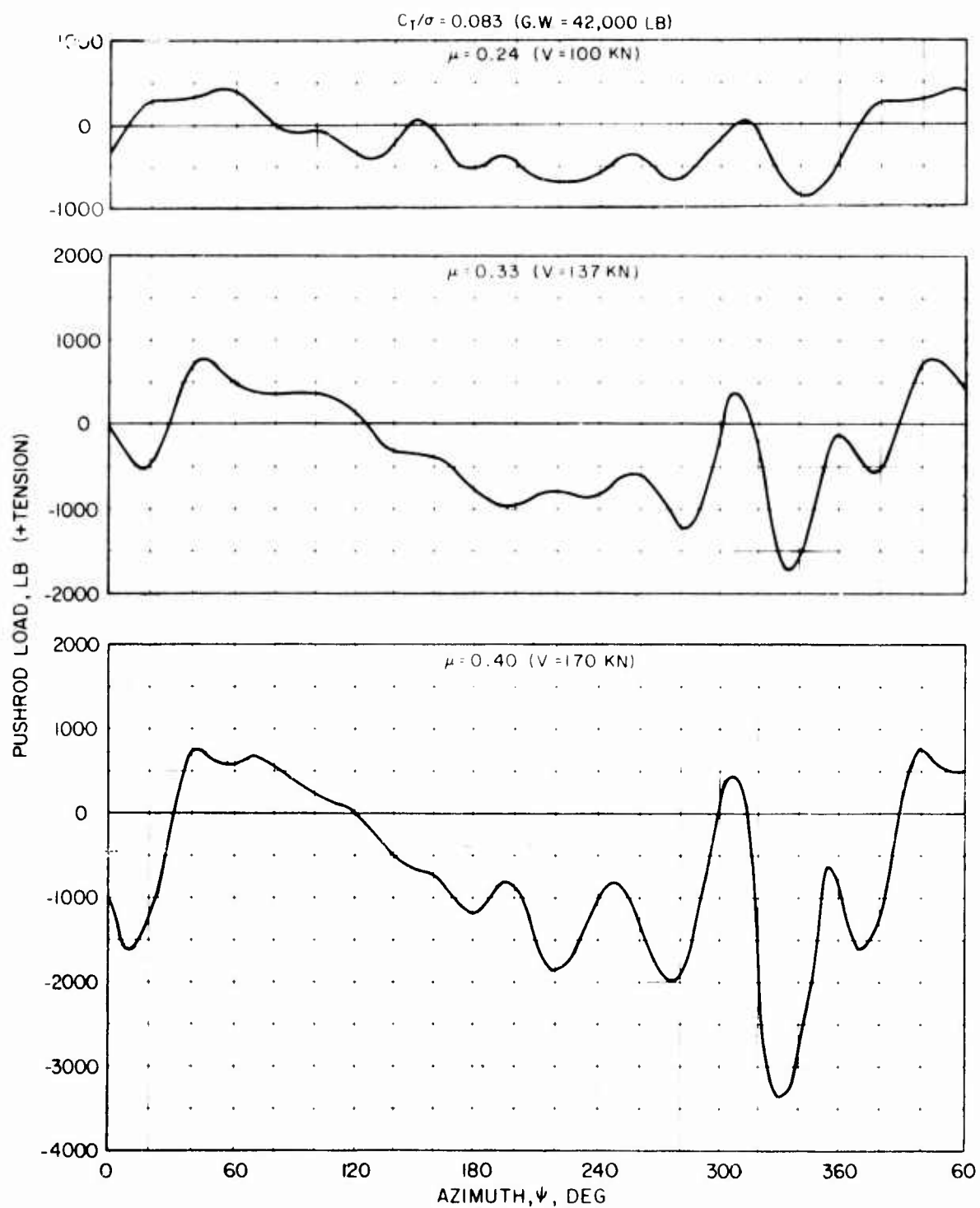


Figure 55. The Buildup of Calculated Pushrod Loads With Airspeed for the CH-53A at $C_T/\sigma = 0.083$.

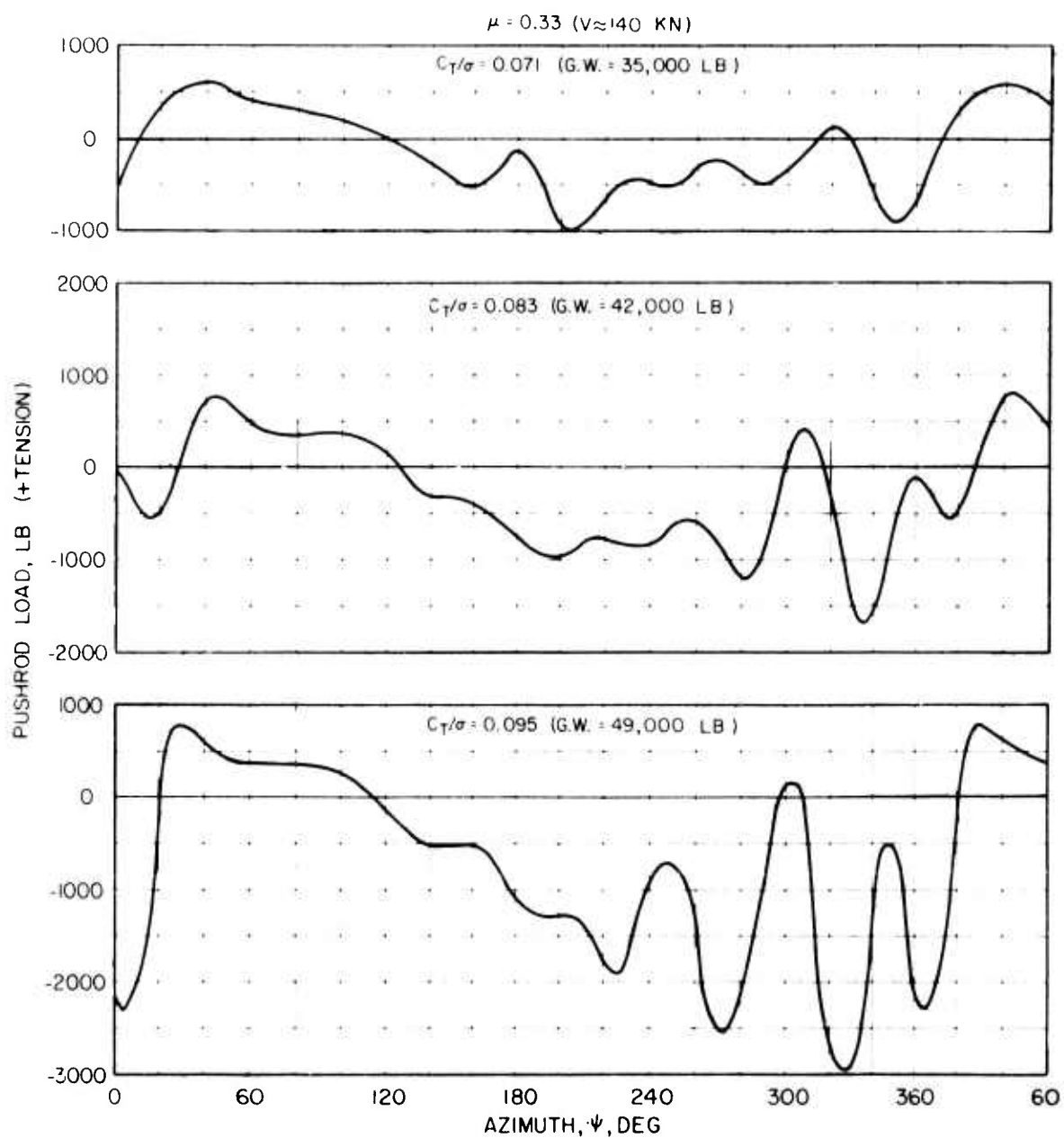


Figure 56. The Buildup of Calculated Pushrod Loads With Thrust Coefficient at $\mu = 0.33$.

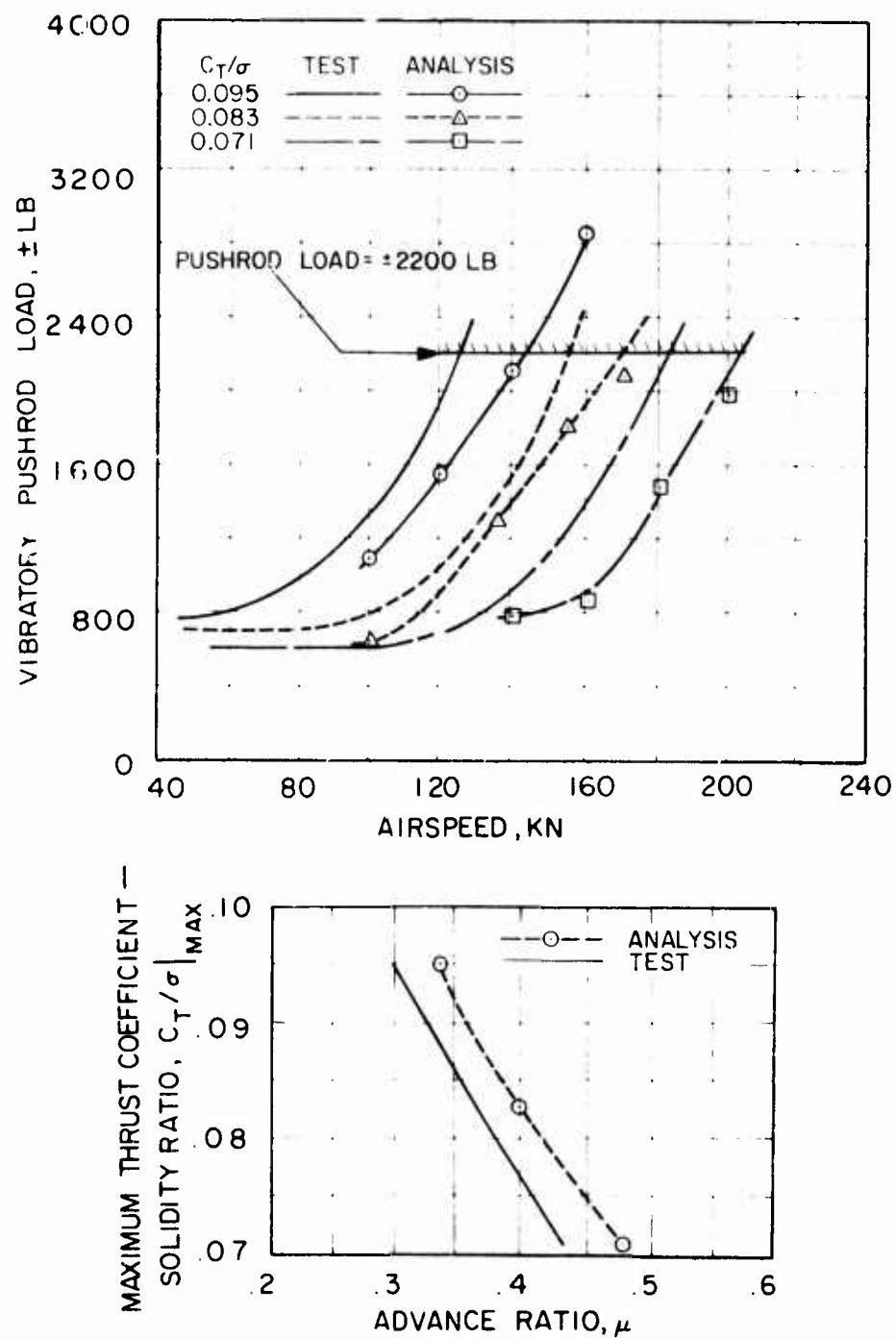


Figure 57. Agreement Between Test and Analytical Pushrod Load Amplitudes and Stall Boundaries for the CH-53A.

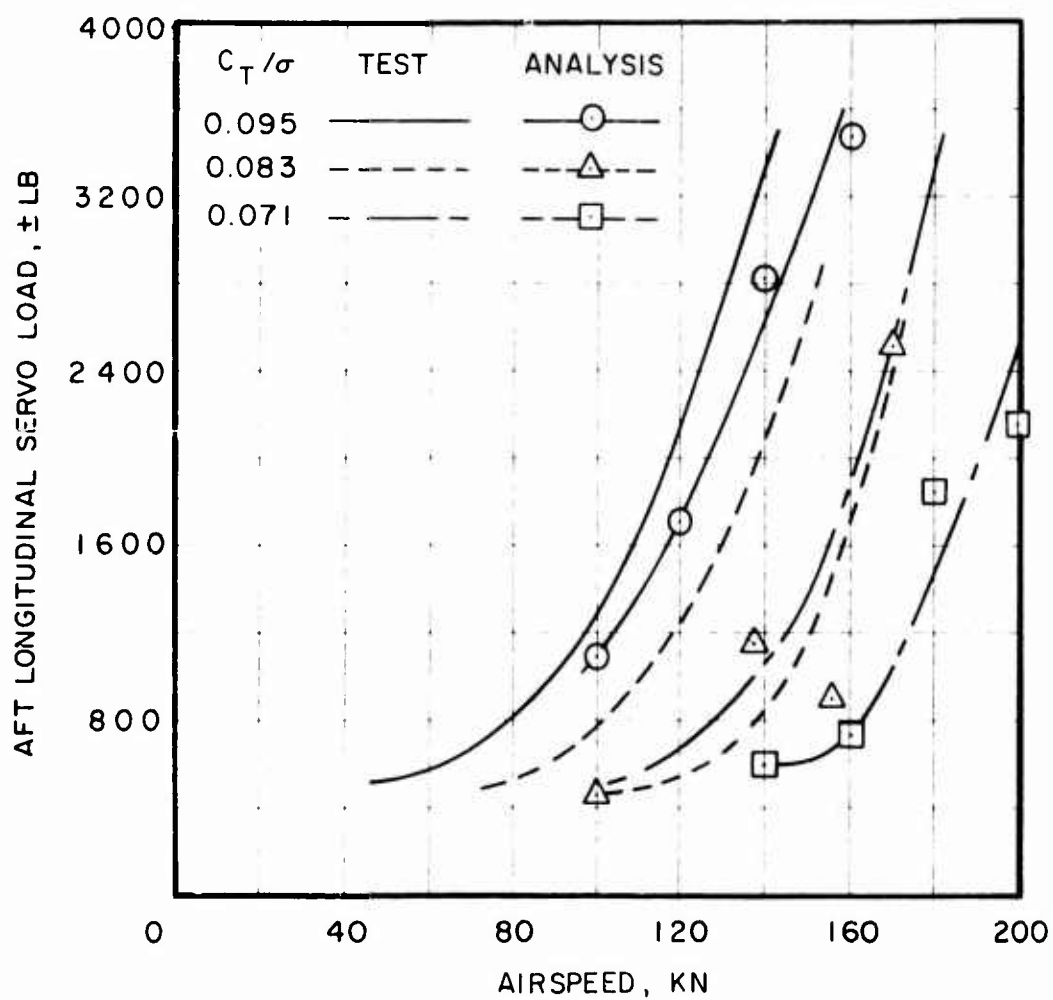


Figure 58. Calculation of CH-53A Fixed System Control Load Amplitudes.

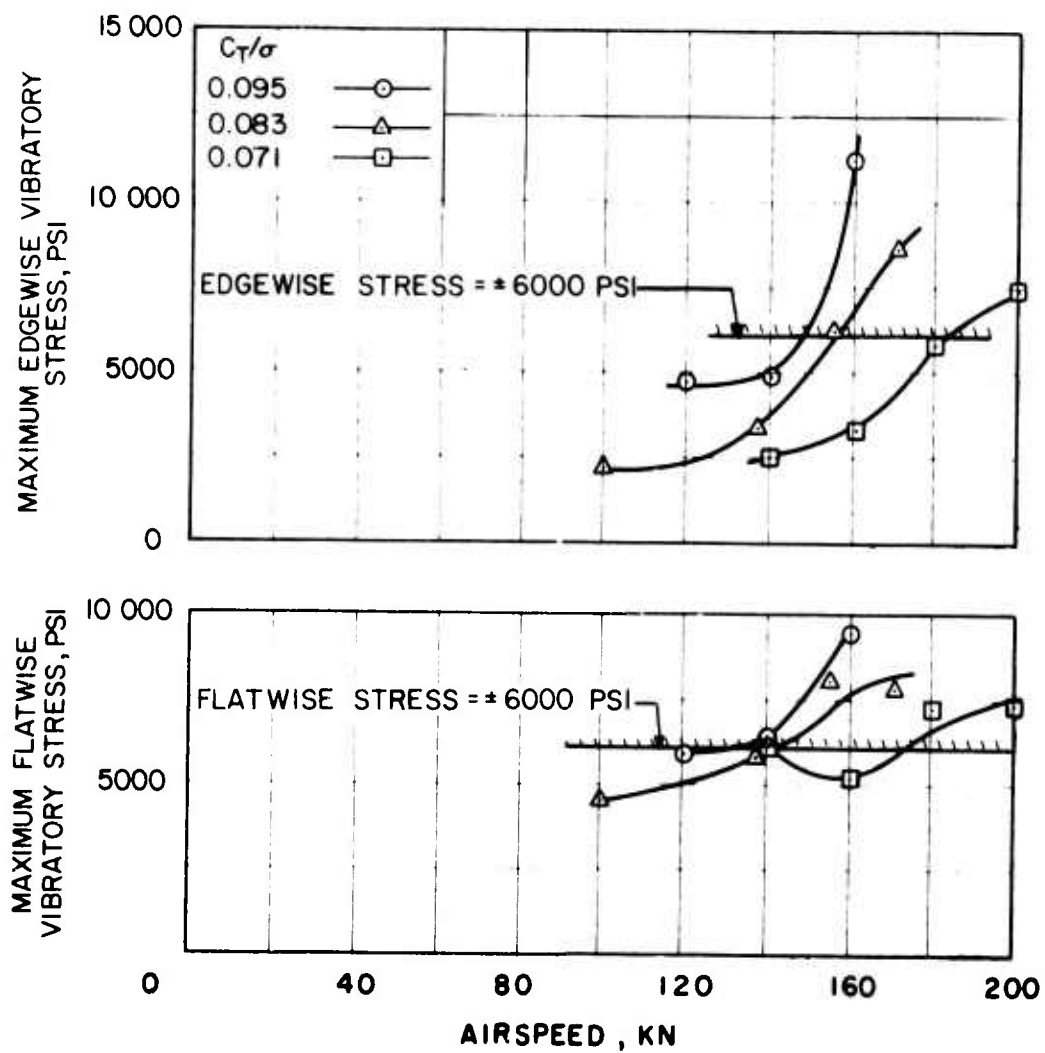


Figure 59. Calculated Buildup of CH-53A Vibratory Blade Stresses.

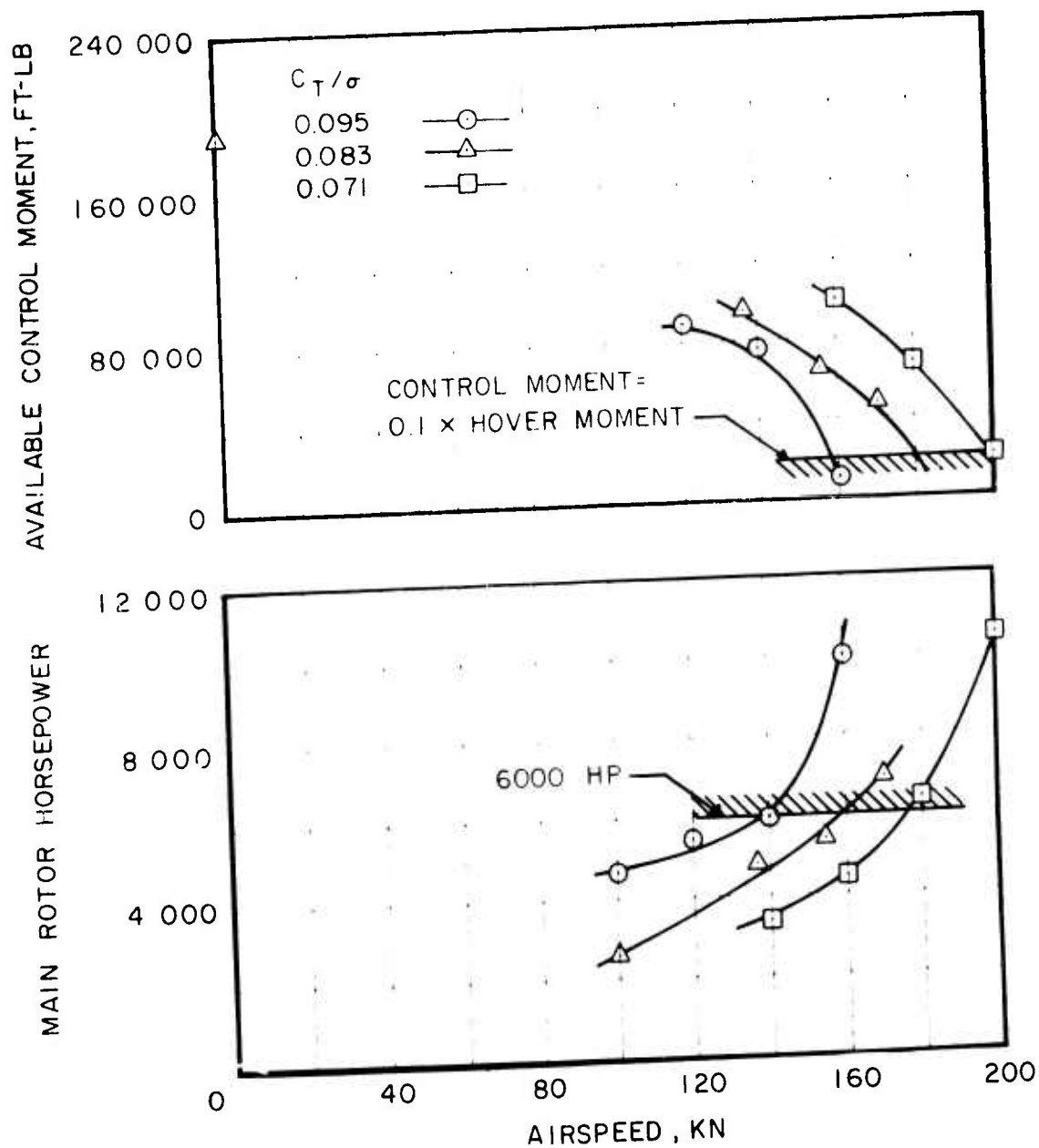


Figure 60. Variation of CH-53A Available Control Moment and Required Power With Airspeed and Thrust Coefficient.

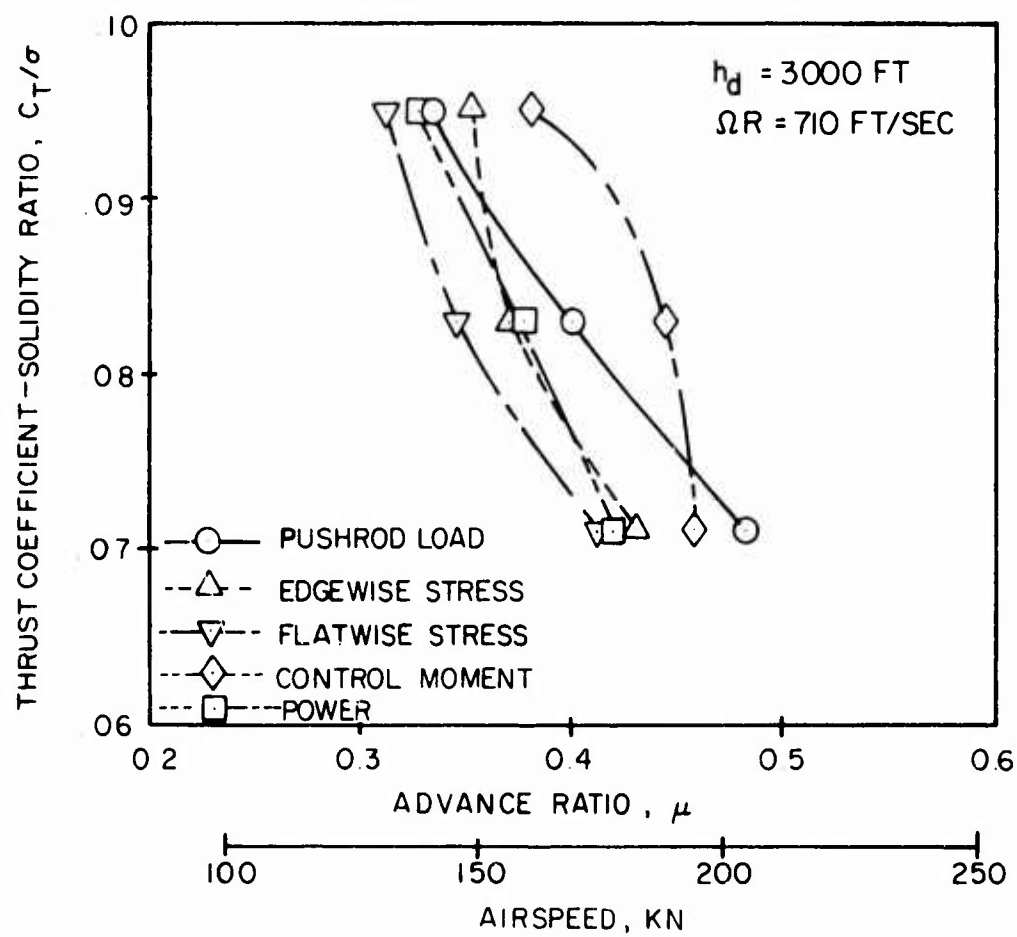


Figure 61. Calculated Stall Boundaries for the CH-53A Rotor.

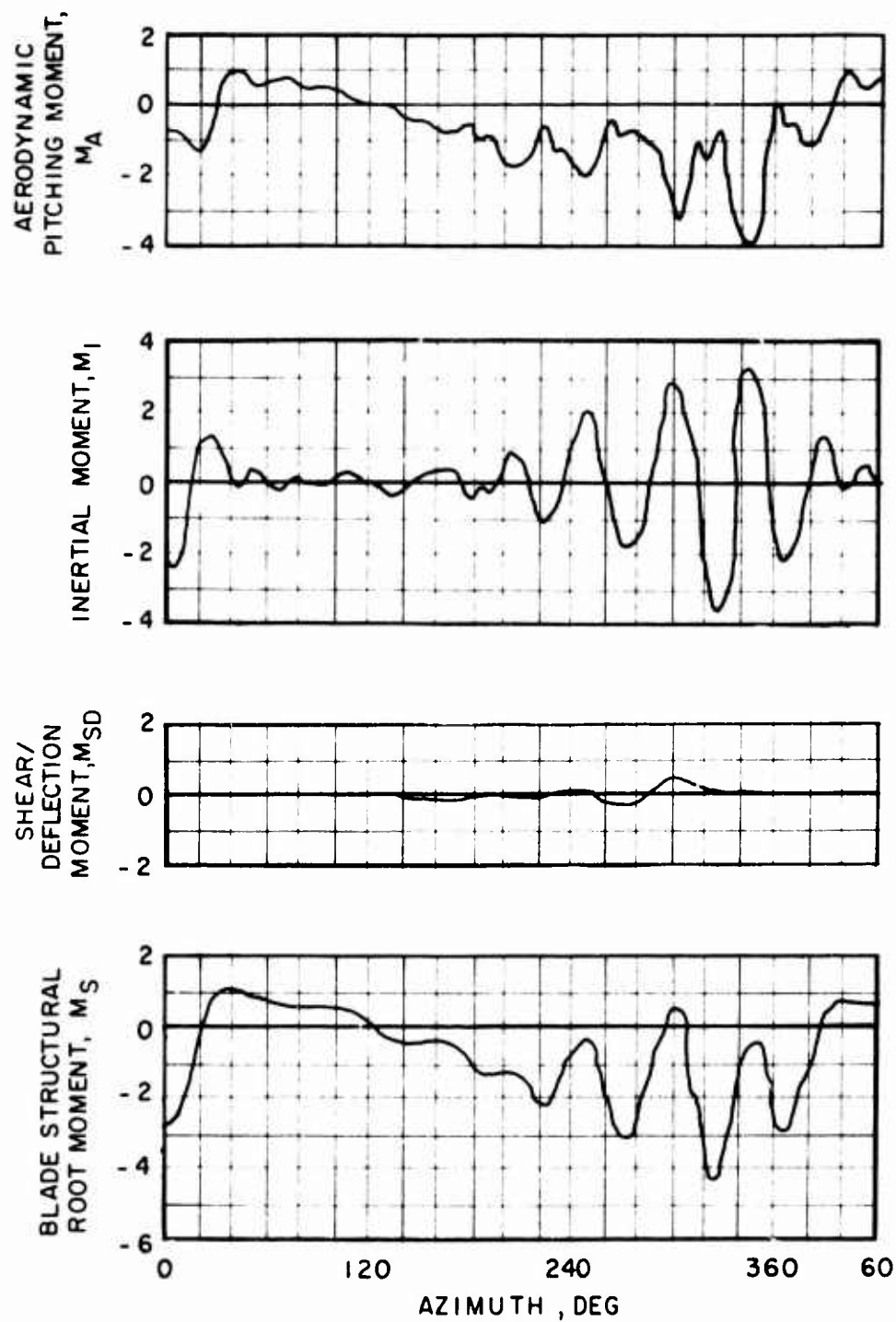


Figure 62. Calculated CH-53A Blade Torsional Moments at 140 Kn and 49,000 lb Gross Weight.

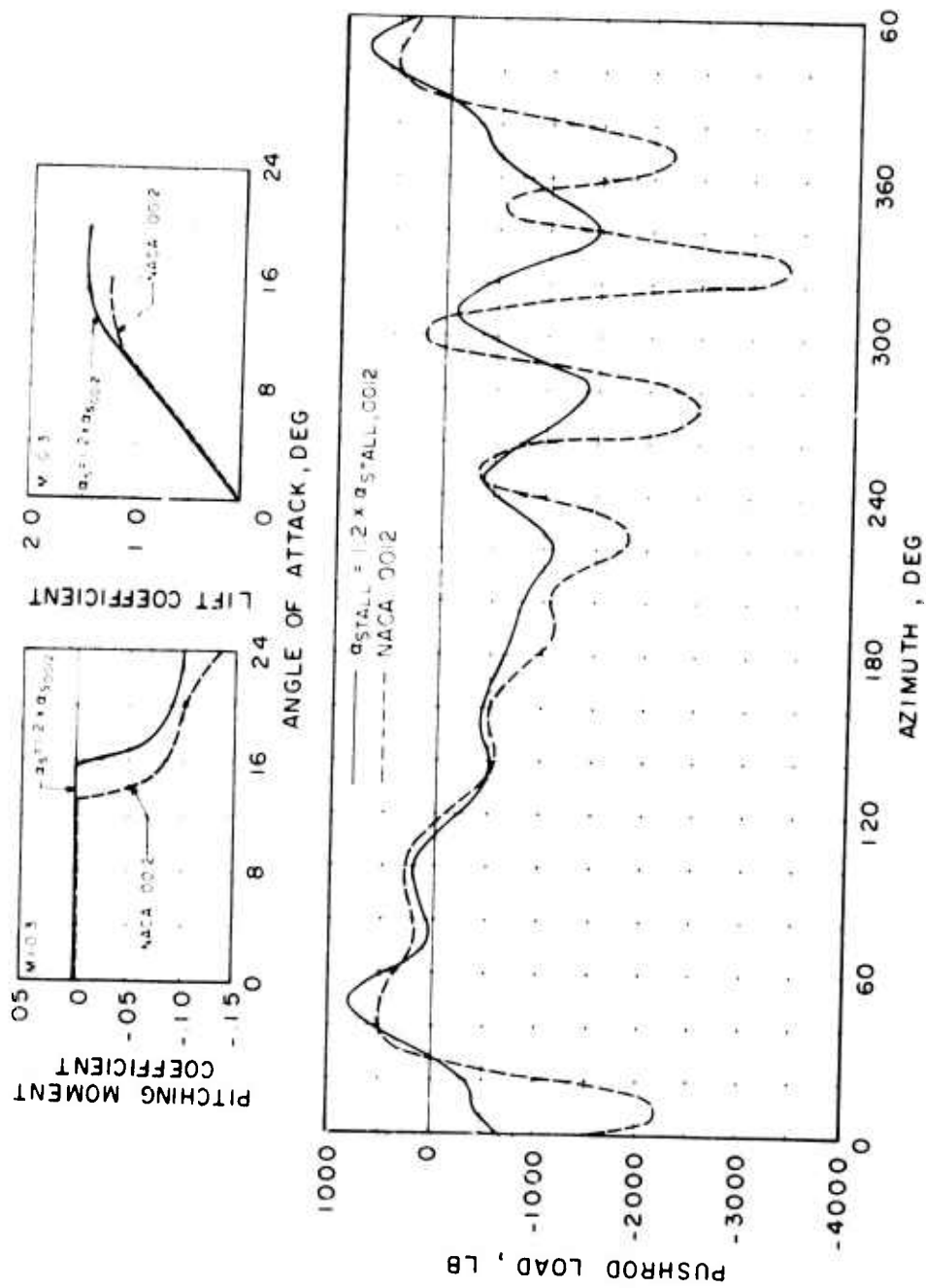


Figure 63. Effect of Increased Airfoil Stall Angle on CH-53A Pushrod Load Time History at 140 Kn and 49,000 Lb Gross Weight.

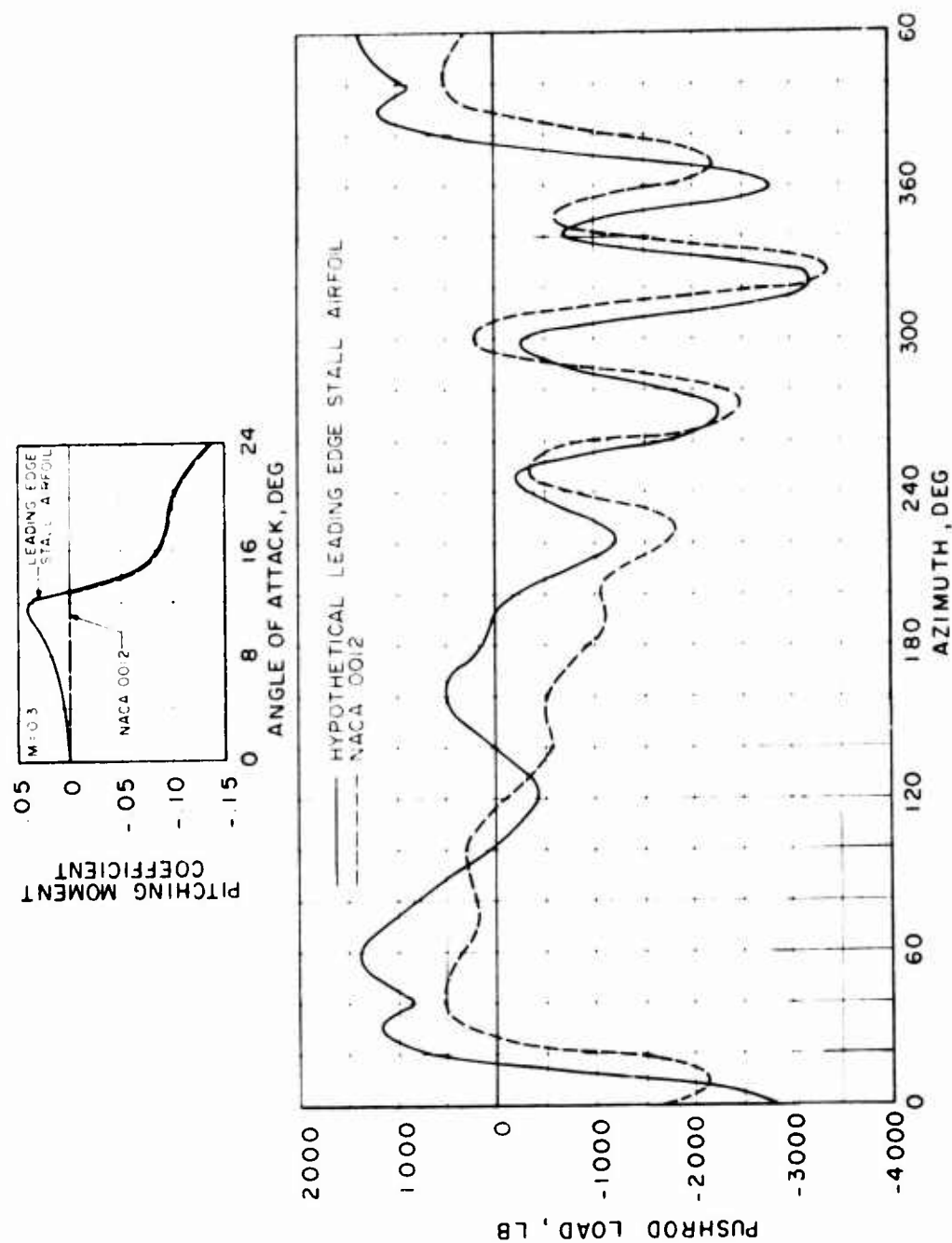


Figure 64. Effect of Airfoil Stall Characteristics on CH-53A Pushrod Load Time History at 140 Kn and 49,000 Lb Gross Weight.

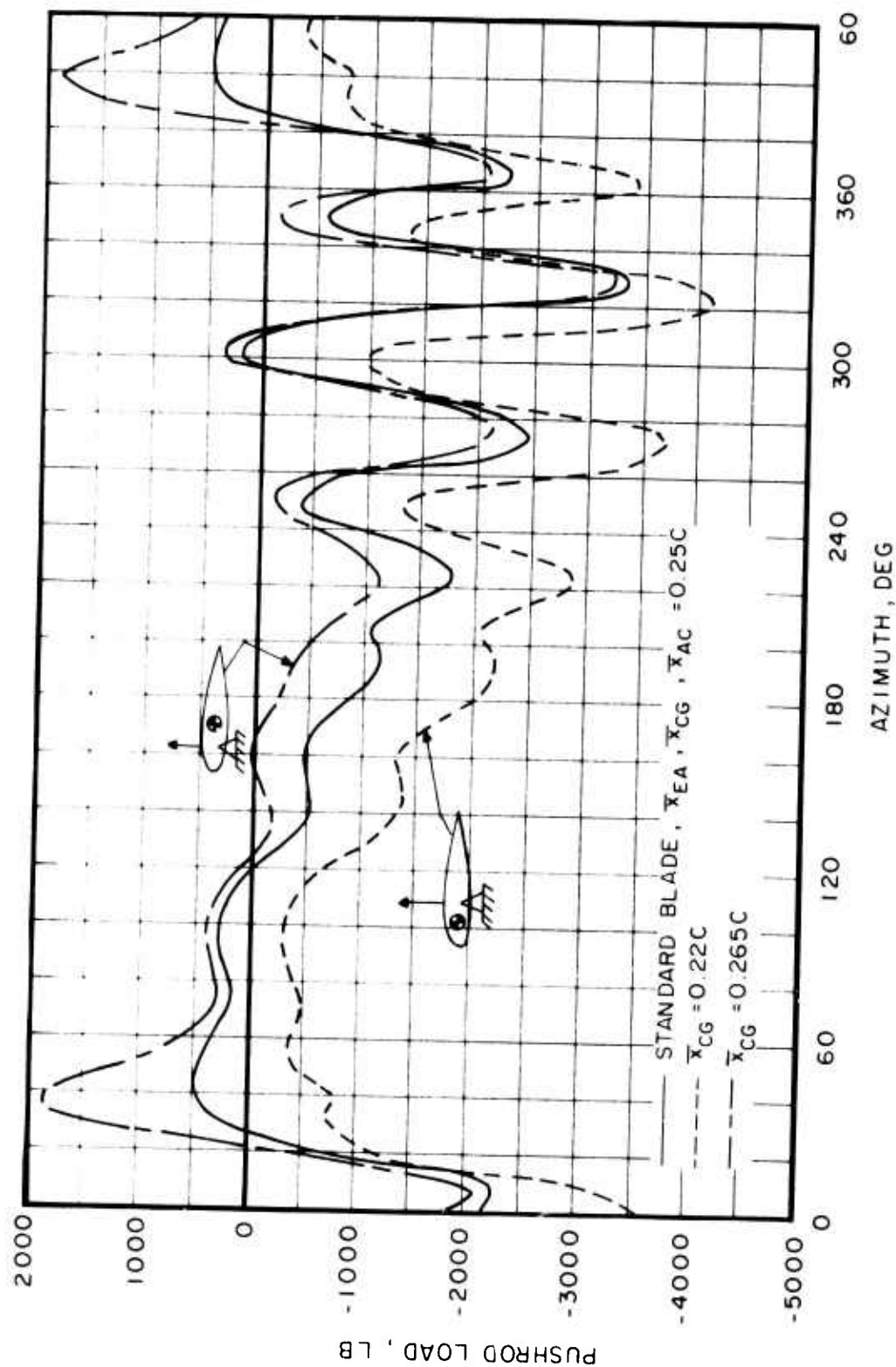


Figure 65. Effect of Blade C.G. Location on CH-53A Pushrod Load Time History at 140 Kn and 49,000 Lb Gross Weight.

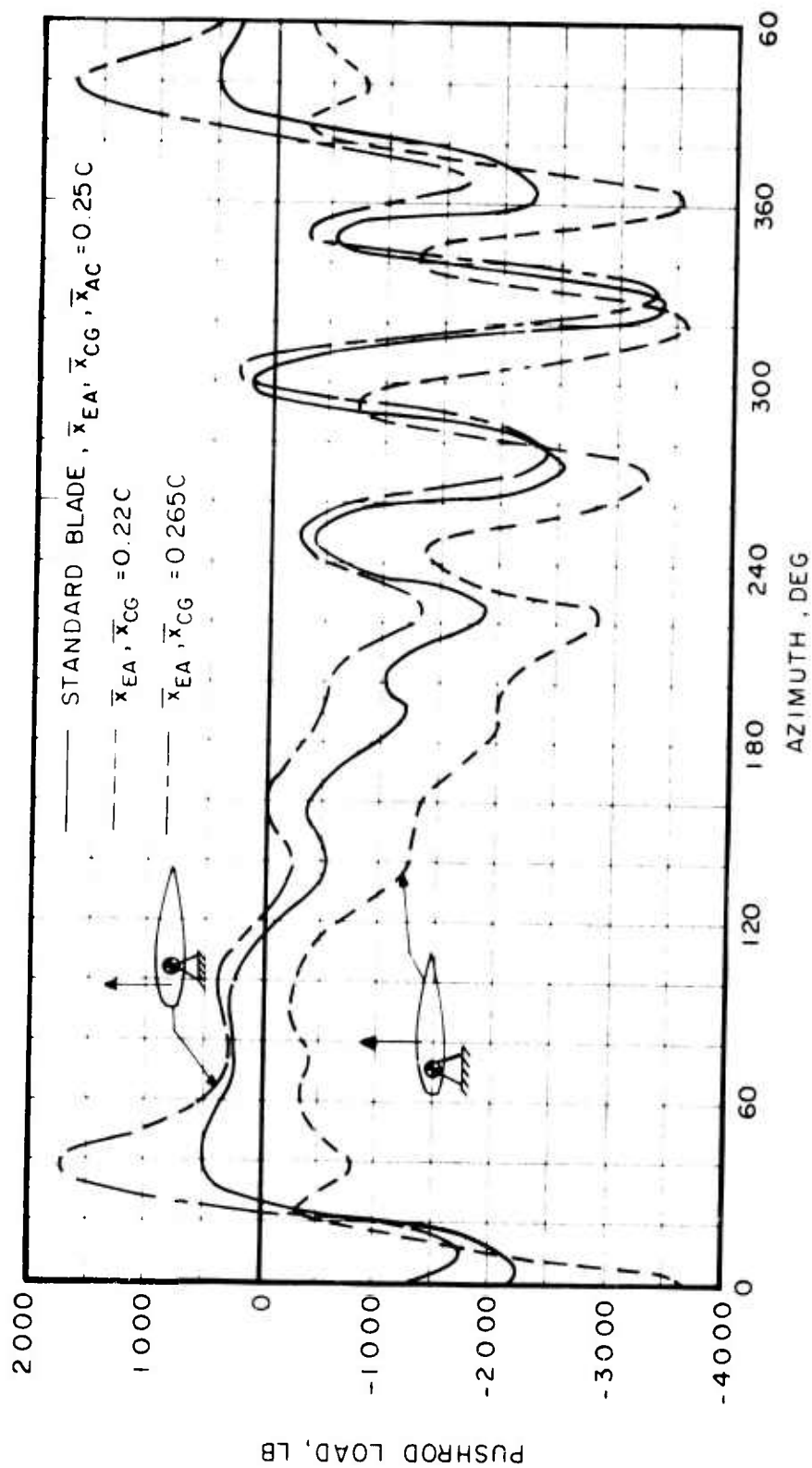


Figure 66. Effect of Displacing Blade Elastic and Center-of-Gravity Axes
From the Aerodynamic Center on the CH-53A Pushrod Load Time History
at 140 Kn and 49,000 Lb Gross Weight.

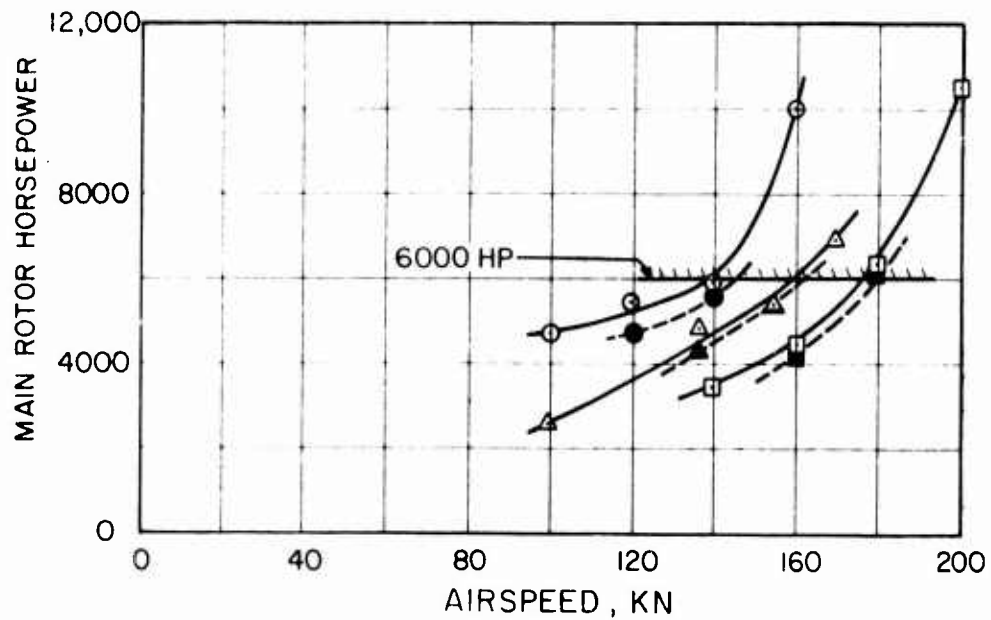
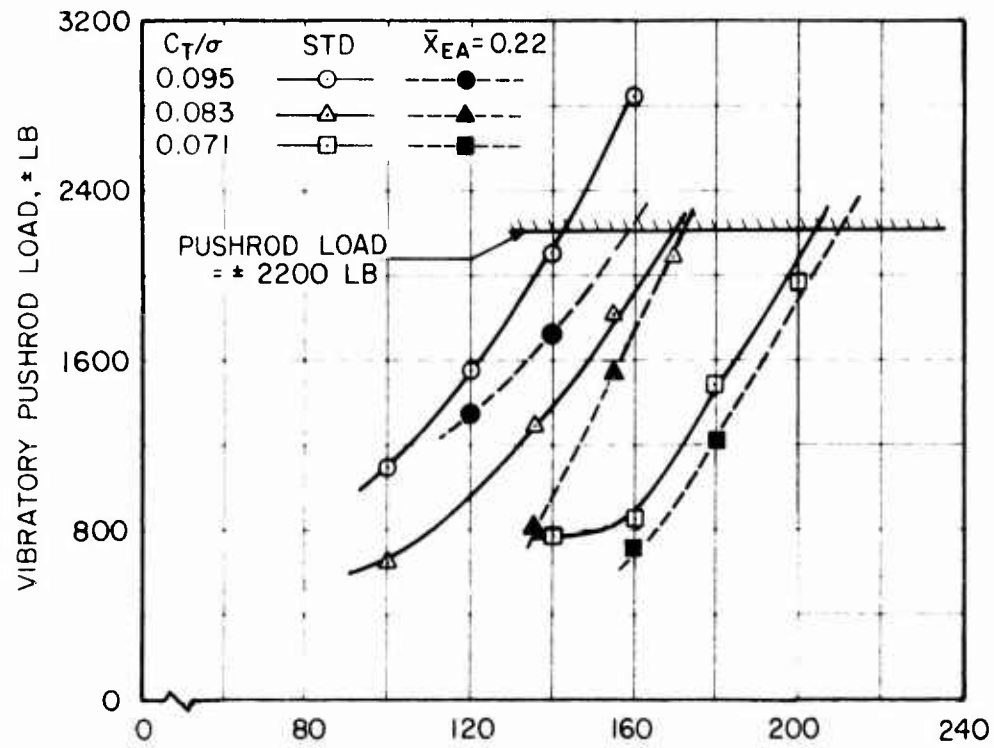


Figure 67. Effect of Forward Movement of Elastic and Center-of-Gravity Axes on CH-53A Vibratory Pushrod Loads and Required Power.

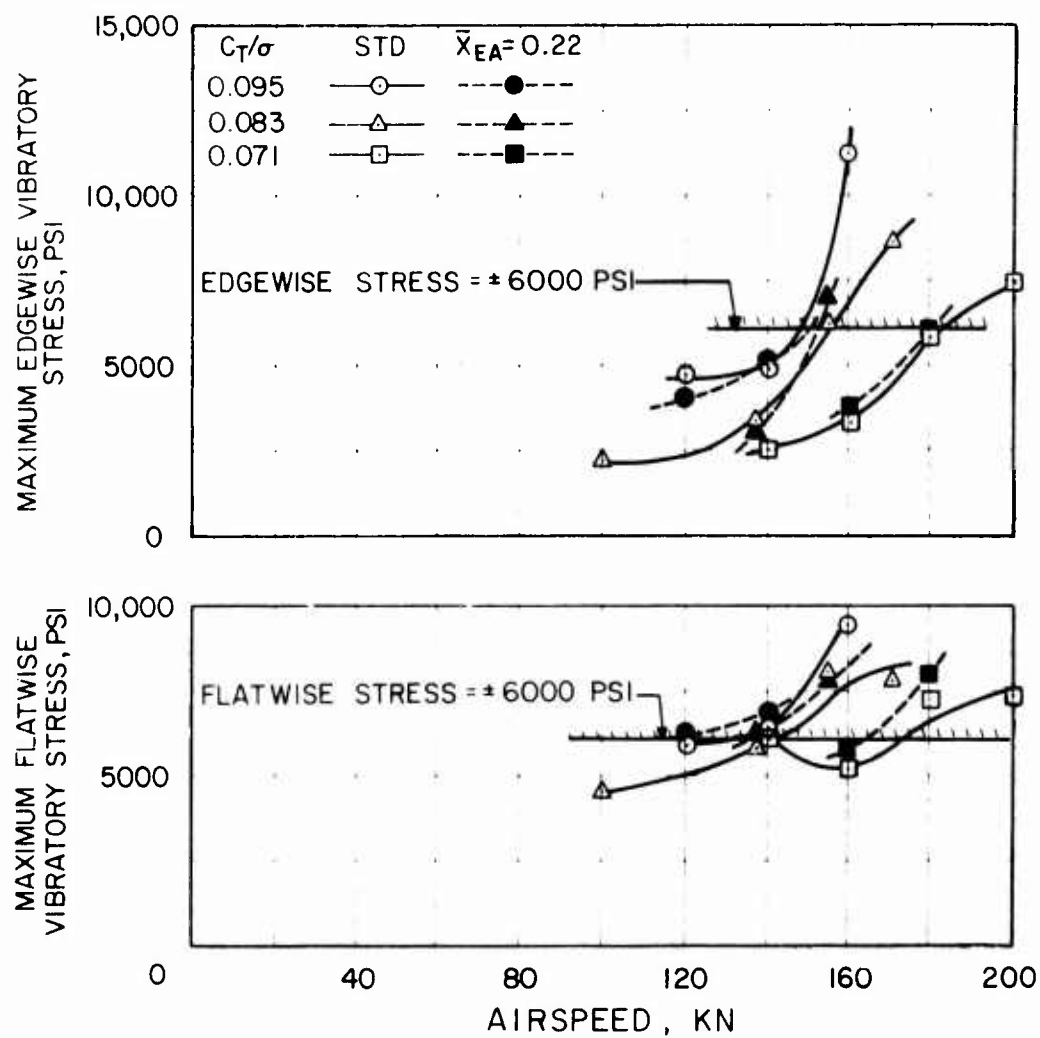


Figure 68. Effect of Forward Movement of Elastic and Center-of-Gravity Axes on CH-53A Vibratory Blade Stresses.

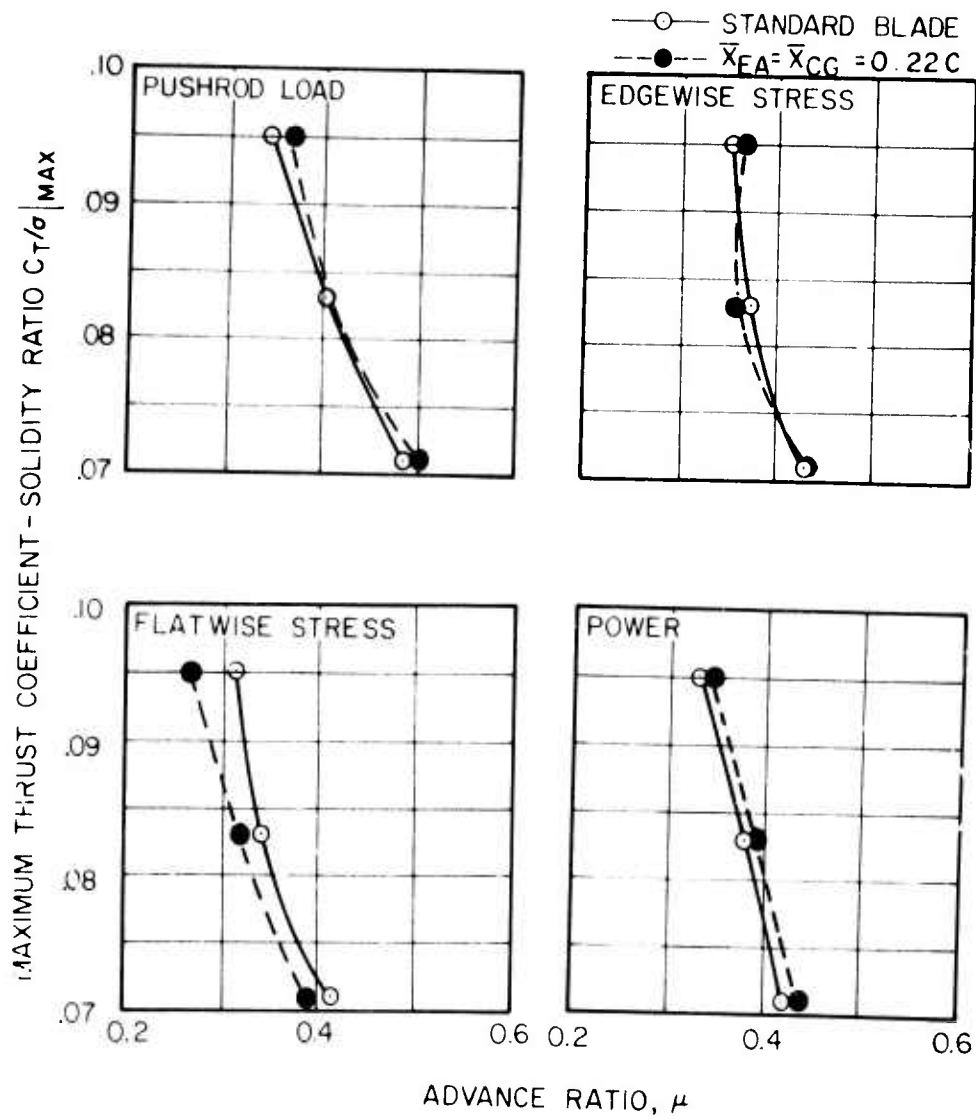


Figure 69. Effect of Forward Movement of Elastic and Center-of-Gravity Axes on CH-53A Stall Boundaries.

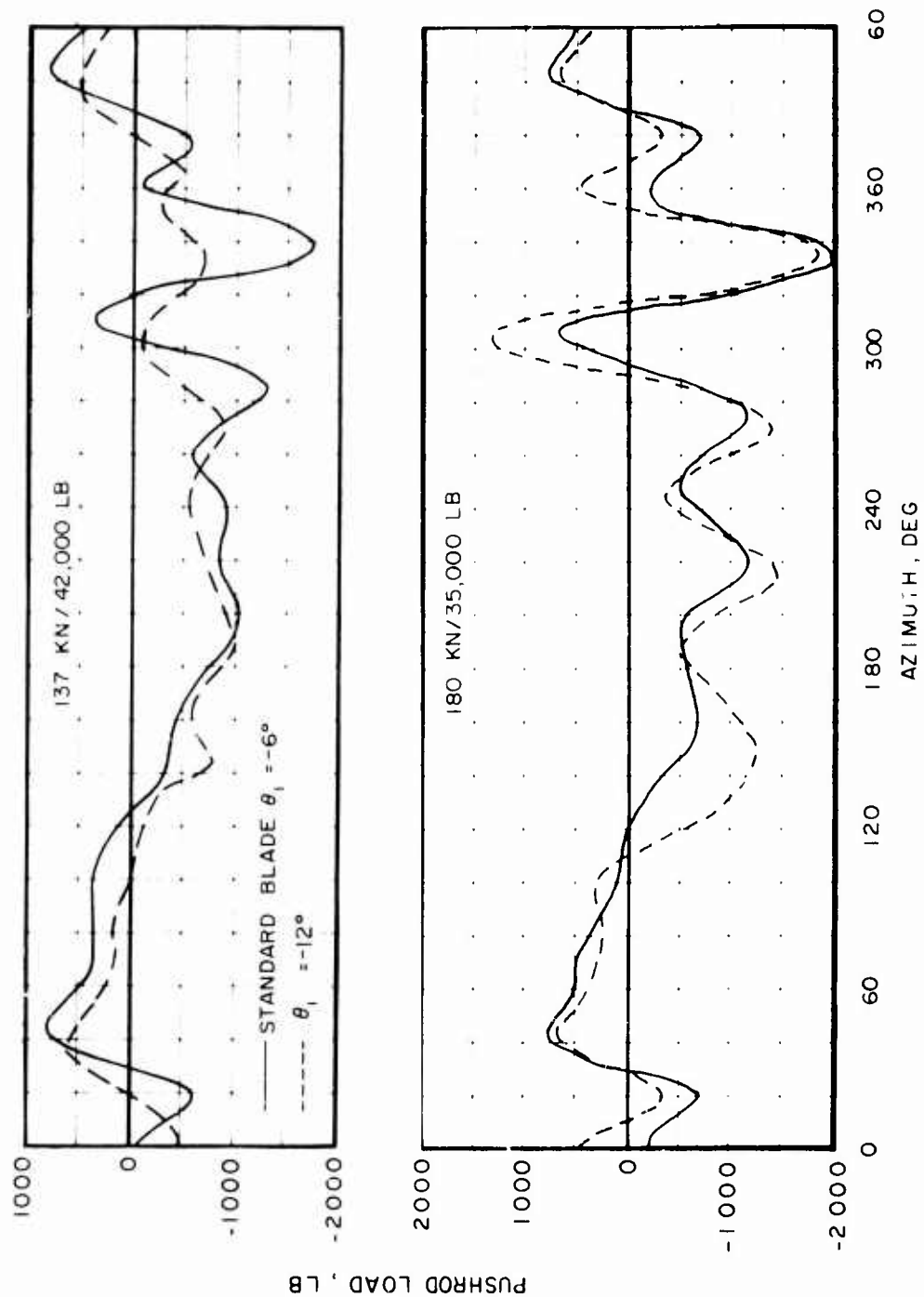


Figure 70. Effect of Increased Blade Twist on CH-53A Pushrod Load Time Histories.

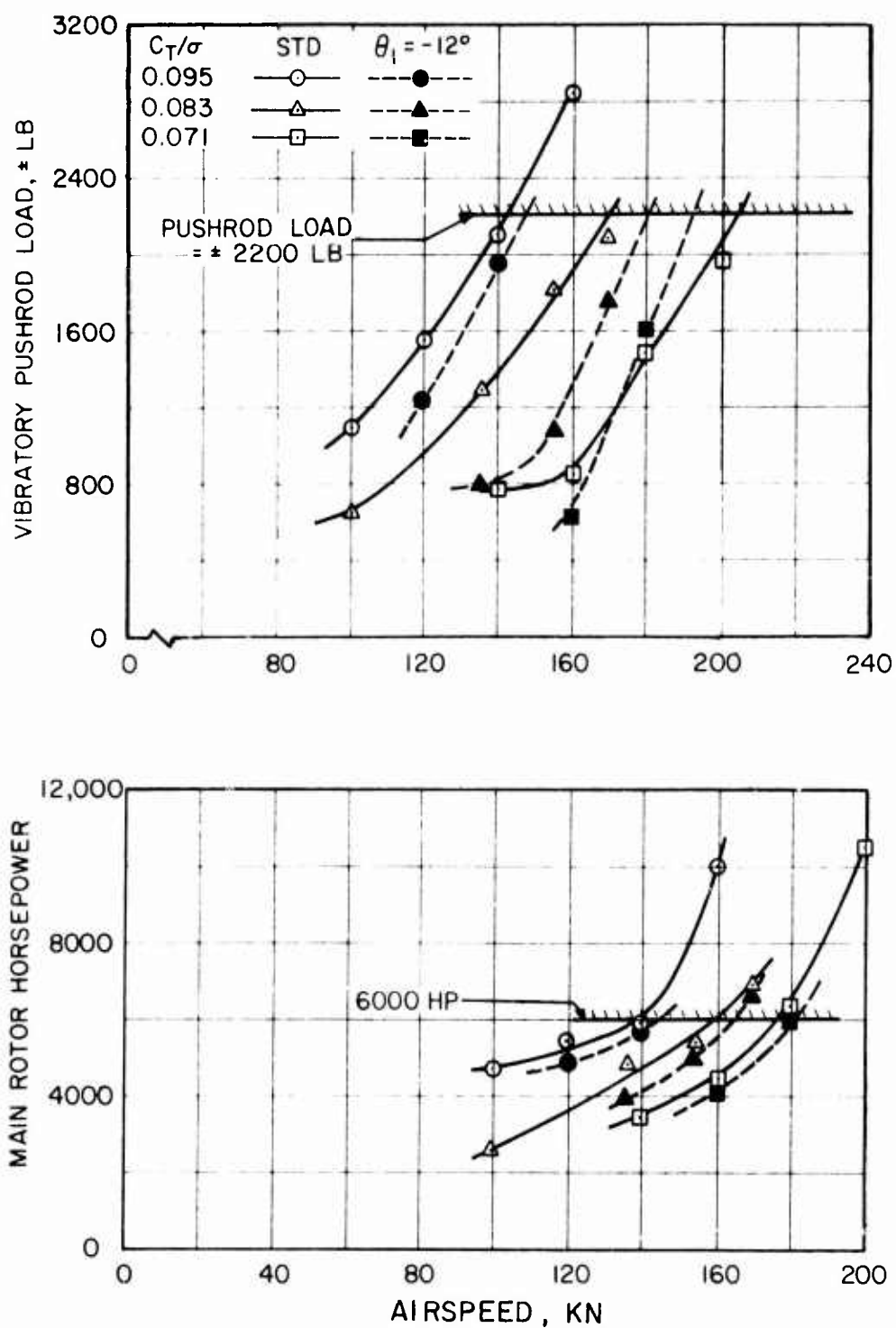


Figure 71. Effect of Increased Blade Twist on CH-53A Vibratory Pushrod Load and Required Power.

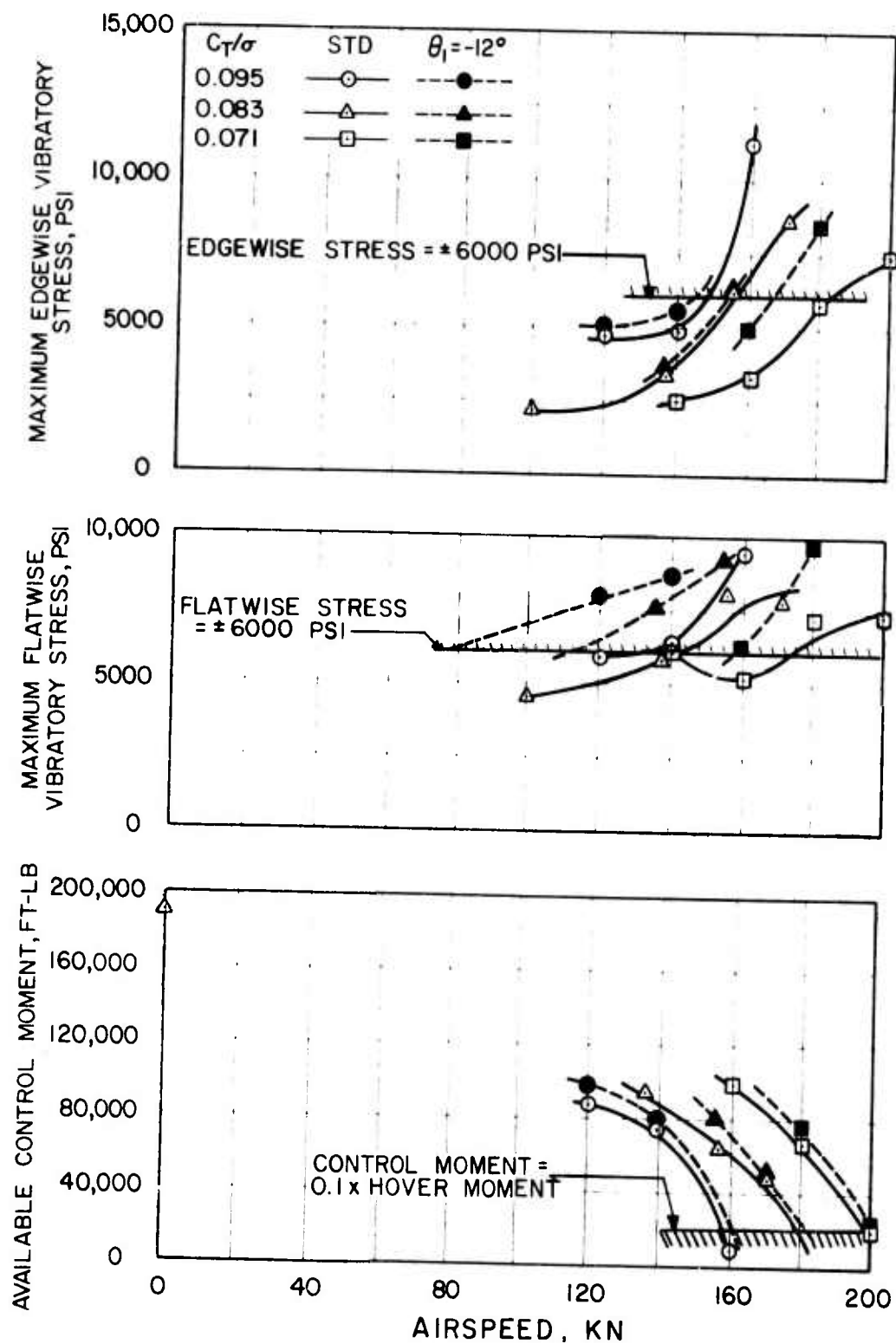


Figure 72. Effect of Increased Blade Twist on CH-53A Blade Stresses and Available Control Moment.

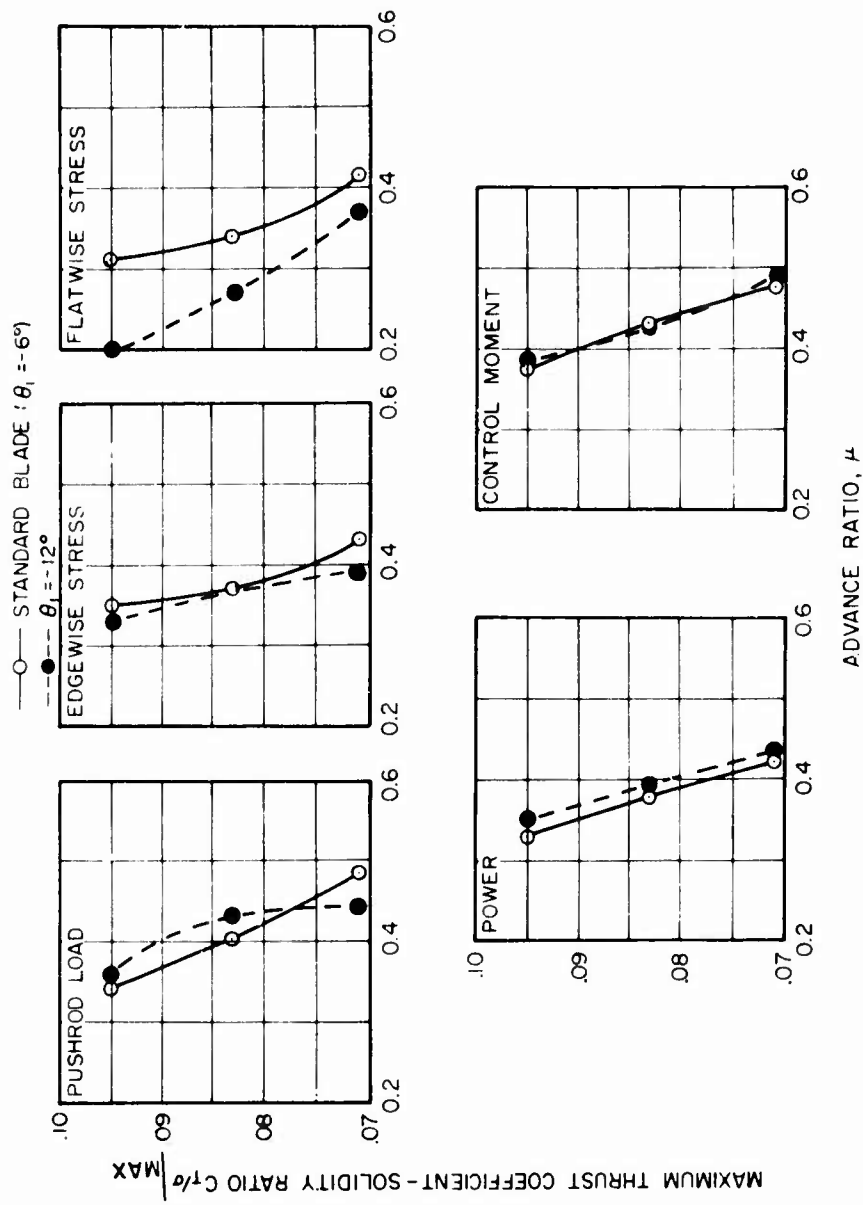


Figure 73. Effect of Increased Blade Twist on CH-53A Stall Boundaries.

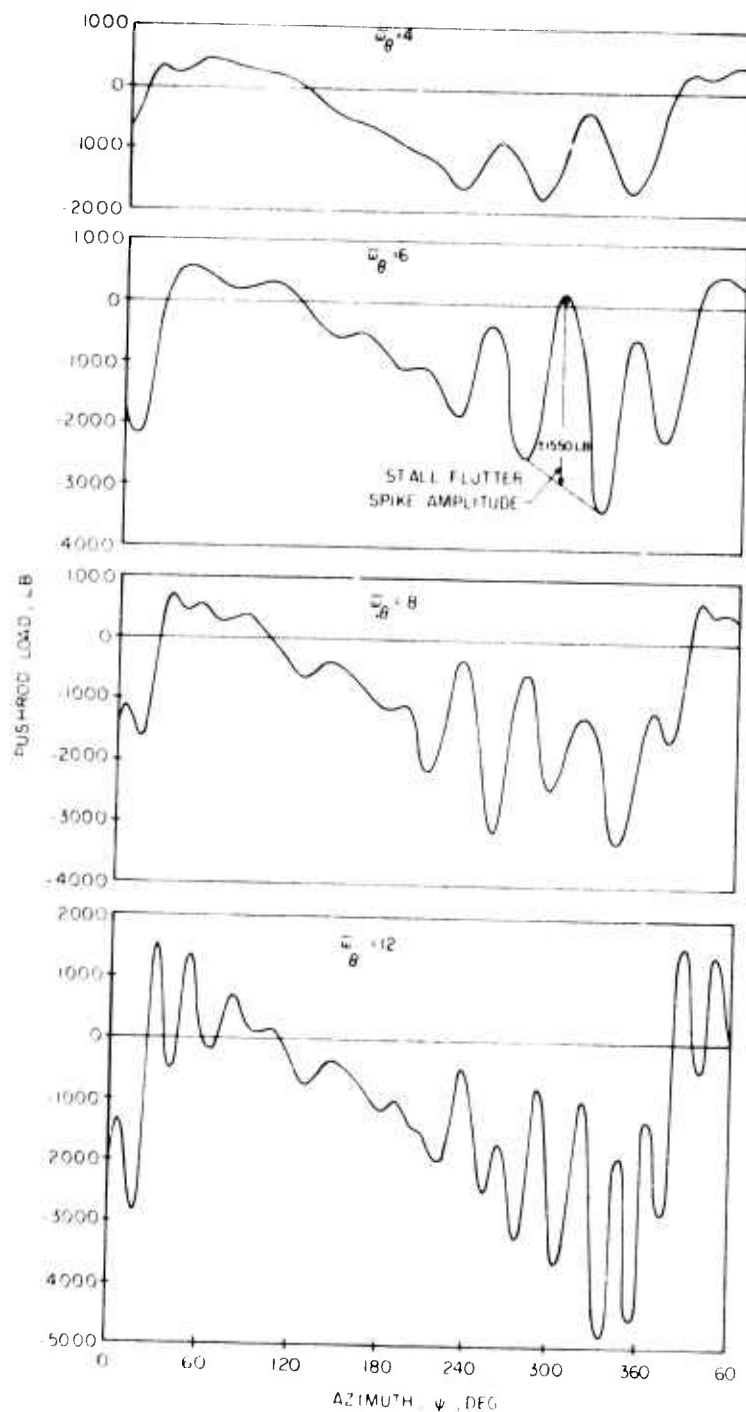


Figure 74. Effect of Torsional Frequency on Calculated CH-53A Pushrod Load Time Histories at 140 Kn and 49,000 Lb Gross Weight.

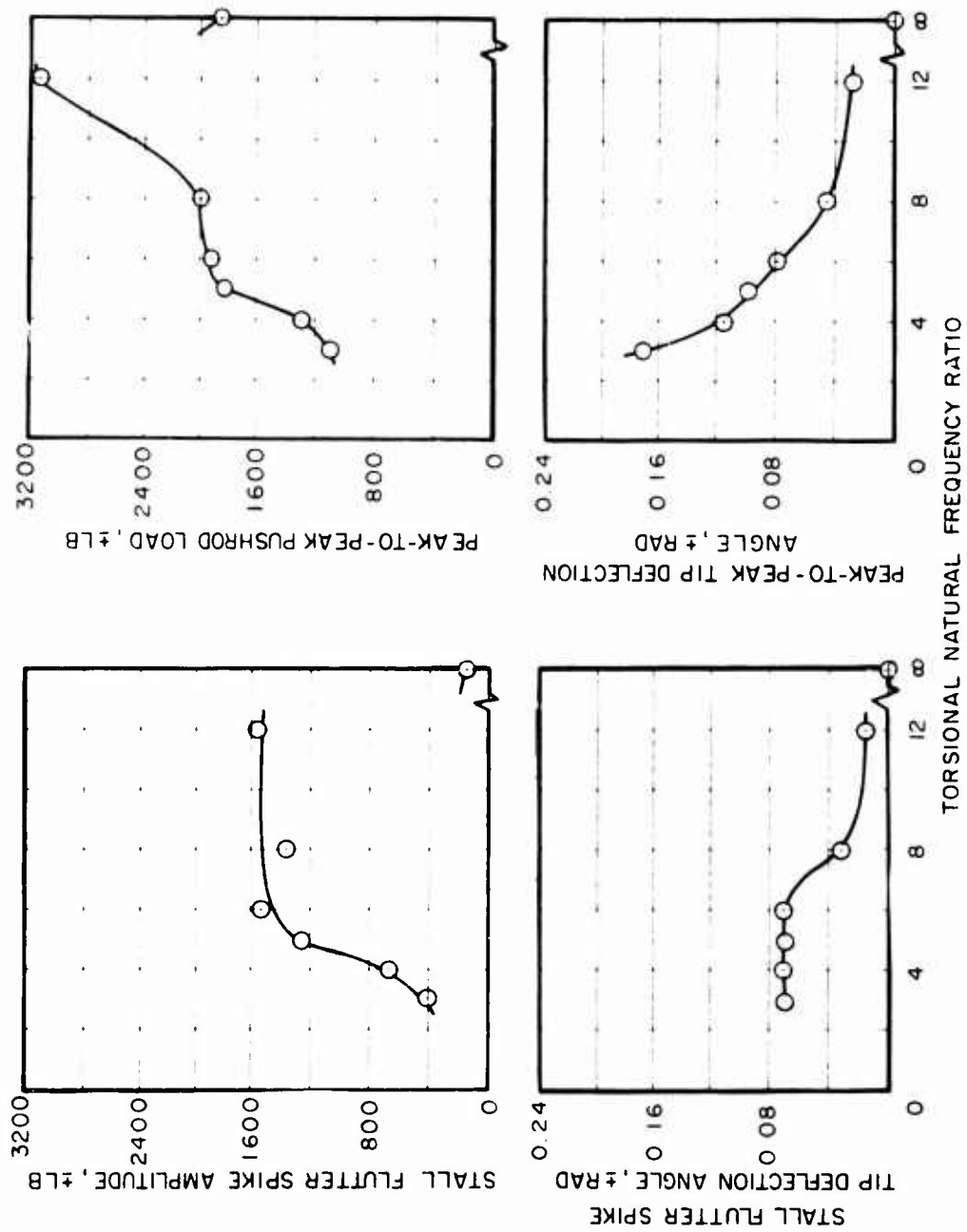


Figure 75. Variation of Stall Flutter Pushrod Load and Elastic Tip Deflection Amplitudes for the CH-53A at 140 Kn and 49,000 lb Gross Weight.

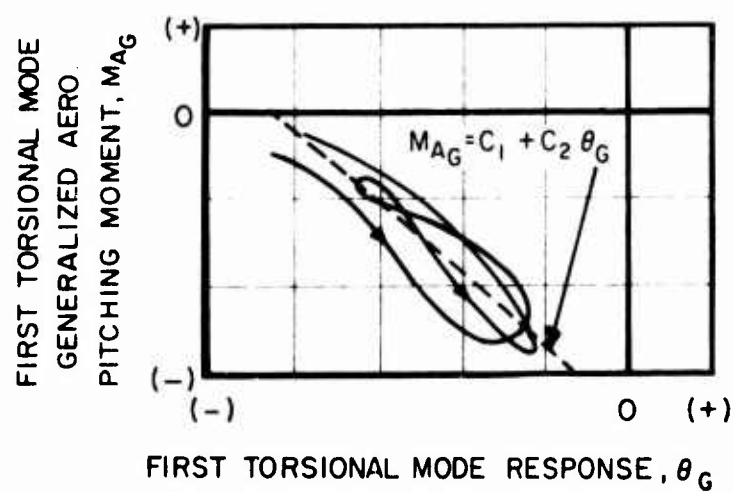
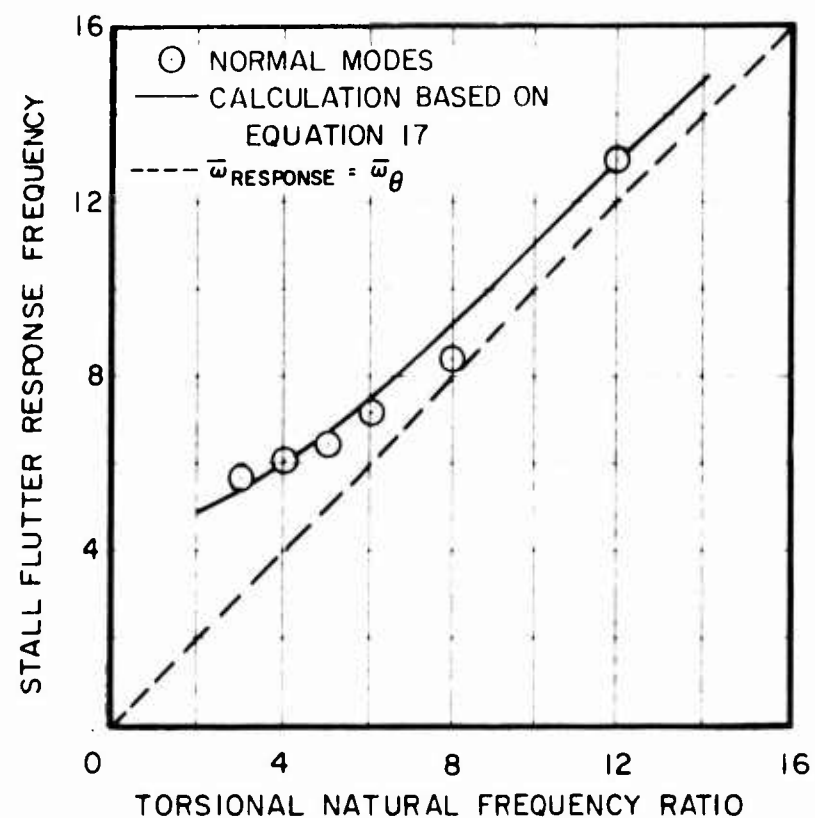
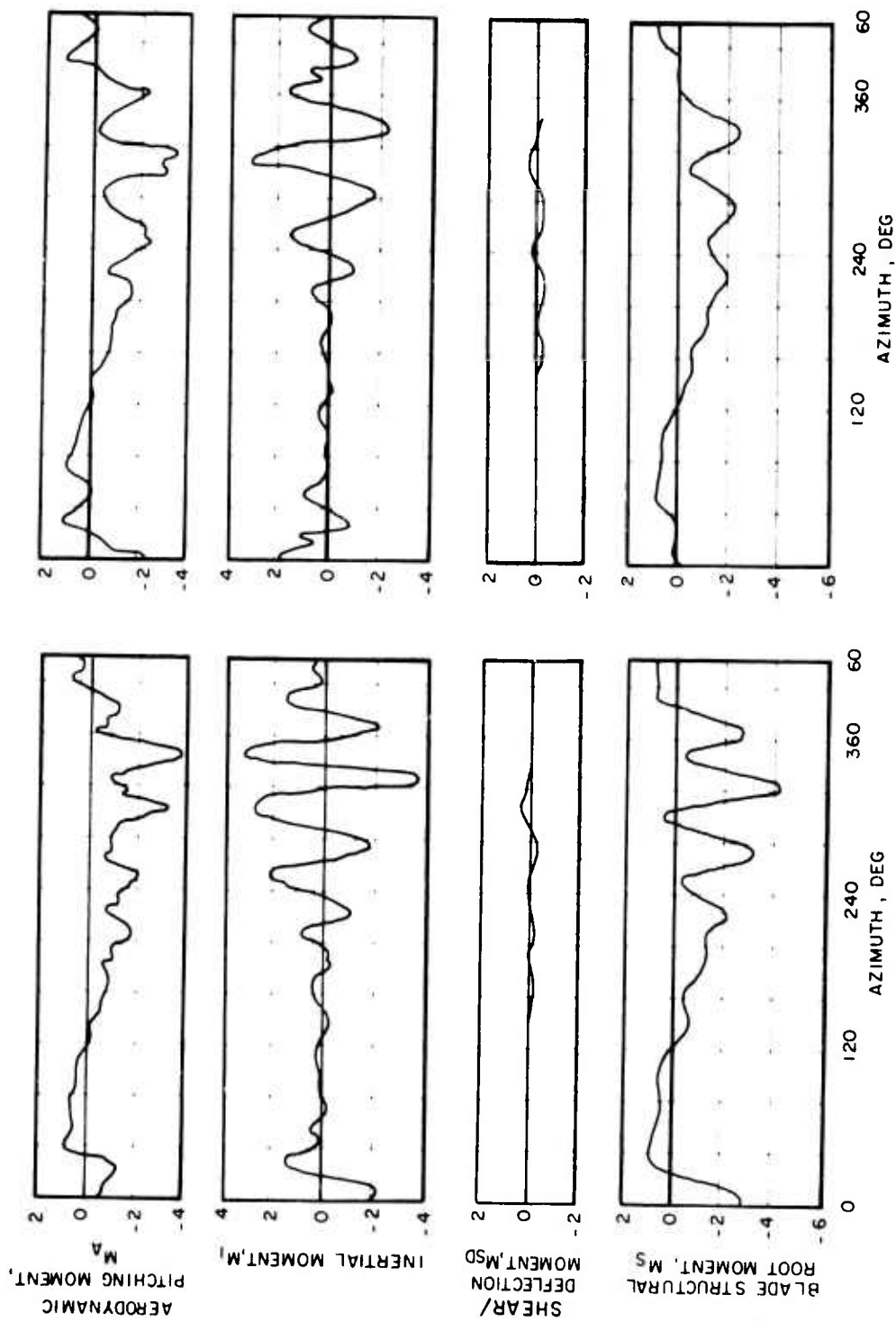


Figure 76. Variation of Torsional Response Frequency With Natural Frequency.



a) STANDARD BLADE, $\bar{\omega}_\theta = 6.0$

b) $\bar{\omega}_\theta = 4.0$

Figure 77. Effect of Decreasing Torsional Natural Frequency on Calculated CH-53A Torsional Moments at 140 Kn and 49,000 lb Gross Weight.

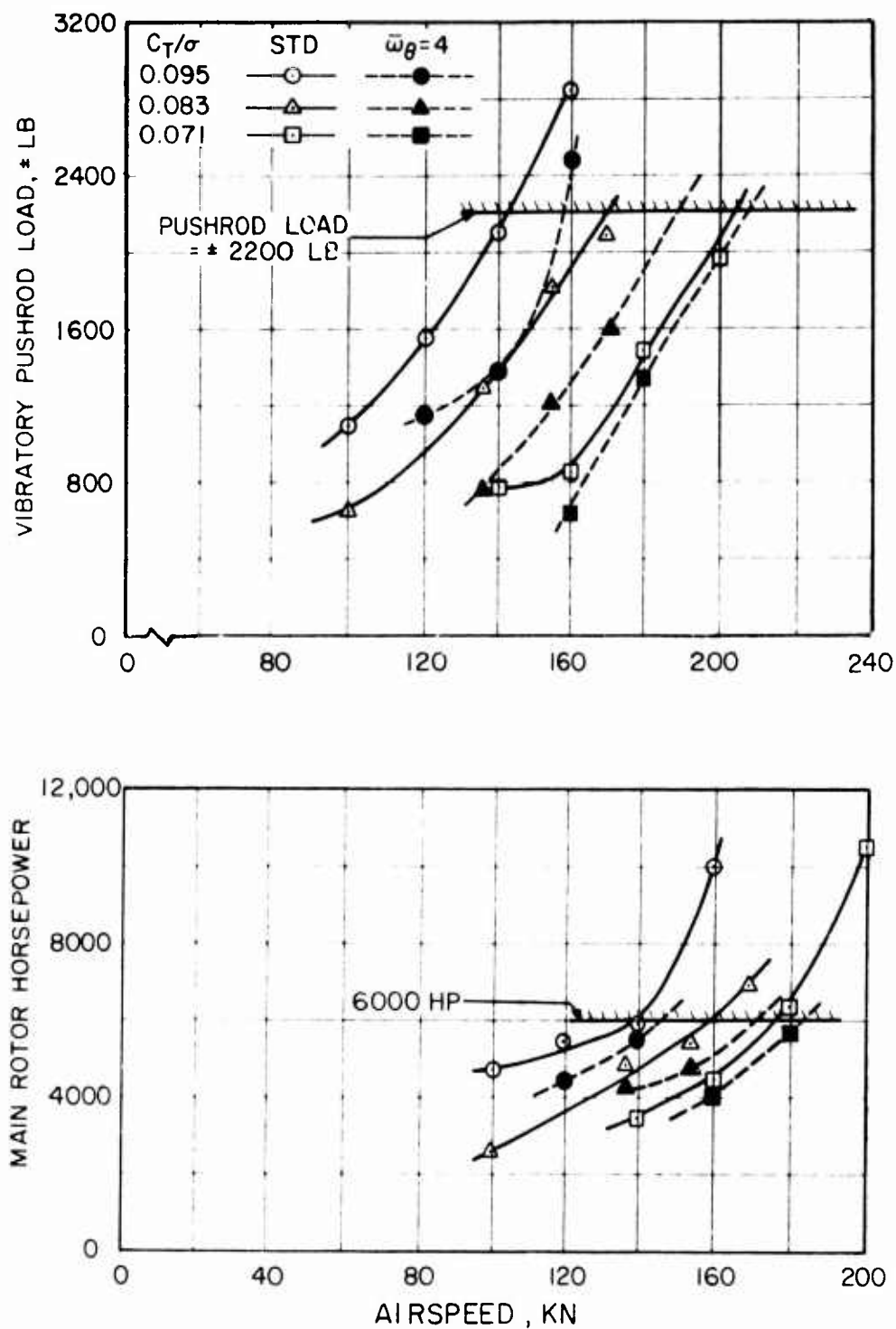


Figure 78. Effect of Reducing Torsional Natural Frequency on CH-53A Vibratory Pushrod Load and Required Power.

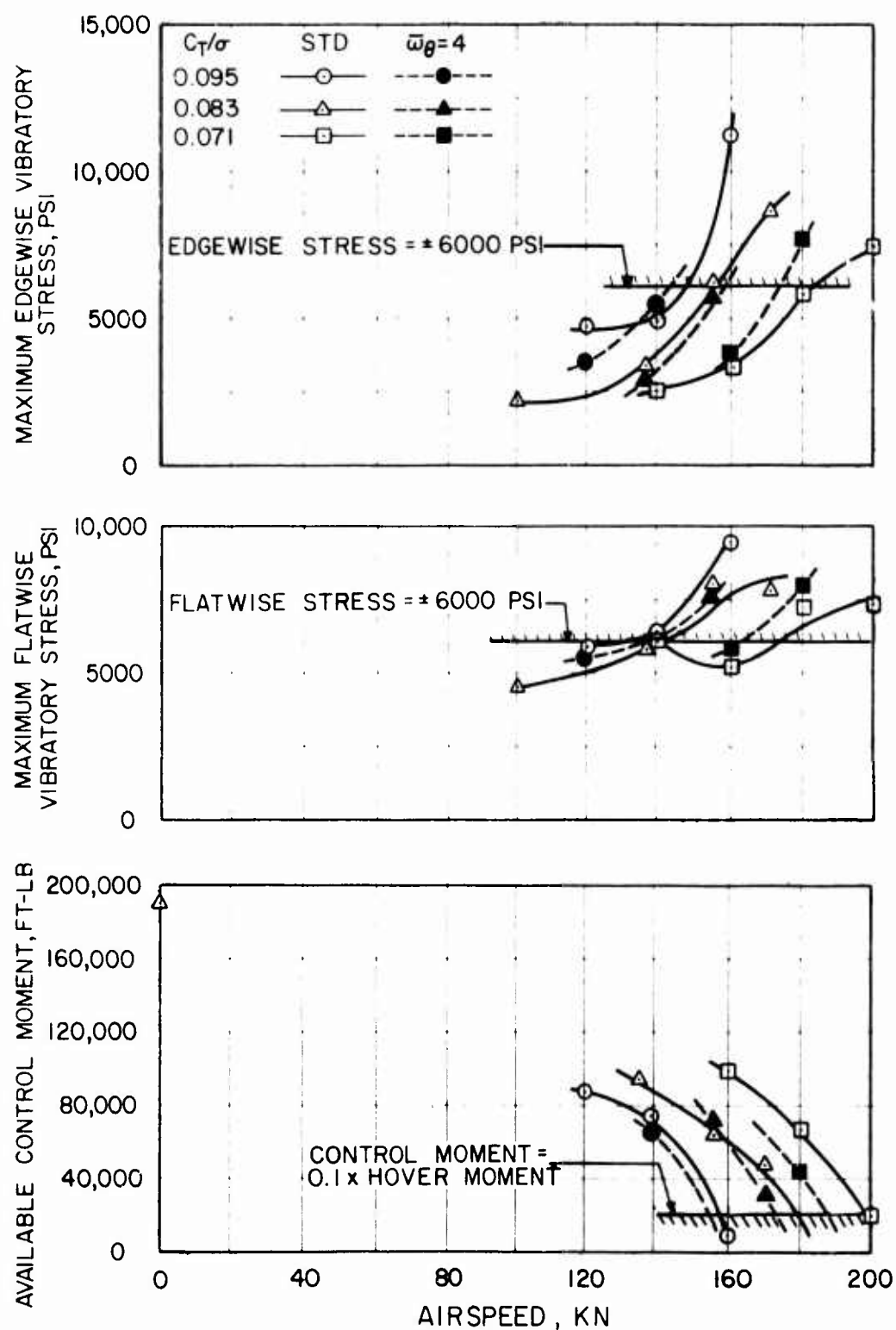


Figure 79. Effect of Reducing Torsional Natural Frequency on CH-53A Blade Stresses and Available Control Moment.

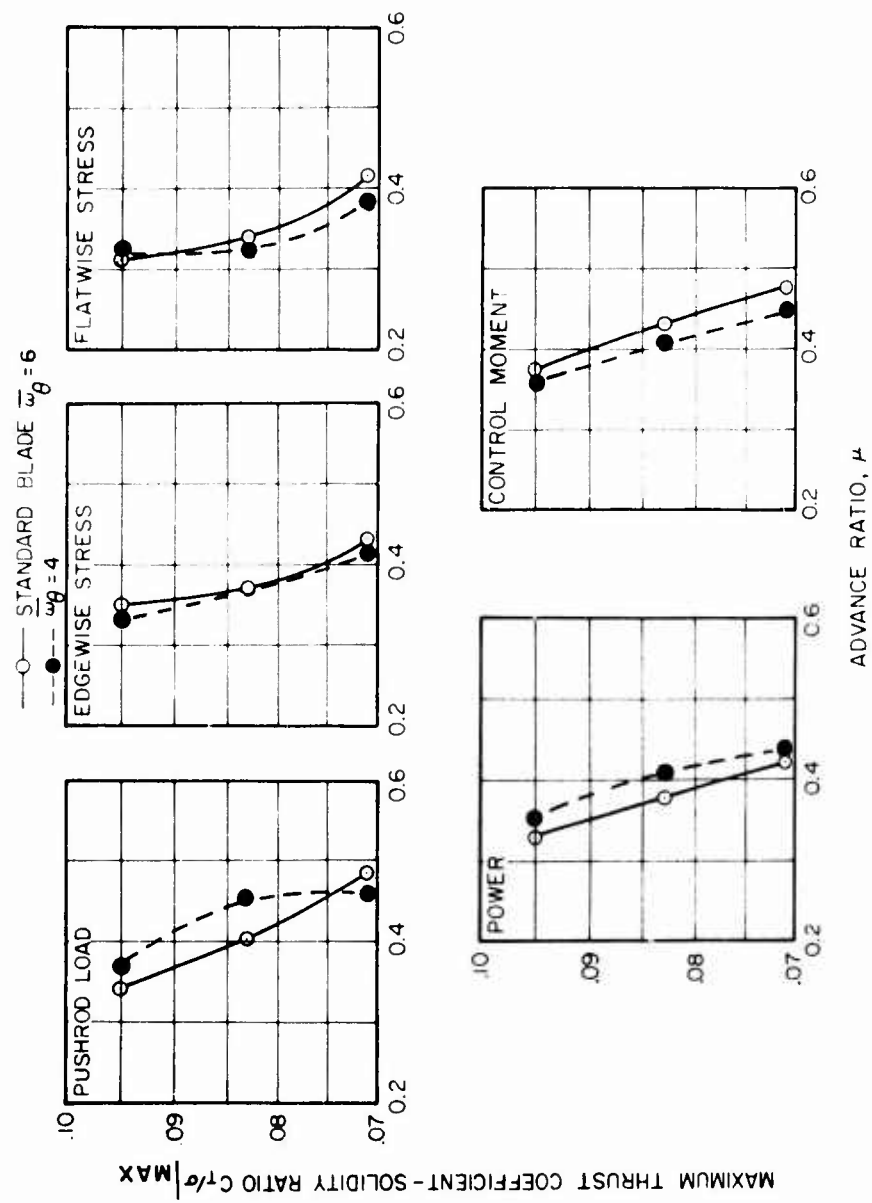


Figure 80. Effect of Reducing Torsional Natural Frequency on CH-53A Stall Boundaries.

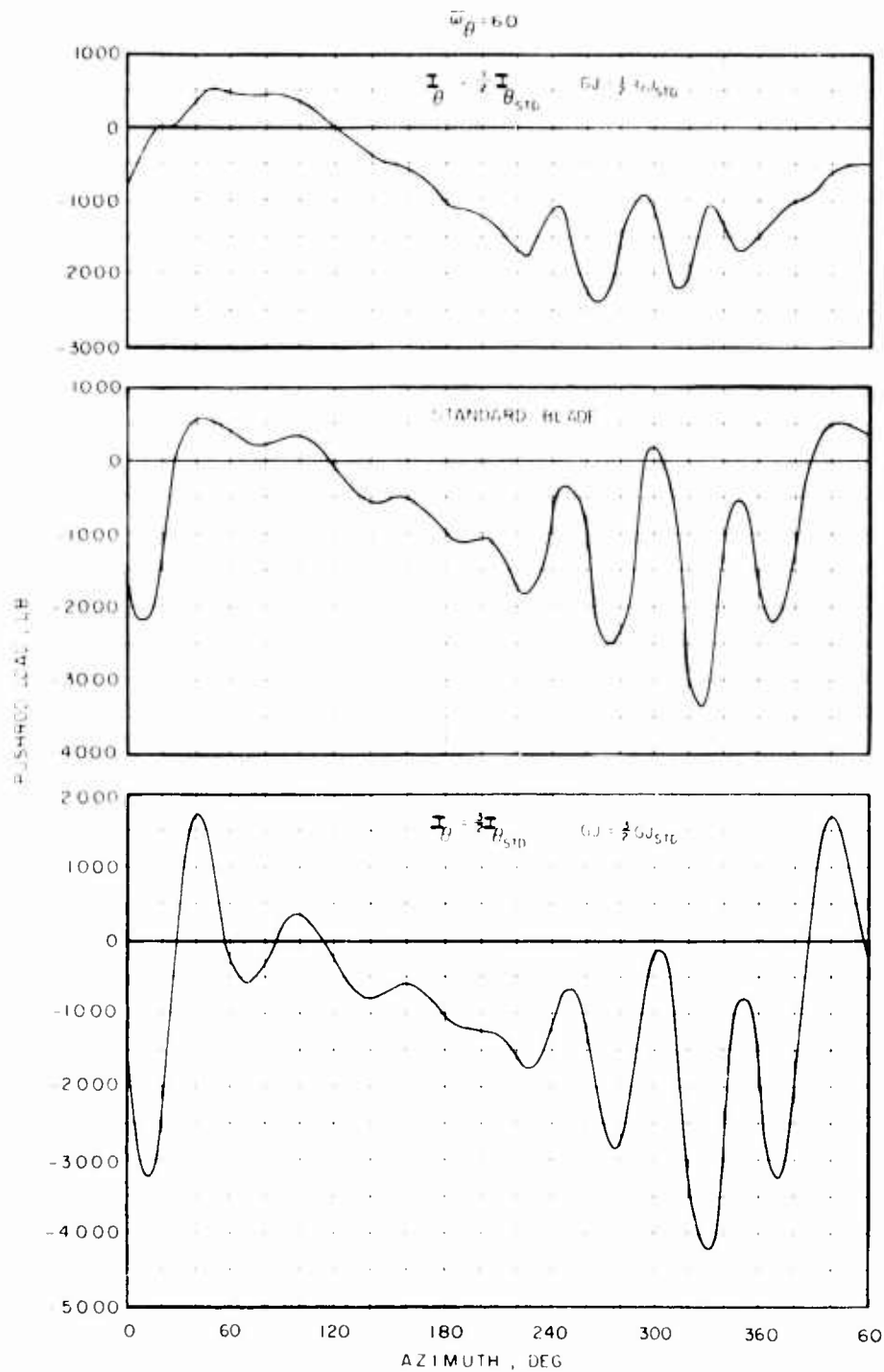


Figure 81. Variation in CH-53A Pushrod Load Time History With Changes in Torsional Inertia and Stiffness at 140 Kn and 49,000 Lb Gross Weight.

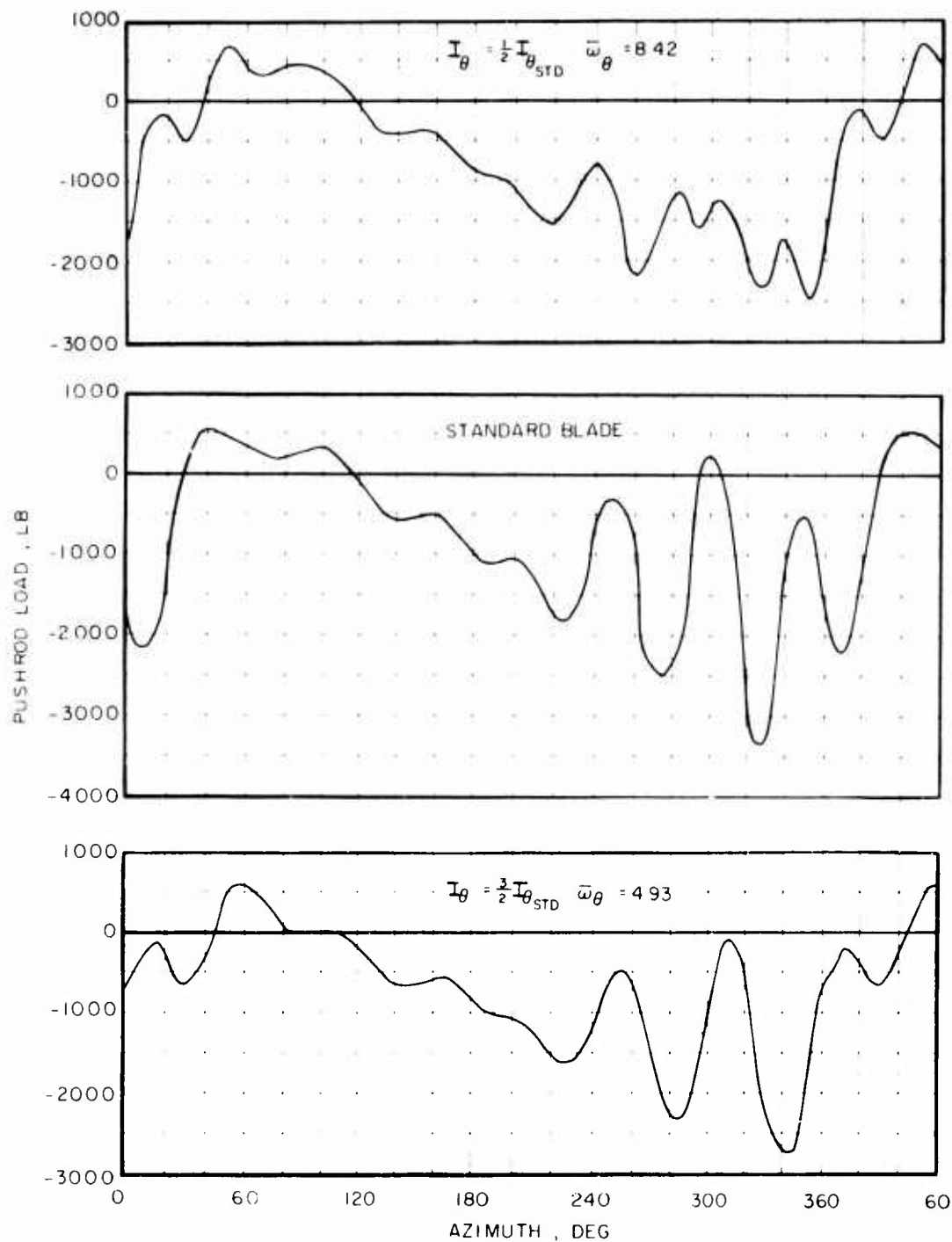


Figure 82. Variation in CH-53A Pushrod Load Time History With Changes in Torsional Inertia at 140 Kn and 49,000 Lb Gross Weight

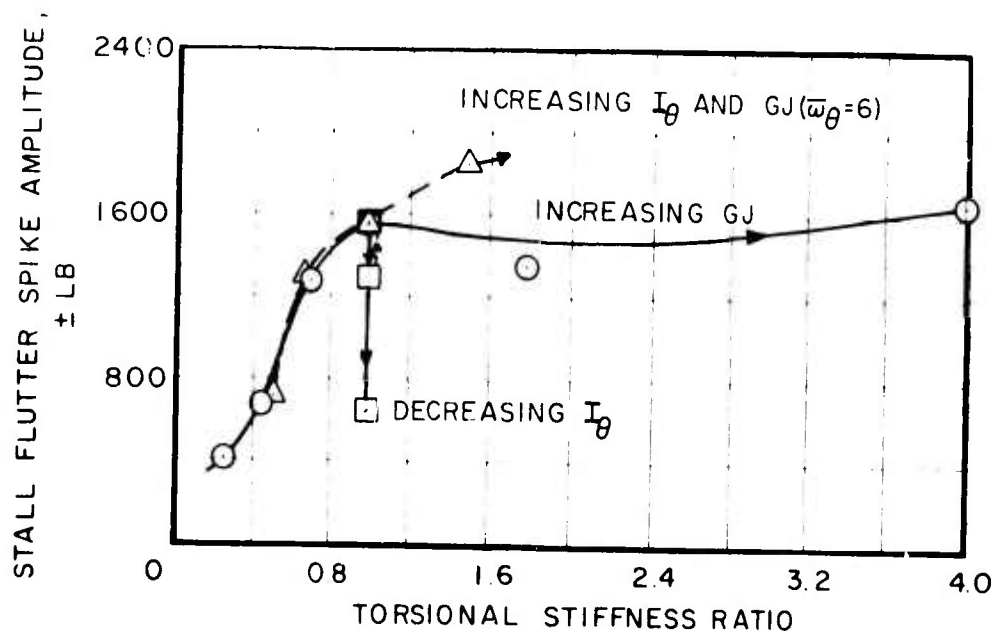
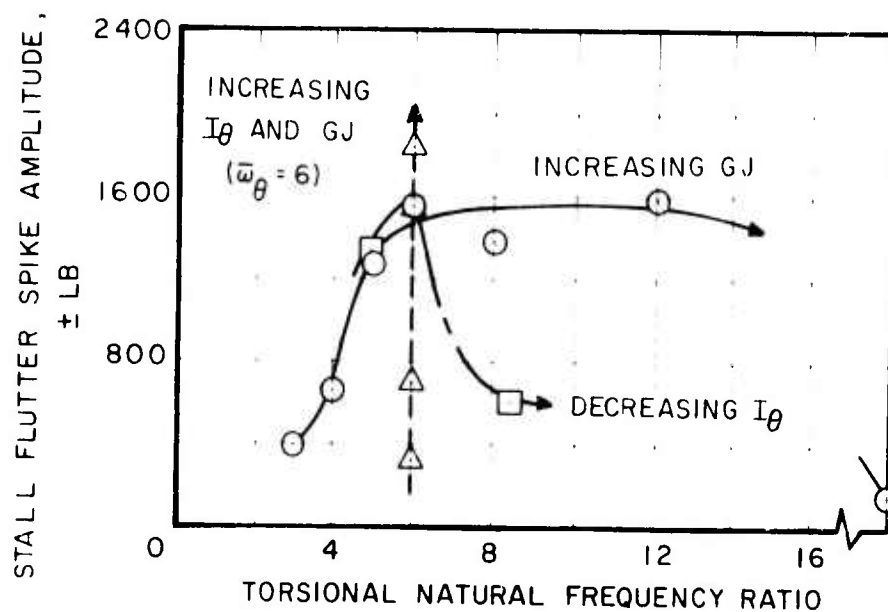


Figure 83. Trends of Stall Flutter Spike Amplitude With Torsional Frequency and Stiffness Ratios.

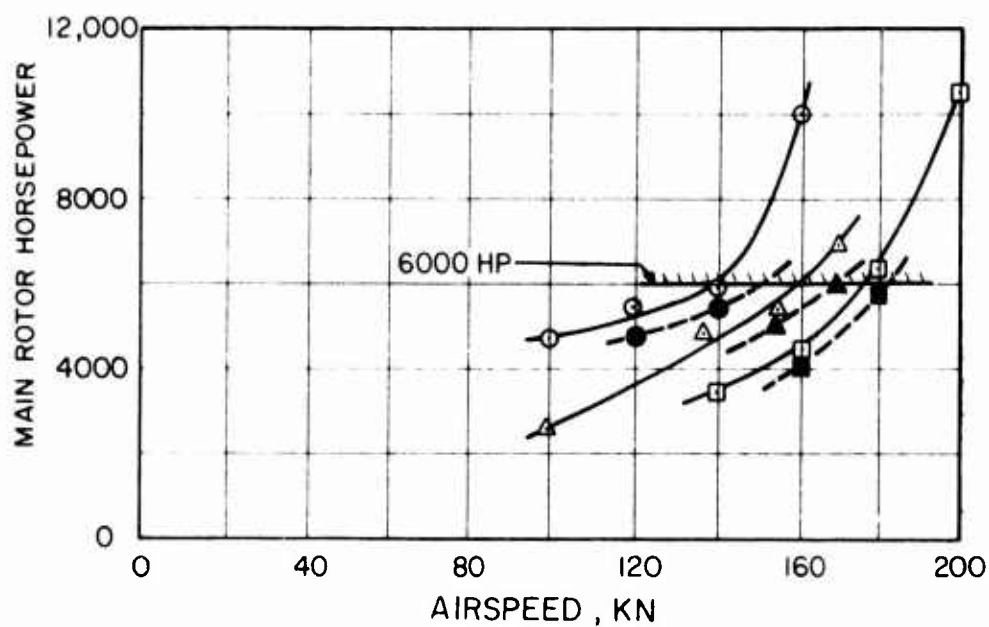
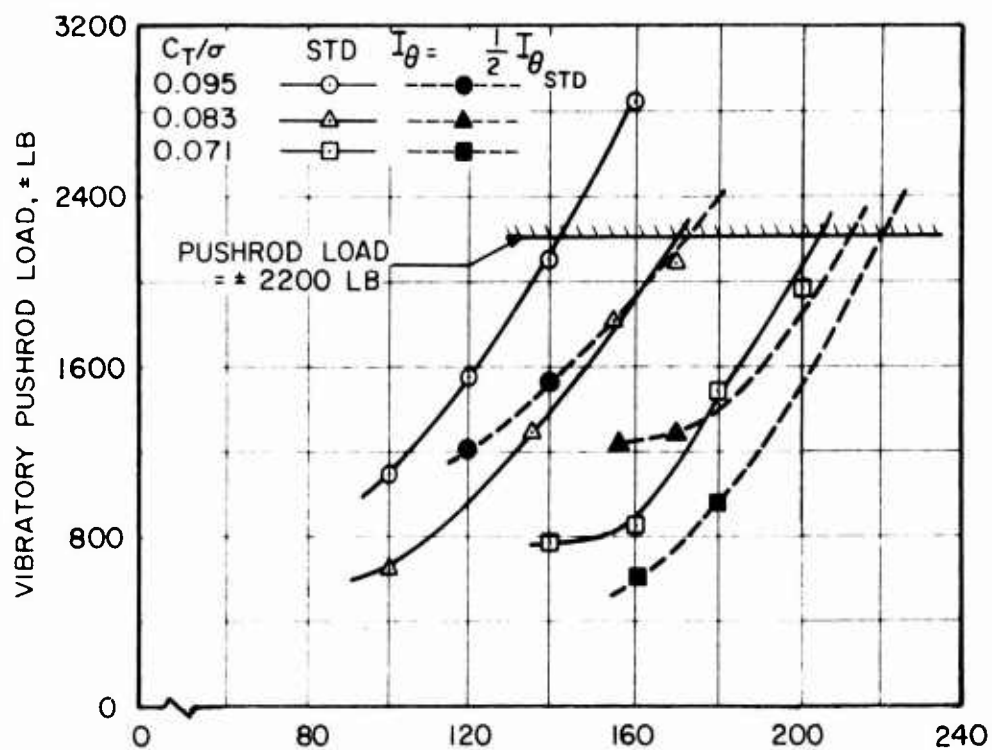


Figure 84. Effect of Decreased Torsional Inertia and Torsional Stiffness on CH-53A Vibratory Pushrod Load and Required Power.

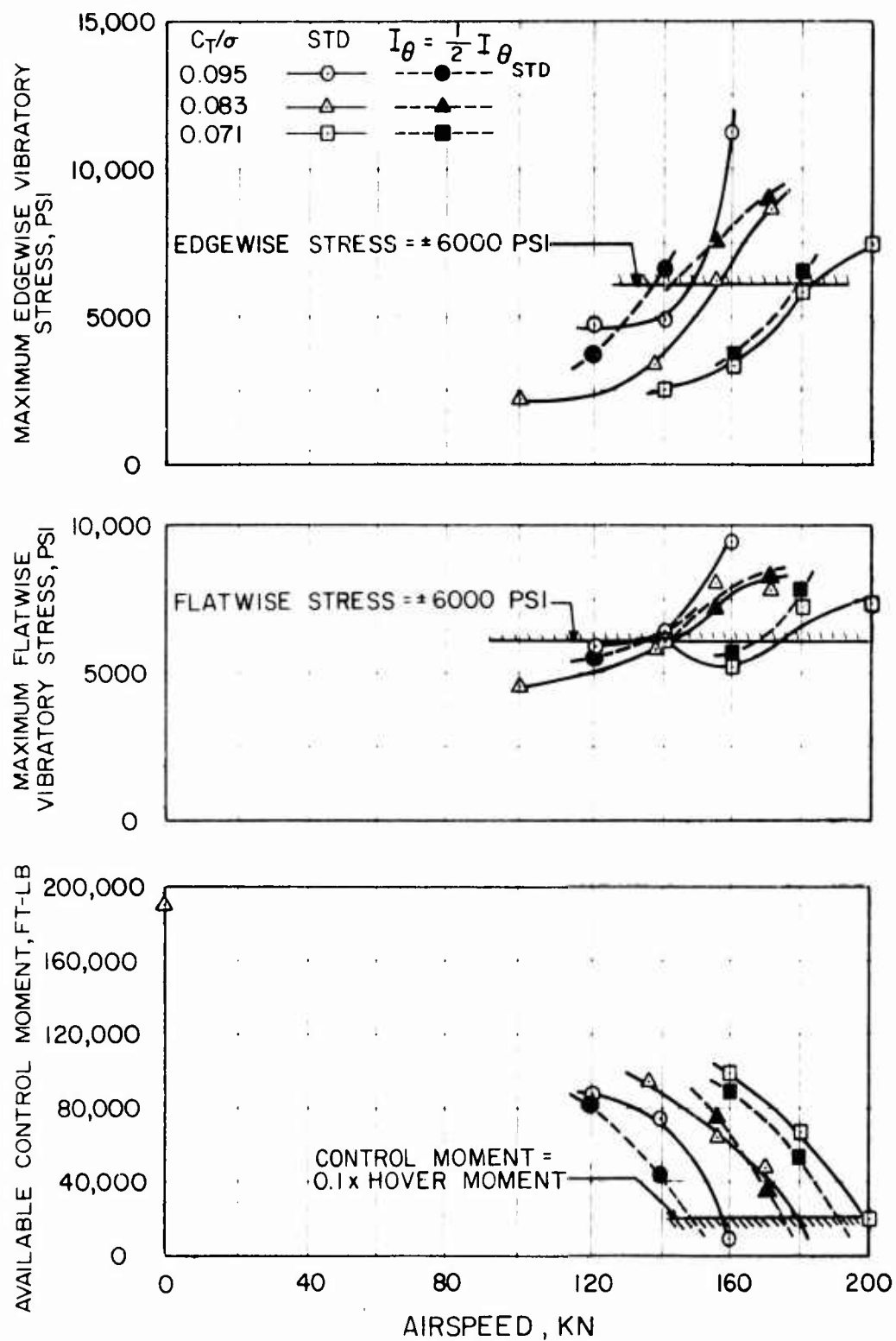


Figure 85. Effect of Decreased Torsional Inertia and Torsional Stiffness on CH-53A Blade Stress and Available Control Moment.

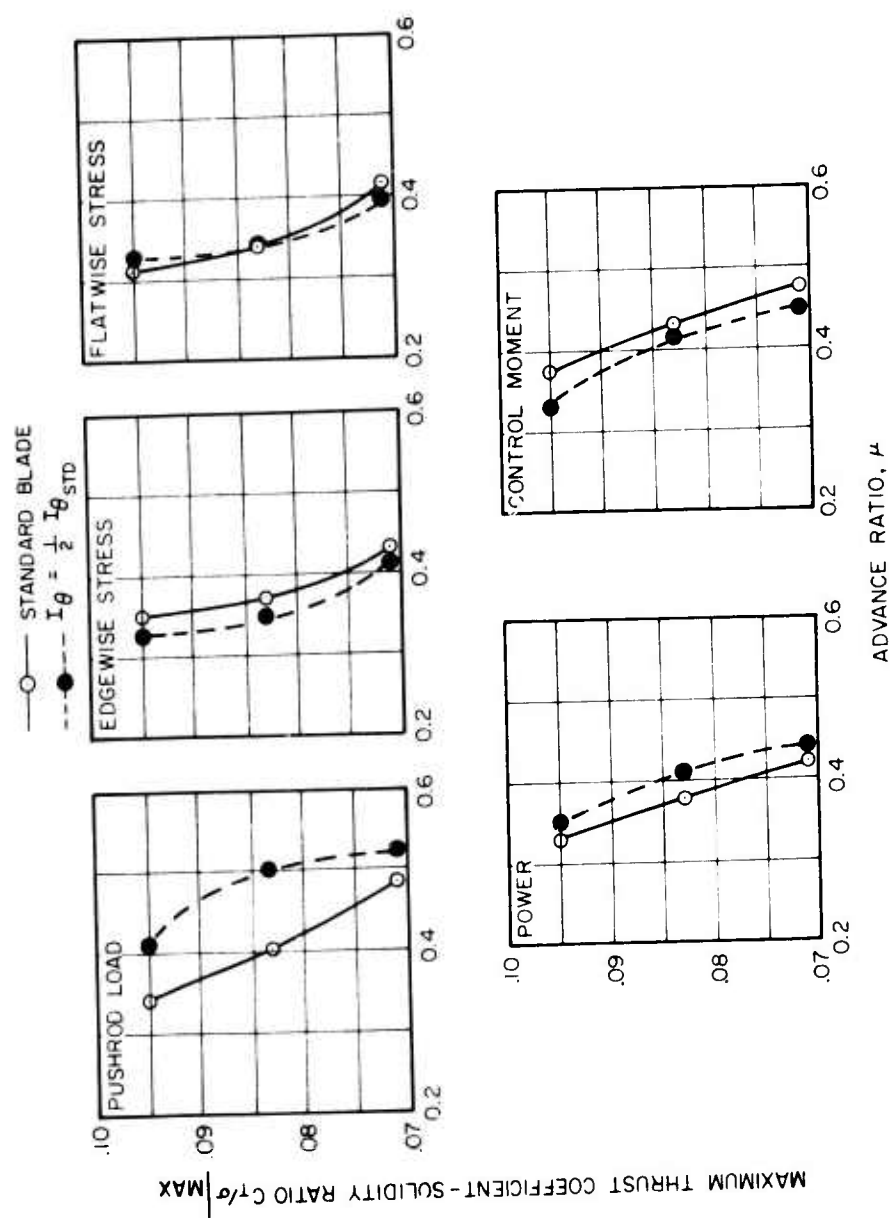


Figure 86. Effect of Decreased Torsional Inertia and Torsional Stiffness on CH-53A Stall Boundaries.

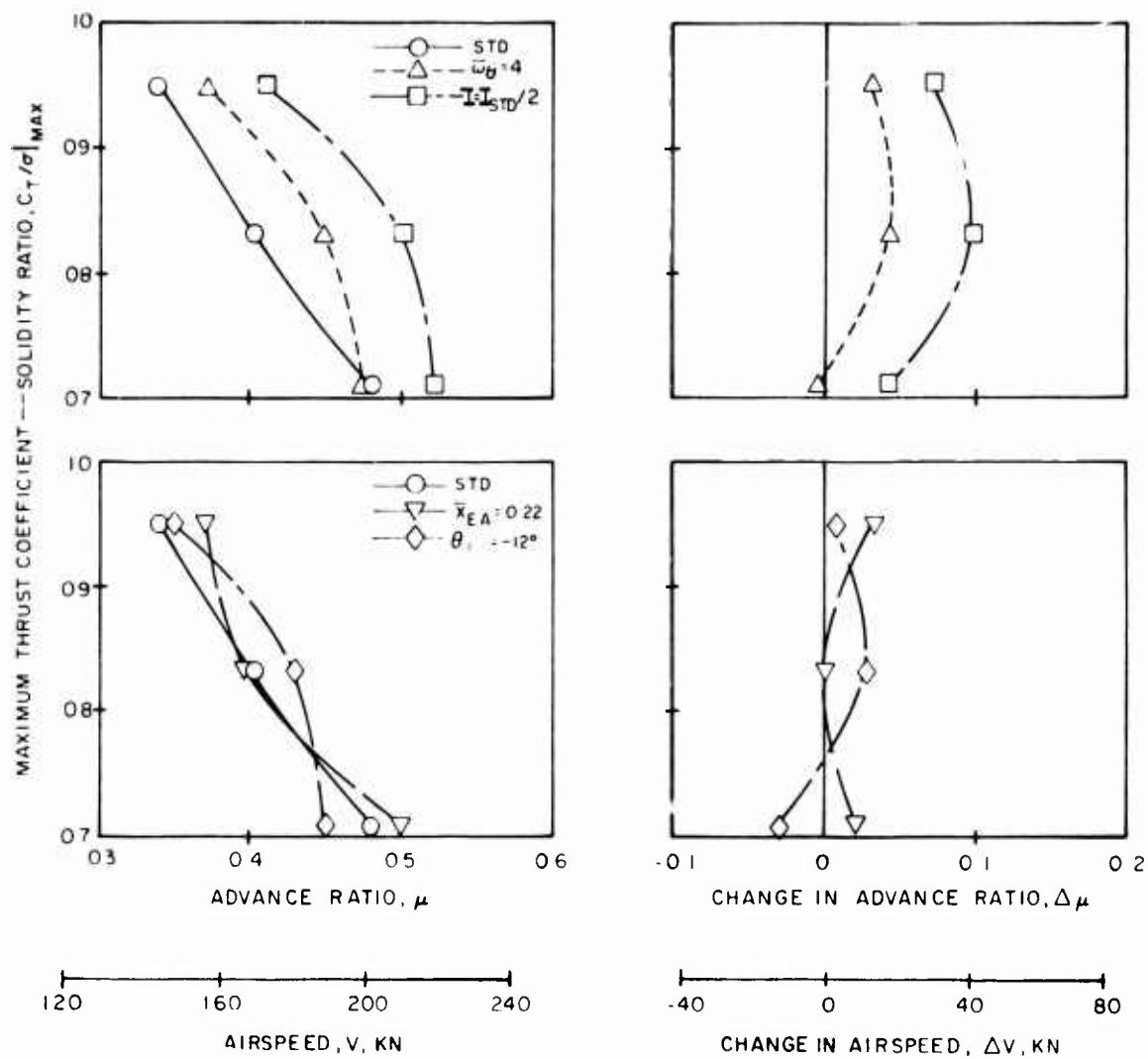


Figure 87. Effect of Blade Design Changes on the CH-53A Control Load Boundary.

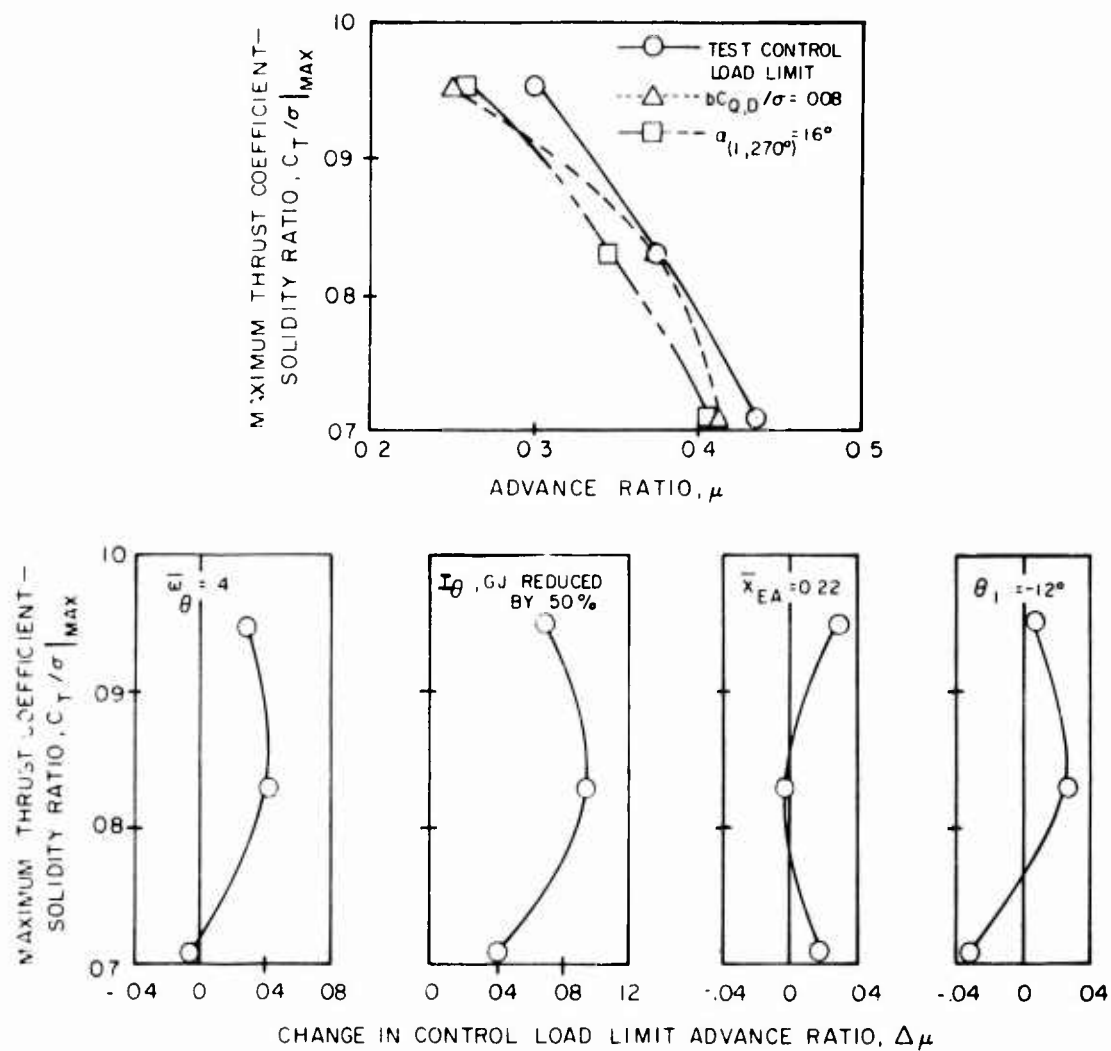


Figure 88. Modifications to the Control Load Stall Boundary To Be Used in Preliminary Design.

LIST OF SYMBOLS

A	dimensionless angular velocity
b	number of blades
B	dimensionless angular acceleration
B _{ls}	longitudinal cyclic pitch, deg, positive for increased pitch angle at 270 deg azimuth
c	airfoil chord, ft
C	mechanical damping per unit span, (ft-lb-sec/rad)/ft, Equation (5)
c _d	section drag coefficient
c _l	section lift coefficient
c _{lPOT}	potential flow section lift coefficient, Figure 18
c _{lSEP}	fully separated section lift coefficient, Figure 18
c _m	section pitching moment coefficient
c _{mc/4}	section pitching moment about quarter chord position
c _{mXPA}	section pitching moment coefficient around pitch axis
C.P.	airfoil section center of pressure, Figure 18
C _{Q,D}	rotor profile drag torque coefficient
C _T	rotor thrust coefficient $\frac{T}{\pi R^2 \rho (\Omega R)^2}$
c ₁ , c ₂	constants, Equation 13
f	frequency, cycles/sec
GJ	blade torsional stiffness per unit length, in.-lb/rad
h	jet height, ft, Equation (1)
h _D	density altitude, ft
I	airfoil torsional moment of inertia in pitch per unit span, (ft-lb-sec ²)/ft, Equation (5)

I_{REF}	reference value of airfoil torsional moment of inertia per unit span, (ft-lb-sec ²)/ft
I_O	airfoil or blade torsional inertia, ft-lb-sec ²
k	reduced frequency $\frac{c\omega_O}{2U_O}$
K	pitch spring stiffness per unit span, (ft-lb/rad)/ft, Equation (5)
K_{eq}	equivalent spring stiffness of flexure, in.-lb/rad
LF	load factor, Equation (10)
M	Mach number
M_a	applied aerodynamic moment per unit span, ft-lb/ft, Equation (5)
M_A	nondimensionalized blade aerodynamic pitching moment, positive for noseup twisting moment, Equation (11)
M_{CG}	nondimensionalized blade center-of-gravity offset torsional moment, positive for noseup twisting moment, Equation (11)
M_I	nondimensionalized blade torsional inertia moment, positive for noseup twisting moment, Equation (11)
M_S	nondimensionalized blade structural moment, positive for noseup twisting moment, Equation (11)
M_{SD}	nondimensionalized blade torsional moment caused by shear deflection effects, positive for noseup twisting moment, Equation (11)
M_O	flexure torsional moment, in.-lb
N_R	normal rotor rotational speed, rpm
P	period of model airfoil driving motion, sec
PM	rotor pitching moment, ft-lb, positive for nosedown moment
r	rotor section radial coordinate, ft
R	rotor radius, ft
t	time, sec
T	rotor thrust, lb
T_O	applied torque per unit span, ft-lb/ft, Equation (5)

U_o	free-stream velocity, ft/sec
V_c	calibrated airspeed, kn
W	aircraft gross weight, lb, Equation (10)
\bar{x}_{AC}	nondimensional chordwise aerodynamic center location
\bar{x}_{CG}	nondimensional chordwise center-of-gravity location
\bar{x}_{EA}	nondimensional chordwise elastic axis location
\bar{x}_{PA}	nondimensional chordwise pitch axis location
α_M	airfoil mean angle of attack, deg or rad
$\bar{\alpha}$	angular amplitude, deg or rad
α_1	static pitching moment stall angle, deg or rad, Figure 18
α_2	angle of attack above which center of pressure is assumed fixed, deg or rad, Figure 18
δc_l	c_l correction for scaling unsteady lift coefficient, Equation (7)
δc_m	c_m correction for scaling unsteady pitching moment coefficient, Equation (8)
δ_m	pitching moment coefficient correction curve for leading edge stall airfoil, rad, Equation (12)
$\delta \alpha_1$	angle of attack correction for scaling unsteady lift coefficient, rad, Equation (7)
δc_m	angle of attack correction for scaling unsteady moment coefficient, rad, Equation (8)
$\Delta \alpha$	angle of attack correction for open jet effects, rad, Equation (1)
Δc_d	open jet drag coefficient correction, Equation (2)
$\Delta c_{mC}/4$	open jet pitching moment correction, Equation (3)
Δt_{SEP}	time between static stall and dynamic lift stall, sec, Figure 18
$\Delta \theta_1$	half amplitude of airfoil torsional deflection, deg or rad, Figure 14
θ	airfoil or rotor torsional elastic deformation, deg, Equation (4)

θ_1	blade linear twist angle, deg, positive for tip twisted up relative to root
$\theta_{\frac{1}{2}PTP}$	half amplitude of overall airfoil torsional deflection, deg or rad, Figure 14
μ	rotor advance ratio
$\Xi_{\alpha 2}$	two-dimensional aerodynamic damping in pitch
ρ	air density, slugs/ft ³
σ	rotor solidity
τ	nondimensional time, t/P
τ_2, τ_3	nondimensional elapsed time, Figure 18
τ^*	nondimensional time delay constant for lift stall
τ_s	nondimensional time delay constant for moment stall
ψ	blade root azimuth angle measured from downstream blade position
ω_0	torsional natural frequency, cycles/sec
$\bar{\omega}_0$	torsional natural frequency ratio, ω_0/Ω
Ω	airfoil or rotor driving frequency, cycles/sec
$(\dot{})$	first derivative with respect to time
$(\ddot{})$	second derivative with respect to time
$()_G$	first generalized torsional mode